

THESIS  
3  
1999



This is to certify that the  
dissertation entitled  
INTERCALATED POLYMER-LAYERED INORGANIC  
NANOCOMPOSITES

presented by

Lei Wang

has been accepted towards fulfillment  
of the requirements for

Ph. D degree in Chemistry



Major professor

Date 5/10/99

**LIBRARY**  
**Michigan State**  
**University**

**PLACE IN RETURN BOX** to remove this checkout from your record.  
**TO AVOID FINES** return on or before date due.  
**MAY BE RECALLED** with earlier due date if requested.

| DATE DUE              | DATE DUE | DATE DUE |
|-----------------------|----------|----------|
| <del>MAR 12 200</del> |          |          |
|                       |          |          |
|                       |          |          |
|                       |          |          |
|                       |          |          |
|                       |          |          |

INTERCALATED POLYMER-LAYERED INORGANIC  
NANOCOMPOSITES

By

Lei Wang

A DISSERTATION

Submitted to  
Michigan State University  
in partial fulfillment of the requirements  
for the degree of

DOCTOR OF PHILOSOPHY

Department of Chemistry

1999

## ABSTRACT

### INTERCALATED POLYMER-LAYERED INORGANIC NANOCOMPOSITES

By

Lei Wang

The exfoliation-encapsulative precipitation (EEP) method, which was introduced by Kanatzidis and Bissessur in 1993, is both convenient and general. It enables the formation of an intercalated polymer-layered inorganic nanocomposite when a polymer solution and an inorganic monolayer suspension are mixed. Many MoS<sub>2</sub>/polymer nanocomposites were synthesized.

In this dissertation, we expand the investigation of the MoS<sub>2</sub> system, contribute a better understanding and provide a better manipulation of the reactions. Moreover, we further develop the EEP method by extending its application to other layered materials such as TaS<sub>2</sub>, MoO<sub>3</sub>,  $\alpha$ -RuCl<sub>3</sub> and WS<sub>2</sub>, and by modifying the method so that the intercalation of intractable polymers such as polypyrrole is possible.

In the research, it was found that “LiMoS<sub>2</sub>” would not be oxidized completely to MoS<sub>2</sub> upon exposure to water or air, and the exfoliation of “LiMoS<sub>2</sub>” in water is a process of solvation of Li<sub>x</sub>(H<sub>2</sub>O)<sub>y</sub>MoS<sub>2</sub> ( $x \sim 0.18$ ). Like A<sub>x</sub>(H<sub>2</sub>O)<sub>y</sub>TiS<sub>2</sub> (A = Li, Na, K), Li<sub>x</sub>(H<sub>2</sub>O)<sub>y</sub>MoS<sub>2</sub> can be exfoliated by stirring. Additional polymers such as polyacrylamide, polyvinylalcohol, polypropylene, polystyrene, polymethylmethacrylate, polybenzimidazole,

polyethyleneterephthalate and polypyrrole were encapsulated in MoS<sub>2</sub>. A convenient method to prepare “LiMoS<sub>2</sub>” was developed, which uses LiBH<sub>4</sub> as a reagent and runs at elevated temperatures (300-350 °C). This method can also be used to lithiate other layered transition metal dichalcogenides.

The lithium intercalated materials exfoliate well and encapsulate polymers better than the sodium intercalated materials, at least in the systems of 2H-TaS<sub>2</sub> and MoO<sub>3</sub>. At room temperature, LiBH<sub>4</sub> was proven a good lithiation reagent for 2H-TaS<sub>2</sub>, MoO<sub>3</sub> and  $\alpha$ -RuCl<sub>3</sub>. The amount of LiBH<sub>4</sub> used in the reaction is crucial to the exfoliation and encapsulation properties of the products. Water-soluble polymers such as poly(ethylene oxide) (PEO) and polyvinylpyrrolidone were intercalated in all three layered materials and polypyrrole was intercalated in RuCl<sub>3</sub>.

In addition,  $\alpha$ -RuCl<sub>3</sub>/polyaniline nanocomposites were prepared by the *in situ* redox intercalative polymerization method, which up to now was only applicable to FeOCl, V<sub>2</sub>O<sub>5</sub> and VOPO<sub>4</sub>. The reaction is driven by the reduction of some of the Ru<sup>3+</sup> centers to Ru<sup>2+</sup> and completed by the participation of ambient oxygen as an electron acceptor.

The large variety of new polymer-nanocomposites thus prepared have many interesting physical properties. For example, TaS<sub>2</sub> nanocomposites are superconductors at low temperatures; RuCl<sub>3</sub> nanocomposites have adjustable magnetic properties. The arrangement of PEO chains in the interlayer galleries was explored and we believe that MoS<sub>2</sub>/PEO, TaS<sub>2</sub>/PEO and RuCl<sub>3</sub>/PEO nanocomposites contain in each gallery two sheets of PEO chains in the type II PEO-HgCl<sub>2</sub> complex conformation. The two sheets of PEO chains are believed to have -O- atoms facing each other at the center of the gallery and provide Li<sup>+</sup> ions a good two-dimensional migration channel.

**To My Family, Who Have Believed Faithfully in and Dedicated Heartily to  
Science for Generations.**

## ACKNOWLEDGMENTS

I gratefully acknowledge the people who have helped me in all these years to fulfill the requirements for the Ph. D. degree. It would have been impossible to achieve such a high goal without the love and support from many people who are listed and not listed below.

First of all, I would like to thank my advisor, Prof. Mercuri Kanatzidis, for his guidance, encouragement and financial support. I have benefited substantially from his wise choosing of a productive research project for me, his requirement of a serious and aggressive research manner, and his priceless advice in many aspects.

I would like to express my great appreciation for Prof. John Allison for my admission to the Ph. D. program in the Department of Chemistry, which provided me the opportunity to pursue this degree. I would like to thank Prof. Thomas Pinnavaia, Prof. Gregory Baker and Prof. Marcos Dantus, who serve as my guidance committee members and lead me successfully to the completion of this degree. I also thank Prof. Pinnavaia and Prof. Baker for their generous permission for letting me use their instruments and facilities.

I enjoyed being a member in the Kanatzidis' group, in which one is always given assistance and offered friendship. I am in gratitude to the day-to-day help from every member of the group, especially from Joy Heising, Rhonda Patschke, Jason Hanco, Jennifer Aitken, Andy Axtell, Chenggang Wang, Rabin Bisserssur, Dr. Xianzhong Chen and Dr. Francois Bonhomme. I also thank other people in the department for their help, especially the people in Dr. Baker's group, Dr. Pinnavaia's group and Dr. Smith's group.

I thank Dr. Rui Huang for many training and measurements, Kermit Johnson for help with the solid state NMR measurements, Dr. Thomas Atkinson for the help with computers, Dr. John Heckman and Dr. Stanley Flegler in the Center for Electron Optics for their help in using TEM and SEM, and Dr. Reza Loloee in the Department of Physics and Astronomy for his help in using the SQUID. I also thank Prof. Kannewurf and his group at Northwestern University for the measurements of electrical conductivity and thermopower and Prof. Jin-Ho Choy at Seoul National University in Korea for the measurements of ion conductivity.

I thank the Department of Chemistry for guaranteeing assistantships for five years. Thanks also for the research funding from the National Science Foundation, and the Center for Fundamental Materials Research and the Center for Sensor Materials at MSU.

Finally, thanks to my wife and family for their deepest love and reserveless support.

## TABLE OF CONTENTS

|  |      |
|--|------|
| List of Tables .....   | xiii |
| List of Figures .....  | xv   |
| List of Abbreviations .....  | xx   |
| Introduction .....   | 1    |
| 1. Intercalation Reactions and Layered Host Materials .....  | 1    |
| 2. The Development of Polymer Intercalation .....  | 7    |
| 3. Exfoliation-Encapsulative Precipitation: An Effective<br>Method for Polymer Intercalation .....   | 11   |
| 4. Applications of Intercalation Compounds and Nanocomposites .....  | 14   |
| 5. Important Contributions of the Present Dissertation Work .....  | 18   |
| References .....   | 22   |
| Chapter 1. Further Exploration of Exfoliated MoS <sub>2</sub> and Synthesis of<br>New MoS <sub>2</sub> Nanocomposites with the Exfoliation-Encapsulative<br>Precipitation Method ..... | 32   |
| Introduction .....   | 32   |
| Experimental Section .....   | 35   |
| 1. Reagents .....  | 35   |
| 2. Lithiation and Exfoliation of MoS <sub>2</sub> .....  | 35   |
| 3. Investigation of LiMoS <sub>2</sub> and Freshly Restacked MoS <sub>2</sub> .....  | 38   |
| 4. Preparation of MoS <sub>2</sub> /Polymer Nanocomposites .....   | 39   |
| 5. Instrumentation .....   | 44   |

|  |    |
|--|----|
| Results and Discussion .....   | 46 |
| 1. The $\text{LiBH}_4$ Method of Producing $\text{LiMoS}_2$ .....  | 46 |
| 2. Manipulation and Properties of Exfoliated and Restacked $\text{MoS}_2$ .....  | 49 |
| 3. $(\text{PEO})_x\text{MoS}_2$ and $(\text{PVP})_x\text{MoS}_2$ Nanocomposites .....  | 51 |
| 4. Investigations in $(\text{PA6})_x\text{MoS}_2$ Nanocomposites .....   | 55 |
| 5. Synthesis of $(\text{PS})_x\text{MoS}_2$ Nanocomposites .....   | 59 |
| 6. Synthesis of Other $\text{MoS}_2$ /Polymer Nanocomposites .....   | 61 |
| 7. The Phase Transition in Restacked $\text{MoS}_2$ and $\text{MoS}_2$ Nanocomposites .....  | 64 |
| 8. Thermal Stability of $\text{MoS}_2$ Nanocomposites .....  | 67 |
| Concluding Remarks .....   | 70 |
| Appendix A .....   | 72 |
| References .....   | 75 |
| <br>Chapter 2. Insertion of Polypyrrole and Poly(N-methyl pyrrole) in $\text{MoS}_2$ and $\text{WS}_2$ by <i>in situ</i> Polymerization-Encapsulative Precipitation Method ..... | 78 |
| Introduction .....   | 78 |
| Experimental Section .....   | 80 |
| 1. Reagents .....  | 80 |
| 2. Preparation of $\text{MoS}_2$ /PPY Nanocomposites .....   | 80 |
| 3. Preparation of $\text{WS}_2$ /PPY Nanocomposites .....  | 83 |
| 4. Instrumentation .....   | 84 |

|   |     |
|---|-----|
| Results and Discussion .....  | 85  |
| 1. MoS <sub>2</sub> /PPY Nanocomposites .....   | 85  |
| 2. WS <sub>2</sub> /PPY Nanocomposites .....  | 92  |
| 3. An Analysis of Polymer Arrangements inside<br>the Interlayer Galleries Based on the Dimensions of<br>the Polymer Molecules ..... | 94  |
| 4. Thermal Properties .....   | 96  |
| 5. Charge Transport Properties .....  | 100 |
| Concluding Remarks .....  | 104 |
| Appendix B .....  | 106 |
| References .....  | 111 |
| Chapter 3. Lamellar TaS <sub>2</sub> /Polymer Nanocomposites through<br>Encapsulative Precipitation of Exfoliated Layers .....      | 116 |
| Introduction .....  | 116 |
| Experimental Section .....  | 118 |
| 1. Reagents .....   | 118 |
| 2. Synthesis of 2H-TaS <sub>2</sub> .....   | 119 |
| 3. Synthesis and Exfoliation of Li <sub>x</sub> TaS <sub>2</sub> .....  | 119 |
| 4. Encapsulative Precipitation of Polymers .....  | 120 |
| 5. Instrumentation and Measurements .....   | 121 |
| Results and Discussion .....  | 125 |
| 1. Exfoliation Properties of Li <sub>x</sub> TaS <sub>2</sub> .....   | 125 |
| 2. Polymer Encapsulation .....  | 126 |

|  |     |
|--|-----|
| 3. Characterization of $\text{Li}_x\text{TaS}_2$ /Polymer Nanocomposites .....                     | 127 |
| 4. Structural Studies: The Conformation of PEO in<br>$\text{Li}_x(\text{PEO})_y\text{TaS}_2$ ..... | 132 |
| 5. Superconductive State .....   | 137 |
| 6. Electrical Transport Properties .....   | 143 |
| 7. Solid State NMR Spectroscopy .....  | 146 |
| Concluding Remarks .....   | 153 |
| References .....   | 155 |
| <b>Chapter 4. Lamellar <math>\text{Li}_x\text{MoO}_3</math>/Polymer Nanocomposites</b>             |     |
| <i>Via Encapsulative Insertion</i> .....   | 159 |
| Introduction .....   | 159 |
| Experimental Section .....   | 160 |
| 1. Reagents .....  | 160 |
| 2. Synthesis of $\text{Li}_x\text{MoO}_3$ ( $0.30 < x < 0.40$ ) .....                              | 161 |
| 3. Preparation of $\text{Li}_x\text{MoO}_3$ /Polymer Nanocomposites .....                          | 162 |
| 4. Instrumentation .....   | 162 |
| Results and Discussion .....   | 163 |
| 1. Synthesis and Characterization of $\text{Li}_x\text{MoO}_3$ .....                               | 163 |
| 2. Exfoliation and Polymer Encapsulation Chemistry .....   | 165 |
| 3. Solid State NMR Spectroscopy .....  | 176 |
| 4. Magnetism .....   | 178 |
| 5. Electrical Conductivity .....   | 181 |

|  |     |
|--|-----|
| Concluding Remarks .....   | 181 |
| References .....   | 183 |
| Chapter 5. $\alpha$ -RuCl <sub>3</sub> /Polymer Nanocomposites: the First Group of<br>Intercalative Nanocomposites with Transition-Metal-Halides ..... | 186 |
| Introduction .....   | 186 |
| Experimental Section .....   | 189 |
| 1. Reagents .....  | 189 |
| 2. Reactions and Sample Preparations .....   | 189 |
| 3. Instrumentation .....   | 194 |
| Results and Discussion .....   | 194 |
| 1. Preparation of (PANI) <sub>x</sub> RuCl <sub>3</sub> by <i>in situ</i> Redox Intercalative<br>Polymerization .....                                  | 194 |
| 2. Nanocomposites of $\alpha$ -RuCl <sub>3</sub> with Water Soluble Polymers ..  | 202 |
| 3. $\alpha$ -RuCl <sub>3</sub> /Polypyrrole Nanocomposites .....   | 204 |
| 4. Charge Transport Properties .....   | 206 |
| 5. Magnetic Susceptibility Studies .....   | 209 |
| 6. One-Dimensional Electron Density Calculation and<br>Arrangement of Polymer Chains in Li <sub>x</sub> (PEO) <sub>y</sub> RuCl <sub>3</sub> .....     | 217 |
| 7. PEO Conformation from IR Spectra .....  | 226 |
| Concluding Remarks .....   | 229 |
| References .....   | 231 |

## LIST OF TABLES

|  |     |
|--|-----|
| Table 1. Elements forming layered transition metal dichalcogenides .....   | 2   |
| Table 1.1. Nylon-6 intercalation reactions with PA6/CF <sub>3</sub> CH <sub>2</sub> OH solution .....                                    | 59  |
| Table 1.2. Information about the synthesis of MoS <sub>2</sub> /PS nanocomposites .....  | 60  |
| Table 1.3. Characteristics of some new MoS <sub>2</sub> nanocomposites .....   | 63  |
| Table 1.4. Evolution rates of restacked MoS <sub>2</sub> and nanocomposites derived from the change of electrical resistivity .....      | 67  |
| Table 1.5. The effect of high temperature annealing to some nanocomposites .....   | 68  |
| Table 2.1. Parameters of (PPY) <sub>x</sub> MoS <sub>2</sub> prepared with different pyrrole ratios .....                                | 88  |
| Table 2.2. Structural data of PPY and PMPY nanocomposites .....  | 94  |
| Table 2.3. Room temperature electrical conductivities of PPY nanocomposites and restacked MoS <sub>2</sub> and WS <sub>2</sub> .....     | 100 |
| Table 3.1. The annealing procedure to produce 2H-TaS <sub>2</sub> .....  | 119 |
| Table 3.2. Polymer Intercalation in Li <sub>x</sub> TaS <sub>2</sub> .....   | 127 |
| Table 3.3. Properties of Li <sub>0.2</sub> TaS <sub>2</sub> and polymer nanocomposites .....   | 129 |
| Table 3.4. Properties of the superconductive state for TaS <sub>2</sub> intercalates .....   | 138 |
| Table 3.5. Effect of film orientation on the <sup>7</sup> Li-NMR spectrum of Li <sub>0.2</sub> (PEO) <sub>y</sub> TaS <sub>2</sub> ..... | 153 |
| Table 4.1. Chemical and structural characteristics of Li <sub>x</sub> MoO <sub>3</sub> /polymer nanocomposites .....                     | 166 |

|  |     |
|--|-----|
| Table 4.2. Composition and physicochemical properties of the $\text{Li}_x\text{MoO}_3$ /polymer nanocomposites ..... | 175 |
| Table 5.1. Magnetic properties of $\alpha\text{-RuCl}_3$ and nanocomposites .....                                    | 213 |
| Table 5.2. A comparison of IR absorptions ( $\text{cm}^{-1}$ ) of PEO .....  | 228 |

## LIST OF FIGURES

|   |    |
|---|----|
| Figure 1.1. Experimental set-up for the high temperature $\text{LiBH}_4$ lithiation reaction .....  | 37 |
| Figure 1.2. XRD patterns of a $(\text{PEO})_x\text{MoS}_2$ nanocomposite used to calculate the one-dimensional electron density map .....                               | 53 |
| Figure 1.3. One-dimensional electron density map of a $(\text{PEO})_x\text{MoS}_2$ nanocomposite .....  | 53 |
| Figure 1.4. Structural model for the $(\text{PEO})_x\text{MoS}_2$ nanocomposite .....   | 54 |
| Figure 1.5. XRD patterns of the new nanocomposite phases .....  | 56 |
| Figure 1.6. Evolution of the electrical resistivity of a restacked $\text{MoS}_2$ sample as a function of time .....  | 65 |
| Figure 1.7. XRD patterns of the $(\text{PEO})_x\text{MoS}_2$ and $(\text{PP})_x\text{MoS}_2$ nanocomposites before and after the high temperature annealing .....       | 68 |
| Figure 1.8. Intensity of the 001 peak in the XRD patterns of a $(\text{PEO})_x\text{MoS}_2$ sample at increasing temperatures .....                                     | 69 |
| Figure 1.9. Curve fitting for the time dependence of electrical conductivity of $(\text{PEO})_x\text{MoS}_2$ .....  | 74 |
| Figure 2.1. XRD patterns of $\text{MoS}_2$ nanocomposites .....   | 86 |
| Figure 2.2. IR spectra of PPY and a $\text{MoS}_2/\text{PPY}$ nanocomposite prepared by procedure 1 .....   | 87 |
| Figure 2.3. IR spectrum of a $\text{MoS}_2/\text{PPY}$ nanocomposite prepared by procedure 1 and heating treated twice up to 300 °C under $\text{N}_2$ atmosphere ..... | 87 |
| Figure 2.4. IR spectra of a nanocomposite $(\text{PPY})_{0.51}(\text{H}_2\text{O})_{0.18}\text{MoS}_2$ prepared by procedure 2 .....                                    | 90 |
| Figure 2.5. XRD patterns of $\text{WS}_2/\text{PPY}$ nanocomposites .....   | 93 |

|   |     |
|---|-----|
| Figure 2.6. IR spectrum of $(\text{PPY})_{0.25}(\text{H}_2\text{O})_{0.53}\text{WS}_2$ heating treated twice up to 320 °C under $\text{N}_2$ atmosphere .....                                       | 93  |
| Figure 2.7. DSC measurements at different heating rates for $(\text{PPY})_{0.51}(\text{H}_2\text{O})_{0.18}\text{MoS}_2$ .....  | 97  |
| Figure 2.8. Plot of the DSC heating rate versus the temperature of the $\text{MoS}_2$ structural transition for $(\text{PPY})_{0.51}(\text{H}_2\text{O})_{0.18}\text{MoS}_2$ .....                  | 97  |
| Figure 2.9. DSC measurement for $(\text{PPY})_{0.25}(\text{H}_2\text{O})_{0.53}\text{WS}_2$ .....   | 98  |
| Figure 2.10. Plot of the DSC heating rate versus the $\text{WS}_2$ structural transition temperature in $(\text{PPY})_{0.25}(\text{H}_2\text{O})_{0.53}\text{WS}_2$ .....                           | 98  |
| Figure 2.11. Variable temperature electrical conductivity measurements on pressed pellets for pristine $\text{MoS}_2$ and a $\text{MoS}_2/\text{PPY}$ nanocomposite prepared with Procedure 1 ..... | 102 |
| Figure 2.12. Thermoelectric power measurement on a pressed pellet for $(\text{PPY})_{0.25}(\text{H}_2\text{O})_{0.16}\text{MoS}_2$ prepared with Procedure 1 .....                                  | 102 |
| Figure 2.13. Variable temperature electrical conductivity measurements on pressed pellets for restacked $\text{WS}_2$ and $(\text{PPY})_{0.25}(\text{H}_2\text{O})_{0.53}\text{WS}_2$ .....         | 103 |
| Figure 2.14. Thermoelectric power measurement on a pressed $(\text{PPY})_{0.25}(\text{H}_2\text{O})_{0.53}\text{WS}_2$ pellet .....   | 103 |
| Figure 2.15. Schematic structures and dimensions of PPY and PMPY .  | 109 |
| Figure 2.16. Views of PMPY .....  | 110 |
| Figure 3.1. XRD patterns of $\text{Li}_x\text{TaS}_2/\text{polymer}$ nanocomposites .....   | 128 |
| Figure 3.2. DSC of a $\text{Li}_{0.2}(\text{PEO})_y\text{TaS}_2$ nanocomposite .....  | 130 |
| Figure 3.3. SEM photograph of a $\text{Li}_{0.2}(\text{PEO})_y\text{TaS}_2$ film .....  | 131 |
| Figure 3.4. Powder XRD patterns of a folded $\text{Li}_{0.2}(\text{PEO})_y\text{TaS}_2$ film ...  | 133 |
| Figure 3.5. One-dimensional electron density maps for the $\text{Li}_x(\text{PEO})_y\text{TaS}_2$ nanocomposite .....   | 134 |

|   |     |
|---|-----|
| Figure 3.6. Structural model for the $\text{Li}_{0.2}(\text{PEO})_y\text{TaS}_2$ nanocomposite ..   | 135 |
| Figure 3.7. Variable temperature magnetic susceptibility for $\text{Li}_{0.2}\text{TaS}_2$ and $\text{Li}_{0.2}(\text{PEO})_y\text{TaS}_2$ powders .....  | 140 |
| Figure 3.8. Variable temperature magnetic susceptibility for $\text{Li}_{0.2}(\text{PEO})_y\text{TaS}_2$ films .....  | 141 |
| Figure 3.9. Variable temperature electrical conductivity measurements for pressed pellets of $\text{Li}_{0.2}(\text{PEO})_y\text{TaS}_2$ .....  | 144 |
| Figure 3.10. Variable temperature thermopower data of pressed pellets of $\text{Li}_{0.2}(\text{PEO})_y\text{TaS}_2$ .....  | 144 |
| Figure 3.11. Electron diffraction pattern and superstructure of $\text{Li}_{0.2}\text{TaS}_2$ .....   | 145 |
| Figure 3.12. Static solid state $^7\text{Li}$ NMR spectra of $\text{Li}_{0.2}\text{TaS}_2$ and $\text{Li}_{0.2}(\text{PEO})_y\text{TaS}_2$ .....  | 148 |
| Figure 3.13. Temperature dependence of the linewidth of $^7\text{Li}$ NMR resonance peaks for $\text{Li}_{0.2}\text{TaS}_2$ and $\text{Li}_{0.2}(\text{PEO})_y\text{TaS}_2$ .....                           | 149 |
| Figure 3.14. Room temperature $^7\text{Li}$ NMR spectra for a $\text{Li}_{0.2}(\text{PEO})_y\text{TaS}_2$ film .....  | 152 |
| Figure 4.1. DSC diagram of $\text{Li}_x\text{MoO}_3$ .....  | 164 |
| Figure 4.2. IR spectra of $\text{Li}_x(\text{H}_2\text{O})_y(\text{PVP})_z\text{MoO}_3$ .....   | 167 |
| Figure 4.3. Solid-state optical absorption spectra of the $\text{Li}_x\text{MoO}_3/\text{polymer}$ nanocomposites .....   | 168 |
| Figure 4.4. Typical XRD patterns of nanocomposites with poly(ethylene glycol) and poly(ethylene oxide) of different molecular mass .....  | 169 |
| Figure 4.5. Typical XRD patterns of the various $\text{Li}_x\text{MoO}_3/\text{polymer}$ nanocomposites .....   | 170 |
| Figure 4.6. XRD patterns of $\text{Li}_x(\text{H}_2\text{O})_y(\text{PEO-2000})_z\text{MoO}_3$ showing the effect of annealing on the stacking regularity of the layered structure of a nanocomposite ..... | 174 |

|   |     |
|---|-----|
| Figure 4.7. Static $^7\text{Li}$ NMR spectra of $\text{Li}_x\text{MoO}_3$ and $\text{Li}_x(\text{H}_2\text{O})_y(\text{PEO})_z\text{MoO}_3$ at $-80\text{ }^\circ\text{C}$ .....  | 177 |
| Figure 4.8. Temperature dependence of the linewidth of the resonance peak in solid-state $^7\text{Li}$ MNR spectra of $\text{Li}_x\text{MoO}_3$ and $\text{Li}_x(\text{H}_2\text{O})_y(\text{PEO})_z\text{MoO}_3$ ..... | 177 |
| Figure 4.9. Temperature dependence of magnetic susceptibility of $\text{Li}_x\text{MoO}_3$ and $\text{Li}_x(\text{H}_2\text{O})_y(\text{PEO})_z\text{MoO}_3$ .....  | 179 |
| Figure 4.10. Variable-temperature electrical conductivity measurements for $\text{Li}_x\text{MoO}_3$ and $\text{Li}_x(\text{H}_2\text{O})_y(\text{PEO})_z\text{MoO}_3$ .....  | 180 |
| Figure 5.1. The structure of $\alpha\text{-RuCl}_3$ .....   | 188 |
| Figure 5.2 Experimental set-up for the synthesis of $\alpha\text{-RuCl}_3$ .....  | 190 |
| Figure 5.3. X-ray diffraction patterns of $\alpha\text{-RuCl}_3$ and nanocomposites .....   | 196 |
| Figure 5.4. Transmission X-ray diffraction patterns of $\alpha\text{-RuCl}_3$ and $(\text{PANI})_x\text{RuCl}_3$ with indexing .....  | 197 |
| Figure 5.5(a). Infrared spectra of $(\text{PANI})_x\text{RuCl}_3$ , PANI and aniline ....   | 198 |
| Figure 5.5(b). Infrared spectra of $(\text{PPY})_x\text{RuCl}_3$ and PPY.....   | 199 |
| Figure 5.5(c). Infrared spectra of $\text{Li}_x(\text{PEO})_y\text{RuCl}_3$ and PEO .....   | 200 |
| Figure 5.5(d). Infrared spectra of $\text{Li}_x(\text{PVP})_y\text{RuCl}_3$ and PVP .....   | 201 |
| Figure 5.6. Electron diffraction patterns with the electron-beam perpendicular to the planess for $\alpha\text{-RuCl}_3$ and $\text{Li}_x\text{RuCl}_3$ .....   | 203 |
| Figure 5.7. Variable temperature electrical conductivity measurements for pressed pellets of $\alpha\text{-RuCl}_3$ and nanocomposites .....  | 207 |
| Figure 5.8. Thermopower measurements for pressed pellets of $\text{Li}_x\text{RuCl}_3$ ( $x \sim 0.2$ ) and nanocomposites .....  | 208 |
| Figure 5.9(a). Magnetic susceptibility measurements for a sample of $\alpha\text{-RuCl}_3$ .....  | 211 |

|   |         |
|---|---------|
| Figure 5.9(b). Magnetic susceptibility measurements for $\text{Li}_x\text{RuCl}_3$ .....  | 211     |
| Figure 5.9(c). Magnetic susceptibility measurements for $\text{Li}_x(\text{PEO})_y\text{RuCl}_3$ .....  | 212     |
| Figure 5.9(d). Magnetic susceptibility measurements for $(\text{PANI})_x\text{RuCl}_3$ .....  | 212     |
| Figure 5.10(a). Magnetic susceptibility measurements for “ $\text{Br}_2$ oxidized $\text{Li}_x\text{RuCl}_3$ ” ( <i>i.e.</i> $\text{RuCl}_3$ ) .....                                | 214     |
| Figure 5.10(b). Magnetic susceptibility measurements for “ $\text{Br}_2$ oxidized $\text{Li}_x(\text{PEO})_y\text{RuCl}_3$ ” ( <i>i.e.</i> “ $(\text{PEO})_x\text{RuCl}_3$ ”) ..... | 214     |
| Figure 5.10(c). Magnetic hysteresis measurements for “ $\text{Br}_2$ oxidized $\text{Li}_x\text{RuCl}_3$ ” ( <i>i.e.</i> $\text{RuCl}_3$ ) .....                                    | 215     |
| Figure 5.10(d). Magnetic hysteresis measurements for “ $\text{Br}_2$ oxidized $\text{Li}_x(\text{PEO})_y\text{RuCl}_3$ ” ( <i>i.e.</i> “ $(\text{PEO})_x\text{RuCl}_3$ ”) .....     | 215     |
| Figure 5.11. Possible PEO conformations .....   | 219     |
| Figure 5.12. X-ray powder diffraction pattern of oriented $\text{Li}_x(\text{PEO})_y\text{RuCl}_3$ film used for the calculation of one-dimensional electron density maps .....     | 220     |
| Figure 5.13. One-dimensional electron density maps for $\text{Li}_x(\text{PEO})_y\text{TaS}_2$ and $\text{Ag}_x(\text{PEO})_y\text{TaS}_2$ .....                                    | 220-222 |
| Figure 5.14. Structural model for $\text{Li}_x(\text{PEO})_y\text{RuCl}_3$ .....  | 223     |

## LIST OF ABBREVIATIONS

|                             |  |
|-----------------------------|--|
| 1-D ED.....                 | one-dimensional electron density                             |
| 1T-MoS <sub>2</sub> .....   | octahedral form MoS <sub>2</sub>                             |
| 2H- MoS <sub>2</sub> .....  | hexagonal form MoS <sub>2</sub>                              |
| AF.....                     | antiferromagnetism   |
| $\chi_{\text{dia}}$ .....   | diamagnetic susceptibility                                   |
| cm.....                     | centimeter   |
| $\chi_{\text{molar}}$ ..... | molar susceptibility   |
| $\chi_{\text{para}}$ .....  | paramagnetic susceptibility                                  |
| $\chi_{\text{TIP}}$ .....   | susceptibility of temperature-independent paramagnetism      |
| DSC.....                    | differential scanning calorimeter                            |
| $E_a$ .....                 | activation energy  |
| EDS.....                    | energy dispersive X-ray microanalysis                        |
| EEP.....                    | exfoliation-encapsulative precipitation                      |
| FM.....                     | formamide  |
| FTIR .....                  | Fourier transform infrared spectroscopy                      |
| g .....                     | gram   |
| GR .....                    | Guaranteed Reagent (suitable for uses in analytic chemistry) |
| h .....                     | hour   |
| i-PrOH.....                 | isopropynol  |
| ICP.....                    | inductively coupled plasma                                   |
| IR.....                     | infrared spectroscopy  |
| kJ.....                     | kilojoule  |
| M.....                      | molarity   |
| $\mu_B$ .....               | Bohr magneton  |
| Mcel .....                  | methyl cellulose   |
| $\mu_{\text{eff}}$ .....    | effective magnetic moment                                    |
| min.....                    | minute   |
| ml .....                    | milliliter   |
| mmol.....                   | millimole  |
| mol.....                    | mole   |
| MW.....                     | molecular weight   |
| NMF.....                    | N-methylformamide  |
| NMR .....                   | nuclear magnetic resonance                                   |
| PA6.....                    | nylon-6  |
| PAM.....                    | polyacrylamide   |
| PANI.....                   | polyaniline  |
| PBI.....                    | polybenzimidazole  |
| PE.....                     | polyethylene   |
| PEG .....                   | poly(ethylene glycol)  |

|                              |  |
|------------------------------|--|
| PEI.....                     | polyethylenimine                                 |
| PEO.....                     | poly(ethylene oxide)                             |
| PETP.....                    | poly(ethylene terephthalate)                     |
| PLD-CDW.....                 | periodic lattice distortion-charge density wave  |
| PMMA.....                    | poly(methyl methacrylate)                        |
| PMPY.....                    | poly(N-methyl pyrrole)                           |
| PP.....                      | polypropylene                                    |
| PPG.....                     | poly(propylene glycol)                           |
| PPY.....                     | polypyrrole                                      |
| PS.....                      | polystyrene                                      |
| PVA.....                     | poly(vinyl alcohol)                              |
| PVP.....                     | poly(N-vinyl pyrrolidone)                        |
| $\theta$ (in magnetism)..... | Weiss constant                                   |
| $\theta$ (in XRD).....       | Bragg angle                                      |
| s.....                       | second   |
| SEM.....                     | scanning electron microscopy                     |
| $T_c$ .....                  | critical temperature of superconducting state    |
| TEM.....                     | transmission electron microscope                 |
| TGA.....                     | thermal gravimetric analysis                     |
| UV-VIS-NIR.....              | ultraviolet-visible-(near infrared) spectroscopy |
| XRD.....                     | X-ray diffraction                                |

# INTRODUCTION

## 1. Intercalation Reactions and Layered Host Materials

In chemistry, the term "intercalation" has been used to describe reactions in which guest atoms, molecules or ions are inserted into layered host lattices while the host lattices reserve their essential structural features. Literally, intercalation chemistry dates from 1840 when Schafhäütl inserted sulfate ion in graphite [1]. Nevertheless, the subject had not drawn the attention of chemists, physicists and scientists in other fields until 1926 when Fredenhagen and Cadenbach discovered the insertion of potassium atoms from the vapor into graphite [2]. In the 1960s, research in this area grew significantly and extended into many scientific disciplines. Most of the work has focused on the intercalation phenomenon and the effect of intercalation on the physical properties of the host materials [3]. An important aspect of this research is the alkali metal intercalation in transition metal dichalcogenides, which modifies both the lattice structures and the electronic properties of the hosts [4]. The discovery in the late 1960s by Gamble et al [5], which showed that the critical temperature ( $T_c$ ) for the onset of superconductivity in 2H-TaS<sub>2</sub> could shift from 0.8 K to about 7 K upon amine intercalation, was one of the most exciting events in intercalation chemistry. An eye-catching research at present is the intercalation of inorganic or organic compounds in the high- $T_c$  superconductors to adjust the properties and explore the mechanism of the superconductivity [6]. In recent years, with the accumulation of a substantial amount of knowledge about intercalation materials and the improvement of the synthetic skills, the aim is set to explore the use of intercalation reactions to synthesize novel and potentially applicable materials [7]. The investigation of inorganic/polymeric intercalation compounds, or

ceramic/polymeric nanocomposites, is accelerated by this aim, and bursts into a major branch in the field of nanophase-materials [8, 9].

The materials which are intensively studied by intercalation are members of the seven most common groups of layered materials, including graphite, layered transition metal dichalcogenides, layered transition metal oxides, layered metal oxyhalides, layered metal phosphorus trichalcogenides, layered acid salts of tetravalent metals, and sheet silicates<sup>[10]</sup>. Graphite is the simplest host material and it shows diverse intercalation chemistry due to its stability to both oxidation and reduction. The known intercalating reagents range from strong oxidants to powerful reductants <sup>[11]</sup>.

Table 1. Elements forming layered transition metal dichalcogenides

| Transition Metal |     |      |     |      | Chalcogen |
|------------------|-----|------|-----|------|-----------|
| IV               | V   | VI   | VII | VIII | VI        |
|                  |     |      |     |      | S         |
| Ti               | (V) | (Cr) |     |      | Se        |
| Zr               | Nb  | Mo   |     | Pd   | Te        |
| Hf               | Ta  | W    | Re  | Pt   |           |

Other layered materials have been explored since the beginning of the sixties. Layered transition metal dichalcogenides form a large group, since most of the transition metals from group IV, V, VI and some from group VII and VIII can form dichalcogenides of layered structures (Table 1). The intercalation chemistry of the layered dichalcogenides is mainly characterized by the reduction of the host lattices. Simple and hydrated cations, and organic and organometallic ions can be included between the layers of the lattices through electron donating processes. The layered

dichalcogenides have many unusual physical properties due to their electronic structures (partial d-orbital filling) as well as their low dimensionality, and these properties are adjustable by intercalation [4].

Similar to layered dichalcogenides are the layered oxides, which exhibit quite the same intercalation chemistry. The best known of these are molybdenum oxide, tungsten oxide and vanadium oxide, which form various bronzes with alkali metals [12]. Layered oxyhalides MOCl ( M= Fe, Ti, V and Cr) [13] and InOX ( X= Cl, Br and I) [10b] exhibit some interesting intercalation chemistry.

Metal phosphorus trisulfides of the formula MPS<sub>3</sub> form a broad and diverse class of compounds. The metal M includes Mg, Ca, V, Mn, Fe, Co, Ni, Zn, Pd, Cd, Hg, In, Sn, and Pb. Metal phosphorus triselenides of the similar layered structure also exist. Examples are FePSe<sub>3</sub>, MgPSe<sub>3</sub>, MnPSe<sub>3</sub>, CdPSe<sub>3</sub>, SnPSe<sub>3</sub>, PbPSe<sub>3</sub> and HgPSe<sub>3</sub>. Like transition metal dichalcogenides, metal phosphorus trisulfides react with electron donors and their intercalation chemistry is mostly confined to 3 major classes of guests: alkali metals, organic amines and organometallic molecules. Ion exchange reactions with intralayer M<sup>2+</sup> ions and non-redox intercalation reactions have also been developed recently [14].

Layered silicates and layered acid salts are currently of considerable interest, because of technological applications in heterogeneous catalysis, and as sorbents and inorganic ion-exchangers. Their intercalation chemistry is predominantly of reactions with cations by ion-exchange, or with neutral molecules [15]. Layered silicates include many naturally existing and synthetic clay minerals [16]. Layered acid salts of tetravalent metals have the general formula M<sup>IV</sup>(HXO<sub>4</sub>)<sub>2</sub>.nH<sub>2</sub>O (X=P, As). The most extensively investigated species is  $\alpha$ -zirconium bis(monohydrogen orthophosphate) [ $\alpha$ -Zr(HPO<sub>4</sub>)<sub>2</sub>.H<sub>2</sub>O] [17]. The protons of these acid salts can

be easily replaced by other cations, so the layered acid salts are considered attractive inorganic ion-exchangers. Also included in layered acid salts are hydrogen uranyl phosphate and arsenate,  $\text{H}_2\text{UO}_2\text{PO}_4 \cdot 4\text{H}_2\text{O}$  and  $\text{H}_2\text{UO}_2\text{AsO}_4 \cdot 4\text{H}_2\text{O}$  [18], while vanadyl and niobyl compounds of the type  $\text{VO}_2\text{XO}_4$  and  $\text{NbO}_2\text{XO}_4$  ( $\text{X} = \text{S}, \text{P}, \text{As}, \text{Mo}$ ) are quite similar compounds [19].

Besides the seven large groups of layered materials, some groups of layered inorganic compounds and some individuals that are not so common have also been studied in intercalation. Reduced halides such as  $\text{ZrCl}_2$ ,  $\text{ZrBr}_2$  and  $\text{ThI}_2$  possess an important property involving reversible hydrogen uptake to form ordered, stoichiometric phases.  $\alpha\text{-RuCl}_3$ ,  $\text{Ni}(\text{CN})_2$  and  $\beta\text{-ZrNCl}$  also undergo intercalation reactions [10b].  $\text{HFe}(\text{SO}_4)_2 \cdot 4\text{H}_2\text{O}$  intercalates monovalent or divalent ions along with the reduction of Fe(III) centers [20].

Lamellar double hydroxides of the general formula  $[\text{M}^{\text{II}}_{1-x}\text{M}^{\text{III}}_x(\text{OH})_2][\text{X}^{\text{m-}}_{x/m} \cdot n\text{H}_2\text{O}]$  (where the  $\text{X}^{\text{m-}}$  is a halide anion or an oxo-anion) are designated as "anionic clays", and are of great interest for their capability to anion exchange [21].  $[\text{Zn}_{1-x}\text{Al}_x(\text{OH})_2][\text{Cl}_x \cdot n\text{H}_2\text{O}]$  and  $[\text{Cu}_{1-x}\text{Cr}_x(\text{OH})_2][\text{Cl}_x \cdot n\text{H}_2\text{O}]$  are examples of them. Basic copper acetate is another anion exchangeable layered compound [7b]. A large series of layered niobates, titano-niobates and titanates with perovskite related structure and with alkali metal cations in interlayer sites have been developed in recent years [15, 22]. Ion-exchange, intercalation of amines, exfoliation and even electrochemical alkali metal insertion can be applied to this group of layered oxides. Recently, intercalation chemistry is also found in the pillaring of buaerite ( $\text{Na}_4\text{Mn}_{14}\text{O}_{26} \cdot x\text{H}_2\text{O}$ ) [23], the ion-exchange of birnessite ( $\text{Na}_{0.32}\text{MnO}_2 \cdot n\text{H}_2\text{O}$ ) [24], and the metal atom or simple molecule insertion in the misfit layered sulfides [25].

The variety of layered inorganic compounds mentioned above provides a broad choice of layered materials. To make these materials constituents of nanocomposites, the chemistry of intercalation reaction is the decisive factor. The common synthetic methods for intercalation include direct insertion, ion-exchange, exfoliation and flocculation, and electro-intercalation [10b]. The intercalation of alkali metals and other metals into graphite, transition metal dichalcogenides, transition metal oxides and oxyhalides, and metal phosphorus trichalcogenides can be realized by direct intercalation. The insertion processes are accompanied by the charge transfer from the intercalants to the host lattices. It is believed that the tendency for this charge transfer is the driving force for the intercalation reaction. Organic molecules can also be intercalated into the same type of hosts through direct intercalation. Only Lewis-base (electron-donating) organic compounds can be intercalated. The nature of the bond between an intercalated molecule and the host layer is inquired. An old model proposed a weak covalent bond involving no charge transfer<sup>[26]</sup>. More recent studies suggest that the molecule-host “bond” is substantially ionic. In the new model, part of the intercalated molecules are ionized by donation of an electron to the layer, whereas the remainder of the molecules are neutral and solvate the ionized species [27].

Ion-exchange can be used to prepare intercalation compounds with hosts of charged layers, such as clays, layered acid salts, and lamellar double hydroxides. When a charged layered compound is immersed in a concentrated solution containing a replacing ion, the interlayer ion can often be replaced by the other ion. The exchange reaction is driven by the great excess of the replacement ion. In the cases of neutral oxidizing layered hosts such as transition metal chalcogenides, once a metal ion has been intercalated it can subsequently be ion-exchanged. In many cases, the

approach of pre-intercalating with an alkali metal ion and ion-exchanging the alkali metal cation with the target guest cation provides a useful strategy for the intercalation of large guest cations which do not intercalate directly.

Frequently, ion-exchange cannot be achieved in one step because the replacing ion is very large whereas the interlayer gallery and the resident ion are small. Multi-step ion-exchange processes are needed to overcome this difficulty. By replacing the resident ion with suitable ions of intermediate sizes, the gallery of the host can be opened gradually so that finally the target guest ion can be inserted [17a]. The introduction of large target ions by stepwise ion-exchanges clearly demonstrates the fact that the high activation energies associated with the deformation of the layered structures to accommodate the incoming guests can be overcome if the host lattices can be expanded by pre-intercalation of smaller molecules or ions. If this strategy is taken to its extreme and the host layers are completely dispersed or exfoliated, very large molecules or ions can be included. This is the case of intercalation by exfoliation and flocculation. Smectic clays can be swelled in water and then intercalated with large cations such as polyoxometallates [16, 28].  $\text{Na}_{0.33}\text{TaS}_2$  has been exfoliated in N-methylformamide/ $\text{H}_2\text{O}$  solution and intercalated with a large cluster cation  $[\text{Fe}_6\text{S}_8(\text{PEt}_3)_6]^{2+}$  [29].

Finally, electro-intercalation provides a convenient way to prepare metal intercalation complexes. Its advantages over conventional techniques are its simplicity, facile control of stoichiometry, and fast rate of reaction at room temperature. In addition, it provides a convenient method to carry out detailed thermodynamic measurements and study the staging phenomenon [10b].

These four well developed intercalation methods are very effective in the simple ion and small molecule intercalation. They also shine light on the strategies for polymer intercalation. However, because the macromolecules are much greater in size and are usually chemically inert, the practice of polymer intercalation is still full of obstacles and advances slowly. The following section will show that the strategies applied to the polymer intercalation are often different from the simple ion and small molecule intercalation.

## **2. The Development of Polymer Intercalation**

The synthesis of inorganic/polymeric intercalative compounds is aimed at the materials for potential applications. Intercalation provides a molecular level combination of two extremely different components, which is expected to produce materials with superior or novel properties. Small-molecule intercalation complexes are not a preferred choice, because they intend to de-intercalate so that their compositions are not stable. Stability is a prerequisite for a material in practical use. The polymer intercalants, in contrast, stay in the interlayer galleries of inorganic lattices after the formation of intercalative complexes, which assure steady compositions for the nanocomposites. In addition, the polymers possess mechanical strength. The polymer chains dangling from the layered structure hold the layered materials together, so that the nanocomposites can be produced in various forms, such as films and bulk materials, without additional supporting substances. Both polymers and layered hosts are usually air and moisture stable, so the nanocomposites can be used in ambient conditions without much concern.

There exist a large number of layered materials and polymers, so the combinations are numerous. The advance of the intercalative

nanocomposites depends on the development of the synthetic methods for these materials, which are evolving from the conventional intercalation methods. In the 1960s and early 1970s, various types of ions and small molecules had been intercalated into layered inorganic compounds, while the intercalation of large molecules such as organic cations, large clusters and polymers was still rare, even though the synthesis of inorganic/polymeric intercalative complexes had been carried on since 1965 [30]. This situation existed because the intercalation of large molecules is kinetically unfavorable and the reaction is technically harder.

The intercalation of robust cations was realized in later 1970s, which led to the intercalated smectite derivatives with pore sizes larger than those of faujasitic zeolites. These intercalated smectite derivatives are known as "pillared clays" [31].

On the other side, the worldwide interest in polymer intercalation increased substantially in 1987 when Okada et al developed clay/polyamide nanocomposites [32,33] and Kanatzidis et al synthesized inorganic/(conductive polymer) layered complexes [34]. The clay/nylon-6 nanocomposites exhibited extraordinary mechanical and thermal properties, which were remarkably superior to its individual components, and immediately found their use in automobile industry as the materials for timing-belt covers [33, 35]. Other polymers such as rubber [33], poly( $\epsilon$ -caprolactone) [36], epoxy resin [37], polyimide [38] and polystyrene [39] have also been hybridized with clays to make nanocomposites of excellent mechanical and thermal mechanical properties.

Encapsulation of conductive polymers inside layered compounds leads to anisotropically conductive materials. In addition, it is expected that the overlapping and interaction of the electronic bands of the guest and the host will bring up unpredicted novel physical properties. The first complex

of this type was FeOCl/polypyrrole and, since then, this aspect has always been a hot topic in intercalation. So far, conductive-polymer intercalation compounds with hosts such as FeOCl [34, 40], V<sub>2</sub>O<sub>5</sub> [41], MoO<sub>3</sub> [42], MoS<sub>2</sub> [43], metal phosphates [20b,44], halides (CdX<sub>4</sub><sup>2-</sup> and MnX<sub>4</sub><sup>2-</sup>) [45], HFe(SO<sub>4</sub>)<sub>2</sub>·4H<sub>2</sub>O [20b], as well as clays [38b] have been reported. The conductive polymers include polypyrrole, polyaniline, polythiophene, polyfuran, poly(p-phenylenevinylene) and poly(diacetylene). Recently, it has been shown that some of these electronically active nanocomposites have better electrochemical properties than either the hosts or the polymers [46, 47].

The importance of the outcome of the clay/nylon-6 and FeOCl/polypyrrole nanocomposites to the research of polymer intercalation was not only the demonstration of the applications of the nanocomposites, but also the introduction of the new synthetic methodologies associated with the preparation. The surfactant modified clays used in the preparation of the clay/nylon-6 nanocomposites are good starting materials for a lot of clay/polymer nanocomposites, while the *in situ* redox intercalative polymerization used to synthesize the FeOCl/polypyrrole nanocomposite suits for a class of layered hosts and monomers. The procedures of the two methods are easy to carry out, producing nanocomposites of well defined morphologies. Before the establishment of these two methods, polymer intercalation was almost exclusively accomplished by monomer intercalation and subsequent intergallery polymerization. This classical method has not contributed many nanocomposites because neither monomer intercalation nor intergallery polymerization could be accomplished readily.

The success in preparing many new nanocomposites brought more researchers into this field and gave rise to more efforts to develop new

methodologies for polymer intercalation. Nazar et al made MoO<sub>3</sub>/poly(phenylene vinylene) nanocomposites through the insertion of the precursor ionomer by ion-exchange and the subsequent conversion to the polymer [42a, b]. Ruiz-Hitzky et al incorporated poly(ethylene oxide) (PEO) in layered silicate [48] and V<sub>2</sub>O<sub>5</sub> xerogel [49] by treatment of the host with non-aqueous polymer solution. PEO was also intercalated in MPS<sub>3</sub> (M=Mn, Cd) by Lagadic et al by stirring the hosts with an aqueous solution or a methanol solution of PEO [50]. In our group, PEO and other water-soluble polymers were encapsulated in V<sub>2</sub>O<sub>5</sub> xerogel through mixing the aqueous solution of the two [51]. All these accomplishments were reported in a short period in early 1990s. By 1993, the preparation of MoS<sub>2</sub>/polymer nanocomposites by exfoliation-encapsulative precipitation (EEP) was reported by our group [52], while the preparation of MoS<sub>2</sub>/PEO and TiS<sub>2</sub>/PEO was reported by Ruiz-Hitzky's group [53] simultaneously.

The EEP method demonstrated its usefulness by intercalating a large variety of polymers in MoS<sub>2</sub> [52], a host which otherwise is very difficult to intercalate with even small molecules [54]. It has been expected since that the application of the EEP method to other layered materials would bring in many new nanocomposites. This knowledge provided a promising starting point for the present dissertation [43b, 55], as well as the work of other researchers [56, 57]. On the other side, Giannelis et al developed the melt intercalation method for organoclays in 1995 [58]. This method has a great advantage in large-scale preparations, so the development is very important to the commercialization of the organoclay nanocomposites.

### **3. Exfoliation-Encapsulative Precipitation: An Effective Method for Polymer Intercalation**

The exfoliation-encapsulative precipitation (EEP) method corresponds to the exfoliation-flocculation method in conventional intercalation. The latter was developed to intercalate robust cations in negatively charged layered materials in late 1970s and early 1980s [28, 29]. In the case of robust cation intercalation, the driving force was well understood. It is the electrostatic attraction between the positively charged cations and negatively charged layers. The net result of the reaction is the ion-exchange of large cluster cations for small interlayer metal cations.

In the case of neutral polymer intercalation, however, no driving force had been expected in such a situation. The anionic hosts, which can be exfoliated, are considered extremely polar materials. The neutral polymers, on the other hand, are usually non-polar or slightly polar materials. It is hard to see the affinity between the two classes of materials. Although Morrison et al had encapsulated a list of small organic molecules in  $\text{MoS}_2$  by exfoliation-flocculation in 1986 [54], the event seemed not impacting enough to persuade people to generalize this strategy to polymer intercalation. Nazar et al [42a, b] chose an ionomer rather than a polymer to intercalate in an exfoliatable host,  $\text{Na}_x\text{MoO}_3$ . In the work of Ruiz-Hitzky et al on the layered silicates [48] and the work of Lagadic et al on  $\text{MPS}_3$  [50], exfoliation was not applied. On the other hand, in the work of polymer intercalation in  $\text{V}_2\text{O}_5$  xerogel, which was done by our group [51], an exfoliation step was not involved in the synthesis. Although all these efforts enriched the preparation chemistry of inorganic/polymeric nanocomposites, the peculiarities existing in either the polymers, the hosts, or the reactions stopped people from extensively generalizing these methods.

The design of the EEP method [52] was based on the expectation that the monolayers of the inorganic compounds would combine with polymer molecules in solution to form nanocomposites. The success of the method relied on the co-precipitation of the monolayers and the polymer from solution. The design of this reaction was somewhat different from that of Ruiz-Hitzky et al for PEO intercalation in MoS<sub>2</sub> and TiS<sub>2</sub> [53], in which the exfoliation was utilized to facilitate the polymer insertion. The trial of the EEP method on MoS<sub>2</sub> nanocomposites was a brilliant success. The direct intercalation in MoS<sub>2</sub> with a list of polymers, which included water soluble polymers such as poly(ethylene oxide), poly(propylene oxide), poly(ethylenimine), poly(vinyl pyrrolidone) and methyl cellulose, commonly used polymers such as polyethylene and nylon-6, and conducting polymer polyaniline [52], through a very simple procedure, brought the attention of other researchers in this area. The successful application to a common transition metal dichalcogenide using so many polymers showed the generality of the method. The intercalation of these polymers also indicated the existing affinity between the polymers and exfoliated layered materials, which is a critical factor for the on going research in polymer intercalation. Accordingly, the EEP method was established as a new promising method for polymer intercalation.

For the EEP method to apply, the most important issue is the availability of monolayer suspensions of the host materials. Monolayer suspensions have been explored increasingly in the last 20 years as an approach to prepare intercalative compounds with very large guest molecules and high surface areas as catalysts, and to form monolayer coatings and films. They have been reported in clays, layered transition metal disulfides (TiS<sub>2</sub>, 2H-NbS<sub>2</sub>, 2H-TaS<sub>2</sub>, MoS<sub>2</sub> and WS<sub>2</sub>), transition metal oxides (MoO<sub>3</sub>), metal oxychlorides (FeOCl [59]), transition metal

phosphorus sulfides ( $\text{MnPS}_3$ ), metal hydrogen phosphates [ $\text{Zr}(\text{HPO}_4)_2 \cdot \text{H}_2\text{O}$  and  $(\text{H}_3\text{O})\text{UO}_2\text{PO}_4 \cdot 3\text{H}_2\text{O}$  (HUP) <sup>[60]</sup>] and niobium oxides ( $\text{HTiNbO}_5$  and  $\text{HCa}_2\text{Nb}_3\text{O}_{10}$ ). Dispersions of clay minerals have been studied most extensively <sup>[61]</sup>, which led to the synthesis of "pillared clays" and delaminated clay-polymer nanocomposites. Alkali metal or proton intercalated  $\text{TiS}_2$  <sup>[62]</sup>,  $2\text{H-NbS}_2$  <sup>[62, 63]</sup> and  $2\text{H-TaS}_2$  <sup>[62, 63, 64]</sup> exfoliate when mechanical stirring is applied. Lithiated  $\text{MoS}_2$  <sup>[54]</sup> and  $\text{MoO}_3$  <sup>[65]</sup> form monolayer dispersions with the assistance of ultrasonic vibration.  $\text{WS}_2$  <sup>[66, 67]</sup> monolayer suspension has been prepared following  $\text{MoS}_2$ . Lithium ion exchanged  $\text{MnPS}_3$  forms a colloidal dispersion in water spontaneously <sup>[68]</sup>. Acid zirconium phosphates,  $\text{Zr}(\text{HPO}_4)_2 \cdot \text{H}_2\text{O}$  <sup>[69]</sup>, and proton exchanged niobium oxides ( $\text{HTiNbO}_5$  <sup>[70]</sup> and  $\text{HCa}_2\text{Nb}_3\text{O}_{10}$  <sup>[71]</sup>) exfoliate after the interlayer surface modification with pre-intercalated alkylamines. Further development of the surface modification on zirconium phosphates leads to zirconium organophosphates and phosphonates that can exfoliate spontaneously in water <sup>[72]</sup>. A review for colloidal dispersion of layered inorganic compounds was written recently by Jacobson <sup>[73]</sup>. In addition, more reports about exfoliation have come out recently in misfit-layered metal sulfides <sup>[74]</sup>, layered metal phosphates <sup>[75]</sup> and niobium oxides <sup>[76]</sup>, and even high- $T_c$  superconductors <sup>[77]</sup>. Our new success in exfoliation of  $\alpha\text{-RuCl}_3$  is described in Chapter 5. With the increasing interest in colloidal monolayer dispersions, more exfoliated materials will be discovered. Therefore, many host materials exist which might be amenable to the EEP method and this promises a bright future for polymer intercalation and associated nanocomposite materials.

The successful application of the EEP method also depends on the affinity between polymers and the dispersed monolayers. This factor is

more decided by the nature of the dispersed monolayers rather than the manipulation of the chemistry. Thus, even with the monolayer suspension of a host material, intercalation of polymer is not guaranteed. However, it is possible to change the preparative method or condition to adjust the nature of the monolayer dispersions, so that the monolayers become attractive to the polymers. The new preparation procedures for  $\text{Li}_x\text{TaS}_2$  and  $\text{Li}_x\text{MoO}_3$  described in Chapter 3 and 4 are examples of this modification. It is also likely to choose some special conditions of intercalation for some monolayer dispersions so that polymer intercalation is favored. Examples of these reaction designs can be found in Chapter 1. As a result of the factors described above, searching for the best conditions to conduct polymer encapsulation is still inevitable.

#### **4. Applications of Intercalation Compounds and Nanocomposites**

The study of chemical intercalation is not only interesting but also beneficial from a practical viewpoint. Intercalation offers a mild way to modify the structures and properties of the host lattice through electron transfer, ion-exchange, and guest molecule insertion. It is a unique approach to obtain new materials that cannot be prepared by the conventional techniques of solid state chemistry. Searching for new materials for potential applications has been a hot topic in the field of chemical intercalation for many years, and has become an important driving force for research.

The most important application of intercalation materials is as reversible electrodes for rechargeable batteries. The utilization of graphite intercalation compounds as electrode materials in electrochemical generators was initially proposed by Armand in 1973 [78]. In 1977, the idea of intercalative chalcogenide batteries was developed by Whittingham [79].

Several ambient temperature secondary lithium battery systems such as Li-TiS<sub>2</sub>, Li-MoS<sub>2</sub>, Li-NbSe<sub>3</sub>, Li-MoO<sub>2</sub>, Li-V<sub>2</sub>O<sub>5</sub> etc. have been investigated at various battery companies and R&D organizations for consumer and defense purposes [80]. At present, the research on positive electrode materials for secondary lithium batteries is mainly focused on LiCoO<sub>2</sub> and LiMnO<sub>2</sub> [81].

On the other hand, the application or potential application of intercalation materials as catalysts, ion-exchangers and sorbents is well known [82, 83]. Pillared and delaminated clays are studied as shape selective, heterogeneous catalysts for petroleum cracking, and their performance is competitive with zeolite catalysts [16]. Layered double hydroxides are used for the selective conversion of propylene oxide to primary and secondary alcohols, the cross-aldol condensation reactions to form methylvinylketone, the polymerization of lactones and the decomposition of ketones [84]. Pillared MoS<sub>2</sub> can be used in hydrodesulfurization [85]. As sorbents, smectite clays are used for decoloring edible oils, clarifying alcoholic beverages, removing grease from raw wool and treating the radioactive waste solutions [83]. Layered double hydroxides are used to take up acidic impurities such as HCl generated from the photo decomposition of poly(vinyl chloride) [84]. As sorbents, intercalation compounds also have potential applications in the controlled releasing of perfumes, insecticides, fertilizers [86], as well as medicines.

With advances in intercalation chemistry and the increase in the number of investigated host and guest species, intercalation as an approach for materials design is more and more clearly claimed, and more effort is directed towards the synthesis of materials with novel structures and properties. Intercalation readily provides materials with highly anisotropic dielectric, conductive and optical properties [7a]. For example, layered

vanadyl phosphonates are used to place naphthalene units into ordered arrays to achieve the control of their photophysical properties [87]. Intercalation can stabilize materials of nanometer dimensions, which exhibit novel electrical, optical, magnetic, and chemical properties. Intercalates of various functions have been included [88]. Luminescent compounds such as  $\text{Ru}(\text{bpy})_3^{2+}$  have been encapsulated in transparent hosts such as smectite. The luminescent compounds are effectively isolated by the hosts so that self-quenching is suppressed. A molecularly dispersed system is also a basic prerequisite for composing efficient photochemical hole burning (PHB) materials to avoid line broadening due to energy transfer. The intercalation of PHB probes such as 1,4-dihydroxyanthraquinone (DAQ) into transparent hosts is an effective way to achieve this prerequisite [89]. Electrochromic and photochromic compounds such as viologen (1,1'-disubstituted-4,4'-bipyridinium salts) have been intercalated into layered hosts to make electrochromic, photochromic and optical memory materials [89]. Dyes have also been intercalated in order to obtain pigments with special spectral properties [89].

As a major branch of the class of intercalation compounds and probably the most applicable group, nanocomposites currently receive worldwide interest. As mentioned earlier, the organoclay/nylon nanocomposites have already been used in timing-belt covers in automobiles [35] due to their high strength, high yielding temperature and good processibility. In addition, organoclay/polymer nanocomposites have been produced as high-barrier plastic packaging materials [90], which have gas barrier improvements as high as 800%. Nanocomposites can also have better flame retardant properties [91, 9d] and lower dielectric permittivity than the component polymers [92]. The regular void structures, which exist in specially designed nanocomposites, provide low dielectric constants and

may produce good electronic packaging materials. Materials of extremely low dielectric permittivity can also be generated from the restricted motions of ions and electrons in the network structures of nanocomposites. Those materials have potential applications for optoelectronic packaging<sup>[7a]</sup>.

In the field of electrode materials, the preliminary research on V<sub>2</sub>O<sub>5</sub> nanocomposites shows that V<sub>2</sub>O<sub>5</sub>/polyaniline has a better reversibility and an increased Li capacity in the electrochemical redox cycles, implying that it is a better cathode material for Li rechargeable batteries <sup>[47]</sup>. The V<sub>2</sub>O<sub>5</sub>/polyaniline also has a Li chemical diffusion coefficient one order of magnitude higher than that of the host itself, which would provide better performance at high current densities <sup>[47]</sup>. The electroactive polymer intercalated nanocomposites usually have cation diffusion coefficients higher than those of the unexpanded hosts, which makes it worthwhile to explore the possibility of using the nanocomposite analog of a layered electrode material as a substitute.

Polyether intercalation compounds, especially poly(ethylene oxide) intercalation compounds, are of interest in solid state ionics. PEO acts as a solid solvent for different salts. The PEO solutions of salts are polyelectrolytes <sup>[93]</sup> and are used in solid state batteries <sup>[94]</sup> and other electronic devices. The inclusion of PEO in clays and other charged layered hosts provides fast ion conduction for the incorporated cations, while the host materials act as inert, often insulating counter ions. Therefore, the ionic conductivity is exclusively due to cations of the interlayer region. This makes the transference number of the cation equal to 1 ( $t_+ = 1$ ), which is of interest in the study of ion-transport phenomena in polymer electrolyte systems. Finally, the intercalation of PEO in electronically conductive layered solids opens the way to new polyelectrolyte materials of mixed ionic/electronic conductivity. PEO

intercalation compounds have been reported with layered silicates [48], layered metal phosphates [72b], layered metal phosphorus trisulfides [50],  $V_2O_5$  [51],  $MoO_3$  [55, 56b], transition metal dichalcogenides [52, 53, 57] and carbon oxides [56d].

Using polymer intercalative nanocomposites, as precursors to produce new ceramics and graphite films, is another direction of research that carries the polymer intercalation into potential applications. Kato and coworkers used magadiite-poly(acrylonitrile) complex as a precursor to prepare silicon carbide and silicon nitride in carbothermal reduction processes [89]. In an ordinary carbothermal reduction process, a mixture of carbon and  $SiO_2$  is used as the starting material. A carbonized oxide-polymer nanocomposite, in which the carbon and the oxide are intimately mixed, may produce ceramics of better quality. At least, this is the case with silicon nitride. The same group also prepared aluminum nitride by conversion of a hydrotalcite-polyacrylonitrile intercalative nanocomposite through a carbothermal reduction process. Kyotani and coworkers prepared graphite films from montmorillonite-polyacrylonitrile nanocomposites [95]. The films consist of highly crystallized but small graphite crystallites. They have a much weaker mechanical strength and a much poorer electrical conductivity than the graphite films prepared from polymer films, but they have some flexibility.

## **5. Important Contributions of the Present Dissertation Work**

The research described in the present dissertation started at a time when a list of polymers had been intercalated in  $MoS_2$  by the EEP method[52]. To promote the research of polymer intercalation in  $MoS_2$ , which had not been finished by Bissessur [96], the study in the exfoliation of  $MoS_2$ , intercalation of polymers, and properties of hydrated  $MoS_2$ ,

restacked MoS<sub>2</sub> and nanocomposites was continued. The study provides a better understanding of this new group of materials, which leads to a better manipulation of the materials and of the encapsulation reactions. During this study, many new MoS<sub>2</sub> nanocomposites, such as (polystyrene)<sub>x</sub>MoS<sub>2</sub>, (polyacrylamide)<sub>x</sub>MoS<sub>2</sub>, (polyvinylalcohol)<sub>x</sub>MoS<sub>2</sub>, (polypropylene)<sub>x</sub>MoS<sub>2</sub>, (polymethylmethacrylate)<sub>x</sub>MoS<sub>2</sub>, (polybenzimidazole)<sub>x</sub>MoS<sub>2</sub> and (polyethyleneterephthalate)<sub>x</sub>MoS<sub>2</sub> have been synthesized. This part of the research is described in Chapter 1. In order to intercalate insoluble polymers in MoS<sub>2</sub>, a modification was made to the EEP method, which brought in the *in situ* polymerization-encapsulative precipitation method. This method has been successfully applied to the synthesis of MoS<sub>2</sub>/polypyrrole nanocomposites, and is discussed in Chapter 2. The polypyrrole intercalation in WS<sub>2</sub> is also reported in Chapter 2.

The most important achievement with respect to MoS<sub>2</sub>, in this dissertation, is the invention and development of the high temperature LiBH<sub>4</sub> lithiation method. In this procedure, LiBH<sub>4</sub> is proved to be a very powerful reducing reagent at high temperatures. Up to now, this method has been used to prepare other lithium-intercalated materials such as LiWS<sub>2</sub><sup>[67]</sup> and LiNbSe<sub>2</sub><sup>[57]</sup>, which can exfoliate in water. It is expected to be applicable to the lithiation of many additional layered materials. The new lithiation method provides a convenient approach to prepare large quantities of LiMoS<sub>2</sub>.

Believing that the EEP method can be generalized, other hosts were also explored. Polymer intercalation was tried on 2H-TaS<sub>2</sub>, the exfoliation of which had been reported <sup>[62, 63, 64]</sup>. However, exfoliated TaS<sub>2</sub><sup>x-</sup> prepared according to the literature did not include polymers except polyimines. In order to achieve the polymer intercalation, different forms of Li<sub>x</sub>TaS<sub>2</sub>

were prepared with different lithiation reactants and under different reaction conditions. Although most of the  $\text{Li}_x\text{TaS}_2$  phases can be hydrated and dissolve somewhat in water, no polymer other than a polyimine can be included. All this changed after the preparation of consistently uniform  $\text{Li}_x\text{TaS}_2$  phases through a quantitatively controlled lithiation reaction using a 0.2 equivalent of  $\text{LiBH}_4$ . The exfoliation of and polymer intercalation in  $2\text{H-TaS}_2$  is described in Chapter 3.

The two  $\text{LiBH}_4$  lithiation methods, by high temperature solid state reaction and room temperature solution reaction, are complementary. The high temperature lithiation, which has a strong driving force, works with layered materials hard to reduce, such as  $\text{MoS}_2$  and  $\text{WS}_2$ . Over-lithiation should not be a problem in these materials because they oxidize readily when exposed to water in the exfoliation step. The controlled room-temperature solution lithiation, using a low equivalent of  $\text{LiBH}_4$ , can deal with hosts that are readily reduced, such as  $\text{TaS}_2$  and  $\text{MoO}_3$ . Since the reduced forms of these materials are not readily oxidized by water and the high charge density in the layers favors neither exfoliation nor polymer intercalation, the charge carried by the layers should be controlled. The two lithiation methods are expected to cover the exfoliation of a broad range of layered materials.

Since the availability of stable monolayer suspensions is the prerequisite to applying the EEP method, the importance of the two lithiation methods is obvious. The exfoliation and polymer intercalation of  $\text{WS}_2$  [67, 97] and  $\text{NbSe}_2$  [57] is based on the first lithiation method. By using the second lithiation method,  $\text{MoO}_3$  and  $\alpha\text{-RuCl}_3$  are exfoliated and encapsulated with polymers. The nanocomposites with the latter two hosts are described in Chapter 4 and Chapter 5.

The polymer insertion in MoS<sub>2</sub>, WS<sub>2</sub>, NbSe<sub>2</sub> [57], 2H-TaS<sub>2</sub>, MoO<sub>3</sub> and  $\alpha$ -RuCl<sub>3</sub> using the EEP method has demonstrated its effectiveness. The diversity of the host materials shows the generality of this method. At this stage, the EEP method has been firmly established and become one of the most effective tools in polymer intercalation. The present dissertation work contributes a substantial part to the generalization of this new polymer intercalation method and introduces many new lamellar nanocomposites.

## References

- 1 C. Schafhäütl, *J. Prakt. Chem.* **1840**, 3, 129.
- 2 K. Fredenhagen and G. Cadenbach, *Z. Anorg. Allg. Chem.* **1926**, 158, 249.
- 3 (a) L. Pietronero and E. Tosatti ed., *Physics of Intercalation Compounds* (Proceedings of an International Conference, Trieste, Italy, July 6-10, 1981), Springer-Verlag, Berlin/New York, **1981**. (b) M. S. Dresselhaus ed., *Intercalation in layered Materials* (NATO ASI series, Series B: Physics, Vol. 148), Plenum Press, New York, **1986**. (c) A. P. Legrand and S. Flandrois ed., *Chemical Physics of Intercalation* (NATO ASI series, Series B; Physics, Vol. 172), Plenum Press, New York, **1987**. (d) P. Bernier ed., *Chemical Physics of Intercalation II* (NATO ASI series, Series B: Physics, Vol. 305), Plenum Press, New York, **1993**. (e) G. Slobert and T. Bein ed. *Comprehensive Supramolecular Chemistry*, Vol. 7 (Solid-State Supramolecular Chemistry: Two- and Three-Dimensional Inorganic Networks), Elsevier Sci. Ltd., **1996**.
- 4 (a) R. H. Friend and A. D. Yoffe, *Adv. Phys.* **1987**, 36, 1. (b) R. F. Frindt in A. P. Legrand and S. Flandrois ed., *Chemical Physics of Intercalation* (NATO ASI series, Series B; Physics, Vol. 172), Plenum Press, New York, **1987**, pp 195. (c) W. Y. Liang in M. Balkanski ed., *Microionics-Solid State Intergrable Batteries*, Elsevier Science Pub. B. V., **1991**, pp 237. (d) G. Ouvrard in P. Bernier, J. E. Fischer, S. Roth and S. A. Solin ed., *Chemical Physics of Intercalation II* (NATO ASI series, Series B: Physics, Vol. 305), Plenum Press, New York, **1993**, pp 1. (e) J. Rouxel in G. Slobert and T. Bein ed. *Comprehensive Supramolecular Chemistry*, Vol. 7 (Solid-State Supramolecular Chemistry: Two- and Three-Dimensional Inorganic Networks), Elsevier Sci. Ltd., **1996**, Chapter 3, pp 77.
- 5 F. R. Gamble, F. J. DiSalvo, R. A. Klemm and T. H. Geballe, *Science* **1970**, 168, 568.
- 6 (a) J.-H. Choy, N.-G. Park, Y.-I. Kim, S.-H. Hwang, J.-S. Lee and H.-I. Yoo, *J. Phys. Chem.*, **1995**, 99, 7845. (b) J.-H. Choy, N.-G. Park, S.-J. Hwang and D.-H. Kim, *J. Am. Chem. Soc.*, **1994**, 116, 11564. (c) Y. Koike, K. Sasaki, A. Fujiwara, K. Watanabe, M. Kato,

- T. Noji and Y. Saito, *Physica C* **1995**, 245, 332. (d) Z. J. Huang, J. G. Lin, J. J. Lin, C. Y. Huang, L. Grigoryan and K. Yakushi, *Physica C* **1995**, 244, 305.
- 7 (a) E. P. Giannelis, V. Mehrotra and M. W. Russell, *Mat. Res. Soc. Symp. Proc.* Vol. 180, **1990**, 685. (b) S. Yamanaka, *New Functional Materials*, Vol. C (Synthetic Process and Control of Functionality Materials), Elsevier Science Pub. B. V., **1993**, 677.
- 8 (a) G. A. Ozin, *Adv. Mater.* **1992**, 4, 612. (b) R. Schöllhorn, *Chem. Mater.* **1996**, 8, 1747.
- 9 (a) E. Ruiz-Hitzky, *Adv. Mater.* **1993**, 5, 334. (b) E. Ruiz-Hitzky and P. Aranda, *Anales de Quimica* **1997**, 93, 197. (c) E. P. Giannelis, *Adv. Mater.*, **1996**, 8, 29. (d) E. P. Giannelis, *Appl. Organometal. Chem.* **1998**, 12, 675. (e) M. M. Lerner and C. O. Oriakhi, in A. N. Goldstein ed *Handbook of Nanophase Materials*, Marcel Dekker, New York, **1997**, Chap. 7, pp 199.
- 10 (a) M. S. Whittingham and A. J. Jacobson ed., *Intercalation Chemistry* Academic Press, **1982**. (b) D. O'Hare. in D. W. Bruce and D. O'Hare ed. *Inorganic Materials*, John Wiley & Sons Ltd, **1992**, Chapter 4, pp 165.
- 11 M. Arnaud and P. Touzain, *Mater. Sci. Eng.* **1977**, 31, 1.
- 12 (a) C. Schlenker ed., *Low-Dimensional Electronic Properties of Molybdenum Bronzes and Oxides*, Kluwer Academic Publishers, **1989**. (b) A. M. Chippindale, P. G. Dickens and A. V. Powell, *Prog. Solid State Chem.* **1991**, 21, 133.
- 13 (a) A. J. Jacobson in A. K. Cheetham and P. Day ed. *Solid State Chemistry Compounds*, Clarendon, Oxford, **1992**, pp 182. (b) H Schafer-Stahl and R. Abele, *Angew. Chem., Int. Ed. Engl.* **1980**, 19, 477.
- 14 R. Clément, I. Lagadic, A. Léaustic, J. P. Audière and L. Lomas, in P. Bernier, J. E. Fischer, S. Roth and S. A. Solin ed., *Chemical Physics of Intercalation II*, Plenum Press, New York, **1993**, pp 315.
- 15 G. Lagaly and K. Beneke, *Colloid Polym. Sci.* **1991**, 269, 1198.

- 16 T. J. Pinnavaia, in A. P. Legrand and S. Flandrois ed., *Chemical Physics of Intercalation* (NATO ASI Ser., Series B; Physics, Vol. 172), Plenum Press, New York, **1987**, pp 233.
- 17 (a) G. Alberti and U. Costantino, in J. L. Atwood, J. E. D. Davies and D. D. MacNicol ed., *Inclusion Compounds*, Vol. 5, Oxford Sci. Pub., **1991**, pp 136. (b) A. Clearfield and U. Costantino in G. Sliberti and T. Bein ed. *Comprehensive Supramolecular Chemistry*, Vol. 7 (Solid-State Supramolecular Chemistry: Two- and Three-Dimensional Inorganic Networks), Elsevier Sci. Ltd., **1996**, Chapter 4, pp 107.
- 18 (a) B. Morosin, *Phys. Lett.* **1978**, 65A, 53. (b) A. T. Howe and M. G. Shilton, *J. Solid State Chem.* **1979**, 28, 345. (c) A. T. Howe and M. G. Shilton, *J. Solid State Chem.* **1980**, 31, 393. (d) M. G. Shilton and A. T. Howe, *J. Solid State Chem.* **1980**, 34, 137.
- 19 J. Votinský, J. Kalousová and L. Beneš, *J. Inclusion Phenom. Mol. Recognit. Chem.* **1992**, 14, 19.
- 20 (a) D. J. Jones and J. Rozière, *Solid State Ionics* **1989**, 35, 115. (b) D. J. Jones, R. El Mejjad and J. Rozière, in T. Bein ed., *Supramolecular Architecture* (ACS Symposium series 499), **1992**, pp 220.
- 21 (a) F. Cavani, F. Trifirò and A. Vaccari, *Catalysis Today*, **1991**, 11, 173. (b) A. de Roy, C. Forano, K. El. Malki and J.-P. Besse, in *Synthesis of Microporous Materials*, Van Nostrand Reinhold, New York, **1992**, pp 108. (c) K. El Malki, M. Guenane, C. Forano, A. de Roy and J. P. Besse, *Materials Science Forum* **1992**, 91-93, 171.
- 22 A. J. Jacobson, in P. Bernier, J. E. Fischer, S. Roth and S. A. Solin ed., *Chemical Physics of Intercalation II*, Plenum Press, New York, **1993**, pp 117.
- 23 S.-T. Wong and S. Cheng, *Inorg. Chem.* **1992**, 31, 1165.
- 24 (a) X.-M. Shen and A. Clearfield, *J. Solid State Chem.* **1986**, 64, 270. (b) P. Le Goff, N. Baffier, S. Bach and J. P. Pereira-Ramos, *Mater. Res. Bull.* **1996**, 31, 63.
- 25 P. Lavela, J. Morales and J. L. Tirado, *Chem. Mater.* **1992**, 4, 2.

- 26 (a) F. R. Gamble, J. H. Osiecki, M. Cias, R. Pisharody, F. J. DiSalvo and T. H. Geballe, *Science* **1971**, 174, 493. (b) F. R. Gamble, J. H. Osiecki, F. J. DiSalvo, *J. Chem. Phys.* **1971**, 55, 3525.
- 27 R. Schöllhorn and H. D. Zayefka, *Angew. Chem., Int. Ed. Engl.* **1977**, 16, 199.
- 28 (a) D. E. W. Vaughan, R. J. Lussier and J. S. Magee, *U. S. Patent* 4,176,090, **1979**. (b) T. J. Pinnavaia, M. S. Tzou, S. D. Landau and R. H. Raythatha, *J. Mol. Catal.* **1984**, 27, 195.
- 29 L. F. Nazar and A. J. Jacobson, *J. Chem. Soc., Chem. Commun.*, **1986**, 570.
- 30 (a) A. Blumstein, *J. Polym. Sci., A*, **1965**, 3, 2665. (b) C.-H. Hsu, M. M. Labes, J. T. Breslin, D. J. Edmiston, J. J. Winter, H. A. Leupold and F. Rothwarf, *Nature, Phys. Sci.*, **1973**, 246(155), 122. (c) G. Lagaly and K. Beneke, *Am. Mineralogist* **1975**, 60, 650. (d) V. M. Chapela and G. S. Parry, *Nature* **1979**, 281, 134.
- 31 T. J. Pinnavaia, *Science* **1983**, 220(4595), 365.
- 32 (a) A. Okada and M. Kawakado, *Japanese Patent Application* No. Sho 60 [1985]-217396. (b) A. Okada, M. Kawasumi, T. Kurauchi and O. Kamigaito, *Polym. Prepr., Am. Chem. Soc., Div. Polym.* **1987**, 28, 447. (c) Y. Fukushima and S. Inagaki, *J. Inclusion Phenom.* **1987**, 5, 473. (d) Y. Fukushima, A. Okada, M. Kawasumi, T. Kurauchi and O. Kamigaito, *Clay Minerals* **1988**, 23, 27.
- 33 A. Okada and A. Usuki, *Mat. Sci. Eng. C-Biomin.* **1995**, 3, 109.
- 34 M. G. Kanatzidis, L. M. Tonge, T. J. Marks, H. O. Marcy and C. R. Kannewurf, *J. Am. Chem. Soc.* **1987**, 109, 3797.
- 35 T. Kurauchi, A. Okada, T. Nomura, T. Nishio, S. Saegusa, R. Deguchi, *SAE Technical Paper Ser.* **1991**, 910584.
- 36 P. B. Messersmith and E. P. Giannelis, *Chem. Mater.* **1993**, 5, 1064.

- 37 (a) M. S. Wang and T. J. Pinnavaia, *Chem. Mater.* **1994**, 6, 468. (b) T. Lan and T. J. Pinnavaia, *Chem. Mater.* **1994**, 6, 2216. (c) P. B. Messersmith and E. P. Giannelis, *Chem. Mater.* **1994**, 6, 1719.
- 38 (a) T. Lan, P. D. Kaviratna and T. J. Pinnavaia, *Chem. Mater.* **1994**, 6, 573. (b) E. P. Giannelis, V. Mehrotra, O. Tse, R. A. Vaia and T.-C. Sung, *Mat. Res. Soc. Symp. Proc.* Vol. 267, **1992**, pp 969.
- 39 R. A. Vaia, H. Ishii and E. P. Giannelis, *Chem. Mater.* **1993**, 5, 1694.
- 40 M. G. Kanatzidis, C.-G. Wu, D. C. DeGroot, J. L. Schindler, M. Benz, E. LeGoff and C. R. Kannewurf, in P. Bernier, J. E. Fischer, S. Roth and S. A. Solin ed., *Chemical Physics of Intercalation II* Plenum Press, **1993**, pp 63.
- 41 (a) C.-G. Wu, M. G. Kanatzidis, H. O. Marcy, D. C. DeGroot and C. R. Kannewurf, *Polym. Mat. Sci. Eng.* **1989**, 61, 969. (b) M. G. Kanatzidis, C.-G. Wu, H. O. Marcy and C. R. Kannewurf, *J. Am. Chem. Soc.* **1989**, 111, 4139. (c) M. G. Kanatzidis, C.-G. Wu, H. O. Marcy, D. C. DeGroot and C. R. Kannewurf, *Chem. Mater.* **1990**, 2, 222. (d) C.-G. Wu, M. G. Kanatzidis, H. O. Marcy, D. C. DeGroot and C. R. Kannewurf, in R. M. Metzger et al ed., *Lower-Dimensional Systems and Molecular Electronics*, Plenum Press, New York, **1991**, pp 427. (e) Y.-J. Liu, D. C. DeGroot, J. L. Schindler, C. R. Kannewurf and M. G. Kanatzidis, *J. Chem. Soc., Chem. Commun.* **1993**, 593.
- 42 (a) L. F. Nazar, X. T. Yin, D. Zinkweg, Z. Zhang and S. Liblong, *Mat. Res. Soc. Symp. Proc.* **1991**, 210, 417. (b) L. F. Nazar, Z. Zhang and D. Zinkweg, *J. Am. Chem. Soc.* **1992**, 114, 6239. (c) R. Bissessur, D. C. DeGroot, J. L. Schindler, C. R. Kannewurf and M. G. Kanatzidis, *J. Chem. Soc., Chem. Commun.* **1993**, 687.
- 43 (a) M.G. Kanatzidis, R. Bissessur, D. C. DeGroot, J. L. Schindler, C. R. Kannewurf, *Chem. Mater.* **1993**, 5, 595. (b) L. Wang, J. L. Schindler, J. A. Thomas, C. R. Kannewurf and M. G. Kanatzidis, *Chem. Mater.* **1995**, 7, 1753.
- 44 (a) Y.-J. Liu and M. G. Kanatzidis, *Inorg. Chem.* **1993**, 32, 2989. (b) G. Cao and T. E. Mallouk, *J. Solid State Chem.* **1991**, 94, 59.

- 45 (a) P. Day and R. D. Ledsham, *Mol. Cryst. Liq. Cryst.* **1982**, 86, 163. (b) B. Tieke, *Mol. Cryst. Liq. Cryst.* **1983**, 93, 119.
- 46 T. A. Kerr, H. Wu and L. F. Nazar, *Chem. Mater.* **1996**, 8, 2005.
- 47 (a) F. Leroux, B. E. Koene and L. F. Nazar, *J. Electrochem. Soc.*, **1996**, 143(9), L181. (b) F. Leroux, G. Goward, W. P. Power and F. Nazar, *J. Electrochem. Soc.*, **1997**, 144, 3886.
- 48 (a) E. Ruiz-Hitzky and P. Aranda, *Adv. Mater.* **1990**, 2, 545. (b) P. Aranda and E. Ruiz-Hitzky, *Chem. Mater.* **1992**, 4, 1395.
- 49 E. Ruiz-Hitzky, P. Aranda and B. Casal, *J. Mater Chem.* **1992**, 2, 581.
- 50 I. Lagadic, A. Léaustic and R. Clément, *J. Chem. Soc., Chem. Commun.* **1992**, 1396.
- 51 (a) Y.-J. Liu, D. C. DeGroot, J. L. Schindler, C. R. Kannewurf and M. G. Kanatzidis, *Chem. Mater.* **1991**, 3, 992. (b) Y.-J. Liu, D. C. DeGroot, J. L. Schindler, C. R. Kannewurf and M. G. Kanatzidis, *Adv. Mater.* **1993**, 5, 369.
- 52 (a) R. Bissessur, J. L. Schindler, C. R. Kannewurf and M.G. Kanatzidis, *Mol. Cryst. Liq. Cryst.* **1993**, 245, 249. (b) R. Bissessur, M. G. Kanatzidis, J. L. Schindler and C. R. Kannewurf, *J. Chem. Soc., Chem. Commun.* **1993**, 1582.
- 53 E. Ruiz-Hitzky, R. Jimenez, B. Casal, V. Manriquez, A. S. Ana and G. Gonzalez, *Adv. Mater.* **1993**, 5, 738.
- 54 The small organic or inorganic molecules have only been reported being intercalated in MoS<sub>2</sub> by using the MoS<sub>2</sub> monolayer suspension: (a) P. Joensen, R. F. Frindt and S. R. Morrison *Mater. Res. Bull.* **1986**, 21, 457. (b) M. A. Gee, R. F. Frindt, P. Joensen and S. R. Morrison *Mat. Res. Bull.*, **1986**, 21, 543. (c) W. M. R. Divigalpitiya, R. F. Frindt and S. R. Morrison, *Science* **1989**, 246, 369.
- 55 L. Wang, J. Schindler, C. R. Kannewurf and M. G. Kanatzidis *J. Mater.Chem.* **1997**, 7, 1277.

- 56 (a) J. P. Lemmon, J. Wu, C. Oriakhi and M. M. Lerner, *Electrochim. Acta* **1995**, 40, 2245. (b) C. O. Oriakhi, R. L. Nafshun and M. M. Lerner, *Mater. Res. Bull.* **1996**, 31, 1513. (c) L. F. Nazar, H. Wu and W. P. Power, *J. Mater. Chem.* **1995**, 5, 1985. (d) Y. Matsuo, K. Tahara and Y. Sugie, *Carbon* **1996**, 34, 672.
- 57 H.-L. Tsai, J. L. Schindler, C. R. Kannewurf, and M. G. Kanatzidis, *Chem. Mater.* **1997**, 9, 875.
- 58 (a) R. A. Vaia, S. Vasudevan, W. Krawiec, L. G. Scanlon and E. P. Giannelis, *Adv. Mater.* **1995**, 7, 154. (b) R. A. Vaia, K. D. Jandt, E. J. Kramer and E. P. Giannelis, *Macromolecules* **1995**, 28, 8080. (c) R. A. Vaia and E. P. Giannelis, *Macromolecules* **1997**, 30, 7990. (d) R. A. Vaia and E. P. Giannelis, *Macromolecules* **1997**, 30, 8000.
- 59 A. Weiss and E. Sick. *Z. Naturforsch., Teil B*, **1978**, 33, 1087.
- 60 P. Colomban and M. Pham Thi, *Rev. Chim. Miner.* **1985**, 22, 143 (Fr).
- 61 (a) R. E. Grim, *Clay Mineralogy*, 2nd ed., McGraw-Hill, New York, **1968**. (b) P. H. Nadeau, *Appl. Clay Sci.* **1987**, 2, 83. (c) H. Van Olphen, in A. C. D. Newman ed., *Chemistry of Clays and Clay Minerals*, Wiley, New York, **1987**, pp 203. (d) L. Lee Nelson **Eur. Pat. Appl. EP 312,954**, 26 Apr **1989** (US Appl. 110,169, 19 Oct 1987).
- 62 A. Lerf and R. Schöllhorn, *Inorg. Chem.* **1977**, 16, 2950.
- 63 C. Liu, O. Singh, P. Joensen, A. E. Curzon and R. F. Frindt, *Thin Solid Films* **1984**, 113, 165.
- 64 D. W. Murphy and G. W. Hull, Jr., *J. Chem. Phys.* **1975**, 62, 973.
- 65 L. F. Nazar, S. W. Liblong and X. T. Yin, *J. Am. Chem. Soc.*, **1991**, 113, 5889.
- 66 (a) B. K. Miremedi and S. R. Morrison *J. Appl. Phys.* **1988**, 63, 4970. (b) D. Yang and R. F. Frindt, *J. Phys. Chem. Solid* **1996**, 57 (6-8, Proceedings of the 8th International Symposium on Intercalation Compounds, 1995), 1113.

- 67 H.-L. Tsai, J. Heisign, J. L. Schindler, C. R. Kannewurf and M. G. Kanatzidis *Chem. Mater.* **1997**, 9, 879.
- 68 R. Clement, O. Garnier and J. Jegoudez, *Inorg. Chem.* **1986**, 25, 1404.
- 69 G. Alberti, M. Casciola and U. Costantino, *J. Colloid Interface Sci.* **1985**, 107, 256.
- 70 H. Rebbah, M. M. Borel and B. Raveau, *Mater. Res. Bull.* **1980**, 15, 317.
- 71 M. M. J. Treacy, S. B. Rice, Allan J. Jacobson, J. T. Lewandowski *Chem. Mater.* **1990**, 2, 279.
- 72 (a) C. Y. Ortiz-Avila and A. Clearfield, *Inorg. Chem.* **1985**, 24, 1733. (b) A. Clearfield and C. Y. Ortiz-Avila, in T. Bein ed., *Supramolecular Architecture* (ACS Symposium Series 499), American Chemical Society, Washington, DC, **1992**, pp 178. (c) E. W. Stein, Sr., C. Bhardwaj, C. Y. Ortiz-Avila, A. Clearfield and M. A. Subramanian, *Materials Science Forum* **1994**, 152-153 (Soft Chemistry Routes to New Materials), 115. (d) C. Y. Ortiz-Avila, C. Bhardwaj and A. Clearfield, *Inorg. Chem.* **1994**, 33, 2499.
- 73 A. J. Jacobson, in G. Alberti and T. Bein ed., *Comprehensive Supramolecular Chemistry*, Vol. 7 (Solid -State Supramolecular Chemistry: Two- and Three-Dimensional Inorganic Networks), Elsevier Science Ltd., **1996**, pp 315.
- 74 P. Bonneau, J. L. Mansot and J. Rouxel, *Mater. Res. Bull.* **1993**, 28 757.
- 75 J.-S. Xu, Y. Tang, H. Zhang and Z. Gao, *Gaodeng Xuexiao Huaxue Xuebao* **1997**, 18(1), 93(Ch).
- 76 K. Domen, Y. Ebina, S. Ikeda, A. Tanaka, J. N. Kondo and K. Maruya *Catal. Today* **1996**, 28, 167.
- 77 J.-H. Choy et al, unpublished results.

- 78 M. Armand, in W. Van Gool ed., *Fast Ion Transport In Solids*, North Holland, New York, **1973**, pp 655.
- 79 M. S. Whittingham, U. S. Patent 4,009,052, Feb. 22, **1977**.
- 80 (a) B. B. Owens, *Survey of Lithium Ambient Temperature Secondary Systems* (Fifth International Seminar on Lithium Battery Technology and Applications), Deerfield Beach, Fla, March **1989**.  
(b) K. M. Abraham, in S. Subbarao, V. R. Koch and B. B. Owens ed., *Proceedings of the Symposium on Lithium Batteries*, Vol. 90-5 (ECS Fall Meeting 1989), **1990**, pp 1.
- 81 (a) A. R. Armstrong and P. G. Bruce, *Nature* **1996**, 381, 499. (b) P. Le Goff, N. Baffier, S. Bach and J. P. Pereira-Ramos, *Mater. Res. Bull.* **1996**, 31, 63. (c) A. Manthiram and J. Kim, *Chem. Mater.* **1998**, 10, 2895.
- 82 (a) A. Clearfield and M. Kuchenmeister, in T. Bein ed., *Supramolecular Architecture* (ACS Synosium 499), **1992**, Chapter 10, pp 128. (b) A. Clearfield, M. E. Kuchenmeister, K. Wade, R. Cahill and P. Sylvester, in M. L. Occelli et al ed., *Synthesis of Microporous Materials*, **1992**, Chapter 12, pp 245.
- 83 G. Alberti and U. Costantino, in G. Sberty and T. Bein ed., *Comprehensive Supramolecular Chemistry*, Vol. 7 (Solid-State Supramolecular Chemistry: Two- and Three-Dimensional Inorganic Networks), Elsevier Sci. Ltd., **1996**, Chapter 1, pp 1.
- 84 S. Carlino, *Chem. Brit.*, Sept. **1997**, 59.
- 85 J. Brenner, C. L. Marshall, L. Ellis, N. Tomczyk, J. Heising and M. G. Kanatzidis, *Chem. Mater.* **1998**, 10, 1244.
- 86 A. Sopková, *J. Inclusion Phenom. Mol. Recognit. Chem.* **1992**, 14, 5.
- 87 M. R. Torgerson, *Layered Metal Phosphonates as Templates for the Assembly of Ordered Molecular Systems*, Ph. D. Dissertation, Department of Chemistry, Michigan State University, **1996**.
- 88 J.-F. Nicoud, *Science* **1994**, 263, 636.

- 89 (a) C. Kato, in *Memoirs of the School of Science & Engineering, Waseda Univ.*, **1991**, No. 55, pp 41. (b) K. Kuroda, M. Ogawa, T. Yanagisawa and C. Kato, *Mat. Res. Soc. Symp. Proc.* Vol. 286, **1993**, pp 335.
- 90 (a) B. Miyares, *Packaging Strategies* **1995**, (8). (b) P. B. Messersmith and E. P. Giannelis, *J. Polym. Sci., A: Polym. Chem.* **1995**, 33, 1047. (c) J. Gu, *The Barrier Characteristics of Clay/Polyimide Nanocomposites*, M. S. thesis, School of Packaging, Michigan State University, **1997**.
- 91 J. W. Gilman, T. Kashiwagi and J. D. Lichtenhan, *Sample Journal* **1997**, 33(4), 40.
- 92 Y. Kim, W. K. Lee, W. J. Cho, C. S. Ha, M. Ree and T. Chang, *Polymer International* **1997**, 43, 129.
- 93 (a) P. V. Wright, *Br. Polym. J.* **1975**, 7, 319. (b) M. B. Armand, J. M. Chabagno and M. Duclot, in P. Vashishta, J. N. Mundy and G. K. Shenoy ed., *Fast Ion Transport in Solids Electrodes and Electrolytes*, Elsevier, New York, **1979**, pp 131. (c) M. Armand, *Solid State Ionics* **1983**, 9/10, 745. (d) M. Armand, *Adv. Mater.* **1990**, 2, 278.
- 94 M. Gauthier, D. Fauteux, G. Vassort, A. Bélanger, M. Duval, P. Ricoux, J. M. Chabagno, D. Muller, P. Rigaud, M. B. Armand and D. Dercou, *J. Electrochem. Soc.: Electrochem. Sci. Technol.* **1985**, 132, 1333. (b) C. C. Hunter, D. C. Sinclair, R. West and A. Hooper, *J. Power Sources* **1988**, 24, 157.
- 95 T. Kyotani, T. Mori and A. Tomita, *Chem. Mater.* **1994**, 6, 2138.
- 96 R. Bissessur *Synthesis and Characterization of Novel Intercalation Compounds of Molybdenum Trioxide and Molybdenum Disulfide*, Ph. D. Dissertation, Department of Chemistry, Michigan State University, **1994**.
- 97 The intercalation of polypyrrole in WS<sub>2</sub> is reported in Chapter 2. The intercalation of other polymers, done by H.-L. Tsai and M. G. Kanatzidis, is to be published in the future.

## Chapter 1

# FURTHER EXPLORATION OF EXFOLIATED MoS<sub>2</sub> AND SYNTHESIS OF NEW MoS<sub>2</sub> NANOCOMPOSITES WITH THE EXFOLIATION-ENCAPSULATIVE PRECIPITATION METHOD

### Introduction

The intercalation of polymers in layered inorganic solids is much more difficult than the intercalation of small molecules because of their large macromolecular size. The conventional direct intercalation method, which accounts for the intercalation of most simple organic molecules, is usually not applicable to polymers. The alternative route, which involves monomer intercalation followed by intra-gallery polymerization, seems elegant but is hard to carry out. Prior to our exploration of the MoS<sub>2</sub>/polymer system, through which a new convenient synthesis method was developed [1], the majority of the inorganic/polymeric nanocomposites were classified into two categories: (a) nanocomposites of conjugated polymers in oxidative hosts synthesized by the *redox* intercalative polymerization, and (b) nanocomposites of clays fabricated with organoclay precursors which can be delaminated. Due to the lack of highly oxidizing layered materials, the application of the *redox* intercalative polymerization is limited to certain hosts [2]. On the other hand, versatile clay nanocomposites had been prepared with clays swelled and exfoliated by surfactants [3]. This route pointed to a promising approach to new classes of nanocomposites. As for other layered materials, however, the methodology had been seldom applied, since the swelling property of clays is mirrored in only a few layered inorganic compounds. The V<sub>2</sub>O<sub>5</sub> xerogel,

which swells spontaneously in water and encapsulates a variety of water-soluble polymers [4], is an example.

The new intercalation method, which we name exfoliation-encapsulative precipitation (EEP) method, was first reported with the simple organic compound intercalation in MoS<sub>2</sub> [5]. It was then introduced in the field of polymer intercalation in the development of the MoS<sub>2</sub>/polymer nanocomposites [1] and proved to be convenient and effective. In this method, the layered inorganic host is exfoliated and forms a monolayer suspension. The monolayers combine with dissolved polymeric molecules when a polymer solution is added, and the two types of components precipitate out as a lamellar nanocomposite. The successful application of the EEP method to MoS<sub>2</sub>, which is chemically inert, and which cannot be directly intercalated by even simple organic molecules, demonstrates the potential of the delamination methodology to the synthesis of nanocomposites with common layered inorganic compounds. Later, the EEP method was generalized to other layered hosts such as MoO<sub>3</sub> [6], TaS<sub>2</sub>[7], WS<sub>2</sub> [8], NbSe<sub>2</sub> [9] and so on. Nanocomposites prepared with this method are even superior to the clay nanocomposites in respect of compositional and structural simplicity, since no surfactant is involved.

Earlier work in this group [1] succeeded in encapsulating many types of soluble polymers, which included water soluble polymers such as poly(ethylene oxide) (PEO), poly(propylene glycol) (PPG), polyvinylpyrrolidone (PVP), polyethylenimine (PEI) and methyl cellulose (MCel), common plastics such as polyethylene (PE) and nylon-6 (PA6), and conductive polymers such as polyaniline (PANI). The physical properties of the restacked MoS<sub>2</sub> and the synthesized MoS<sub>2</sub>/polymer nanocomposites were also examined. It was noticed at that time that the

restacked MoS<sub>2</sub> probably had the intralayer structure of 1T-MoS<sub>2</sub> [10] in which the Mo atoms were octahedral coordinated. This form was metastable converting exothermically to the normal 2H form of MoS<sub>2</sub> which had Mo atoms in the trigonal-prismatic coordination. Later, it was proved by electron diffraction that the Mo in the exfoliated and freshly restacked MoS<sub>2</sub> has a distorted octahedral coordination [11]. The conversion of the MoS<sub>2</sub> causes many interesting changes in the properties of restacked MoS<sub>2</sub> and nanocomposites. Although extensive, the investigation in exfoliated/restacked MoS<sub>2</sub> and nanocomposites was not completed in Bissessur's dissertation work. Since MoS<sub>2</sub> is a readily available commercial material and has many important applications such as lubrication, the catalyzation in hydrodesulfurization [12] and the rechargeable battery fabrication [13], a more extensive exploration in MoS<sub>2</sub>/polymer nanocomposites was conducted in the present dissertation research. This research was carried in four directions: (a) searching for more economic and convenient methods to prepare exfoliated MoS<sub>2</sub>, (b) further studies to better understand the nature and properties of exfoliated MoS<sub>2</sub>, restacked MoS<sub>2</sub>, and important MoS<sub>2</sub>/polymer nanocomposites such as (PEO)<sub>x</sub>MoS<sub>2</sub>, (c) further development of the EEP method, and (d) exploration of new strategies to synthesize MoS<sub>2</sub> nanocomposites with insoluble polymers. The research on the former three parts is reported in this chapter. The last one will be described in Chapter 2.

## Experimental Section

### 1. Reagents

MoS<sub>2</sub> (99%, 1 μm size aver.) was purchased from Cerac Inc. n-Butyl lithium (2.5 M solution in hexane), LiBH<sub>4</sub> (95%), poly(ethylene oxide) (Molecular Weight 100,000), nylon-6 (MW 10,000), polystyrene (MW 280,000), polyacrylamide (MW 5,000,000), poly(vinyl alcohol) (MW 124,000-186,000), polypropylene (MW 250,000), poly(methyl methacrylate) (MW 120,000), polybenzimidazole (melting point > 300 °C), poly(ethylene terephthalate) (MW 18,000) and high density polyethylene (MW 125,000) were purchased from Aldrich Chemical Company. Polyvinylpyrrolidone (MW 10,000) was from Sigma Chemical Co. CaH<sub>2</sub> (>95%), hexane (GR) and ethyl acetate (GR) were purchased from EM Science Inc. Formic acid (88%, ACS Grade), decalin (purified), 200 proof ethanol and phenol (reagent grade) were from Columbus Chemical Industries Inc., Fisher Chemical Company, Quantum Chemical Company and J. T. Baker Chemical Co. respectively. 2,2,2-Trifluoroethanol (99%) was purchased from both Lancaster Synthesis Inc. and PRG Catalog Inc. Water for experiments and processing was deionized water.

### 2. Lithiation and Exfoliation of MoS<sub>2</sub>

#### a. Preparation of LiMoS<sub>2</sub> by reaction of MoS<sub>2</sub> with n-butyl lithium

In this classical method of preparation of LiMoS<sub>2</sub> [14], MoS<sub>2</sub> was reacted with excess n-butyl lithium (n-LiBu) in solution under an inert atmosphere. In a typical reaction, 4 g of MoS<sub>2</sub> (0.025 mol) was reacted in 75 ml of 1 M n-BuLi/hexane solution (0.075 mol of n-BuLi) for 3 days. The LiMoS<sub>2</sub> was collected by filtration, washed with copious hexane and

pumped to dryness. The reaction and processing were under nitrogen atmosphere. The hexane was distilled from  $\text{CaH}_2$  under nitrogen before use. The product was stored in a nitrogen glove box after preparation.

b. Preparation of  $\text{LiMoS}_2$  by reaction of  $\text{MoS}_2$  with  $\text{LiBH}_4$

This convenient new method of  $\text{LiMoS}_2$  preparation was developed in the present research. In this method,  $\text{MoS}_2$  was combined with  $\text{LiBH}_4$  in a solid state reaction at an elevated temperature to produce  $\text{LiMoS}_2$ . In a typical reaction, 10.00 g of  $\text{MoS}_2$  (0.0625 mol) and 2.04 g of  $\text{LiBH}_4$  (0.0938 mol) were ground and mixed together in a nitrogen glove box. They were put into a ceramic crucible and placed in a quartz tube (2.5 in. diameter, 34.5 in. length) which had a balloon connected to it, see Figure 1.1. The quartz tube was taken out of the glove box and inserted into a programmable furnace so that the crucible was in the middle of the hot zone while the outlet, connected to the balloon, was out of the furnace. The furnace was heat up to 350 °C in 3 h, kept at this temperature for 72 h and then cooled to room temperature in 3 h. The gas produced by the reaction was accumulated in the balloon which expanded, thus avoiding explosion. After the reaction, the quartz tube was separated from the balloon and taken into the nitrogen glove box. The product was collected as a mixture of  $\text{LiMoS}_2$ ,  $\text{LiBH}_4$  and  $\text{LiH}$ , and stored under a nitrogen atmosphere.

c. Exfoliation of  $\text{LiMoS}_2$

The  $\text{LiMoS}_2$  prepared by the LiBu procedure was pure. An amount of 0.2 g of this  $\text{LiMoS}_2$  (1.2 mmol), was typically used in a reaction, and was exfoliated in 20 ml of water by 1 h of stirring. The exfoliated  $\text{MoS}_2$  was collected by centrifugation to separate from the  $\text{LiOH}$  produced

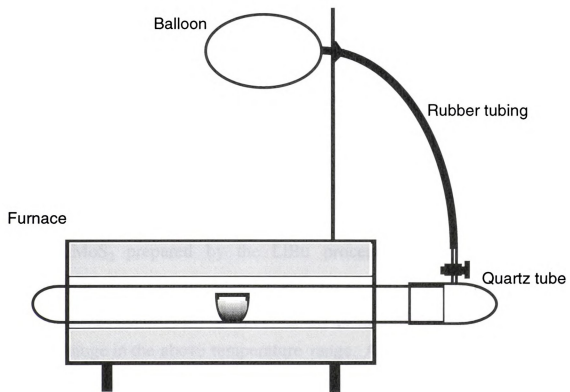


Figure 1.1. Experimental set-up for the high temperature  $\text{LiBH}_4$  lithiation reaction.

by the reaction. It was re-dispersed in 20 ml of fresh water by 30 min of stirring for succeeding reactions.

The product from the  $\text{LiBH}_4$  lithiation method was a mixture of  $\text{LiMoS}_2$ ,  $\text{LiBH}_4$  and  $\text{LiH}$ . An amount 0.213 g of this mixture contained about 0.2 g  $\text{LiMoS}_2$  (1.2 mmol). This amount of the mixture was stirred in 20 ml of water for 1 h. Centrifugation was used to collect exfoliated  $\text{MoS}_2$  from the solution. The restacked  $\text{MoS}_2$  was washed again with 20 ml of water and re-dispersed in 20 ml of fresh water by 30 min of stirring for subsequent reactions.

### 3. Investigation of $\text{LiMoS}_2$ and Freshly Restacked $\text{MoS}_2$

#### a. Thermal stability of $\text{LiMoS}_2$

$\text{LiMoS}_2$  prepared by the LiBu procedure was checked by the differential scanning calorimeter (DSC) up to 300 °C. The curve of DSC did not show exothermic or endothermic peaks, which meant no obvious phase change in the above temperature range. A second heating cycle gave almost the same curve as the first one. The sample could exfoliate after this process.

#### b. Elemental analysis and $^7\text{Li}$ NMR of freshly restacked $\text{MoS}_2$

An amount of 1.07 g of the  $\text{LiBH}_4$ ,  $\text{LiH}$  and  $\text{LiMoS}_2$  mixture, which was produced from the  $\text{LiBH}_4$  lithiation reaction and contained about 1.00 g  $\text{LiMoS}_2$  (6.0 mmol), was washed 6 times by stirring in 100 ml portions of water for 30 min and collecting by centrifugation. The restacked  $\text{MoS}_2$  so obtained was pumped for a week to dryness and used in  $^7\text{Li}$  solid state nuclear magnetic resonance (NMR) experiments and for inductively coupled plasma (ICP) spectroscopy analysis.

NMR experiments detected strong  $^7\text{Li}$  signals which assured the existence of Li inside the sample. The ICP analysis showed 0.686 wt% Li, 51.8 wt% Mo and 35.9 wt% S, which corresponds to  $\text{Li}_{0.18}\text{MoS}_2$ .

#### 4. Preparation of $\text{MoS}_2$ /Polymer Nanocomposites

##### a. Poly(ethylene oxide) (PEO) nanocomposites

The ratio of PEO to  $\text{MoS}_2$  used typically in this work was  $\sim 2$  to 1. In a typical reaction, 20 ml of an aqueous solution containing 0.106 g (2.4 mmol) PEO was mixed with 20 ml of aqueous  $\text{MoS}_2$  monolayer suspension containing 1.2 mmol of  $\text{MoS}_2$ , and stirred for 2 days in a stoppered 125 ml Erlenmeyer flask. The product nanocomposite was collected by centrifugation and washed thrice with 20 ml portions of water. The product was then dried in air and pumped to dryness. To cast a  $(\text{PEO})_x\text{MoS}_2$  film, the paste of the product was spread on a glass plate in air before drying. For reactions using other PEO/ $\text{MoS}_2$  ratios, the amount of polymer varied accordingly.

In reactions designed to produce delaminated  $(\text{PEO})_x\text{MoS}_2$  nanocomposites, the ratios of PEO to  $\text{MoS}_2$  used were 2, 4, 8 and 16, and the concentrations of the polymer in solution were 3%, 4%, 8% and 13% respectively. The concentration of the  $\text{MoS}_2$  monolayer suspension was twice as that of the typical one described above. After the two solutions, 10 ml of  $\text{MoS}_2/\text{H}_2\text{O}$  and a corresponding amount of  $\text{PEO}/\text{H}_2\text{O}$ , were mixed and stirred for 2 days, the mixture was pumped to dryness. X-ray diffraction indicated that the mixture was composed of the known  $(\text{PEO})_x\text{MoS}_2$  phase (d spacing 16.2-17.7 Å) and bulk PEO. Neither delaminated  $(\text{PEO})_x\text{MoS}_2$  nanocomposites nor nanocomposites with widely spaced layers were produced.

b. Poly(N-vinyl pyrrolidone) (PVP) nanocomposites

In a reaction, 20 ml of aqueous MoS<sub>2</sub> monolayer suspension, which contained 0.2 g of MoS<sub>2</sub> (1.2 mmol), was mixed with 20 ml of aqueous PVP solution which contained 0.533 g of PVP (4.8 mmol VP repeat units), and was stirred for 2 days. The (PVP)<sub>x</sub>MoS<sub>2</sub> was collected by centrifugation, washed 3 times with water, dried first in air and then under vacuum. The (PVP)<sub>x</sub>MoS<sub>2</sub> product had a basal spacing ~ 28 Å. Washing with water did not have a significant effect on the d spacing of the product.

c. Nylon-6 (PA6) nanocomposites

Procedure 1: As the first of the two procedures, (PA6)<sub>x</sub>MoS<sub>2</sub> nanocomposites were prepared using PA6/CF<sub>3</sub>CH<sub>2</sub>OH solution. The method was a modification from the one used earlier [1]. In a typical reaction, 10 ml of MoS<sub>2</sub> suspension containing 0.20 g MoS<sub>2</sub> (1.2 mmol) was added dropwise into 20 ml of PA-6/CF<sub>3</sub>CH<sub>2</sub>OH solution under stirring. The CF<sub>3</sub>CH<sub>2</sub>OH solution contained 0.49 g of PA6 (4.32 mmol C<sub>6</sub>H<sub>11</sub>NO repeat units). The solution was stirred for 2 days before it was centrifuged to isolate the nanocomposite from it. The product was washed with 5 ml of CF<sub>3</sub>CH<sub>2</sub>OH/H<sub>2</sub>O (2:1) solution, and dried first in air and then under vacuum.

In the reaction above, the ratio of PA6 to MoS<sub>2</sub> was 3.6:1. Other ratios such as 0.2, 0.5, 1.0, 2.0, 4.0, or 10 to 1 were also used.

Procedure 2: (PA6)<sub>x</sub>MoS<sub>2</sub> nanocomposites can also be synthesized by a reaction between an aqueous MoS<sub>2</sub> monolayer suspension and a PA6 formic-acid solution. In a typical reaction, 20 ml of MoS<sub>2</sub> suspension containing 0.20 g MoS<sub>2</sub> (1.2 mmol) was added dropwise into 100 ml of

PA6/HCOOH solution which contained 0.68 g of PA6 (6.0 mmol C<sub>6</sub>H<sub>11</sub>NO repeat units) under vigorous stirring. A large volume of HCOOH was required to keep PA6 in solution. The solution was stirred for 3 h before it was centrifuged to separate the nanocomposite. The product was washed with water 3 times and methanol once, and dried first in air and then under vacuum.

d. Polystyrene (PS) nanocomposites

(PS)<sub>x</sub>MoS<sub>2</sub> nanocomposites were successfully prepared by mixing and reacting the aqueous MoS<sub>2</sub> monolayer suspension with very concentrated PS/(ethyl acetate) solutions. In a typical reaction, 20 ml of MoS<sub>2</sub> suspension containing 0.20 g MoS<sub>2</sub> (1.2 mmol) was mixed with 20 ml of ethyl acetate solution which contained 5.0 g of PS. The two solutions were immiscible, so the mixture was stirred vigorously for 2 days. When the mixture was centrifuged, it separated in 3 layers: PS/(ethyl acetate) solution on the top, water solution at the middle and (PS)<sub>x</sub>MoS<sub>2</sub> nanocomposite at the bottom. The (PS)<sub>x</sub>MoS<sub>2</sub> nanocomposite was collected and dried without washing. Washing with ethyl acetate de-intercalates PS from MoS<sub>2</sub>.

e. Polyacrylamide (PAM) nanocomposites

In a typical reaction to prepare a (PAM)<sub>x</sub>MoS<sub>2</sub>, 20 ml of MoS<sub>2</sub> suspension containing 0.20 g MoS<sub>2</sub> (1.2 mmol) was mixed with 40 ml of aqueous PAM solution which contained 0.43 g of PAM (containing 6.0 mmol AM units). The mixture was stirred for 2 days before it was centrifuged to collect (PAM)<sub>x</sub>MoS<sub>2</sub>, which was washed with water 3 times, and dried first in air and then under vacuum.



f. Poly(vinyl alcohol) (PVA) nanocomposites

PVA is only slightly water soluble. In a typical reaction to prepare a  $(\text{PVA})_x\text{MoS}_2$  nanocomposite, 20 ml of  $\text{MoS}_2$  suspension containing 0.20 g  $\text{MoS}_2$  (1.2 mmol) was mixed with 80 ml of aqueous PVA solution which contained 0.53 g of PVA (12 mmol VA units). The PVA did not totally dissolve. The mixture was stirred for 9 days before it was filtered through a coarse filter paper to remove undissolved PVA. The solution through the filter paper was centrifuged to collect  $(\text{PVA})_x\text{MoS}_2$ . The nanocomposite was washed and dried as in the case of  $(\text{PAM})_x\text{MoS}_2$  above.

g. Polypropylene (PP) nanocomposites

An amount of 0.056 g PP (1.3 mmol  $\text{C}_3\text{H}_6$  repeat units) was dissolved in 40 ml of hot decalin (100 - 140 °C). The hot PP solution was added into 20 ml of cold aqueous  $\text{MoS}_2$  monolayer suspension, which contained 0.20 g of  $\text{MoS}_2$  (1.2 mmol), under vigorous stirring. The mixture was stirred at 90 °C for 4 h. The product was collected hot by centrifugation, and washed first with copious hot decalin (100 °C) and then with ether.

h. Poly(methyl methacrylate) (PMMA) nanocomposites

Procedure 1: An amount of 0.12 g of PMMA (containing 1.2 mmol MMA units) was dissolved at 50 °C in a mixture of 50 ml ethanol and 5 ml water. 10 ml of aqueous  $\text{MoS}_2$  monolayer suspension, which contained 0.1 g  $\text{MoS}_2$  (0.6 mmol), was added dropwise into the PMMA/ $\text{C}_2\text{H}_5\text{OH}/\text{H}_2\text{O}$  solution while stirring vigorously at 50 °C. The mixture was stirred at 50 °C for 12 h after the addition of  $\text{MoS}_2$ . The product was collected by

centrifugation, washed 3 times with formic acid and 3 times with water, and dried first in air and then in vacuum.

Procedure 2: An amount of 0.60 g of PMMA (containing 6 mmol MMA units) was dissolved in 100 ml of formic acid. 10 ml of aqueous MoS<sub>2</sub> monolayer suspension, which contained 0.1 g MoS<sub>2</sub> (0.6 mmol), was added dropwise into the PMMA/HCOOH solution, which was stirred vigorously. The mixture was stirred for 12 h after the addition of MoS<sub>2</sub>. Since PMMA did not precipitate out, the product was collected by centrifugation. The nanocomposite was washed and dried as in Procedure 1 above.

i. Polybenzimidazole (PBI) nanocomposites

An amount of 10 ml of aqueous MoS<sub>2</sub> monolayer suspension, which contained 0.1 g of MoS<sub>2</sub> (0.6 mmol), was added dropwise into 75 ml of saturated PBI formic-acid solution (containing about 0.37 g PBI, or 1.2 mmol BI units), which was stirred vigorously during addition. After the mixture was stirred for 12 h, the product was isolated and processed the same as described in Procedure 1 above.

j. Poly(ethylene terephthalate (PETP) nanocomposites

An amount of 0.56 g of PETP (containing 3.0 mmol ETP units) was dissolved in 25 ml of phenol at 50 °C. The PETP/phenol solution was added dropwise into 10 ml of aqueous MoS<sub>2</sub> monolayer suspension which contained 0.1 g MoS<sub>2</sub> (0.6 mmol) and which was stirred vigorously at 50 °C. The mixture was stirred at 50 °C for 2 days after the addition. Phenol and water are immiscible, so vigorous stirring was required. The product

was collected by centrifugation at an elevated temperature (50 - 75 °C), washed with 75 °C phenol 3 times, and dried as above.

k. Elevated temperature annealing and variable temperature X-ray powder diffraction measurements for nanocomposites

Samples of nanocomposites,  $(\text{PEO})_x\text{MoS}_2$ ,  $(\text{PA6})_x\text{MoS}_2$ ,  $(\text{PS})_x\text{MoS}_2$ ,  $(\text{PE})_x\text{MoS}_2$  and  $(\text{PP})_x\text{MoS}_2$ , were vacuum sealed in Pyrex tubes and heated in an oven at temperatures between 150 and 175 °C for several days to check the possible thermal decomposition of the nanocomposites.

X-ray powder diffraction patterns were collected as a function of rising temperature for a  $(\text{PEO})_x\text{MoS}_2$  sample (not heat treated) to investigate the decomposition process. The patterns were collected at room temperature, 80 °C, and then every 10 °C from 100 °C to 230 °C. The sample was stabilized at each temperature for 10 min before the pattern was collected. The patterns were collected from  $2\theta$  5° to 8° and then from 13° to 16°. Each temperature step took 40 min.

## 5. Instrumentation

Powder X-ray diffraction (XRD) patterns were obtained on a Rigaku Ru-200B X-ray diffractometer, at 45 kV and 100 mA with a scintillation counter detector and a graphite monochromator to produce Cu  $K\alpha$  beam (wavelength 1.54184 Å). Powder samples and a continuous scanning mode with a scanning speed of 1°/min in  $2\theta$  and an increment of 0.01° were chosen for general purpose spectra. Variable temperature XRD measurements were done with a ceramic heating mask under the protection of nitrogen. The scanning speed was 0.2°/min. XRD experiments for one-

dimensional electron density calculations were done as described in Chapter 3.

The amount of polymers in the nanocomposites was determined by TGA measurements with a Shimadzu TGA-50 under a 46 ml/min oxygen flow, and a heating rate of 10 °C/min. The decomposition temperature of materials was checked with TGA measurements under a 57 ml/min nitrogen flow. DSC was carried out on a Shimadzu DSC-50 under nitrogen flow of a rate of 20 ml/min. The heating and cooling rates were 5 °C/min. Sample cells were made of aluminum, and were annealed at 450 °C in vacuum sealed tubes after they were cleaned. Samples were sealed in cells under a nitrogen atmosphere before measurement.

Infrared spectra were collected with a Nicolet IR/42 FTIR spectrometer in 2 cm<sup>-1</sup> resolution. Generally 64 scans were collected. Samples were measured as KBr pellets. The amount of Li in restacked MoS<sub>2</sub> was measured with Inductively Coupled Plasma (ICP) spectroscopy at Animal Health Diagnostic Laboratory [15] on the MSU campus. Variable temperature solid state <sup>7</sup>Li NMR spectra were taken on a 400 MHz Varian Nuclear Magnetic Resonance Instrument.

Room temperature electrical conductivity measurements for Figures 1.6 and 1.9 were done on pressed sample pellets with a four-probe detector connected to a Keithley-236 source measure unit. Room temperature conductivity measurements for data in Table 1.4 were done on pressed sample pellets with a four-probe detector connected to a Keithley-580 micro-Ohmmeter.

## Results and Discussion

### 1. The LiBH<sub>4</sub> Method of Producing LiMoS<sub>2</sub>

The exfoliated MoS<sub>2</sub>, which is the crucial material in the preparation of MoS<sub>2</sub> nanocomposites using the EEP method, is generated from the reaction of LiMoS<sub>2</sub> with water. In earlier studies of MoS<sub>2</sub>/polymer nanocomposites, LiMoS<sub>2</sub> was prepared by the conventional method [14] which uses LiBu in a room temperature reaction. Despite the strict anaerobic reaction conditions and the large excess of highly reactive LiBu, this method is still the best way to prepare pure LiMoS<sub>2</sub>, especially in small quantities. Here this route was still used occasionally to prepare LiMoS<sub>2</sub> for the reactions in which pure LiMoS<sub>2</sub> was preferred as a starting material. (By “pure”, we mean free of LiH and LiBH<sub>4</sub>, as discussed below.) In the preparation of most of the MoS<sub>2</sub>/polymer nanocomposites, however, the use of pure LiMoS<sub>2</sub> is not necessary, which suggests the possibility of a more convenient and economical route for preparation. The synthesis of LiMoS<sub>2</sub> with LiBH<sub>4</sub> at elevated temperature provides such a route.

LiBH<sub>4</sub>, and its analogs NaBH<sub>4</sub> and KBH<sub>4</sub>, are convenient reducing reagents in terms of storage and manipulation. Their stability in dry air and slow hydration in water [16] requires neither sophisticated equipment nor extreme care in processing. In most of its reducing reactions, the byproducts are B<sub>2</sub>H<sub>6</sub> and H<sub>2</sub>. These gases are separated from the solid or liquid products spontaneously, therefore, the products are usually pure and no additional purification step is needed. In our LiBH<sub>4</sub> route to prepare LiMoS<sub>2</sub>, the reaction also generates these two byproducts:



The reaction probably generates some LiH because of the decomposition of LiBH<sub>4</sub> at high temperature:



The LiH and the excess LiBH<sub>4</sub> stay in the solid phase with LiMoS<sub>2</sub> as a mixture. Fortunately, in order to generate exfoliated MoS<sub>2</sub>, it is not necessary to purify LiMoS<sub>2</sub> from this mixture of products which contains LiBH<sub>4</sub> and probably LiH. When the product is put into water, the LiBH<sub>4</sub> and LiH dissolve and decompose to form LiOH, and the resulting exfoliated MoS<sub>2</sub> can be readily purified by washing with water [17].



Therefore, this new route produces pure exfoliated MoS<sub>2</sub> for intercalation reaction, although the LiMoS<sub>2</sub> from the lithiation reaction is in a mixture with LiH and LiBH<sub>4</sub>.

A high quality monolayer MoS<sub>2</sub> suspension should be free from the unexfoliated material. This requires all MoS<sub>2</sub> to be converted to LiMoS<sub>2</sub> in the lithiation reaction. Since both MoS<sub>2</sub> and LiBH<sub>4</sub> can be ground to fine powder and mixed well before the lithiation reaction, complete lithiation of MoS<sub>2</sub> is achieved. Therefore, the high temperature LiBH<sub>4</sub> lithiation reaction produces high-quality exfoliated MoS<sub>2</sub>.

Since the new reaction is carried out in the solid state, a small reaction vessel can deliver a large quantity of product. The reaction set-up

is simple and no strict air-exclusion is necessary.  $\text{LiBH}_4$  is more expensive than  $\text{LiBu}$  (\$118/mol vs. \$53/mol according to the price of Aldrich Chemical Co.). However, considering the fact that only 1.5 equivalents of  $\text{LiBH}_4$  is used and no solvent purification is required, the  $\text{LiBH}_4$  approach is actually more economic.

$\text{LiBH}_4$  is generally considered as a mild reducing reagent and has been used mostly in organic reactions. In the field of inorganic chemistry, it has been used to reduce  $\text{MO}_3$ ,  $\text{V}_2\text{O}_5$ ,  $\text{FeOCl}$ ,  $\text{TiS}_2$ ,  $\text{TaS}_2$  [18]. At room temperature,  $\text{LiBH}_4$  cannot reduce chemically inert materials such as  $\text{MoS}_2$ , while its usage at elevated temperatures had not been seen reported.

The preparation of  $\text{LiMoS}_2$  with  $\text{LiBH}_4$  at an elevated temperature is the most convenient method to obtain  $\text{LiMoS}_2$  so far. There have existed several other routes to prepare alkali metal dichalcogenide ternary compounds, however, all of them have some shortcomings. The preparation reaction using binary chalcogenides and alkali metals in liquid  $\text{NH}_3$  at ca.  $-30\text{ }^\circ\text{C}$  [19] is even harder to deal with than the reaction with  $\text{LiBu}$ . The reaction of binary chalcogenides with alkali halide melts in a  $\text{H}_2\text{S}$  gas flow [20] needs solid-gas reaction facilities. In addition, the constant blowing of toxic  $\text{H}_2\text{S}$  is undesirable. The reaction of binary chalcogenides with alkali metals at ca  $800\text{ }^\circ\text{C}$  [21] seems convenient. However, when we used this method to prepare alkali metal intercalated  $\text{MoS}_2$  and then exfoliated  $\text{MoS}_2$ , we found the existence of un-reacted  $\text{MoS}_2$  in the product.

The possibility of using another less-expensive reducing reagent such as  $\text{LiAlH}_4$  or  $\text{LiH}$  to substitute  $\text{LiBH}_4$  was also explored without success. Although  $\text{LiAlH}_4$  can produce  $\text{LiMoS}_2$  at temperatures higher than  $300\text{ }^\circ\text{C}$ , the by-product  $\text{AlH}_3$  forms  $\text{Al}(\text{OH})_3$  in water, which is hard to separate from exfoliated  $\text{MoS}_2$  and interferes with the polymer encapsulation

process. It causes the production of low quality nanocomposites with short coherence length. LiH did not lithiate MoS<sub>2</sub> under similar conditions and a more severe condition (720 °C) caused decomposition. Similar to LiBH<sub>4</sub>, NaBH<sub>4</sub> also introduces Na<sup>+</sup> in MoS<sub>2</sub> and the product forms hydrated Na<sub>x</sub>MoS<sub>2</sub> in an aqueous solution. Nevertheless, hydrated Na<sub>x</sub>MoS<sub>2</sub> does not readily include polymers, therefore more investigation is needed to develop it into a starting material for nanocomposites.

## 2. Manipulation and Properties of Exfoliated and Restacked MoS<sub>2</sub>

In the old exfoliation procedure of LiMoS<sub>2</sub>, the suspension was sonicated for 30 min after the material had been put in water. The purpose of this ultrasonic wave treatment was to maximize the possibility of full exfoliation. The strong perturbation associated with this process broke the MoS<sub>2</sub> up into small sized layers and reduced the quality of the nanocomposites. Later we found that this ultrasonic process was not necessary because completely exfoliated MoS<sub>2</sub> can be obtained when LiMoS<sub>2</sub> is just stirred in water.

The cause of exfoliation of LiMoS<sub>2</sub> in water was once suggested to be the splitting of the MoS<sub>2</sub> layers by the violent reaction of the material with water and the vigorous generation of the hydrogen gas inside the interlayer space [5a, 5c]. This mechanism predicts that pre-oxidation of LiMoS<sub>2</sub> would severely affect the exfoliation process, because it would reduce the strength of this explosive reaction. This prediction demanded the strict exclusion of oxygen and moisture from LiMoS<sub>2</sub> before its exfoliation.

The fact that we were able to insert PEO in LiMoS<sub>2</sub>, which was exposed to air for ten hours, showed the ability of exfoliation of freshly

oxidized  $\text{LiMoS}_2$  and demonstrated a negligible effect of the pre-oxidation to the exfoliation property of  $\text{LiMoS}_2$ . Therefore, the splitting mechanism of the exfoliation seems questionable. Further investigations show that the exfoliation is due to the hydration or solvation of the  $\text{MoS}_2$  layers. The above experiments also suggest that storage of the  $\text{LiMoS}_2$  under inert atmosphere for the purpose of exfoliation does not have to be extremely stringent.

It was believed that when  $\text{LiMoS}_2$  was exposed to water, it was fully oxidized back to  $\text{MoS}_2$  and the exfoliated layers were neutral. Researchers in this area were excited by the thought of neutral suspended  $\text{MoS}_2$  monolayers in water because this phenomenon would be an exception among the exfoliated layered inorganic compounds. Other layered inorganic compounds either have charged layers or need assistance from surfactants to form monolayer suspensions. Our experience suggests that the concept of neutral  $\text{MoS}_2$  layers is incorrect and they actually carry negative charge. One reason for believing this is that exfoliated  $\text{MoS}_2$  encapsulates cations more readily than neutral molecules. Another reason is that solid state  $^7\text{Li}$  nuclear magnetic resonance (NMR) of restacked  $\text{MoS}_2$ , which was carefully washed with water, proved the existence of Li in this material. In addition, ICP spectroscopic analysis revealed that the composition of the freshly restacked  $\text{MoS}_2$  was probably  $\text{Li}_x\text{MoS}_2$  ( $x = 0.18$ ). More convincing experiments which prove that the exfoliated and freshly restacked  $\text{MoS}_2$  layers possess charges are those done by Heising and Kanatzidis [11], which include the electron diffraction study revealing the intralayer structure of the freshly restacked  $\text{MoS}_2$  different from  $2\text{H-MoS}_2$ , and  $^1\text{H-NMR}$  experiments which prove that the freshly restacked  $\text{MoS}_2$  evolves hydrogen gas when it is heated. Therefore, restacked  $\text{MoS}_2$  is

analogous to  $\text{Li}_x\text{TiS}_2$  and  $\text{Li}_x\text{TaS}_2$ , which exfoliate in water and some polar solvents because the layers carry charges.

The incomplete oxidation of the  $\text{MoS}_2$  layers when  $\text{LiMoS}_2$  is exposed to water and the charges that the exfoliated  $\text{MoS}_2$  layers carry suggests a solvation mechanism for the exfoliation. The negative charges of the  $\text{MoS}_2$  layers hold  $\text{Li}^+$  cations inside the interlayer galleries to balance the charge, while the  $\text{Li}^+$  cations are solvated by water molecules. The solvation of the  $\text{Li}^+$  cations makes the  $\text{MoS}_2^{x-}$  layers exfoliate. This mechanism explains why the pre-oxidized  $\text{LiMoS}_2$ , which in fact is not  $\text{MoS}_2$  but  $\text{Li}_x\text{MoS}_2$ , can still exfoliate. It also explains why the water molecules are hard to remove out the freshly restacked  $\text{MoS}_2$  [22] and why the freshly hydrated  $\text{MoS}_2$  can exfoliate again. Dehydration at elevated temperature such as 45 or 60 °C [5b] is more effective, since heating accelerates the conversion to  $2\text{H-MoS}_2$  [1] and the additional oxidation of  $\text{Li}_x\text{MoS}_2$ . A similar explanation applies to the fact that the pre-oxidized and high temperature (150 °C) treated  $\text{LiMoS}_2$  could not exfoliate.

### 3. $(\text{PEO})_x\text{MoS}_2$ and $(\text{PVP})_x\text{MoS}_2$ Nanocomposites

In previous work [1], the reaction for  $(\text{PEO})_x\text{MoS}_2$  nanocomposites was carried out exclusively around the stoichiometrical ratio of 1 mol PEO to 1 mol  $\text{MoS}_2$ . In the present research, reactions have been run under different PEO to  $\text{MoS}_2$  ratios to explore other  $(\text{PEO})_x\text{MoS}_2$  nanocomposite phases. Although the ratio of PEO to  $\text{MoS}_2$  has been increased gradually from 1 to 20 in the reactions, the basal spacing of the resulting nanocomposite always falls in the range between 15.3 to 18.5 Å, as indicated by XRD patterns. Even in the reactions designed to produce delaminated  $(\text{PEO})_x\text{MoS}_2$  nanocomposites, in which the aqueous  $\text{MoS}_2/\text{PEO}$

solution was dried under constant agitation, the reaction would not produce nanocomposites of higher d spacing, or delaminated  $(\text{PEO})_x\text{MoS}_2$  nanocomposites. (A constant agitation during drying the mixture is considered the best way to keep the  $\text{MoS}_2$  and PEO from phase separation.) Therefore, basically only one type of  $(\text{PEO})_x\text{MoS}_2$  nanocomposite has been prepared from the solution-encapsulation reaction.

Contrary to the results obtained with 1 to 1 ratio of PEO to  $\text{MoS}_2$ , when the ratio is increased to 2:1 or above, the probability of producing a well ordered nanocomposite product is largely increased, and the products are free from the restacked  $\text{MoS}_2$  phase. The order in the structure of the nanocomposite can be judged from the sharpness of the peaks in the X-ray diffraction patterns. The d spacings of the products usually range between 16 and 17 Å, and the nanocomposites usually contain 1.5 equivalents of PEO instead of 1.0, as revealed by TGA measurements in an oxygen flow. These experiments indicate that some excess of polymer is needed to fully occupy the galleries of  $\text{MoS}_2$ .

It must be mentioned that prolonged excessive washing of the freshly collected nanocomposites with water will lower the quality of the product. After this treatment, the nanocomposites frequently have X-ray patterns of low and broad peaks, which indicates poor stacking orders. From X-ray diffraction patterns, it is calculated that the coherence lengths of the nanocomposites in the stacking direction may decrease from about 120 Å to about 43 Å [23]. In some cases, excessive washing would also cause the appearance of the deintercalated phase.

The one-dimensional electron density map of a  $(\text{PEO})_x\text{MoS}_2$  nanocomposite has been calculated from high quality reflection XRD patterns carefully collected from an oriented nanocomposite film, see

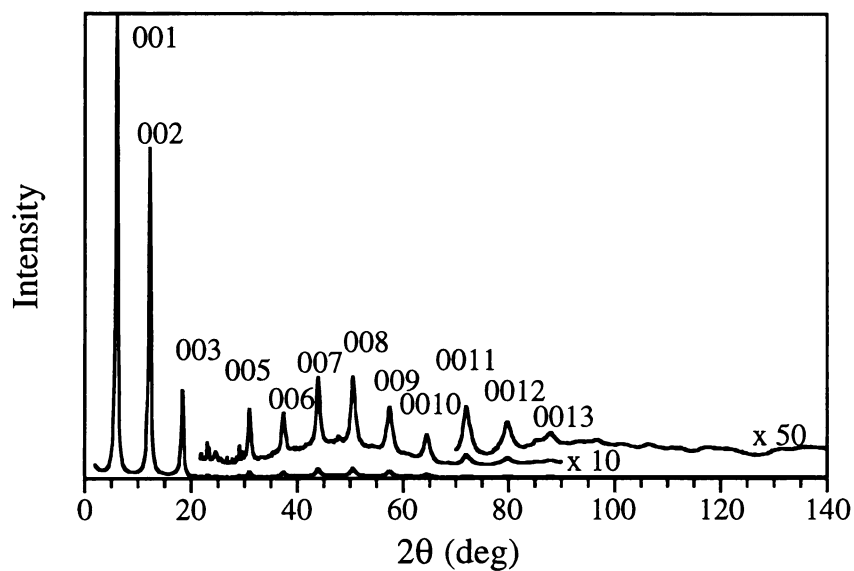


Figure 1.2. XRD patterns of a  $(\text{PEO})_x\text{MoS}_2$  nanocomposite used to calculate the one-dimensional electron density map.

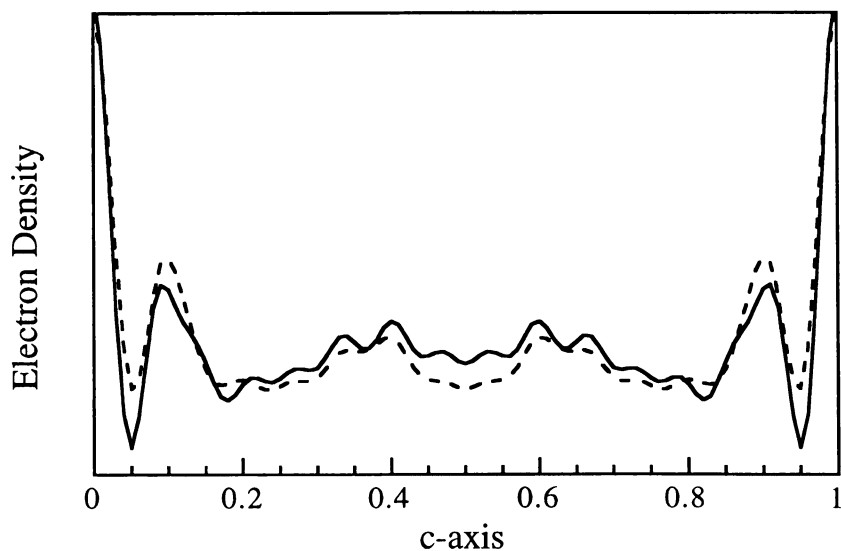


Figure 1.3. One-dimensional electron density map of a  $(\text{PEO})_x\text{MoS}_2$  nanocomposite. (Solid line, calculated from experimental data; dash line, from model.)

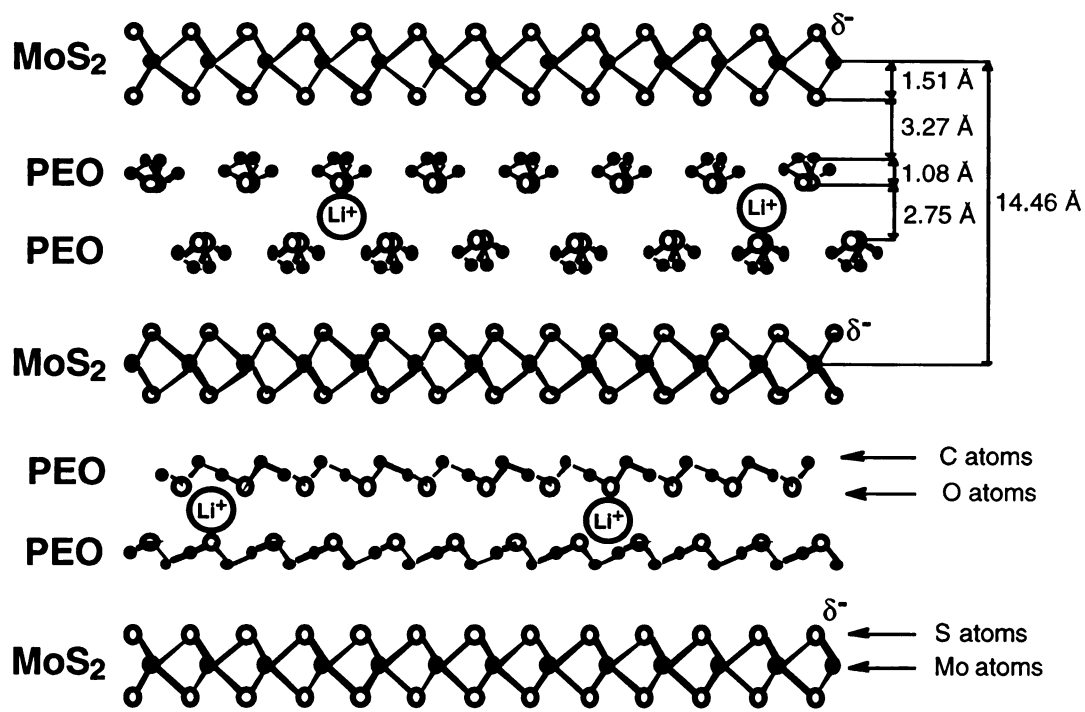


Figure 1.4. Structural model for the  $(\text{PEO})_x\text{MoS}_2$  nanocomposite.

Figures 1.2 and 1.3. The features of the map are almost the same as those for the  $\text{Li}_{0.2}(\text{PEO})_x\text{TaS}_2$  nanocomposite which will be presented in Chapter 3. The model proposed according to the one-dimensional electron density map is shown in Figure 1.4, which is similar to the one for  $\text{Li}_{0.2}(\text{PEO})_x\text{TaS}_2$ . In this model, the PEO chains take a conformation that was found in type II PEO-HgCl<sub>2</sub> complex. Since the one-dimensional electron density map and the model for the  $\text{Li}_{0.2}(\text{PEO})_x\text{TaS}_2$  nanocomposite will be described in detail in Chapter 3, a similar discussion is not given here.

Possible existing phases other than the phases reported in the preceding research have also been searched in  $(\text{PVP})_x\text{MoS}_2$  nanocomposites. In previous work, the PVP to MoS<sub>2</sub> ratio used in the encapsulation reaction was 1 to 1 [1]. It was suspected that the amount of PVP might not have been sufficient to produce the nanocomposite with maximum polymer content. Reactions with excess PVP have verified the suspicion and produced a  $(\text{PVP})_x\text{MoS}_2$  of higher basal spacing, 28.8 Å (see Figure 1.5A) instead of 21.1 Å. The amount of polymer in the nanocomposite is 0.96 VP units rather than 0.76 VP units obtained from the 1:1 ratio. The temperature of the structural transition from the octahedral to the trigonal-prismatic MoS<sub>2</sub>, however, is 174 °C, almost the same as that of the previously reported  $(\text{PVP})_x\text{MoS}_2$ , 177 °C.

#### 4. Investigations in $(\text{PA6})_x\text{MoS}_2$ Nanocomposites

The reaction to encapsulate PA6 in MoS<sub>2</sub> used earlier [1] was modified here. The new procedure makes use of the advantage that a solution composed of 1/3 of water and 2/3 of CF<sub>3</sub>CH<sub>2</sub>OH does not cause PA6 to precipitate, so that no PA6 will come out of solution when the



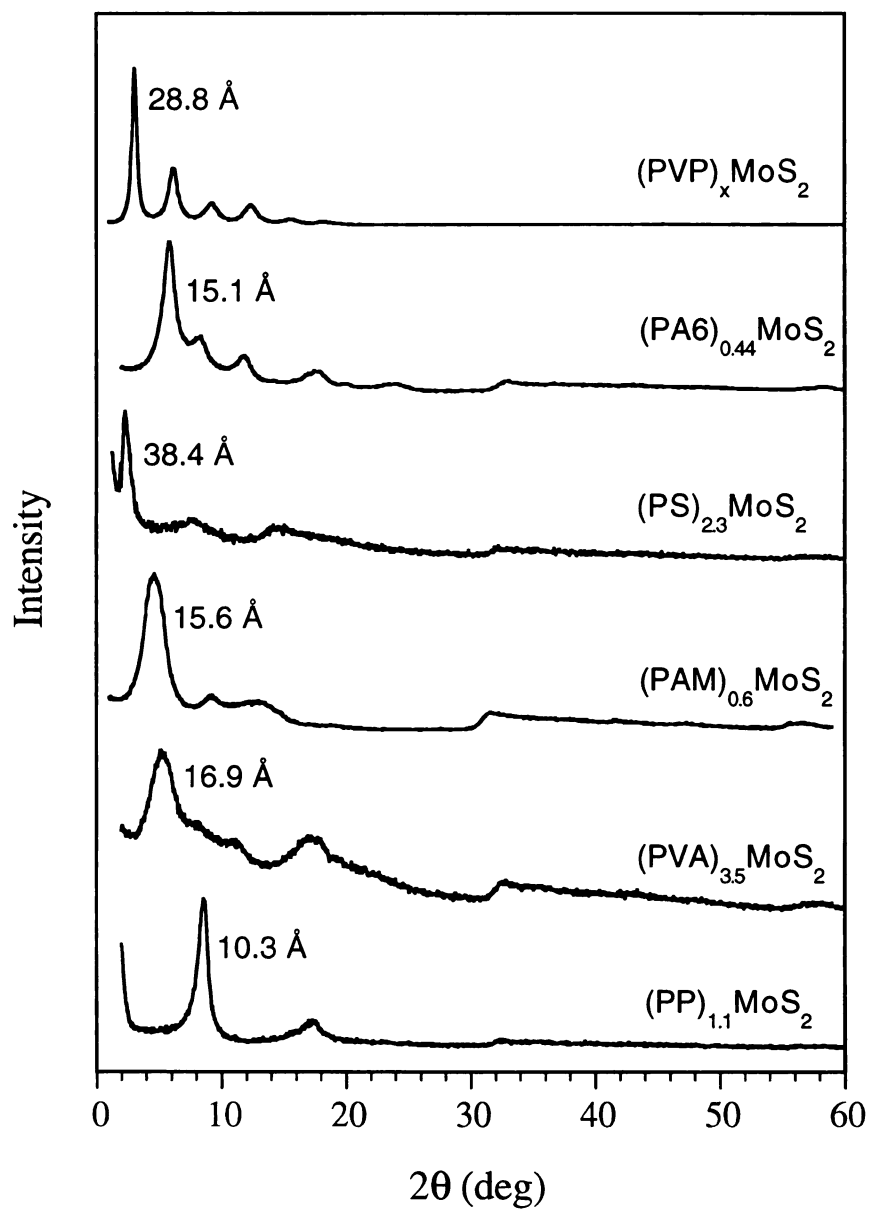


Figure 1.5A. XRD patterns of the new nanocomposite phases (1).

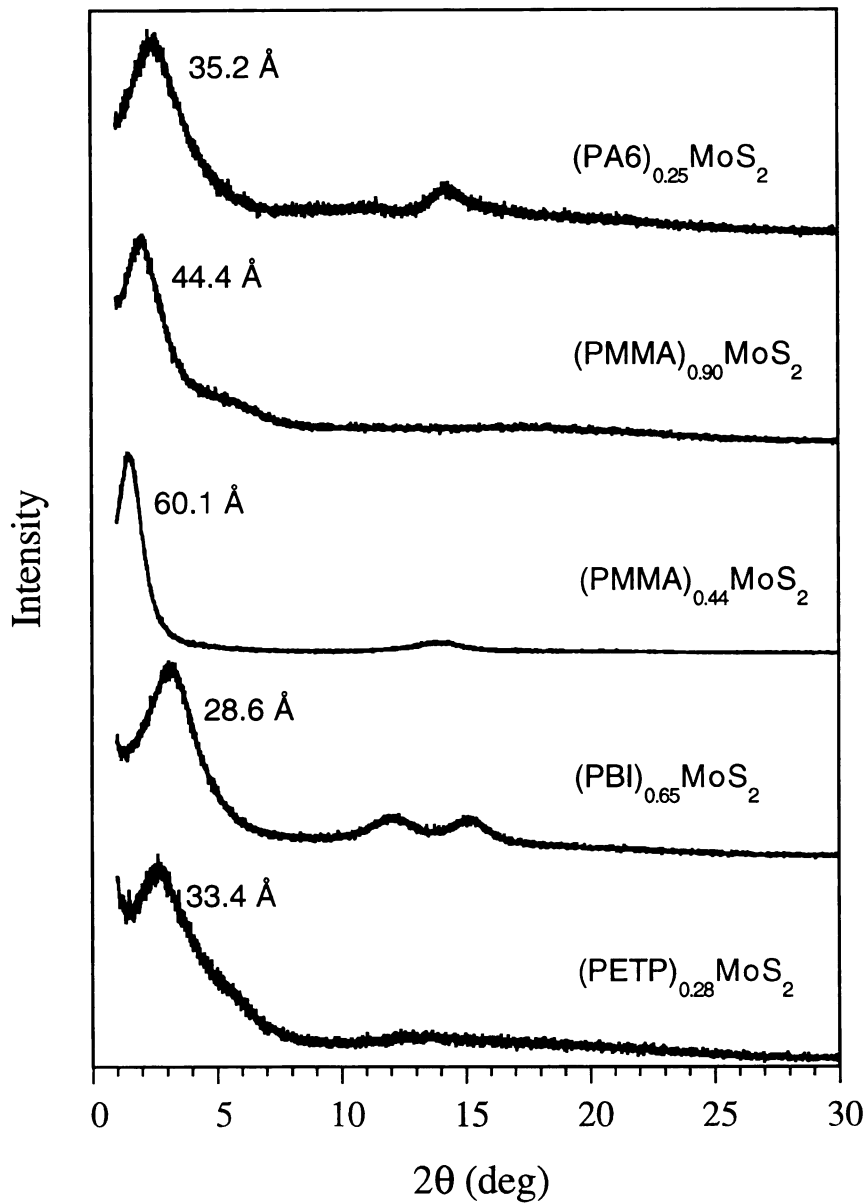


Figure 1.5B. XRD patterns of the new nanocomposite phases (2).

aqueous MoS<sub>2</sub> monolayer suspension is added into the PA6/CF<sub>3</sub>CH<sub>2</sub>OH solution. These conditions are considered good for nylon-6 encapsulation, because they are free from competing side reactions, and the product is free from excess nylon-6. The basal spacing of the nanocomposite is 14.8 Å, smaller than the previously reported value 17.5 Å [1], see Figure 1.5A. The composition determined by TGA is (PA-6)<sub>x</sub>MoS<sub>2</sub> (x=0.26-0.44).

The driving force to form (PA6)<sub>x</sub>MoS<sub>2</sub> is not strong in the CF<sub>3</sub>CH<sub>2</sub>OH/water solution. Although the amount of nylon-6 in the nanocomposite is only about 0.26-0.44 C<sub>6</sub>H<sub>11</sub>NO per MoS<sub>2</sub>, more than 2 equivalents of nylon-6 must be used to make the product free from the restacked MoS<sub>2</sub> phase. When the ratio of nylon-6 to MoS<sub>2</sub> is 1 or less, the (PA6)<sub>x</sub>MoS<sub>2</sub> nanocomposite of 15.0 Å d spacing forms together with restacked MoS<sub>2</sub>. When the ratio decreases from 1 to 0.2, the amount of restacked MoS<sub>2</sub> increases substantially from 1/3 to 2/3 of the total product. When the ratio is 2, no restacked MoS<sub>2</sub> is observed. Instead, a phase that has a basal spacing of 10.6 Å appears. This phase will diminish when the ratio increases, however, it will not be eliminated even when the ratio reaches 10. At a ratio of 2, the amount of the 10.6 Å phase is about 40%; at a ratio of 3.6, the amount is about 30%; at a ratio of 10, it is about 22%. The reactions are summarized in Table 1.1.

The encapsulation using MoS<sub>2</sub> dispersed in CF<sub>3</sub>CH<sub>2</sub>OH did not succeed. The product from this reaction in water-free CF<sub>3</sub>CH<sub>2</sub>OH solution was found to be mostly restacked MoS<sub>2</sub>. The weak driving force to form (PA6)<sub>x</sub>MoS<sub>2</sub> nanocomposite might be the reason for the failure of encapsulation.

CF<sub>3</sub>CH<sub>2</sub>OH is not an ideal solvent for reactions. It is volatile, highly toxic and extremely expensive. An alternative solvent for nylon-6 is formic

Table 1.1. Nylon-6 intercalation reactions with PA6/CF<sub>3</sub>CH<sub>2</sub>OH solution

| PA6:MoS <sub>2</sub><br>(mol:mol) | phase of<br>d=15 Å | phase of<br>d=10.6 Å | phase of<br>6.2 Å |
|-----------------------------------|--------------------|----------------------|-------------------|
| 0.2:1.0                           | 33%                | -                    | 67%               |
| 1.0:1.0                           | 67%                | -                    | 33%               |
| 2.0:1.0                           | 60%                | 40%                  | -                 |
| 3.6:1.0                           | 70%                | 30%                  | -                 |
| 10:1.0                            | 78%                | 22%                  | -                 |

acid, however, it causes the exfoliated MoS<sub>2</sub> to precipitate, which is an unwanted competing side reaction. Delaminated (PA6)<sub>x</sub>MoS<sub>2</sub> nanocomposites or high d-spacing products have been obtained by mixing the aqueous MoS<sub>2</sub> monolayer suspension and the nylon-6 formic-acid solution but some restacked MoS<sub>2</sub> phase often exists. Because the quick precipitation of exfoliated MoS<sub>2</sub> in formic acid solution, the arrangement of polymer chains is poor and loose. A sample with a 35 Å d spacing (see Figure 4B) has only a polymer content of 0.25 C<sub>6</sub>H<sub>11</sub>NO units per MoS<sub>2</sub>.

## 5. Synthesis of (PS)<sub>x</sub>MoS<sub>2</sub> Nanocomposites

Polystyrene (PS) is the most common commercial polymer. It can be dissolved in many organic solvents, including both polar and non-polar solvents. Therefore, it is often a model polymer for basic studies in polymer science. However, a difficulty has been met in the experiments encapsulating polystyrene in exfoliated MoS<sub>2</sub>: polystyrene does not have a strong tendency to combine with the MoS<sub>2</sub> monolayers. The solvents for polystyrene, on the other hand, are more or less prone to combine with

MoS<sub>2</sub> monolayers and stay in the interlayer galleries of MoS<sub>2</sub>. As a result, in many cases the solvents compete with polystyrene to form solvated MoS<sub>2</sub> phases. These solvents include benzene, carbon tetrachloride, chloroform, acetone, toluene, decalin and THF.

Out from all of the solvents we tried, ethyl acetate turns out to be suitable for polystyrene encapsulation. To maximize polystyrene's ability to compete, concentrated polystyrene/(ethyl acetate) solutions were used. The concentration of the solution was 20 wt% or above, which is very high compared to the concentrations of other polymer solutions mentioned above. (PS)<sub>x</sub>MoS<sub>2</sub> nanocomposites prepared are either delaminated nanocomposites, or nanocomposites with a very large d spacing (see Figure 1.5A), depending on the concentration of the polystyrene solution and other encapsulation conditions. Washing (PS)<sub>x</sub>MoS<sub>2</sub> nanocomposites with ethyl acetate causes the deintercalation of polystyrene and produces restacked MoS<sub>2</sub>. The information of some (PS)<sub>x</sub>MoS<sub>2</sub> nanocomposites prepared under different conditions are summarized in Table 1.2.

Table 1.2. Information about the synthesis of MoS<sub>2</sub>/PS nanocomposites

| reaction | PS concentration (V%) | reaction temperature | d spacing (Å) | PS/MoS <sub>2</sub> in composite (mol/mol) |
|----------|-----------------------|----------------------|---------------|--|
| trial 1  | 20%                   | R.T.                 | 38.4~41.4     | 2.3/1.0                                    |
| trial 2  | 23%                   | R.T.                 | -*            | 3.8/1.0                                    |
| trial 3  | 20%                   | 65 °C                | -*            | 6.8/1.0                                    |

\* The latter two samples are delaminated.

The reaction at an elevated temperature (65 °C) favors the completion of intercalation. This phenomenon is reminiscent of the successful high temperature encapsulation of the other two non-polar polymers, polyethylene and polypropylene. At elevated temperature, the exfoliated MoS<sub>2</sub> converts to the 2H form, which probably facilitates the intercalation of non-polar polymers.

## 6. Synthesis of Other MoS<sub>2</sub>/Polymer Nanocomposites

Since many water-soluble polymers were already intercalated in MoS<sub>2</sub> [1] with no difficulty, the effort in the present research was mainly on the intercalation of polymers dissolved only in non-aqueous solutions. The only two new nanocomposites which contain water-soluble polymers are (PAM)<sub>x</sub>MoS<sub>2</sub> (PAM = polyacrylamide) and (PVA)<sub>x</sub>MoS<sub>2</sub> (PVA = polyvinylalcohol) (see Figure 1.5A and Table 1.3). Again, these two polymers are intercalated readily.

It was noticed by Bissessur that polypropylene (PP) can be intercalated in MoS<sub>2</sub> with the same procedure as that for polyethylene. However, because no good sample was obtained, he did not mention this nanocomposite in his dissertation. Satisfactory (PP)<sub>x</sub>MoS<sub>2</sub> samples have been obtained in the present research. Like (PE)<sub>x</sub>MoS<sub>2</sub> nanocomposites, (PP)<sub>x</sub>MoS<sub>2</sub> nanocomposites have basal spacings around 10.2-10.3 Å, see Figure 1.5A. The weight percentage of polymer is also similar in these two nanocomposites. (PE)<sub>1.5</sub>MoS<sub>2</sub> contains 21% polymer while (PP)<sub>1.1</sub>MoS<sub>2</sub> contains 22% polymer.

Poly(methyl methacrylate) (PMMA) is also a very common polymer, which is soluble in many solvents. Encapsulation of PMMA is successfully carried out in formic acid or a 50 °C ethanol/water solution. The

encapsulation using PMMA/(formic acid) solution is similar to the encapsulation of nylon-6 in formic acid. MoS<sub>2</sub> precipitates immediately when it is added into PMMA/(formic acid) solution, encapsulating some polymer to form the nanocomposite. The polymer chains are not well arranged in the interlayer galleries. The product has a large basal spacing, 60 Å (see Figure 1.5B), but a low polymer content, 0.44 MMA units per MoS<sub>2</sub>. If the reaction is not controlled well, restacked MoS<sub>2</sub> phase may appear. In 50 °C ethanol/water solution, neither polymer nor exfoliated MoS<sub>2</sub> precipitates in short time, so the encapsulation can be carried out without strongly competing side reactions. The polymer chains can take time to arrange themselves inside the interlayer galleries and pack more tightly. Therefore, the product should have a better quality (in terms of stacking order) and a higher polymer content. The basal spacing was only 44 Å (see Figure 1.5B) but the polymer content is 0.9 MMA units per MoS<sub>2</sub>. PMMA can also be dissolved in ethyl acetate, however, encapsulation with ethyl acetate solution was not successful.

Polybenzimidazole (PBI) is a high-temperature engineering polymer. The (PBI)<sub>x</sub>MoS<sub>2</sub> nanocomposite synthesized using PBI/(formic acid) solution has a basal spacing of 28.6 Å (see Figure 1.5B) and a polymer content of 0.65 BI units per MoS<sub>2</sub>. Poly(ethylene terephthalate), an important engineering polymer like nylon, was also encapsulated in MoS<sub>2</sub> using a 50 °C phenol solution. The nanocomposite has a basal spacing of 33 Å (see Figure 1.5B) and a polymer content of 0.28 ETP units per MoS<sub>2</sub>. Information on these nanocomposites is summarized in Table 1.3.

Table 1.3. Characteristics of some new MoS<sub>2</sub> nanocomposites

| nanocomposite                           | solvent for reaction                               | T <sub>reaction</sub> | d spacing (Å) | T <sub>Oh--&gt;2H</sub> (°C) |
|---|--|-----------------------|---------------|------------------------------|
| (PEO) <sub>1.5</sub> MoS <sub>2</sub>   | H <sub>2</sub> O                                   | R.T.                  | 17.0          | 159                          |
| (PVP) <sub>0.96</sub> MoS <sub>2</sub>  | H <sub>2</sub> O                                   | R.T.                  | 28.8          | 174                          |
| (PA6) <sub>0.44</sub> MoS <sub>2</sub>  | CF <sub>3</sub> CH <sub>2</sub> OH                 | R.T.                  | 15.1          | 153                          |
| (PA6) <sub>0.25</sub> MoS <sub>2</sub>  | HCOOH  | R.T.                  | 35.2          | 126                          |
| (PS) <sub>2.3</sub> MoS <sub>2</sub>    | CH <sub>3</sub> COOCH <sub>2</sub> CH <sub>3</sub> | R.T.                  | 38.4          | undetected                   |
| (PS) <sub>6.8</sub> MoS <sub>2</sub>    | CH <sub>3</sub> COOCH <sub>2</sub> CH <sub>3</sub> | 65 °C                 | delaminated   | undetected                   |
| (PAM) <sub>0.60</sub> MoS <sub>2</sub>  | H <sub>2</sub> O                                   | R.T.                  | 15.6          | 200                          |
| (PVA) <sub>3.5</sub> MoS <sub>2</sub>   | H <sub>2</sub> O                                   | R.T.                  | 16.9          | -                            |
| (PP) <sub>1.1</sub> MoS <sub>2</sub>    | decalin  | 40-90 °C              | 10.3          | 184                          |
| (PMMA) <sub>0.90</sub> MoS <sub>2</sub> | ethanol  | 50 °C                 | 44.4          | -                            |
| (PMMA) <sub>0.44</sub> MoS <sub>2</sub> | HCOOH  | R.T.                  | 60.1          | 117                          |
| (PBI) <sub>0.65</sub> MoS <sub>2</sub>  | HCOOH  | R.T.                  | 28.6          | -                            |
| (PETP) <sub>0.28</sub> MoS <sub>2</sub> | phenol   | 50 °C                 | 33.4          | -                            |

## 7. The Phase Transition in Restacked MoS<sub>2</sub> and MoS<sub>2</sub> Nanocomposites

The exfoliated MoS<sub>2</sub> and freshly restacked MoS<sub>2</sub> have a metastable structure in which Mo atoms have a distorted local octahedral coordination. This structure originates from the lithiation reaction, which converts the 2H form MoS<sub>2</sub> (trigonal-prismatic coordination) to the 1T form LiMoS<sub>2</sub> (octahedral coordination). The structural conversion takes place to keep a lower coordination energy in the product LiMoS<sub>2</sub> [10]. When LiMoS<sub>2</sub> is converted to exfoliated MoS<sub>2</sub> by reacting with water, Mo changes an oxidation state +3 to an oxidation state close to +4, in which the trigonal prismatic coordination rather than the octahedral coordination provides lower coordination energy. However, exfoliated MoS<sub>2</sub> or freshly restacked MoS<sub>2</sub> does not complete the structural conversion immediately due to a kinetic detainment. Mo adapts a distorted octahedral coordination [10] and slowly converts to the trigonal prismatic coordination over time. The conversion is exothermic and is accelerated at an elevated temperature or under pressure [1].

It is important to have knowledge of the rate of the structural conversion, because the two forms of MoS<sub>2</sub> have different physical properties and the structural conversion of MoS<sub>2</sub> brings about a slow property evolution in restacked MoS<sub>2</sub> and nanocomposites. For example, the octahedral MoS<sub>2</sub> is metallic while the trigonal prismatic MoS<sub>2</sub> is a semiconductor. The conversion of MoS<sub>2</sub> makes the conductivity of restacked MoS<sub>2</sub> drop gradually at room temperature from 12 S/cm to 0.07 S/cm in 4 months. Although the activation energy of the structural transition was measured by Bissessur [1], the room-temperature conversion of the materials was not tracked. Here, the progress of the room-



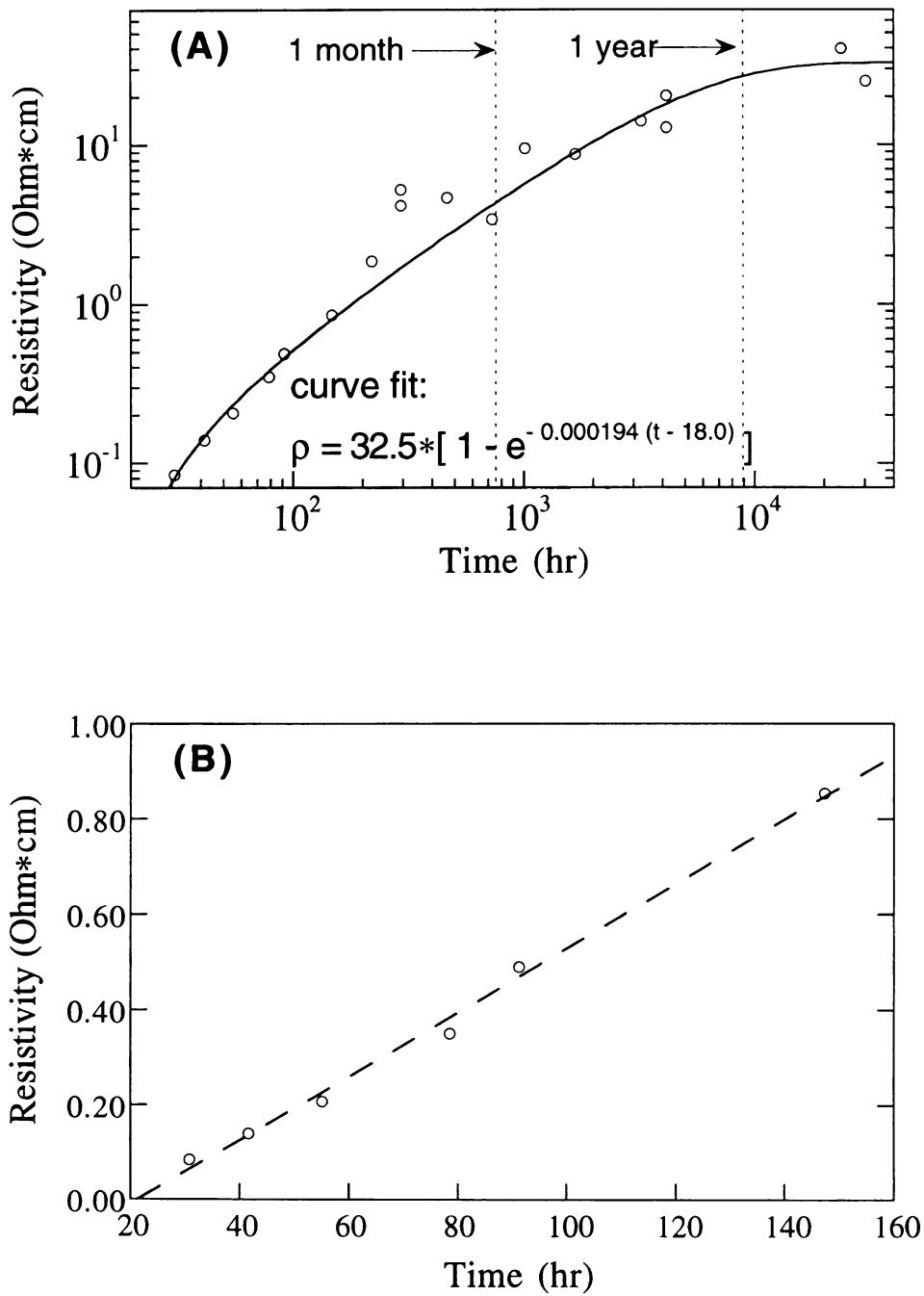


Figure 1.6. Evolution of the electrical resistivity of a restacked MoS<sub>2</sub> sample as a function of time. (The sample was dehydrated by methanol.)

temperature conversion was followed by a time dependent measurement of the materials' electrical conductivity.

Figure 1.6A shows the follow-up of the resistivity of a restacked MoS<sub>2</sub> sample over more than 3 years. In the 3 years, the resistivity increased almost 3 orders of magnitude, with the major change happening in the first four months. DSC experiments showed that the sample after the 3 years of measurement did not have any thermal transition from room temperature up to 300 °C, which indicates the completion of the structural conversion. The profile of resistivity can be roughly fitted with an exponential function as follows [24]:

$$\rho = 32.5 * [1 - e^{-0.000194(t-18.0)}] \quad \Omega \cdot \text{cm} \quad (1)$$

Possible relationships between the change of conductivity (or resistivity) and the conversion of the MoS<sub>2</sub> layers are discussed in Appendix A. Figure 1.6B shows that the resistivity increases linearly along with time in the early stages. Actually, the short-time-period resistivity-time relationship is almost linear in all the ranges. The linear relationship of resistivity and time can be expressed in a first order equation:

$$\rho = \rho_0 + b t \quad (2)$$

This relationship is also observed in other restacked MoS<sub>2</sub> and MoS<sub>2</sub> nanocomposite samples. The coefficient *b*, which reflects the rate of the structural conversion of MoS<sub>2</sub>, is listed in Table 1.4.

The coefficient *b* of a nanocomposite is smaller than the one of restacked MoS<sub>2</sub>, which indicates a slower conversion of MoS<sub>2</sub> in nanocomposites. This agrees well with the previous findings of the higher transition temperatures of nanocomposites detected by DSC. A new fact revealed by the comparison of coefficient *b* is that the additional oxidation in air accelerates the structural conversion of MoS<sub>2</sub>. This conclusion is

Table 1.4. Evolution rates of restacked MoS<sub>2</sub> and nanocomposites derived from the change of electrical resistivity

| samples                             | environment | $b$ ( $\Omega \cdot \text{cm} \cdot \text{day}^{-1}$ ) |
|-------------------------------------|-------------|--|
| restacked MoS <sub>2</sub>          | air         | 3.3, 5.0, 6.7 [25]                                     |
| (PEO) <sub>x</sub> MoS <sub>2</sub> | air         | 0.066, 0.40  |
| (PA6) <sub>x</sub> MoS <sub>2</sub> | air         | 1.0, 2.7, 3.4  |
| restacked MoS <sub>2</sub>          | nitrogen    | 1.0, 1.5   |

\* The different  $b$  values of the same nanocomposite were obtained from different samples.

drawn because the coefficients  $b$  of the restacked MoS<sub>2</sub> samples in air are larger than those in nitrogen.

## 8. Thermal Stability of MoS<sub>2</sub> Nanocomposites

Annealing at high temperatures, for example 160-170 °C, causes a slow decomposition in some of the nanocomposites. Deterioration has been seen in samples of (PEO)<sub>x</sub>MoS<sub>2</sub> and (PA6)<sub>x</sub>MoS<sub>2</sub> heated at 160-170 °C for 2.5 days. X-ray patterns of the nanocomposites after annealing show a significant weakening and broadening of the 001 peaks. The 001 peaks also shift to lower  $d$  spacings. After annealing at 160-170 °C for 2.5 days, the (PS)<sub>x</sub>MoS<sub>2</sub> sample that had a broad 001 peak around 38.4 Å lost its peak in the X-ray pattern and became amorphous. However, annealing at this temperature seems to have no effect on (PE)<sub>x</sub>MoS<sub>2</sub> and (PP)<sub>x</sub>MoS<sub>2</sub> nanocomposites. The higher stability of these two nanocomposites probably originates from the PE and PP's higher heat resistance and stronger tendency to align and pack in lattices or templates. In all the five nanocomposites, annealing does not bring up an intense restacked MoS<sub>2</sub> peak in the X-ray patterns. Table 1.5 summarizes the effects of annealing

Table 1.5. The effect of high temperature annealing to some nanocomposites

| sample                                 | $d_{\text{before}}$<br>(Å) | $d_{\text{after}}$<br>(Å) | comments on XRD pattern<br>after the annealing |
|--|----------------------------|---------------------------|--|
| (PEO) <sub>1.5</sub> MoS <sub>2</sub>  | 17.0                       | 16.4                      | 001 peak intensity decreased                   |
| (PA6) <sub>0.1</sub> MoS <sub>2</sub>  | 16.8                       | 15.2                      |  |
| (PA6) <sub>0.25</sub> MoS <sub>2</sub> | 35.2                       | -                         | 001 peak intensity decreased                   |
| (PS) <sub>2.3</sub> MoS <sub>2</sub>   | 38.4                       | amorphous<br>like         | a very low peak at 6.4 Å                       |
| (PE) <sub>4.5</sub> MoS <sub>2</sub>   | 10.2                       | 10.2                      | no change in the peak                          |
| (PP) <sub>1.1</sub> MoS <sub>2</sub>   | 10.3                       | 10.3                      | no change in the peak                          |

\* The samples were annealed at 160-170 °C for 60 hours.

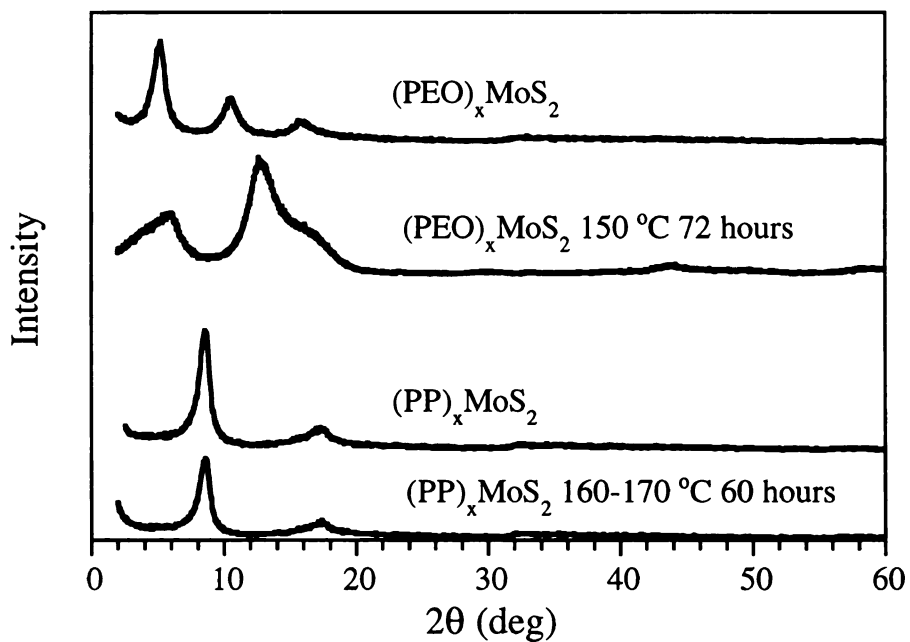


Figure 1.7. XRD patterns of the (PEO)<sub>x</sub>MoS<sub>2</sub> and (PP)<sub>x</sub>MoS<sub>2</sub> nanocomposites before and after the high temperature annealing.

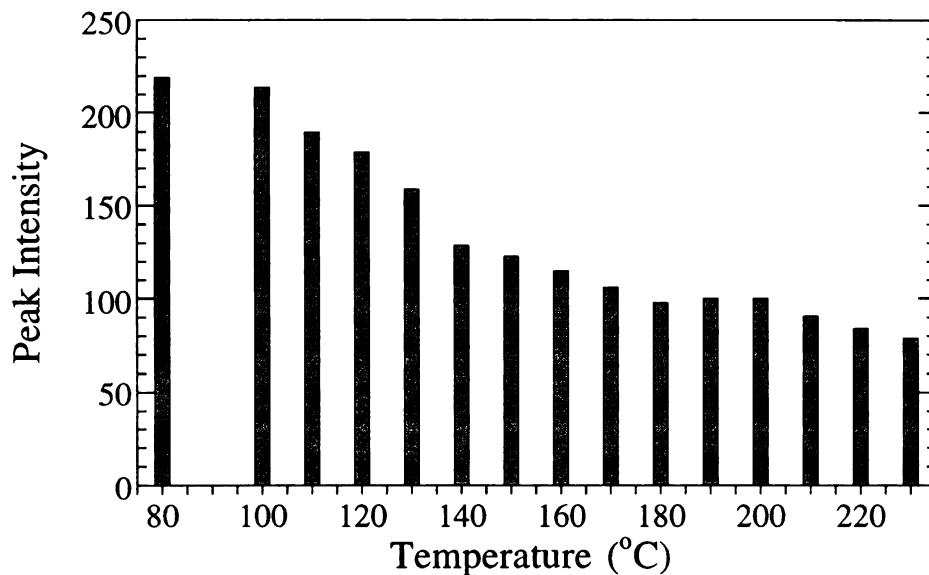


Figure 1.8. Intensity of the 001 peak in the XRD patterns of a  $(\text{PEO})_x\text{MoS}_2$  sample at increasing temperatures.

on the  $\text{MoS}_2$  nanocomposites. In Figure 1.7, the X-ray patterns of some annealed  $(\text{PEO})_x\text{MoS}_2$  and  $(\text{PP})_x\text{MoS}_2$  samples are compared with those of the original samples.

A variable temperature powder X-ray diffraction experiment was done on a  $(\text{PEO})_x\text{MoS}_2$  sample to investigate the effect of temperature on the rate of the deterioration. Figure 1.8 shows the result of the experiment with a plot which displays the variation of the intensity of the 001 peak at increasing temperatures. The plot shows that the deterioration was slow when the temperature was less than 100 °C. In the range of 100 to 140 °C, the deterioration speeded up. After 140 °C, the intensity change of the 001 peak slowed down, probably due the fact that the order of the lamellar structure had been so poor that additional deterioration did not bring up a more significant disorder. In this high temperature XRD experiment, the 6.2 Å peak, which belongs to restacked  $\text{MoS}_2$ , was not observed.

## Concluding Remarks

This chapter presents extensive results on the exfoliation and polymer intercalation of MoS<sub>2</sub>. A significant achievement was the development of the high temperature LiBH<sub>4</sub> lithiation method, which provides a convenient way to produce large quantities of exfoliated MoS<sub>2</sub> and which promises to be applicable to many other layered metal chalcogenides. Further investigation was devoted to the exfoliated MoS<sub>2</sub> and restacked MoS<sub>2</sub> in order to identify the material, explain the mechanism of the exfoliation and seek better design of intercalation reactions. We learned that the identity of the exfoliated MoS<sub>2</sub> and restacked MoS<sub>2</sub> is hydrated Li<sub>x</sub>MoS<sub>2</sub>, with x about 0.18. This material exfoliates in water under weak shearing forces, similar to hydrated Li<sub>x</sub>TiS<sub>2</sub> and Li<sub>x</sub>TaS<sub>2</sub>. Once the hydrated Li<sub>x</sub>MoS<sub>2</sub> is dehydrated, it cannot be re-hydrated or re-exfoliated, probably due to the additional oxidation involved in those de-intercalation experiments, and the conversion to 2H-MoS<sub>2</sub>.

Better synthesis methods were found for known nanocomposites. For example, (PEO)<sub>x</sub>MoS<sub>2</sub> and (PPV)<sub>x</sub>MoS<sub>2</sub> of higher polymer content were produced when sufficient polymer was provided in the encapsulation reaction. In addition, many new MoS<sub>2</sub> nanocomposites were synthesized and added to the list, which include (PS)<sub>x</sub>MoS<sub>2</sub>, (PAM)<sub>x</sub>MoS<sub>2</sub>, (PVA)<sub>x</sub>MoS<sub>2</sub>, (PP)<sub>x</sub>MoS<sub>2</sub>, (PMMA)<sub>x</sub>MoS<sub>2</sub>, (PBI)<sub>x</sub>MoS<sub>2</sub> and (PETP)<sub>x</sub>MoS<sub>2</sub>. One-dimensional electron density maps obtained for (PEO)<sub>x</sub>MoS<sub>2</sub> based on XRD powder patterns suggest a (PEO)<sub>x</sub>MoS<sub>2</sub> model in which the PEO chains take a conformation found in type II PEO-HgCl<sub>2</sub> complex, similar to

the cases of  $\text{Li}_{0.2}(\text{PEO})_x\text{TaS}_2$  and  $\text{Li}_{0.2}(\text{PEO})_x\text{RuCl}_3$  which will be presented in Chapters 3 and 5.

The evolution of the electrical conductivity of the restacked  $\text{MoS}_2$  was monitored. The curve of the increasing resistivity can be roughly fit with an exponential function of time. The electrical conductivity, which is inversely proportional to the resistivity, mainly changes in the first 4 months, by almost 3 orders of magnitude. The electrical conductivity studies also demonstrate that the intercalation of polymers slows down the process of the structural conversion of the  $\text{MoS}_2$  layers. In addition, they show that the conversion is slower in nitrogen than in air. Many  $\text{MoS}_2$ /polymer nanocomposites are not stable at temperatures higher than  $100\text{ }^\circ\text{C}$ . Heat treatment not only causes the structural conversion of the  $\text{MoS}_2$  layers, but also destroys the lamellar structure.

## Appendix A

The decrease of the conductivity of restacked MoS<sub>2</sub> is caused by the gradual conversion of the MoS<sub>2</sub> layers, from a metallic form to a semiconducting form. There must exist some relationship between the conductivity (or resistivity) and the amount of MoS<sub>2</sub> converted. On the other hand, the conversion of MoS<sub>2</sub> is a certain function of time. These two events together decide the evolution of the conductivity (or resistivity). This section provides a discussion about the possible mathematical functions in these two events by deducing the equations which express the conductivity as a time function and which fit the experimental data.

In conductor-insulator mixtures, the conductivity often follows a simple power law:

$$\sigma = c_2(\phi - \phi_p)^\alpha \quad (3)$$

where  $\sigma$  is the conductivity,  $c_2$  a constant,  $\phi$  the volume fraction of the conductor, and  $\phi_p$  the percolation threshold. Percolation theory [26] predicts that the  $\phi_p$  for a three-dimensional network of conducting globular aggregates in an insulating matrix should be  $\sim 0.16$ . In many conductor-insulator mixtures, however, this threshold is not seen or is extremely small [27].

Equation 4, which generally fits the conductivity profile (see Figure 1.9), is deduced supposing that the simple power law suits the mixture of the restacked MoS<sub>2</sub> and the conversion of MoS<sub>2</sub> precedes as a second order reaction.

$$\sigma = 28.3*[1 + k(t-18.0)]^{-\alpha} + 0.035*\{1 + [k(t-18.0)]^{-1}\}^{-\beta} \quad (4)$$

$$k=0.06155, \alpha=1.517, \beta=2.701$$

The coefficients in the equation are derived by curve fitting to the experimental data. The unit of time, the moment of  $t = 0$ , and the time adjustment of 18.0 hours, are the same as explained in discussion section 7 [24]. The deduction of equation 4 uses the equations of the second order reaction

$$[\phi_{1T}(t)]^{-1} - [\phi_{1T}(t=0)]^{-1} = kt, \quad (5)$$

$$\phi_{1T}(t=0) = 1, \quad (6)$$

and the equation of the simple power law

$$\sigma = C_{1T} * [\phi_{1T}(t)]^\alpha + C_{2H} * [\phi_{2H}(t)]^\beta. \quad (7)$$

If the assumption above is correct, the time for half of the 1T-MoS<sub>2</sub> to convert is  $k^{-1}$ , which is about 16 hours.

In nature, most self conversion reactions are first order reactions, for example, the decay of the radioactive isotopes. The combination of the first order reaction of the restacked form of MoS<sub>2</sub> and the simple power law of conductivity can not produce a function which fits the experimental conductivity data. As described in the discussion section, the profile of resistivity can be roughly fit with an exponential function, equation 1:

$$\rho = 32.5 * [1 - e^{-0.000194(t-18.0)}] \quad \Omega * \text{cm} \quad (1)$$

If the conversion of MoS<sub>2</sub> layers from the octahedral to the prismatic coordination proceeds as a first order reaction

$$\phi_{1T}(t) = e^{-kt}, \quad (8)$$

to derive an equation of the above type the resistivity need to be proportional to the amount of the converted MoS<sub>2</sub>

$$\rho = \rho_0 * [1 - \phi_{1T}(t)]. \quad (9)$$

Nevertheless, the assumption that the resistivity is proportional to the amount of converted MoS<sub>2</sub> does not have a solid experimental or theoretical basis, so this second curve fitting is less likely than the first one.

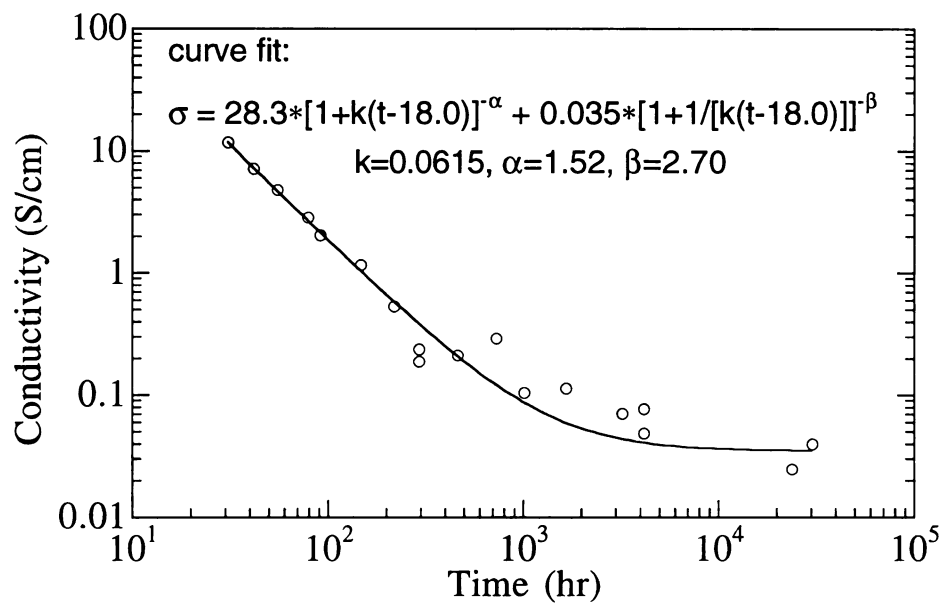


Figure 1.9. Curve fitting for the time dependence of electrical conductivity of  $(\text{PEO})_x\text{MoS}_2$ .

## References

- 1 (a) R. Bissessur, M. G. Kanatzidis, J. L. Schindler, C. R. Kannewurf, *J. Chem. Soc., Chem. Commun.* **1993**, 1582. (b) R. Bissessur, *Synthesis and Characterization of Novel Intercalation Compounds of Molybdenum Trioxide and Molybdenum Disulfide*, Ph. D. Dissertation, Department of Chemistry, Michigan State University, **1994**.
- 2 (a) M. G. Kanatzidis, L. M. Tonge, T. J. Marks, H. O. Marcy and C. R. Kannewurf, *J. Am. Chem. Soc.* **1987**, 109, 3797. (b) M. G. Kanatzidis, C.-G. Wu, H. O. Marcy and C. R. Kannewurf, *J. Am. Chem. Soc.* **1989**, 111, 4139. (c) G. Matsubayashi and H. Nakajima, *Chem. Lett.* **1993**, 31.
- 3 (a) Y. Kojima, A. Usuki, M. Kawasumi, A. Okada, T. Kurauchi and O. Kamigaito, *J. Polym. Sci. A: Polym Chem.*, **1993**, 31, 983. (b) H. Shi, T. Lan and T. J. Pinnavaia, *Chem. Mater.* **1996**, 8, 1584. (c) E. P. Giannelis, *Adv. Mater.*, **1996**, 8, 29.
- 4 Y. -J. Liu, D. C. DeGroot, J. L. Schindler, C. R. Kannewurf and M. G. Kanatzidis, *Adv. Mater.* **1993**, 5, 369.
- 5 (a) P. Joensen, R. F. Frindt and S. R. Morrison *Mater. Res. Bull.* **1986**, 21, 457. (b) M. A. Gee, R. F. Frindt, P. Joensen and S. R. Morrison *Mat. Res. Bull.*, **1986**, 21, 543. (c) W. M. R. Divigalpitiya, R. F. Frindt and S. R. Morrison, *Science* **1989**, 246, 369.
- 6 L. Wang, J. Schindler, C. R. Kannewurf and M. G. Kanatzidis *J. Mater. Chem.* **1997**, 7, 1277.
- 7 (a) Chapter 3. (b) L. Wang, J. Schindler, C. R. Kannewurf and M. G. Kanatzidis, paper in preparation.
- 8 H.-L. Tsai, L. Wang, J. Schindler, C. R. Kannewurf and M. G. Kanatzidis, paper in preparation.
- 9 H.-L. Tsai, J. L. Schindler, C. R. Kannewurf and M. G. Kanatzidis, *Chem. Mater.* **1997**, 9, 875.
- 10 (a) F. Wypych and R. Schöllhorn, *J. Chem. Soc., Chem. Commun.*

- 1992, 1386. (b) D. Yang, S. J. Sandoval, W. M. R. Divigalpitiya, J. C. Irwin and R. F. Frindt, *Phys. Rev. B.* **1991**, 43, 12053. (c) M. A. Py and R. R Haering, *Can. J. Phys.* **1983**, 61, 76.
- 11 (a) J. Heising and M. G. Kanatzidis, *J. Am. Chem. Soc.* **1999**, 121, 638. (b) J. Heising, *Synthesis and Characterization of Novel Intercalation Compounds of Molybdenum Trioxide and Molybdenum Disulfide*, Ph. D. Dissertation, Department of Chemistry, Michigan State University, **1999**.
- 12 O. Weisser and S. Landa, *Sulfided Catalysts, Their Properties and Applications*, Pergamon, New York, 1973.
- 13 (a) H. Tributsch, *Faraday Discuss. Chem. Soc.* **1980**, 70, 190. (b) C. Julien, S. I. Saikh and G. A. Nazri, *Mater. Sci. Eng.* **1992**, B15, 73.
- 14 (a) M. B. Dines, *Mat. Res. Bull.* **1975**, 10, 287. (b) D. W. Murphy, F. J. Di Salvo, G. W. Hull, Jr., and J. V. Waszczak, *Inorg. Chem.* **1976**, 15, 17.
- 15 We thank Dr. W. Emmett Brazelton and Kirk J. Stuart for the measurements.
- 16 F. A. Cotton and G. Wilkinson, *Advanced Inorganic Chemistry, 5th Ed.*, John Wiley & Sons, New York, **1988**, pp 190-191.
- 17  $\text{LiMoS}_2$  itself also generates  $\text{LiOH}$  when it reacts with water. The presence of the  $\text{LiOH}$  will usually not significantly affect the polymer intercalation reaction.
- 18 M. G. Kanatzidis and T. J. Marks, *Inorg. Chem.* **1987**, 26, 783.
- 19 (a) W. Rüdorff, *Chimia*, **1965**, 19, 489. (b) J. Rouxel, M. Danot and J. Bichon, *Bull. Soc. Chim. Fr.* **1971**, 3930.
- 20 R. Schöllhorn and A. Lerf, *J. Less-Common Met.* **1975**, 42, 89.
- 21 W. P. Omloo and F. Jellinek, *J. Less-Common Met.* **1970**, 20, 121.
- 22 A restacked  $\text{MoS}_2$  freshly collected from an aqueous monolayer suspension was a hydrated phase with a basal spacing of 12.1 Å. Two days of pumping the sample, at room temperature, only dehydrated about 50% of the material giving a basal spacing of 6.2 Å.

Washing the freshly restacked MoS<sub>2</sub> with anhydrous methanol altered the basal spacing of MoS<sub>2</sub> from 12.1 Å to 9.4 Å. The de-intercalation of methanol could have been accomplished by one to two days of dynamic pumping, to produce a phase with a 6.2-6.3 Å basal spacing. This dehydrated MoS<sub>2</sub> could not be re-exfoliated.

- 23 For the calculation of the X-ray scattering coherence length of the nanocomposites in the restacking direction, see Reference 18 of Chapter 2.
- 24 The unit of time in the equation is hour. The time at which the LiMoS<sub>2</sub> was exposed to water is chosen as  $t = 0$ . Since the structural conversion of MoS<sub>2</sub> probably started at some time after the first exposure to water, a time adjustment is imposed in the equation. The time adjustment of 18.0 hours is decided by the best fitting of the equation to the experimental data. This time adjustment also compensates the fact that the MoS<sub>2</sub> converted at a slower speed when it was stirred in a closed reaction flask or dried in a vacuum chamber than when it was stored and measured in air.
- 25 The  $b$  value calculated from Figure 5B is  $0.16 \Omega \cdot \text{cm} \cdot \text{day}^{-1}$ . Since the measurements for Figure 5 were done with pressed pellets and a four-probe detector connected to a Keithley-236 source measure unit rather than the Keithley-580 micro-Ohmmeter, the values should not be compared to those in this table.
- 26 R. Zallen, *The Physics of Amorphous Solids*, Wiley, New York, **1983**, Chapter 4.
- 27 A. J. Heeger and P. Smith, in J. L. Brédas and R. Silbey ed., *Conjugated Polymers*, Kluwer Academic Pub., Dordrecht/Boston/London, **1991**, pp 141.

## Chapter 2

### INSERTION OF POLYPYRROLE AND POLY(N-METHYL PYRROLE) IN MoS<sub>2</sub> AND WS<sub>2</sub> BY AN *IN SITU* POLYMERIZATION- ENCAPSULATIVE PRECIPITATION METHOD

#### Introduction

Great effort has been dedicated to the development of transition-metal-compound/conductive-polymer nanocomposites [1] under the expectation that novel electrochemical properties will be obtained by the molecular level interaction of the two electrochemically active components. These expectations now begin to materialize based on recent research which reveals that certain polymer nanocomposites indeed possess better electrical or electrochemical properties, especially in ion conductivity [2] and ion mobility [3]. Early transition metal dichalcogenides make a large class of layered materials which possesses interesting electronic, photoconductive and other physical properties [4]. It is an important class of host materials and has been subject to intensive studies [5]. Many papers have been published on the intercalation of metal atoms and small organic compounds in these dichalcogenides in the past 25 years [5, 6]. In addition, there have been a few reports about polymer intercalation in these compounds [7], including the recent reports from our group [1d, 1e]. However, reports about conductive polymer intercalated nanocomposites of these compounds are still scarce. Further work to synthesize and characterize more nanocomposites with conductive polymers and this group of layered chalcogenides would be useful.

Polypyrrole (PPY) is an important conductive polymer which has attracted considerable attention due to its high electrical conductivity. It has

been investigated as an electrode material for solid-state batteries [8a] and capacitors [8b], as an anode material for polymer light-emitting diodes [8c], an electromagnetic interference shielding material [8d] and sensor material [8e]. Therefore, PPY intercalative nanocomposites could be promising materials for applications.

PPY is an intractable polymer, however, which does not dissolve in any solvent. The exfoliation-encapsulative precipitation (EEP) method, which was described in Chapter 1, cannot be applied to PPY. By 1994, when we started the exploration of encapsulating PPY in MoS<sub>2</sub>, the material had already been intercalated in a number of layered inorganic compounds such as FeOCl [1a] V<sub>2</sub>O<sub>5</sub> [1b] and VOPO<sub>4</sub> [1f]. The intercalation was achieved by the method of *in situ* redox intercalative polymerization, which requires oxidative hosts and is suitable for only a few layered inorganic compounds. Some non-oxidative hosts can be rendered oxidative (suitable to the conductive polymer intercalation) by incorporating in them oxidizing ions such as Cu<sup>2+</sup> [9]. However, this may not be a good method for restacked MoS<sub>2</sub> and WS<sub>2</sub>, because these materials themselves could reduce Cu<sup>2+</sup>. Therefore, we tried a new methodology to intercalate PPY in this type of hosts.

Besides mixing with polymers in solution, exfoliated layered compounds can be mixed with monomers or monomer solutions. When polymerization is initiated in such mixtures, nanocomposites are frequently formed. The important clay/polyamide nanocomposites were synthesized with this strategy [10]. This approach also leads to the new polymer-intercalation method described here, namely the *in situ* oxidative polymerization-encapsulative precipitation. This new procedure has given several new PPY nanocomposites such as MoS<sub>2</sub>/PPY, WS<sub>2</sub>/PPY and

RuCl<sub>3</sub>/PPY nanocomposites. The former two nanocomposites will be presented in this chapter. The last one will be reported in Chapter 5.

Since this procedure of PPY-nanocomposite preparation involves the reaction between pyrrole, FeCl<sub>3</sub> and exfoliated host materials, and unavoidably includes some side reactions such as the restacking of the host materials and the formation of the bulk polymer, the formation of nanocomposite products and their morphologies depends not only on the thermodynamics but also on the kinetics of these reactions. Therefore, reaction parameters such as the ratio of the reactants, the order of addition of reactants, reactant concentrations and temperature are all important. It will be seen in the following sections that the change of the pyrrole/FeCl<sub>3</sub> ratio alone causes changes in the structure of MoS<sub>2</sub>/PPY nanocomposites, and affects the formation of WS<sub>2</sub>/PPY nanocomposites.

## **Experimental Section**

### **1. Reagents**

Pyrrole (98%), N-methyl pyrrole (99%), anhydrous FeCl<sub>3</sub> (purified grade) and WS<sub>2</sub> (99.8%) were purchased from Mallinckrodt Chemical Inc., Aldrich Chemical Co., Fisher Scientific and Alfa Aesar respectively. Acetone was industry grade purchased from Quantum Chemical Company. Other chemicals were the same as in Chapter 1. Deionized water was used.

### **2. Preparation of MoS<sub>2</sub>/PPY Nanocomposites**

#### **a. Procedure 1: preparation with a controlled amount of pyrrole**

The MoS<sub>2</sub>/PPY nanocomposite was prepared by oxidizing pyrrole in an aqueous monolayer MoS<sub>2</sub> suspension with FeCl<sub>3</sub>. In this particular procedure described here, pyrrole and exfoliated MoS<sub>2</sub> were chosen as the

limiting reactants in the reaction. In a typical reaction, an amount of 0.20 g  $\text{LiMoS}_2$  (1.20 mmol) was exfoliated in 20 ml of  $\text{H}_2\text{O}$ . To this solution 0.016 g of pyrrole (0.24 mmol) dissolved in 5 ml of  $\text{H}_2\text{O}$  was added. The mixture was stirred in an ice bath for 15 min and to it an aqueous solution of 0.156 g  $\text{FeCl}_3$  (0.96 mmol) was added dropwise. The reaction mixture was stirred in an ice bath for ~24 h. The product was collected by centrifugation as a black solid. It was washed with acetone and dried in vacuum. Elemental analysis, which was done by Oneida Research Services, Inc., Whitesboro, New York, showed a composition C 6.59%, H 0.59%, N 1.31% and Cl 0.00%. The corresponding formula is  $(\text{C}_4\text{H}_3\text{N})_{0.25}(\text{H}_2\text{O})_{0.16}\text{MoS}_2$ . (Calculated: C 6.70%, H 0.60%, N 1.95%.) [11] Thermal gravimetric analysis (TGA) experiments in oxygen indicated a loss around 20.0 wt% at 650 °C, while the above formula suggests a loss of 19.6 wt% supposing that the residue is  $\text{MoO}_3$  [12]. Energy dispersive X-ray microanalysis (EDS) indicated that there was some Fe compound existing in the product. The ratio of Fe to Mo was about 0.19:1. After having been washed with 1 M HCl, the ratio changed to 0.02:1. No chlorine was found by EDS.

The ratio of pyrrole to  $\text{MoS}_2$  in the reaction above was 0.2:1.0. In other reactions, the pyrrole to  $\text{MoS}_2$  ratio varied from 0.1 to 0.6 (0.1, 0.2, 0.25, 0.3, 0.4 and 0.6, etc.), while the ratio of  $\text{FeCl}_3$  to pyrrole was always held at 4:1. A pyrrole/ $\text{MoS}_2$  ratio of ~0.2-0.3 provided well ordered product.

Similarly, corresponding  $\text{MoS}_2$ /poly(N-methyl pyrrole) ( $\text{MoS}_2$ /PMPY) nanocomposites were also prepared. Elemental analysis showed: C 7.63%, H 0.77%, N 1.38%; C 7.65%, H 0.77%, N 1.38% [13]. This corresponds to a formula  $(\text{C}_5\text{H}_5\text{N})_{0.23}(\text{H}_2\text{O})_{0.12}\text{MoS}_2$ . (Calculated: C 7.65%, H 0.77%, N 1.78%.) A nanocomposite with this formula should

lose 20.1% of the weight assuming the residue is MoO<sub>3</sub>, which agrees with the TGA experiments of 21.6 wt% loss at 650 °C in air.

b. Procedure 2: preparation with an excess amount of pyrrole

In this procedure, FeCl<sub>3</sub> was kept to be equal to or less than 0.5 equivalent to MoS<sub>2</sub>. In a typical reaction, an amount of 0.20 g LiMoS<sub>2</sub> (1.20 mmol) was exfoliated in 20 ml of H<sub>2</sub>O. To this solution 0.32 g of pyrrole (4.8 mmol) dissolved in 40 ml of H<sub>2</sub>O was added. The mixture was stirred in an ice bath for 15 min and to it an aqueous solution of 0.098 g FeCl<sub>3</sub> (0.60 mmol) was added dropwise. The reaction mixture was stirred in an ice bath for ~24 h. The product was collected by centrifugation as a black solid, washed with water, dried in air for 1 day, and then dried in vacuum. Elemental analysis of a sample showed: C 12.64%, H 0.99%, N 3.19%; C 12.40%, H 0.94%, N 3.15%. The corresponding formula is (C<sub>4</sub>H<sub>3</sub>N)<sub>0.51</sub>(H<sub>2</sub>O)<sub>0.18</sub>MoS<sub>2</sub>. (Calculated: C 12.46%, H 0.96%, N 3.64%.) A nanocomposite with the above formula should lose 26.7% of its weight and convert to MoO<sub>3</sub>. This agrees well with the TGA experiments which detected a loss around 26.4 wt% at 650 °C in air.

MoS<sub>2</sub>/PMPY nanocomposites were also prepared this way. Elemental analysis showed a composition: C 14.30%, H 1.37%, N 3.01%; C 14.22%, H 1.26%, N 2.95%. The corresponding formula is (C<sub>5</sub>H<sub>5</sub>N)<sub>0.475</sub>(H<sub>2</sub>O)<sub>0.13</sub>MoS<sub>2</sub>. (Calculated: C 14.26%, H 1.32%, N 3.33%.) A nanocomposite with the above formula should lose 28.0 wt% on the basis that the residue is MoO<sub>3</sub>. This agrees with the TGA experiments, which showed a loss of 27.5 wt% at 650 °C in air.

### 3. Preparation of WS<sub>2</sub>/PPY Nanocomposites

LiWS<sub>2</sub> was prepared by reacting WS<sub>2</sub> with 3.0 equiv. of LiBH<sub>4</sub> at 350 °C for 3 days, similar to LiMoS<sub>2</sub> in Chapter 1.

The PPY was encapsulated in WS<sub>2</sub> with a procedure similar to the Procedure 2 used to prepare MoS<sub>2</sub>/PPY. In a typical reaction, 0.40 g mixture of LiWS<sub>2</sub>/LiBH<sub>4</sub>/LiH (~1:2:1) (about 1.34 mmol) was stirred in 20 ml of H<sub>2</sub>O for 2 h. Hydrated WS<sub>2</sub> was collected by centrifugation, washed with 20 ml of fresh water, and suspended in 20 ml water by 30 min stirring. The resulting suspension was mixed with 10 ml water solution which contained 0.225 g pyrrole (3.35 mmol) and stirred in an ice bath. To this mixture, 10 ml of cold (~ 0–1 °C) aqueous solution of 0.109 g FeCl<sub>3</sub> (0.67 mmol) was added dropwise. The mixture was stirred for 24 h. The product was collected by centrifugation as a black solid, washed with water, dried in air for 1 day, and then dried under vacuum.

Elemental analysis gave: C 4.71%, H 0.88%, N 1.17%; C 4.67%, H 0.87%, N 1.16%, corresponding to (C<sub>4</sub>H<sub>3</sub>N)<sub>0.27</sub>(H<sub>2</sub>O)<sub>0.82</sub>WS<sub>2</sub> [14]. (Calculated: C 4.62%; H 0.87%; N 1.35%.) The elemental analysis of restacked WS<sub>2</sub> which was washed by hydrochloric acid and had a d spacing of 6.3 Å showed a result: C 0.30%, H 0.23%, N 0.07%; C 0.28%, H 0.21%, N 0.07. If the contents of C, H and N from the control experiment is deducted from the results of the elemental analysis of (PPY)<sub>x</sub>WS<sub>2</sub>, the suggested formula becomes (C<sub>4</sub>H<sub>3</sub>N)<sub>0.25</sub>(H<sub>2</sub>O)<sub>0.53</sub>WS<sub>2</sub>. The formula above should lose 15.3 wt% if the nanocomposite is converted to WO<sub>3</sub>, which does not match the TGA experiments [15] well. An EDS measurement detected only a trace of Fe existing in the product. The ratio of Fe to Mo was about 0.07:1.

#### 4. Instrumentation

The instrumentation in the measurements such as powder X-ray diffraction (XRD), thermal gravimetric analysis (TGA), differential scanning calorimetry (DSC), infrared (IR) spectroscopy and inductively coupled plasma (ICP) spectroscopy were the same as described in Chapter 1.

Room temperature conductivity measurements were done on pressed sample pellets with a four-probe detector connected to a Keithley-236 source measure unit. Variable temperature direct-current electrical conductivity measurements and thermopower measurements were made on pressed pellets, by Dr. Kannewurf's group at Northwestern University, with 60 and 25  $\mu\text{m}$  gold wires used for the current and voltage electrodes respectively. Measurements of the pellet cross-sectional area and voltage probe separation were made with a calibrated binocular microscope. Electrical conductivity data were obtained with a computer-automated system described elsewhere <sup>[16]</sup>. Magnetic susceptibility measurements were done with a Quantum Design MPMS2 SQUID magnetometer at the Department of Physics and Astronomy at MSU. Samples were sealed in low density polyethylene (LDPE) bags under a nitrogen atmosphere. The magnetic moments of the bags were acquired and deducted from the measurements. To obtain the paramagnetic susceptibility, the diamagnetic susceptibility and  $\chi_{\text{TIP}}$  were subtracted from the total susceptibility. The former was derived by adding up the diamagnetic susceptibility of each component, which was obtained from the literature <sup>[17]</sup>. The latter was determined by adjusting its value by a try-and-error process so that the paramagnetism optimally fit Curie-Weiss law.

## Results and Discussion

### 1. MoS<sub>2</sub>/PPY Nanocomposites

The synthesis of MoS<sub>2</sub>/PPY nanocomposites with a controlled amount of pyrrole and an excess amount of FeCl<sub>3</sub> (Procedure 1) produces a single phase nanocomposite product with a basal spacing around 10.5 Å, based on X-ray diffraction, see Figure 2.1(b). The interlayer expansion of ~4.3 Å indicates the successful inclusion in the interlayer gallery of a guest species, which is obviously PPY, as supported by infrared spectra. The IR spectrum of the nanocomposite displayed in Figure 2.2 is of a sample from a reaction with relatively high pyrrole ratio, ~0.4. The nanocomposites produced from reactions using  $\leq 0.25$  equivalent of pyrrole have IR spectra showing almost no peaks of organic species, due to the strong reflectivity of the samples originated from the conductive MoS<sub>2</sub> layers. Heat treatment of the samples causes the structural transition of MoS<sub>2</sub> from the octahedral to the trigonal prismatic coordination (2H-MoS<sub>2</sub>), which alters the MoS<sub>2</sub> from a metallic to a semiconducting state. This reduces the infrared reflectivity of the MoS<sub>2</sub> layers, so that the absorbance of the intercalated species becomes visible. Figure 2.3 shows the IR spectrum of a heating treated (PPY)<sub>0.25</sub>(H<sub>2</sub>O)<sub>0.16</sub>MoS<sub>2</sub> sample, which had been produced with 0.2 equivalent pyrrole and was heated up to 300 °C. In both spectra in Figures 2.2 and 2.3, the observed peaks are related to PPY.

To explore the possible nanocomposite phases and the optimum conditions to produce nanocomposites, the ratio of pyrrole to exfoliated MoS<sub>2</sub> in the reaction was altered from 0.1 to 0.6. As summarized in Table 2.1, the products have d spacings varying from 10.2 to 12.3 Å. It seems that higher pyrrole ratios result in slightly higher expansions. Since the corresponding interlayer gallery expansion is between 4.0 and 6.1 Å,

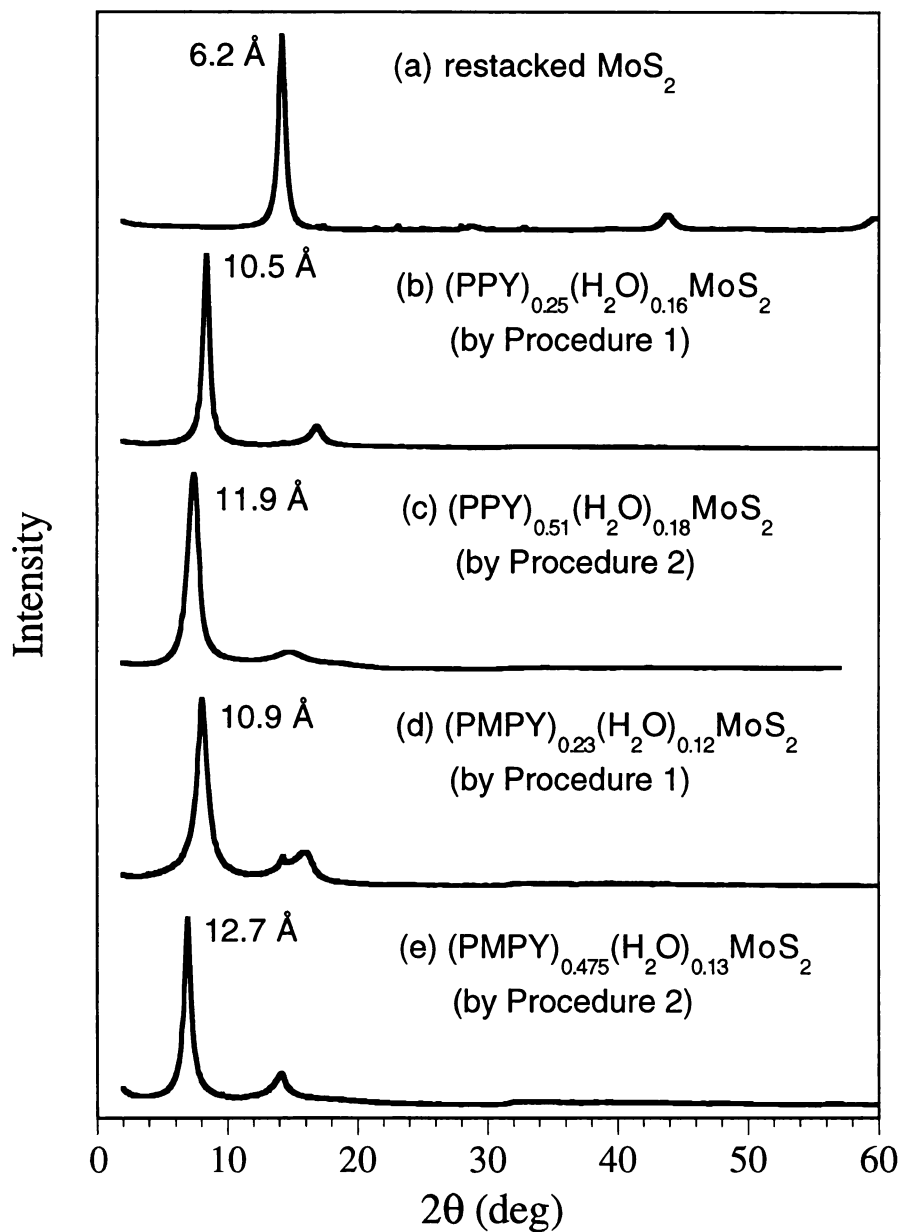


Figure 2.1. XRD patterns of  $\text{MoS}_2$  nanocomposites.

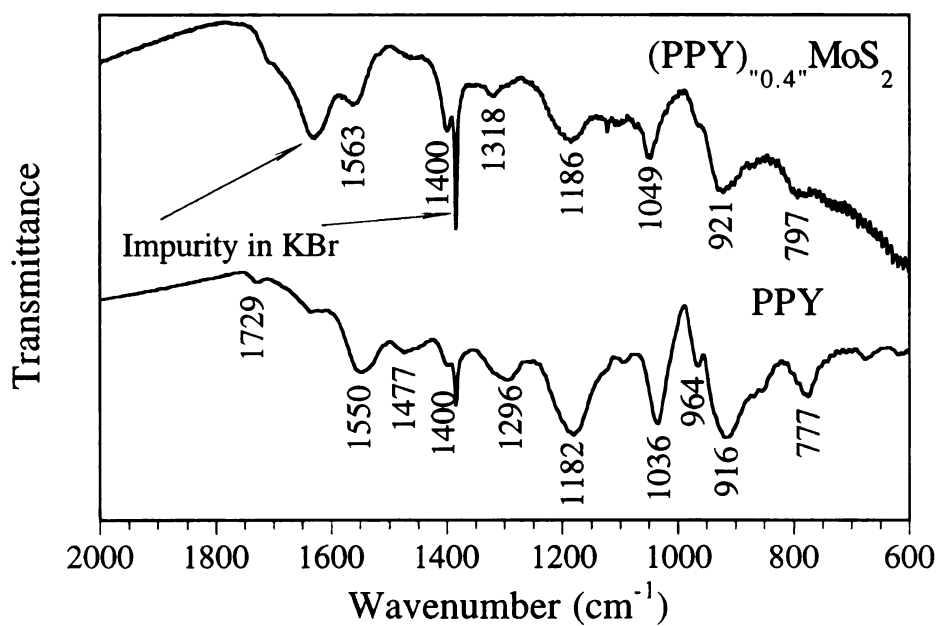


Figure 2.2. IR spectra of PPY and a  $MoS_2/PPY$  nanocomposite prepared by procedure 1.

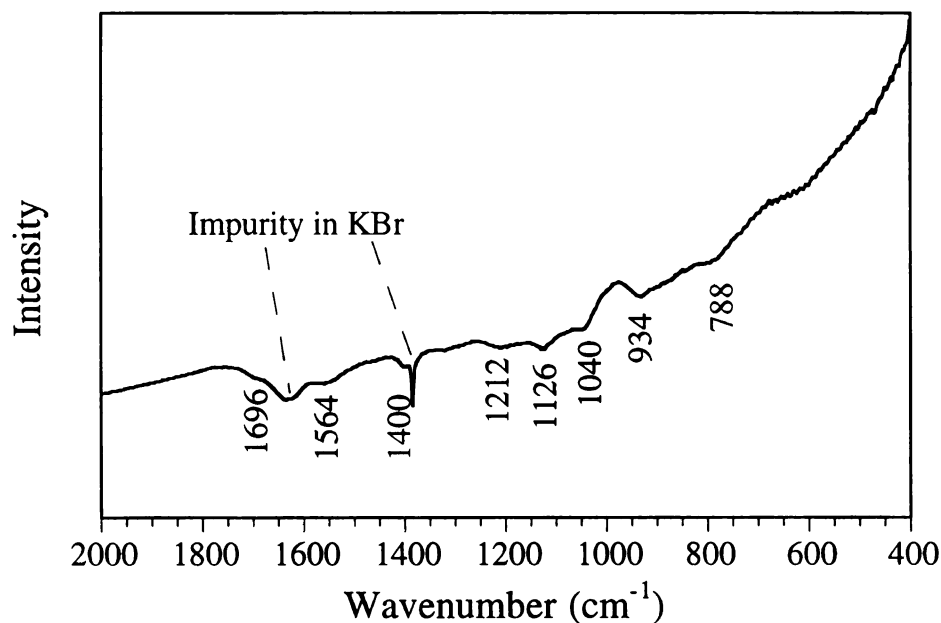


Figure 2.3. IR spectrum of a  $MoS_2/PPY$  nanocomposite prepared by procedure 1 and heating treated twice up to 300  $^{\circ}C$  under  $N_2$  atmosphere at a heating rate of 5  $^{\circ}C/min$ .

Table 2.1. Parameters of (PPY)<sub>x</sub>MoS<sub>2</sub> prepared with different pyrrole ratios

| pyrrole/MoS <sub>2</sub><br>ratio | d spacing of<br>nanocomposites (Å) | coherence length *[18]<br>(Å) |
|-----------------------------------|------------------------------------|-------------------------------|
| 0.1                               | 10.2                               | 40                            |
| 0.2                               | 10.9, 10.6, 10.5                   | 102, 102, 124                 |
| 0.25                              | 10.7, 10.5                         | 149, 131                      |
| 0.3                               | 11.2                               | 89                            |
| 0.4                               | 12.3                               | 52                            |
| 0.6                               | 11.8, 11.5                         | 40, 47                        |

\* The X-ray scattering coherence length in a *hkl* direction is calculated from the peak broadening of the *hkl* reflection and is an index of the structural order in that direction.

the space can only accommodate one molecular layer of PPY. It is likely that the pyrrole rings of the polymer lie almost parallel to the inorganic layers when the gallery height is low, while they rise more vertically when the gallery height is high. According to the molecular dimensions of the polymer, which will be discussed in detail in Appendix B, the 4.0 Å height is appropriate for the flat orientation of the pyrrole rings. When the gallery is higher and the pyrrole rings tilt up, more polymer chains can be packed in the gallery.

Since all pyrrole forms PPY upon oxidation with FeCl<sub>3</sub>, the ratio of pyrrole to MoS<sub>2</sub> in the reaction needs to be controlled. When this ratio is high, excess polymer forms, which cannot be accommodated as a single molecular layer in the gallery. As a result, it forms bulk polymer, which makes the product a mixture of phases. On the other hand, deficiency of pyrrole makes the gallery partially filled, which is also not an ideal situation because it gives rise to restacked MoS<sub>2</sub>. Furthermore, too much or

too little PPY hurts the lamellar structure of the nanocomposites. The structural order (*i.e.* stacking order) in the nanocomposites is indicated by the coherence length <sup>[18]</sup> of the materials along the stacking direction. The coherence lengths of the products clearly show that the stacking of the layers is poor when the ratio of pyrrole is lower than 0.2 or higher than 0.3. When the ratio is 0.25, the reaction produces nanocomposites of the highest coherence length (*i.e.* sharpest diffraction peaks).

The PPY nanocomposites can also be prepared using excess pyrrole and limited FeCl<sub>3</sub> (Procedure 2). Contrary to when excess FeCl<sub>3</sub> is used, adjusting the amount of pyrrole does not affect the coherence length of the nanocomposites significantly when the FeCl<sub>3</sub> is limited or deficient. The resulting nanocomposites always have fairly high coherence length along the restacking direction. The basal spacing and the amount of polymer in the nanocomposites remains unchanged, *i.e.* ~11.9 Å and ~0.5 repeat-unit per MoS<sub>2</sub> respectively. Figure 2.1(c) shows the powder X-ray pattern of a nanocomposite (PPY)<sub>0.51</sub>(H<sub>2</sub>O)<sub>0.18</sub>MoS<sub>2</sub>, prepared with these conditions.

The claim that the nanocomposites from Procedure 2 contain PPY rather than pyrrole is supported by the IR spectra, see Figure 2.4. In addition, it is supported by the fact that the nanocomposites cannot be de-intercalated. Pumping at 60 °C did not cause a shrinkage in the gallery spacing. In Procedure 2, the amount of PPY present in the product is more than what the FeCl<sub>3</sub> alone could have produced. The greater amount of PPY is explained by the fact that ambient oxygen takes part in the reaction as an electron acceptor. It has been proven that the ambient oxygen can oxidize and polymerize pyrrole in the presence of FeCl<sub>3</sub> <sup>[19]</sup>. The whole process can be described as follows: the addition of FeCl<sub>3</sub> causes or initiates polymerization of pyrrole producing radical cationic oligomers which

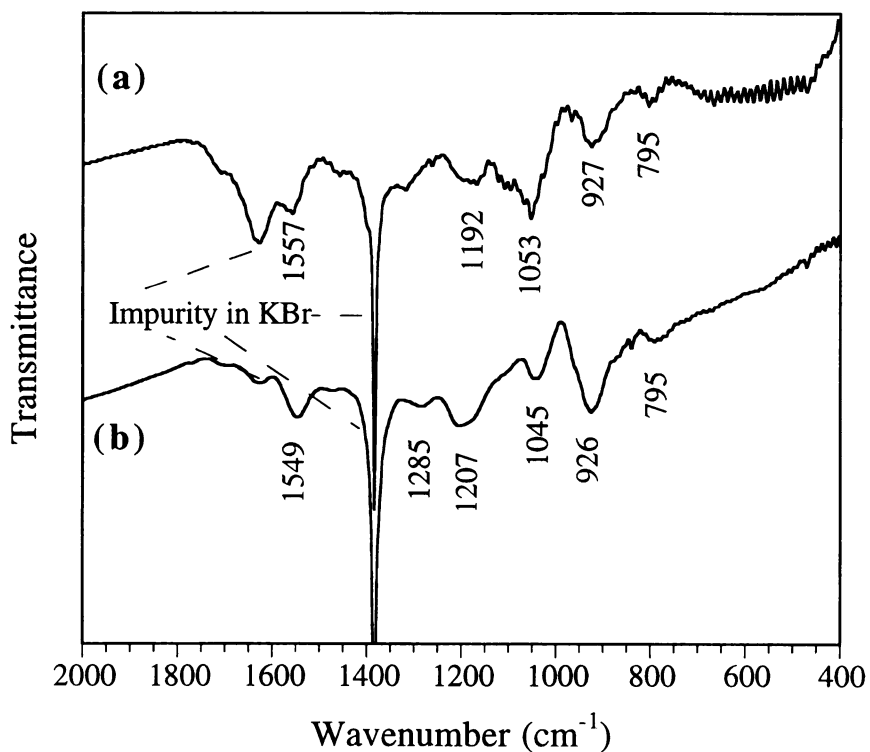


Figure 2.4. IR spectra of a nanocomposite  $(\text{PPY})_{0.51}(\text{H}_2\text{O})_{0.18}\text{MoS}_2$  prepared by procedure 2. (a) vacuum dried at room temperature only, and (b) heat treated twice up to 300 °C under  $\text{N}_2$  atmosphere at a heating rate of 5 °C/min.

themselves are more reducing than the pyrrole monomer.

The IR spectra of the  $(\text{PPY})_x\text{MoS}_2$  from both procedures show polymer stretching vibrations occurring at energies higher than those found in bulk PPY, prepared under similar experimental conditions (minus the  $\text{MoS}_2$  layers). The average blue-shift for most peaks is  $\sim 10 \text{ cm}^{-1}$  and it reflects the lower molecular weight (MW) of the intercalated polymer. Similar observations were made in previous work where the MW of *in situ* intercalated polymers is always found to be considerably smaller than that of the corresponding bulk materials [1a, 1b, 20]. This is a consequence of polymer growth under kinetically restricted conditions.

As it has already been mentioned, the interaction among pyrrole,  $\text{FeCl}_3$  and exfoliated host materials could potentially give rise to a number of undesirable side reactions such as the restacking of the host materials and the formation of bulk polymer. The formation of the single phase nanocomposites is therefore remarkable. Explanations for this include the possible formation of a  $\text{MoS}_2$ -pyrrole complex in solution before the addition of  $\text{FeCl}_3$ , or more likely the strong electrostatic attraction between the negatively charged  $[\text{MoS}_2]^{x-}$  layers to the positively charged polymer chains.

Since the polymer is produced in the doped form, an important issue to be addressed here is: what is the dopant anion in PPY? This has not been simple to resolve. There are several possible candidates for counter ions in  $(\text{PPY})_x\text{MoS}_2$ , which include  $[\text{FeCl}_4]^-$ ,  $\text{Cl}^-$ ,  $[\text{MoS}_2]^{x-}$  and  $[\text{OH}]^-$ . Elemental analysis found no chlorine in the nanocomposite sample, which excluded the possibility of  $[\text{FeCl}_4]^-$ , and  $\text{Cl}^-$ . It is possible that negatively charged  $[\text{MoS}_2]^{x-}$  acts as the dopant, as is the case with  $\text{FeOCl}$  and  $\text{V}_2\text{O}_5$ . Indirect

experiment data to be presented below are consistent with  $[\text{MoS}_2]^{x-}$  being the most likely counterion.

## 2. $\text{WS}_2/\text{PPY}$ Nanocomposites

The  $\text{WS}_2/\text{PPY}$  nanocomposites were prepared using excess pyrrole and limited  $\text{FeCl}_3$ . The successful production of a PPY nanocomposite is indicated by the strong reflections in the XRD pattern, which has seven  $00l$  reflections in the  $2\theta$  range from  $2^\circ$  to  $60^\circ$ , see Figure 2.5. The basal spacing of the  $(\text{PPY})_{0.25}(\text{H}_2\text{O})_{0.53}\text{WS}_2$ , 11.0 Å, corresponds to an interlayer expansion of 4.8 Å which is comparable to that of  $(\text{PPY})_{0.25}(\text{H}_2\text{O})_{0.16}\text{MoS}_2$  at 4.3 Å. The IR spectra of the nanocomposite are shown in Figure 2.6.

Contrary to the case of  $\text{MoS}_2$ , single-phase products of  $\text{WS}_2/\text{PPY}$  nanocomposites cannot be prepared with controlled amount of pyrrole and excess  $\text{FeCl}_3$  (Procedure 1). Reactions under those conditions always produced restacked  $\text{WS}_2$  mixed with the  $\text{WS}_2/\text{PPY}$  products. In addition, the nanocomposites were much less ordered with very broad X-ray diffraction peaks. This dissimilarity between the exfoliated  $\text{MoS}_2$  and  $\text{WS}_2$  systems could stem from the small differences in the charge density of the layers and their affinity for the polymer. According to ICP analysis, the exfoliated layers carry a charge of  $0.15 \text{ e}^-/\text{WS}_2$  [21], a little less than that of  $\text{MoS}_2$  layers,  $0.18 \text{ e}^-/\text{MoS}_2$ . This small charge difference does not seem enough to explain all the differences in reaction and nanocomposite composition. The observation in PPY intercalation reactions and the fact that much higher poly(ethylene oxide) quantities are needed to achieve a  $\text{WS}_2/\text{PEO}$  nanocomposite phase [22], may suggest a lower affinity of  $\text{WS}_2$ , than exfoliated  $\text{MoS}_2$ , for organic polymers.

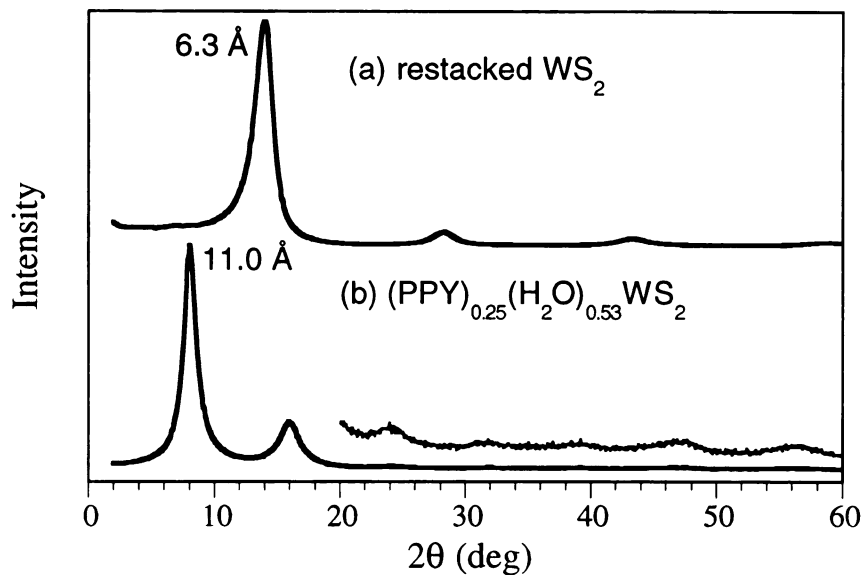


Figure 2.5. XRD patterns of WS<sub>2</sub>/PPY nanocomposites.

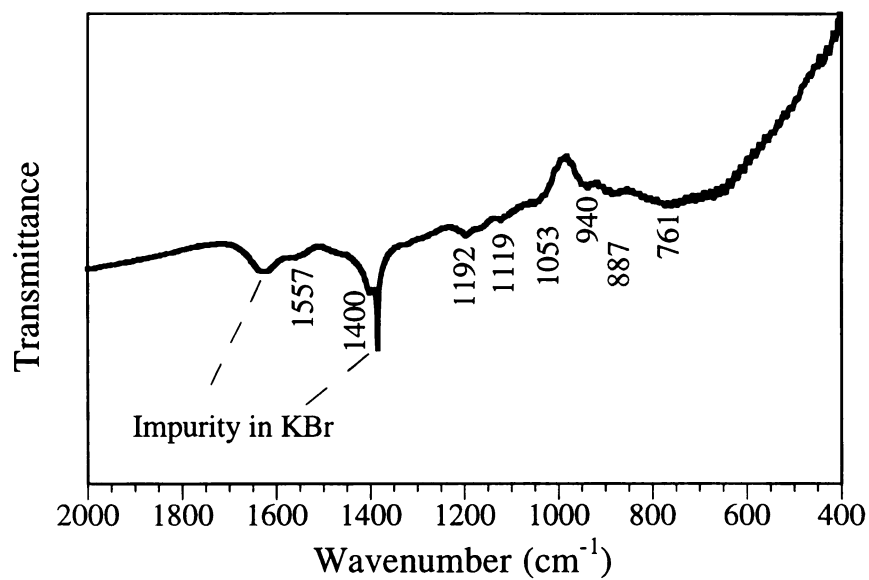


Figure 2.6. IR spectrum of (PPY)<sub>0.25</sub>(H<sub>2</sub>O)<sub>0.53</sub>WS<sub>2</sub> heating treated twice up to 320 °C under N<sub>2</sub> atmosphere at a heating rate of 5 °C/min.

### 3. An Analysis of Polymer Arrangements inside the Interlayer Galleries Based on the Dimensions of the Polymer Molecules

The structural parameters of the PPY nanocomposites and the poly(N-methyl pyrrole) (PMPY) nanocomposites, prepared with the two procedures are presented in Table 2.2. The temperatures for the octahedral to trigonal prismatic structural transition, which will be discussed in the next section, are also listed. The chosen nanocomposites prepared with Procedure 1 are those of good structural order, which have smaller d spacings and lower polymer contents.

Table 2.2. Structural data of PPY and PMPY nanocomposites

| sample  | reaction procedure | d spacing (Å) | coherence length | T <sub>trans</sub> (°C) | d spacing after DSC |
|---|--------------------|---------------|------------------|-------------------------|---------------------|
| (PPY) <sub>0.25</sub> (H <sub>2</sub> O) <sub>0.16</sub> MoS <sub>2</sub>   | 1                  | 10.5          | 124              | 192                     | 9.6                 |
| (PPY) <sub>0.51</sub> (H <sub>2</sub> O) <sub>0.18</sub> MoS <sub>2</sub>   | 2                  | 11.9          | 88               | 208                     | 11.1                |
| (PMPY) <sub>0.23</sub> (H <sub>2</sub> O) <sub>0.12</sub> MoS <sub>2</sub>  | 1                  | 10.9          | 95               | 198                     | 9.9                 |
| (PMPY) <sub>0.475</sub> (H <sub>2</sub> O) <sub>0.13</sub> MoS <sub>2</sub> | 2                  | 12.7          | 155              | 216                     | 12.3                |

As mentioned above, when the polymer content is low the pyrrole rings lie almost flat with respect to the inorganic layers, while they rise more vertically when the polymer content is high. An analysis of the dimensions of a PPY chain is necessary for a correct insight into the possible polymer chain arrangement in the galleries. According to the geometric calculation described in Appendix B, which is based on the bond lengths and angles, and the van der Waals' radii of the atoms, the PPY chain looks like a ribbon, which has a width of about 7.8 Å. The thickness of the ribbon is about 3.5 Å, which is decided by the van der Waals' diameter of C atoms. At the edges, the ribbon is a little narrower, 2.8 Å, corresponding to the van der Waals' diameter of the H atoms. If the PPY



chains lie totally flat, the nanocomposite would have a d spacing of 9.7 Å. This arrangement can accommodate a maximum of 0.31 equivalent of PPY. In  $(\text{PPY})_{0.25}(\text{H}_2\text{O})_{0.16}\text{MoS}_2$  which has a d spacing of 10.5 Å, the polymer chain can tilt at an angle of  $\sim 18^\circ$  to the  $\text{MoS}_2$  layers. This tilt increases the maximum PPY content to 0.32 equivalent. The 0.25 equivalent content of polymer in the nanocomposite is less than this maximum value, and thus quite reasonable. In the nanocomposite with  $d \sim 11.9$  Å, *i.e.*  $(\text{PPY})_{0.51}(\text{H}_2\text{O})_{0.18}\text{MoS}_2$ , the polymer chain can tilt  $\sim 36^\circ$ . This relatively large tilt makes the partial overlap of the polymer chains possible, so the content of PPY can reach as high as 0.51 equivalent.

$\text{MoS}_2/\text{PMPY}$  nanocomposites have also been synthesized with the two procedures used to synthesize  $\text{MoS}_2/\text{PPY}$  analogs. It is hoped that a comparison of the PPY and PMPY nanocomposites will lead to a better understanding of the arrangement of polymers inside the galleries. A PMPY ribbon is a little thicker than a PPY ribbon due to the bulky methyl group. The thickness of the ribbon becomes about 4.9 Å, a 1.3-1.4 Å increase from PPY. The width of PMPY is about the same as PPY, 7.8 Å. The two PMPY nanocomposites listed in Table 2.2 have d spacings around 10.9 and 12.7 Å respectively. The interlayer gallery height of the first nanocomposite, 4.7 Å, is just enough for a monolayer of PMPY to lie with its pyrrole rings parallel to the  $\text{MoS}_2$  layers. This arrangement of PMPY will let the  $\text{MoS}_2$  nanocomposite accept a maximum of 0.31 equivalent of polymer. The detected amount of polymer in the nanocomposite, 0.23 equivalent, is therefore a reasonable value. The interlayer gallery height of the second nanocomposite, 6.5 Å, allows the PMPY chains tilt about  $22^\circ$ . This small tilt angle will not diminish the projection area that an N-methyl pyrrole ring produces. Therefore, the  $\text{MoS}_2$  will not accept, in its galleries,

an amount of PMPY as much as 0.475 equivalent, unless the PMPY chains partially overlap or arrange themselves in an inter-digitated fashion.

#### 4. Thermal Properties

As discussed in Chapter 1, the electronic structure of MoS<sub>2</sub> changes after intercalation of lithium, corresponding to the structural transition from the trigonal prismatic MoS<sub>2</sub> to the octahedral MoS<sub>2</sub> [1d]. In the restacked MoS<sub>2</sub>, which preserves the octahedral coordination of Mo, the layers are similar to the 1T-MoS<sub>2</sub> which is metastable [23]. The MoS<sub>2</sub> layers in (PPY)<sub>x</sub>MoS<sub>2</sub> are, accordingly, also prone to conversion to the 2H-MoS<sub>2</sub>-like modification upon standing or with application of temperature or even pressure. The activation energy of this transition in restacked MoS<sub>2</sub> is relatively small, ~53 kJ/mol [24a], so the transition temperature measured by DSC is only 100 °C at a heating rate of 5 °C/min. The intercalation of polymers raises the activation energy as judged by the higher transition temperature. For example, the (PEO)<sub>1.0</sub>MoS<sub>2</sub> has an activation energy 82.2 kJ/mol and a transition temperature 138 °C.

The intercalation of PPY raises the transition temperature higher than any of the other polymers thus far. The value for (PPY)<sub>0.25</sub>(H<sub>2</sub>O)<sub>0.16</sub>MoS<sub>2</sub> and (PPY)<sub>0.51</sub>(H<sub>2</sub>O)<sub>0.18</sub>MoS<sub>2</sub> are 185 °C and 208 °C respectively, as listed in Table 2.2. To determine the activation energy for the transition of (PPY)<sub>0.51</sub>(H<sub>2</sub>O)<sub>0.18</sub>MoS<sub>2</sub>, a series of DSC measurements was done under different heating rates, see Figure 2.7. Different heating rates provided different transition temperatures, although the heat of transition detected by DSC was always around 37 kJ/mol. The heating rate and the transition temperature are related by the Arrhenius equation [25],

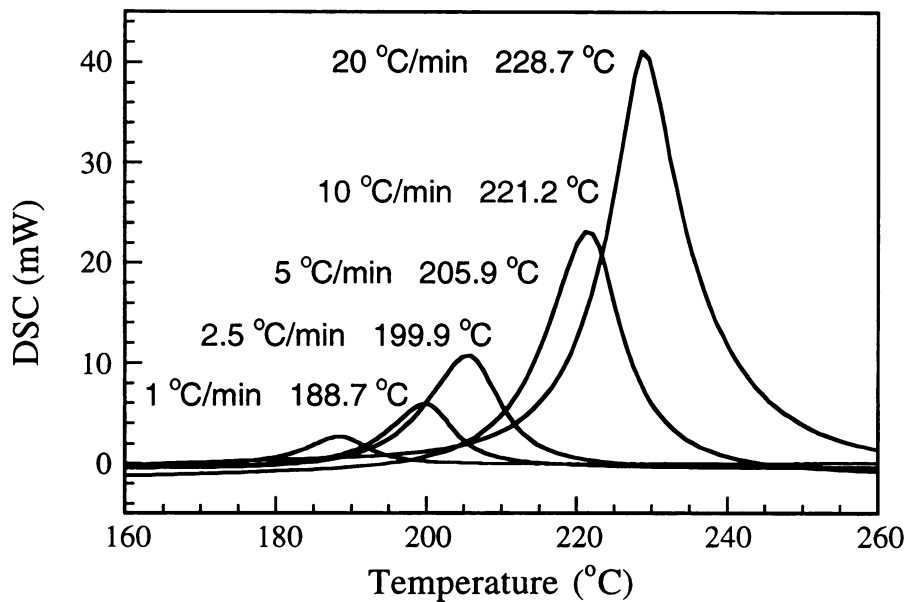


Figure 2.7. DSC measurements at different heating rates for  $(\text{PPY})_{0.51}(\text{H}_2\text{O})_{0.18}\text{MoS}_2$ .

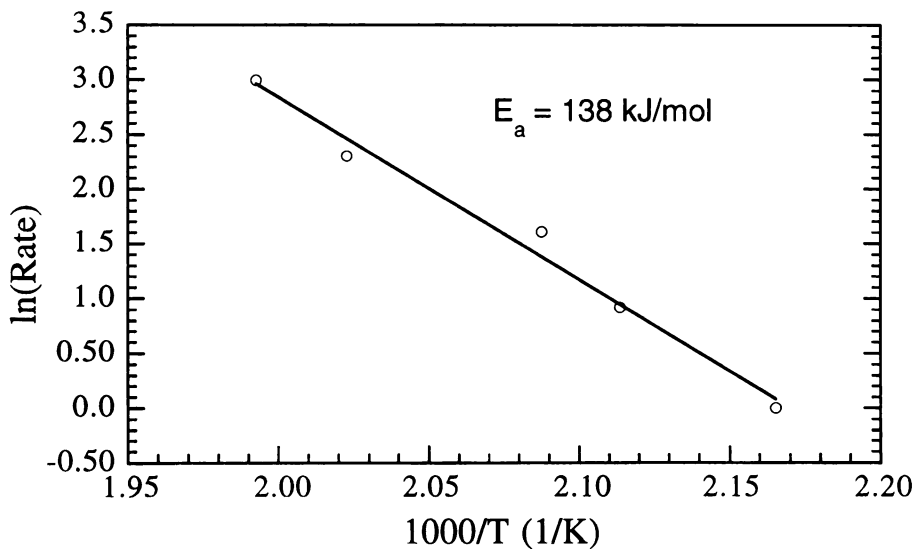


Figure 2.8. Plot of the DSC heating rate versus the temperature of the  $\text{MoS}_2$  structural transition for  $(\text{PPY})_{0.51}(\text{H}_2\text{O})_{0.18}\text{MoS}_2$ .



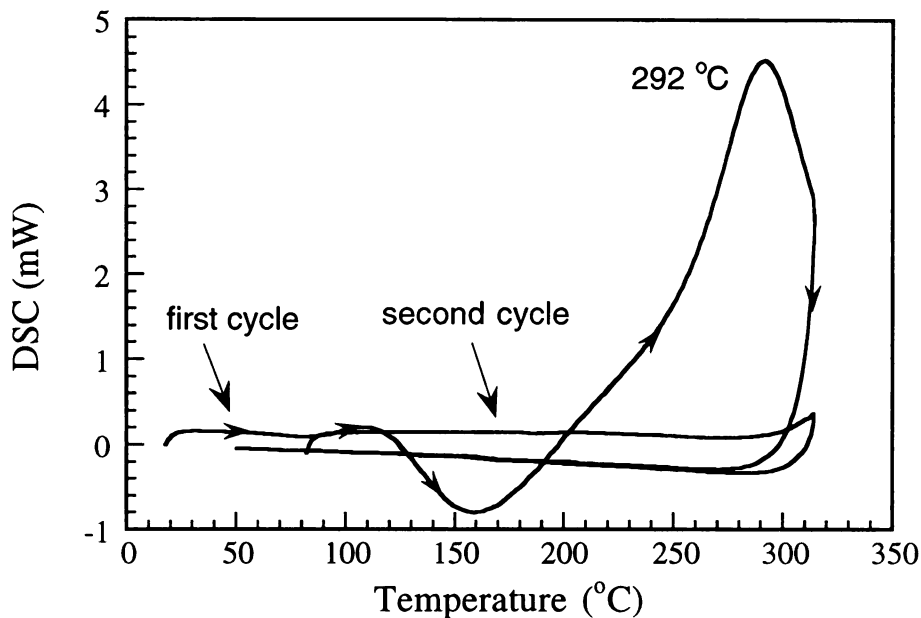


Figure 2.9. DSC measurement for  $(\text{PPY})_{0.25}(\text{H}_2\text{O})_{0.53}\text{WS}_2$ . The measurement was done in 2 heating cycles up to 320 °C at a rate of 5 °C/min. The curve of the first heating cycle is labeled with the arrows.

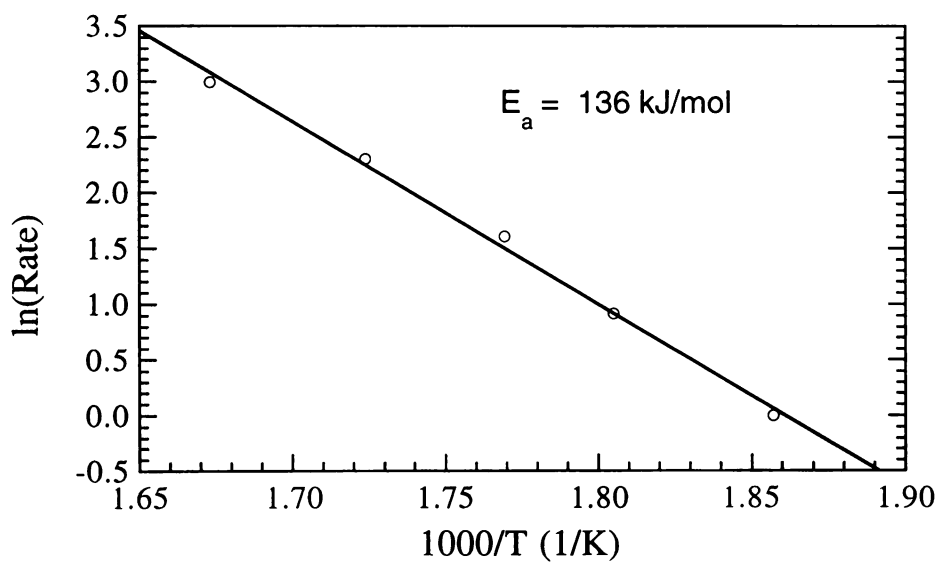


Figure 2.10. Plot of the DSC heating rate versus the  $\text{WS}_2$  structural transition temperature in  $(\text{PPY})_{0.25}(\text{H}_2\text{O})_{0.53}\text{WS}_2$ .



$$\text{Rate} = A * e^{-E_a/RT}$$

where A is the pre-exponential coefficient, R the gas constant and  $E_a$  the activation energy. The activation energy can be calculated from the slope of the  $\ln(\text{Rate}) \sim 1/T$  plot. The plot for  $(\text{PPY})_{0.51}(\text{H}_2\text{O})_{0.18}\text{MoS}_2$  gives an activation energy of 138 kJ/mol (see Figure 2.8), which is much higher than those of restacked  $\text{MoS}_2$  or  $(\text{PEO})_{1.0}\text{MoS}_2$ . The large increases in the transition temperature and activation energy may result from the reducing nature of PPY, thus stabilizing  $[\text{MoS}_2]^{x-}$ .

The same situation exists in restacked  $\text{WS}_2$  and  $(\text{PPY})_x\text{WS}_2$  nanocomposite, but the transition temperatures are higher than  $\text{MoS}_2$  compounds. The values for restacked  $\text{WS}_2$  and  $(\text{PPY})_{0.25}(\text{H}_2\text{O})_{0.53}\text{WS}_2$  are 207 °C [26] and 292 °C respectively. A DSC measurement for  $(\text{PPY})_{0.25}(\text{H}_2\text{O})_{0.53}\text{WS}_2$  is shown in Figure 9. The change of the transition temperature, by 85 °C, is the same as in the case of  $(\text{PPY})_{0.25}(\text{H}_2\text{O})_{0.16}\text{MoS}_2$ . Under heating rates of 1.0, 2.5, 5.0, 10.0 and 20 °C/min, the transition temperatures of  $(\text{PPY})_{0.25}(\text{H}_2\text{O})_{0.53}\text{WS}_2$  detected by DSC were 265.3, 280.9, 292.1, 307.0 and 324.5 °C respectively. The activation energy of the transition calculated from the  $\ln(\text{Rate}) \sim 1/T$  plot (see Figure 2.10) is 136 kJ/mol, much higher than the value of restacked  $\text{WS}_2$ , 82.4 kJ/mol [26], but close to that of  $(\text{PPY})_{0.51}(\text{H}_2\text{O})_{0.18}\text{MoS}_2$ . The heat of transition detected by DSC was around 20 kJ/mol, slightly higher than the 18 kJ/mol of restacked  $\text{WS}_2$ , but less than 37 kJ/mol found for  $(\text{PPY})_{0.51}(\text{H}_2\text{O})_{0.18}\text{MoS}_2$ .

After the transition, samples of these nanocomposites still have well ordered lamellar structure. The d spacings of the  $\text{MoS}_2$  nanocomposites after the DSC experiments are listed in Table 2.2. The d spacing of the

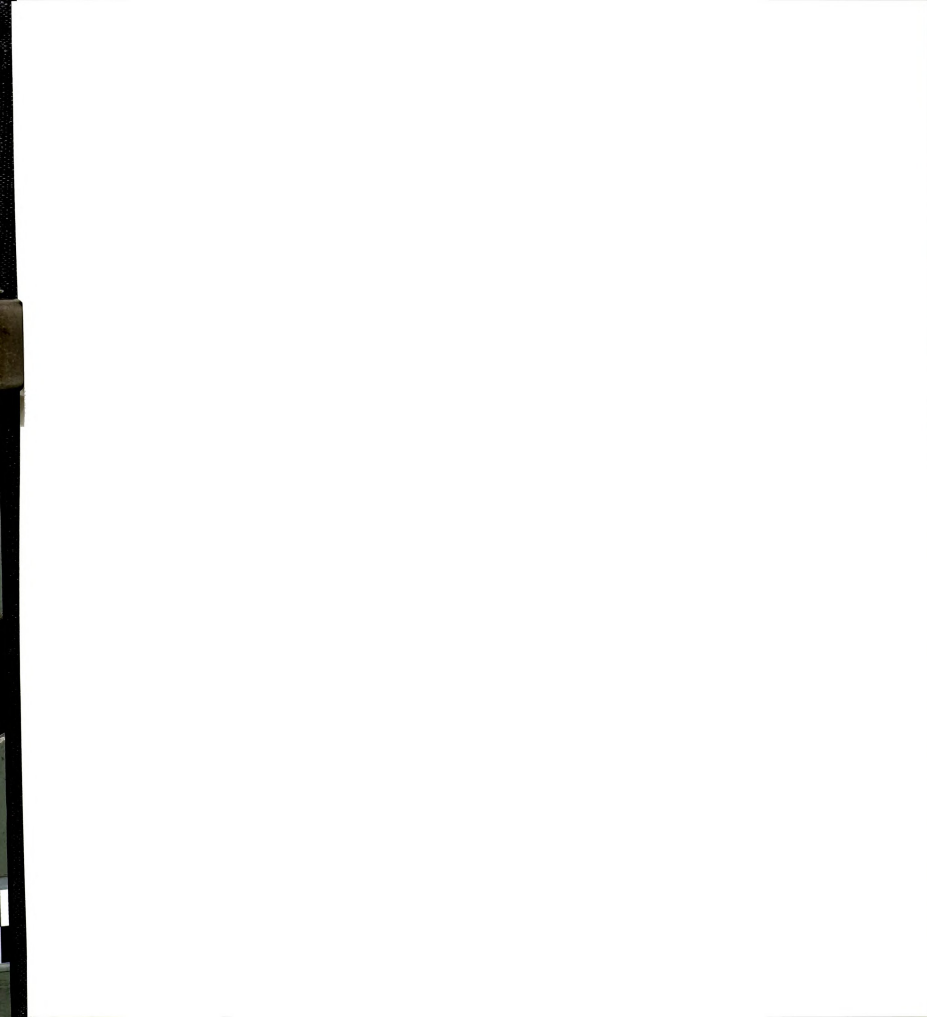
WS<sub>2</sub>/PPY nanocomposite after the DSC measurement is 10.3 Å. The IR spectra of the heated nanocomposites show only PPY peaks.

## 5. Charge Transport Properties

Room temperature electrical conductivity values of the materials described here are listed in Table 2.3 [27]. The conductivities of the restacked WS<sub>2</sub> and the fresh restacked MoS<sub>2</sub> are high, about 100 and 12 S/cm respectively, as measured with pressed pellets. The conductivity of restacked MoS<sub>2</sub> diminishes quickly, due to the gradual structural transition of restacked MoS<sub>2</sub> at room temperature. According to experiments, the transition proceeded almost completely in about 4 months and the conductivity reached about 0.07 S/cm. The conductivity stayed at about 0.06 S/cm for the subsequent 3 years. Comparing the samples more than 6 months old, the intercalation of PPY raises the conductivity more than 10 times. A higher PPY content gives the material a higher conductivity. In contrast, the intercalation of PPY reduces the conductivity of restacked

Table 2.3. Room temperature electrical conductivities of PPY nanocomposites and restacked MoS<sub>2</sub> and WS<sub>2</sub>

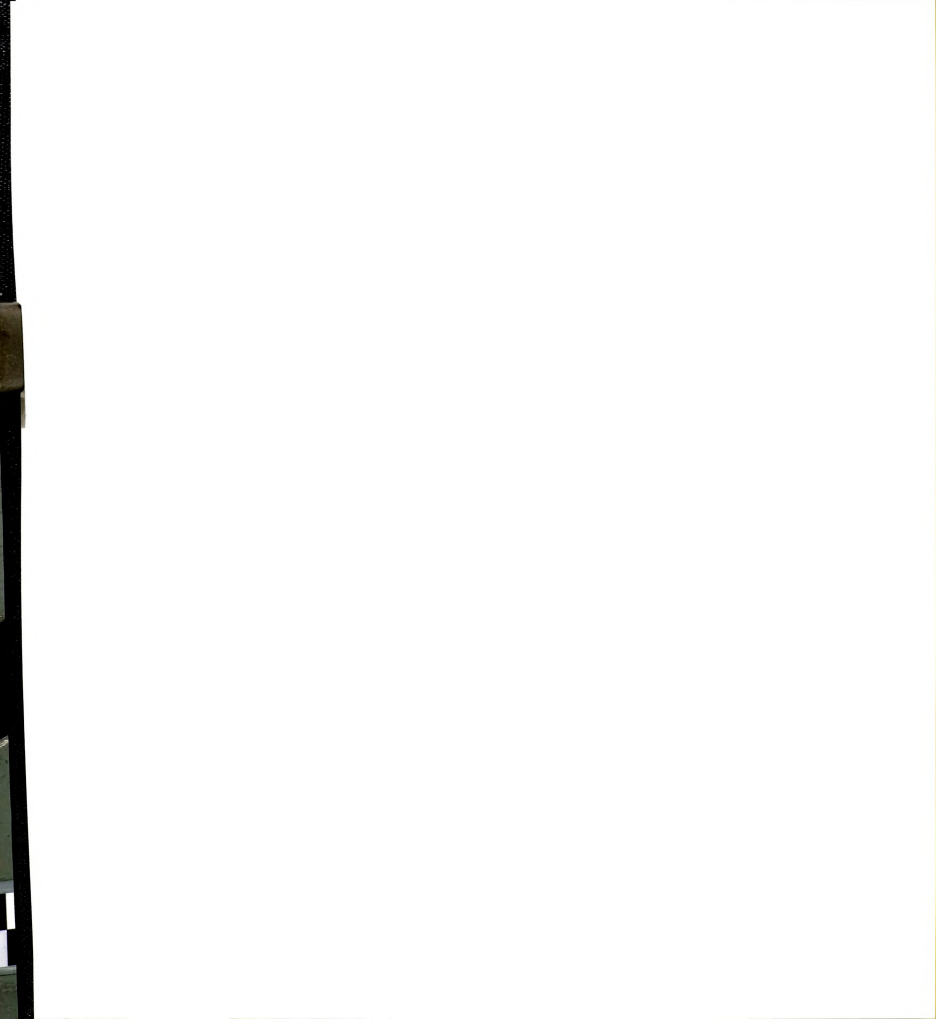
| sample  | R.T. conductivity (S/cm) |
|---|--------------------------|
| restacked MoS <sub>2</sub> (1 day)  | 12                       |
| restacked MoS <sub>2</sub> (3 years)                                      | ~0.06                    |
| (PPY) <sub>0.25</sub> (H <sub>2</sub> O) <sub>0.16</sub> MoS <sub>2</sub> | 0.8                      |
| (PPY) <sub>0.51</sub> (H <sub>2</sub> O) <sub>0.18</sub> MoS <sub>2</sub> | 2.5                      |
| restacked WS <sub>2</sub> (10 days)                                       | 100                      |
| (PPY) <sub>0.25</sub> (H <sub>2</sub> O) <sub>0.53</sub> WS <sub>2</sub>  | 27                       |



WS<sub>2</sub>, because the conductivity of bulk PPY is only 13 S/cm, smaller than that of restacked WS<sub>2</sub>. In addition, (PPY)<sub>x</sub>WS<sub>2</sub> may have more grain boundaries giving resistance.

Variable-temperature electrical conductivity measurements for pressed (PPY)<sub>0.25</sub>(H<sub>2</sub>O)<sub>0.16</sub>MoS<sub>2</sub> pellets indicate a considerable higher conductivity with respect to pristine MoS<sub>2</sub>, as shown in Figure 2.11. In the temperature range 50-300 K, the material exhibits weak, thermally activated behavior, which is common in conductive granular nanocomposites. The plot of conductivity versus reciprocal temperature does not follow a straight line, which indicates that the thermal activation is more likely through the boundary areas between the conductive domains. The conductivity is similar in magnitude to that of (PANI)<sub>x</sub>MoS<sub>2</sub> consistent with the similar nature of the materials. The corresponding thermoelectric power measurements show relatively large and positive Seebeck coefficient values which indicate a p-type conductor, see Figure 2.12. The relatively large values and the curved thermoelectric power plot indicate a deviation from an ideal metallic behavior.

Similar to (PPY)<sub>0.25</sub>(H<sub>2</sub>O)<sub>0.16</sub>MoS<sub>2</sub>, (PPY)<sub>0.25</sub>(H<sub>2</sub>O)<sub>0.53</sub>WS<sub>2</sub> has also a thermally activated electrical conductivity. A variable temperature conductivity measurement for (PPY)<sub>0.25</sub>(H<sub>2</sub>O)<sub>0.53</sub>WS<sub>2</sub> is shown in Figure 2.13 together with that for restacked WS<sub>2</sub>. The comparison demonstrates that (PPY)<sub>0.25</sub>(H<sub>2</sub>O)<sub>0.53</sub>WS<sub>2</sub> is not as electrically conductive as the restacked WS<sub>2</sub>, which has been seen in the room temperature conductivity measurements. Thermoelectric measurements for (PPY)<sub>0.25</sub>(H<sub>2</sub>O)<sub>0.53</sub>WS<sub>2</sub> show typical p-type metallic behavior, with small positive values which decreases linearly with falling temperatures, see Figure 2.14. The restacked WS<sub>2</sub> has similar thermoelectric behavior [28].



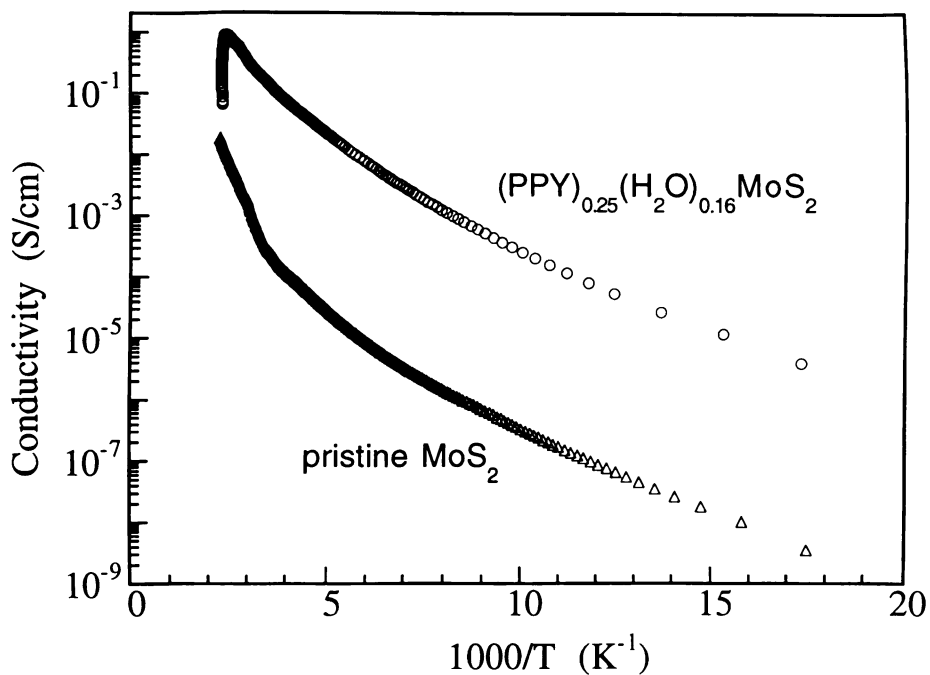


Figure 2.11. Variable temperature electrical conductivity measurements on pressed pellets for pristine  $\text{MoS}_2$  and a  $\text{MoS}_2/\text{PPY}$  nanocomposite prepared with Procedure 1.

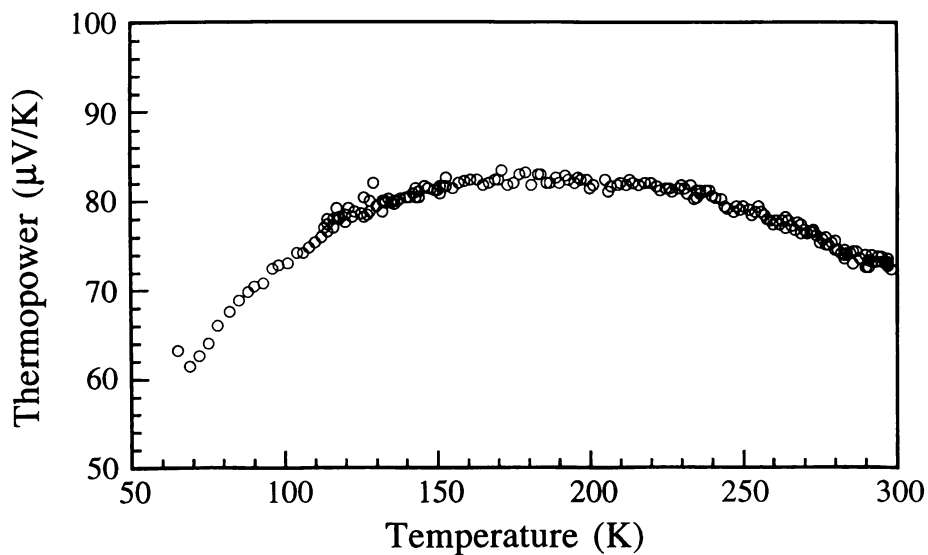


Figure 2.12. Thermoelectric power measurement on a pressed pellet for  $(\text{PPY})_{0.25}(\text{H}_2\text{O})_{0.16}\text{MoS}_2$  prepared with Procedure 1.

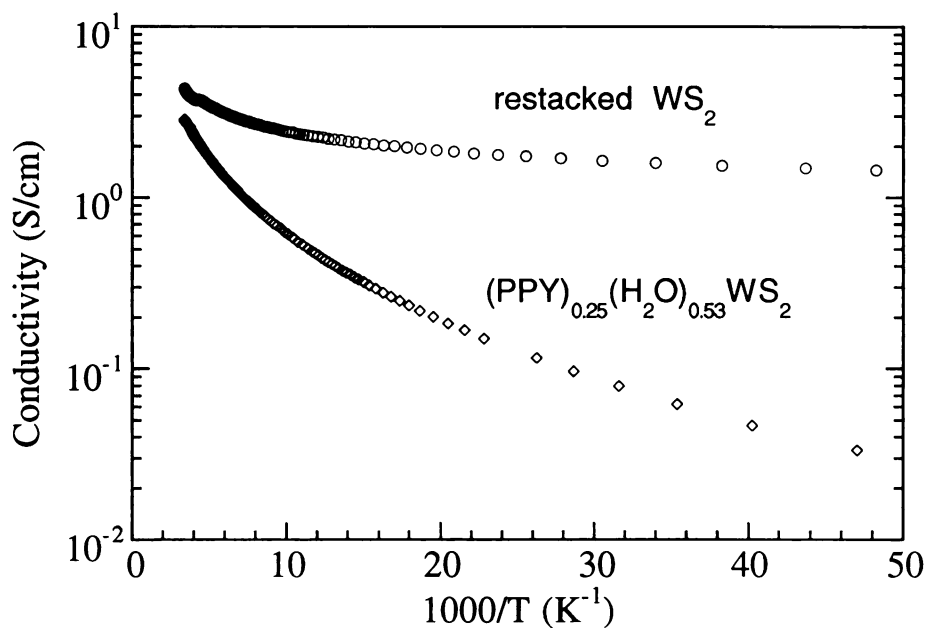


Figure 2.13. Variable temperature electrical conductivity measurements on pressed pellets for restacked WS<sub>2</sub> and (PPY)<sub>0.25</sub>(H<sub>2</sub>O)<sub>0.53</sub>WS<sub>2</sub>.

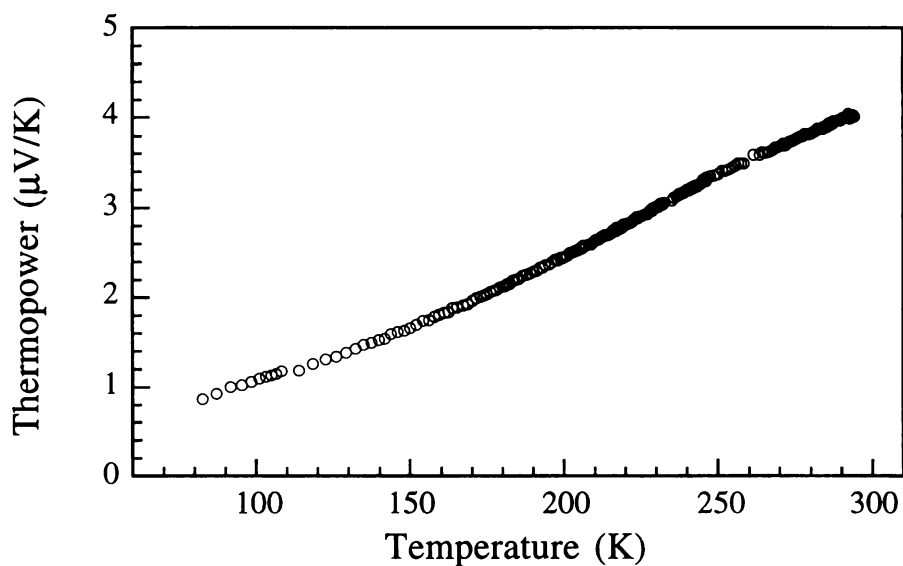
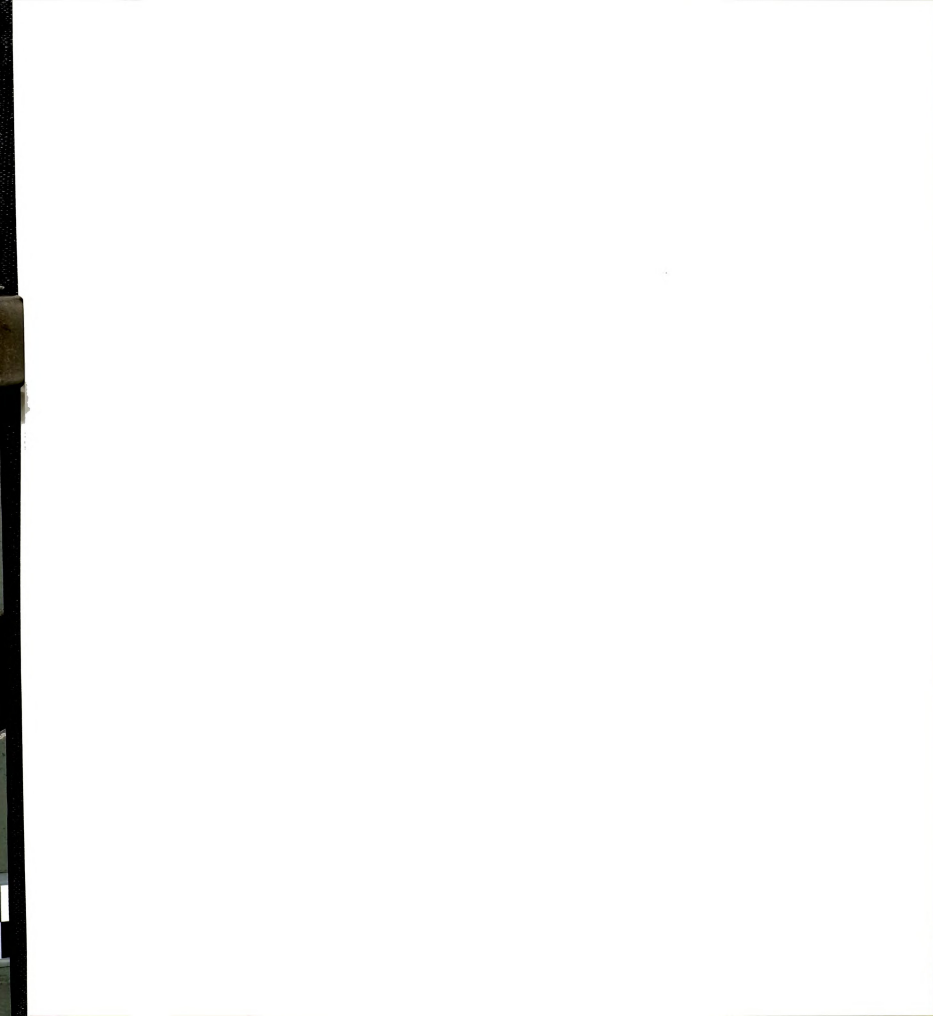


Figure 2.14. Thermoelectric power measurement on a pressed (PPY)<sub>0.25</sub>(H<sub>2</sub>O)<sub>0.53</sub>WS<sub>2</sub> pellet.



## Concluding Remarks

MoS<sub>2</sub>/PPY, WS<sub>2</sub>/PPY and MoS<sub>2</sub>/PMPY nanocomposites have been successfully synthesized using the new *in situ* oxidative polymerization-encapsulative precipitation reaction. This reaction is kinetically controlled, so some optimization to find the optimum conditions to produce the nanocomposites, or conditions to get the most ordered structure, is crucial. A great effect has been made in this research to optimize the reactions and the best conditions are reported and discussed. The MoS<sub>2</sub>/PPY, WS<sub>2</sub>/PPY and MoS<sub>2</sub>/PMPY nanocomposites synthesized have ordered structures and large coherence lengths along the stacking direction.

The new nanocomposites were characterized and identified. A discussion about the arrangement of polymer chains inside the MoS<sub>2</sub>/PPY nanocomposites suggests that the polymer chains lie almost flat inside the galleries when the polymer content is about 0.25 equivalent. The chains tilt up and overlap when the polymer content becomes about 0.5. The intercalation of PPY stabilizes the metastable restacked MoS<sub>2</sub> and WS<sub>2</sub> layers, by raising structural transition temperatures to 208 and 292 °C respectively. These increases in transition temperature are the largest ones observed yet in MoS<sub>2</sub> and WS<sub>2</sub> nanocomposites. Both MoS<sub>2</sub>/PPY and WS<sub>2</sub>/PPY nanocomposites are good conductors.

The development of a synthetic strategy to intercalate an intractable, infusible polymer in non-oxidizing hosts is the most important achievement in this research. This is an advance from prior work where (a) an oxidizing host was required to proceed polymer intercalation, (b) a soluble polymer was necessary for insertion into a non-oxidizing host, or (c) a monomer intercalation was required followed by a second step of polymerization. The methodology developed here can be applied further to

other intractable polymers such as polythiophene. This development broadens the field of organic/inorganic nanocomposite materials as it enables interesting new inorganic/polymer combinations for study and development.



## Appendix B

Based on the conjugated structure of PPY, we assume that it is a flat or nearly flat molecule. As shown in Figure 2.15(a), the distance between the farthest two atoms in the direction perpendicular to the polymer chain (two H atoms) is  $2.48 \text{ \AA} * 2 = 4.96 \text{ \AA}$ . By adding the van der Waals radius of H atom,  $1.4 \text{ \AA}$ , the width of the PPY chain should be  $7.8 \text{ \AA}$ . The thickness of the chain should be about  $3.54 \text{ \AA}$ , which is deduced from the van der Waals radius of the C atom,  $1.77 \text{ \AA}$ .

The length of each pyrrole unit is  $3.59 \text{ \AA}$ , so the area that each pyrrole unit occupies is  $3.59 \text{ \AA} * 7.8 \text{ \AA} = 27.9 \text{ \AA}^2$  [29]. The area of each  $\text{MoS}_2$  unit is  $8.653 \text{ \AA}^2$ , according to the  $a$  and  $\gamma$  of the 2H- $\text{MoS}_2$ ,  $3.161 \text{ \AA}$  and  $120^\circ$  [30]. This indicates that the  $\text{MoS}_2$  nanocomposite can accept a maximum of 0.31 equivalent of PPY in the galleries if the PPY chains lie flat.

In the  $\text{MoS}_2$  nanocomposite of a  $d$  spacing  $10.5 \text{ \AA}$ , where the gallery is  $4.3 \text{ \AA}$  high, the polymer chain can tilt at an angle of  $\sim 18^\circ$  to the  $\text{MoS}_2$  layers according to the following calculation:

$$\arcsin[(4.3\text{\AA}-2*1.4\text{\AA})/(7.8\text{\AA}-2*1.4\text{\AA})] = 17.5^\circ$$

$1.4 \text{ \AA}$  is the van der Waals radius of the H atoms which are on the two sides. When a PPY chain tilts  $18^\circ$ , the area of a projection of a pyrrole unit is  $(4.96 \text{ \AA} * \cos 18^\circ + 2 * 1.4 \text{ \AA}) * 3.59 \text{ \AA} = 27.0 \text{ \AA}^2$ . The  $\text{MoS}_2$  can accept a maximum of 0.32 equivalent of PPY arranged this way.

When the expansion is  $5.7 \text{ \AA}$ , the polymer chains can tilt  $\sim 36^\circ$ :

$$\arcsin[(5.7\text{\AA}-2*1.4\text{\AA})/(7.8\text{\AA}-2*1.4\text{\AA})] = 35.5^\circ$$



The projection of a pyrrole unit in a such placed chain will have an area of  $(4.96 \text{ \AA} * \cos 36^\circ + 2 * 1.4 \text{ \AA}) * 3.59 \text{ \AA} = 24.4 \text{ \AA}^2$ . The PPY content can reach a maximum of 0.35 equivalent if there is no overlapping of the chains. The high PPY content in the nanocomposite, 0.51, can be best explained by the partial overlapping of the PPY chains in the galleries. Since the edge of the PPY chain is only  $\sim 2.8 \text{ \AA}$ , the  $5.7 \text{ \AA}$  gallery height is just enough for the edges of two chains to overlap.

In the case of PMPY, the bulky methyl group makes the PMPY chain thicker,  $4.87 \text{ \AA}$ , as obtained in the following calculation [also see Figures 2.16(b) and (c)]:

$$2 * (\text{C-H} * \sin 110^\circ + 1.4 \text{ \AA}) = 2 * (1.10 * \sin 110^\circ + 1.4 \text{ \AA}) = 4.9 \text{ \AA}.$$

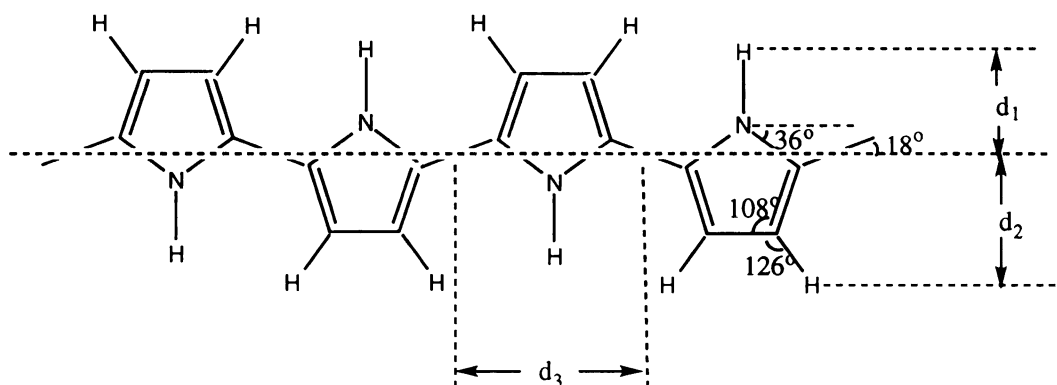
Again,  $1.4 \text{ \AA}$  is the van der Waals radius of a H atom. The  $(\text{PMPY})_{0.23}(\text{H}_2\text{O})_{0.12}\text{MoS}_2$  has a d spacing of  $10.9 \text{ \AA}$ . Its  $4.7 \text{ \AA}$  gallery spacing is just enough for the PMPY chains to lie flat inside. The width of the PMPY chains is the same as that of PPY chains, because the added methyl groups are buried inside the grooves of the PPY chain, see Figure 2.15(b). If the PMPY chains lie flat, each N-methyl pyrrole unit will cover an area approximately the same as a pyrrole unit. Correspondingly, the  $\text{MoS}_2$  nanocomposite will accommodate a maximum of 0.31 equivalent of PMPY.

The PMPY chains must tilt in  $(\text{PMPY})_{0.23}(\text{H}_2\text{O})_{0.12}\text{MoS}_2$ , which has a d spacing of  $12.7 \text{ \AA}$ . The tilt of the chains is calculated by the following approach, which is different from the calculation for PPY. As shown in Figure 2.16(b), the distance between the diagonal H atoms in the two methyl groups on the two sides,  $d_6$ , is  $5.27 \text{ \AA}$ . When a PMPY chain lies flat, the  $d_6$  direction of the chain tilts by an angle of  $\arcsin(2.07 \text{ \AA} / 5.27 \text{ \AA}) = 23.1^\circ$ , see Figure 2.16(c). In a gallery  $6.5 \text{ \AA}$  high, the chain can tilt so

that the  $d_6$  vector tilts a maximum angle of  $\arcsin[(6.5 \text{ \AA} - 2*1.4 \text{ \AA}) / 5.27 \text{ \AA}] = 44.6^\circ$ . The tilt of the chain is the change of the angle of the diagonal plane,  $21.5^\circ$ , see Figure 2.16(d).

The  $21.5^\circ$  tilt of the PMPY chain produces a larger projection on the  $\text{MoS}_2$  plane, as shown in Figure 2.16(d). The PMPY chains in the nanocomposite must partially overlap to accept a 0.475 equivalent of polymer. Otherwise, according to the calculation, the polymer content would not exceed 0.29 equivalent. The  $6.5 \text{ \AA}$  gallery height does not exceed the sum of the thicknesses of the methyl group and H atom,  $4.9$  and  $2.8 \text{ \AA}$  respectively. In order to achieve a partial overlap with nearby polymer chains, a polymer chain must match its edge H atoms or methyl groups with those of the neighbor chains in an inter-digitated fashion.

**(a) polypyrrole**



Length of covalent bonds:

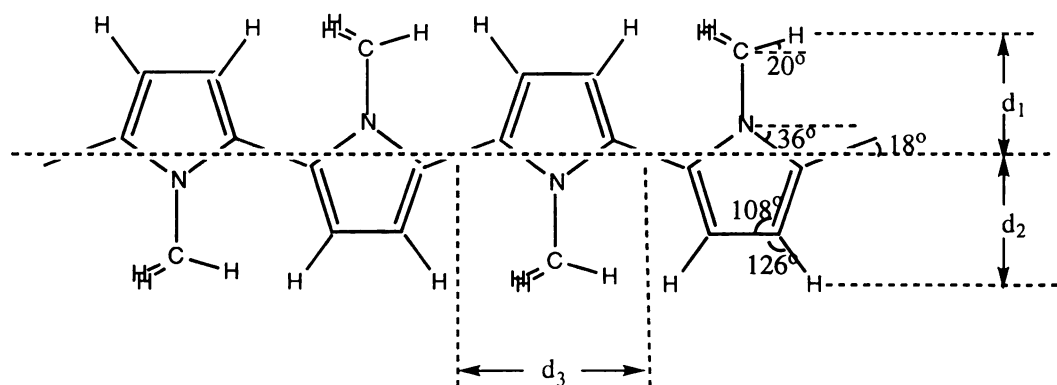
C-C 1.54 Å, C=C 1.34 Å, C-N 1.47 Å, C=N 1.27 Å, N-H 0.98 Å, C-H 1.10 Å.

$$d_1 = \text{N-H} + [(\text{C-N} + \text{C=N}) * \sin 36^\circ] / 2 - [(\text{C-C} + \text{C=C}) * \sin 18^\circ] / 4 = 1.56 \text{ \AA}$$

$$d_2 = \text{C-H} * \sin 126^\circ + [(\text{C-C} + \text{C=C}) * \sin 108^\circ] / 2 + [(\text{C-C} + \text{C=C}) * \sin 18^\circ] / 4 = 2.48 \text{ \AA}$$

$$d_3 = 2 * [(\text{C-N} + \text{C=N}) * \cos 36^\circ] / 2 + [(\text{C-C} + \text{C=C}) * \cos 18^\circ] / 2 = 3.59 \text{ \AA}$$

**(b) poly(N-methyl pyrrole)**



$$d_1 = \text{C-H} * \sin 20^\circ + \text{C-N} + [(\text{C-N} + \text{C=N}) * \sin 36^\circ] / 2 - [(\text{C-C} + \text{C=C}) * \sin 18^\circ] / 4 = 2.43 \text{ \AA}$$

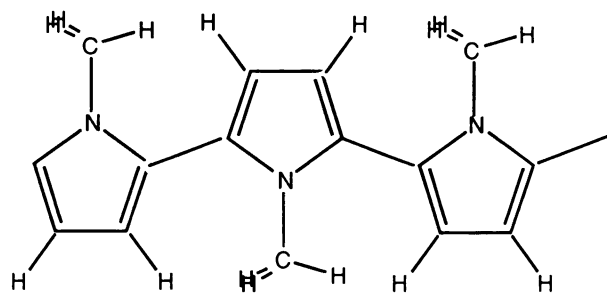
$$d_2 = 2.48 \text{ \AA}$$

$$d_3 = 3.59 \text{ \AA}$$

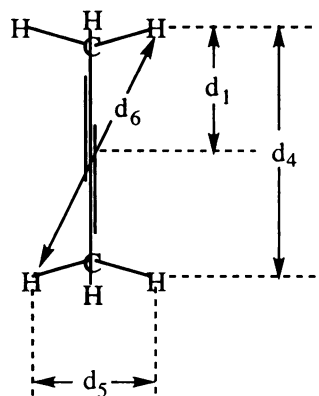
Figure 2.15. Schematic structures and dimensions of PPY and PMPY.



(a) Front view of poly(N-methyl pyrrole)

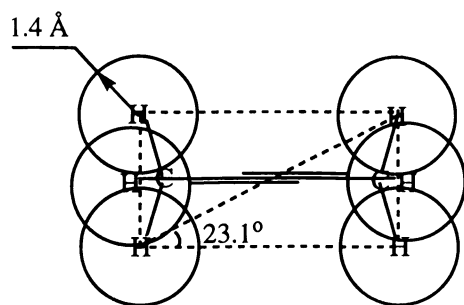


(b) Side view of poly(N-methyl pyrrole)



$$d_4 = 2 * d_1 = 2 * 2.43 \text{ \AA} = 4.86 \text{ \AA}$$
$$d_5 = 2 * 1.10 \text{ \AA} * \sin 110^\circ = 2.07 \text{ \AA}$$
$$d_6 = (d_4^2 + d_5^2)^{1/2} \text{ \AA} = 5.27 \text{ \AA}$$

(c) Contour of a flat lay poly(N-methyl pyrrole)



(d) Tilted poly(N-methyl pyrrole) in a 6.7 \AA gallery

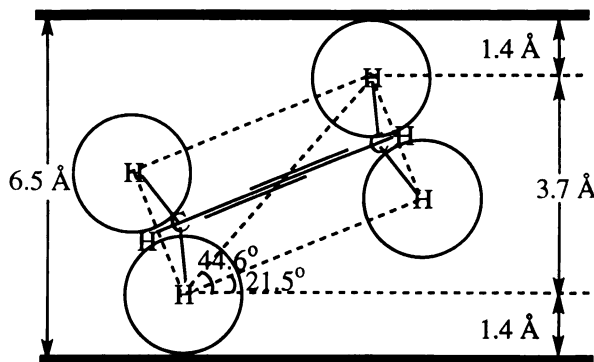


Figure 2.16. Views of PMPY.



## References

- 1 (a) M. G. Kanatzidis, L. M. Tonge, T. J. Marks, H. O. Marcy and C. R. Kannewurf, *J. Am. Chem. Soc.* **1987**, 109, 3797. (b) M. G. Kanatzidis, C.-G. Wu, H. O. Marcy and C. R. Kannewurf, *J. Am. Chem. Soc.* **1989**, 111, 4139. (c) L. F. Nazar, X. T. Yin, D. Zinkweg, Z. Zhang and S. Liblong, *Mat. Res. Soc. Symp. Proc.* **1991**, 210, 417. (d) R. Bissessur, D. C. DeGroot, J. L. Schindler, C. R. Kannewurf and M. G. Kanatzidis, *J. Chem. Soc., Chem. Commun.* **1993**, 687. (e) M. G. Kanatzidis, R. Bissessur, D. C. DeGroot, J. L. Schindler and C. R. Kannewurf, *Chem. Mater.* **1993**, 5, 595. (f) G. Matsubayashi and H. Nakajima, *Chem. Lett.* **1993**, 31.
- 2 F. Croce, G. B. Appetecchi, L. Persi and B. Scrosati, *Nature* **1998**, 394, 456.
- 3 (a) L. F. Nazar, H. Wu and W. P. Power, *J. Mater. Chem.* **1995**, 5, 1985. (b) F. Leroux, B. E. Koene and L. F. Nazar, *J. Electrochem. Soc.*, **1996**, 143, L181. (c) T. A. Kerr, H. Wu and L. F. Nazar, *Chem. Mater.* **1996**, 8, 2005. (d) B. E. Koene and L. F. Nazar, *Solid State Ionics* **1996**, 89, 147. (e) K. Ramachandran and M. M. Lerner *J. Electrochem. Soc.* **1997**, 144, 3739. (f) F. Leroux, G. Goward, W. P. Power and F. Nazar *J. Electrochem. Soc.*, **1997**, 144, 3886.
- 4 (a) J. A. Wilson and A. D. Yoffe, *Adv. Phys.* **1969**, 18, 193. (b) L. F. Mattheiss, *Phys. Rev. B* **1973**, 8, 3719.
- 5 F. R. Gamble and T. H. Geballe, in N. B. Hannay ed., *Treatise on Solid State Chemistry*, Vol 3, Plenum Press **1976**, pp 89.
- 6 (a) R. H. Friend and A. D. Yoffe, *Adv. Phys.* **1987**, 36, 1. (b) W. R. McKinnon, in A. P. Legrand and S. Flandrois ed., *Chemical Physics of Intercalation (NATO ASI Ser., B: Phys.)*, Vol. 172, Plenum Press, New York **1987**, pp 181.
- 7 (a) C.-H. Hsu, M. M. Labes, J. T. Breslin, D. J. Edmiston, J. J. Winter, H. A. Leupold and F. Rothwarf, *Nature, Phys. Sci.*, **1973**, 246 (155), 122. (b) V. M. Chapela and G. S. Parry, *Nature*, **1979**, 281, 134. (c) W. M. R. Divigalpitiya, R. F. Frindt and S. R. Morrison, *J. Mater. Res.* **1991**, 6, 1103. (d) E. Ruiz-Hitzky, R. Jimenez, B. Casal, V. Manriquez, A. S. Ana and G. Gonzalez, *Adv.*

- Mater.* **1993**, 5, 738. (e) J. P. Lemmon, J. Wu, C. Oriakhi and M. M. Lerner, *Electrochim. Acta* **1995**, 40, 2245. (f) C. O. Oriakhi, R. L. Nafshun and M. M. Lerner, *Mater. Res. Bull.* **1996**, 31, 1513.
- 8 (a) L. W. Shacklette, R. R. Chance, D. M. Ivory, G. G. Miller and R. H. Baughman, *Synth. Met.* **1979**, 1, 101. (b) M. Satoh, H. Yageta, K. Amano and E. Hasegawa *Synth. Met.* **1997**, 84, 167. (c) J. Cao, A. J. Heeger, J. Y. Lee and C. Y. Kim *Synth. Met.* **1996**, 82, 221. (d) H. Kuhn, R. Gregory and W. Kimbrell, *Int. SAMPE Electron. Conf.* **1989**, 3, 570. (e) M. D. Imisides, R. John, P. J. Reiley and G. G. Wallace, *Electroanalysis* **1991**, 3, 879.
- 9 E. P. Giannelis, V. Mehrotra, O. Tse, R. A. Vaia and T. -C. Sung, *Mat. Res. Soc. Symp. Proc.* **1992**, 267, 969.
- 10 (a) Y. Fukushima and S. Inagaki, *J. Inclusion Phenom.* **1987**, 5, 473. (b) Y. Fukushima, A. Okada, M. Kawasumi, T. Kurauchi and O. Kamigaito, *Clay Minerals* **1988**, 23, 27.
- 11 Because the polymer exists inside the nanocomposite, it could experience somewhat incomplete oxidation in the process of elemental analysis experiments. This may lead to lower N amount detected. The formula is derived based on the amounts of C and H.
- 12 An elemental analysis of another sample done in our department at MSU showed: C 7.28%, H 0.85%, N 1.40%; C 7.19%, H 0.82%, N 1.36%. The corresponding formula is  $(C_4H_3N)_{0.28}(H_2O)_{0.35}MoS_2$ . Calculated: C 7.28%; H 0.83%; N 2.12%. A nanocomposite with the formula above should lose 22.0% of the weight if the final residue is  $MoO_3$ . This agrees well with the result of the TGA experiment in oxygen which had a loss around 21.0 wt% at 650 °C.
- 13 This measurement and elemental analysis measurements hereafter were done by Dr. R. Huang in this department.
- 14 Another analysis showed C 4.11%, H 0.71% and N 1.19%, which suggests a formula  $(C_4H_3N)_{0.235}(H_2O)_{0.62}WS_2$ : C 4.11%; H 0.71%; N 1.20%.
- 15 Two TGA experiments in oxygen had losses around 11.5 wt% and 11.7 wt% up to 650 °C.

- 16 (a) B. N. Diel, T. Inabe, J. W. Lyding, K. F. Schock, Jr., C. R. Kannewurf and T. J. Marks, *J. Am. Chem. Soc.*, **1983**, 105, 1551. (b) J. W. Lyding, H. O. Marcy, T. J. Mark and C. R. Kannewurf, *IEEE. Trans. Instrum. Meas.* **1988**, 37, 76.
- 17 (a) P. W. Selwood, *Magnetochemistry* (2nd Ed.), Interscience Publishers, New York, **1956**, pp 78. (b) R. S. Drago, *Physical Methods for Chemists* (2nd Ed.), Saunders College Publishing, Philadelphia/San Diego/New York, **1992**, Chapter 11. (c) For polyaniline: A. J. Epstein, J. M. Ginder, A. F. Richter and A. G. MacDiarmid, in L. Alcácer ed., *Conducting Polymers*, D. Reidel Publishing Company, Dordrecht, **1986**, pp 121.
- 18 X-ray scattering coherence lengths were calculated from the Scherrer formula  $L_{hkl}=K\lambda/\beta\cos\theta$ : (a) D. M. Moore and R. C. Reynolds, Jr., *X-Ray Diffraction and the Identification and Analysis of Clay Minerals*, Oxford University Press: Oxford/Newyork, **1989**, pp 83. (b) H. P. Klug and L. E. Alexander, *X-ray Diffraction Procedures for Polycrystalline and Amorphous Materials*, John Wiley & Sons, New York, **1962**, pp 491. In the formula, K is a constant close to 1. It is assigned 0.9 in the calculation.  $\lambda$  is the X-ray wavelength, which is 1.5419Å.  $\beta$  is the broadening of the reflection peak (in  $2\theta$ ) in the XRD pattern, and is calculated according to the following equation:
- $$\beta = \sqrt{b^2 - b_0^2}$$
- b is the width of the peak at a half height.  $b_0$  is the instrumental broadening, which is  $0.14^\circ$  according to the width of pristine 2H-MoS<sub>2</sub>. The unit of  $\beta$  is in arc rather than degrees, so there is a factor of  $\pi/180$ .
- 19 N. Toshima and O. Ihata, *Synth. Met.* **1996**, 79, 165.
- 20 (a) M. G. Kanatzidis, C.-G. Wu, H. O. Marcy and C. R. Kannewurf, *Adv. Mater.* **1990**, 2, 364. (b) M. G. Kanatzidis, H. O. Marcy, W. J. McCarthy, C. R. Kannewurf and T. J. Marks, *Solid State Ionics*, **1989**, 32-33, 594. (c) C.-G. Wu, M. G. Kanatzidis, H. O. Marcy, D. C. DeGroot and C. R. Kannewurf, *Polym. Mat. Sci. Eng.* **1989**, 61, 969. (d) M. G. Kanatzidis, C.-G. Wu, H. O. Marcy, D. C. DeGroot, C. R. Kannewurf, *Chem. Mater.* **1990**, 2, 222.

- 21 Freshly restacked WS<sub>2</sub> was carefully prepared for the inductively coupled plasma (ICP) analysis by stirring and washing the LiBH<sub>4</sub>, LiH and LiWS<sub>2</sub> mixture in water 6 times, similar to the procedure used for the Li<sub>x</sub>MoS<sub>2</sub> ICP sample described in Chapter 1. ICP showed Li 0.383 wt% and S 23.0 wt%, which suggest a formula Li<sub>0.15</sub>MoS<sub>2</sub>. The amount of W was not analyzed because of the lack of W standard.
- 22 H.-L. Tsai, L. Wang and M. G. Kanatzidis, paper in preparation.
- 23 F. Wypych and R. Schöllhorn *J. Chem. Soc., Chem. Commun.* **1992**, 19, 1386.
- 24 (a) R. Bissessur, *Synthesis and Characterization of Novel Intercalation Compounds of Molybdenum Trioxide and Molybdenum Disulfide*, Ph. D. Dissertation, Department of Chemistry, Michigan State University, **1994**, pp 186. (b) idib, pp 183 and 193.
- 25 Annual Book of ASTM Standards **1979**, E-698, pp 601-608.
- 26 H.-L. Tsai, J. Heising, J. L. Schindler, C. R. Kannewurf and M. G. Kanatzidis, *Chem. Mater.* **1997**, 9, 879.
- 27 The room temperature electrical conductivity data listed in Table 3 were measured at Michigan State University. Although the data are a little different from the room temperature values of the variable temperature conductivity measurements, because of the differences in sample, instrument and manipulation, the set of data in this table should be comparable among themselves..
- 28 J. Heising, *Synthesis and Characterization of Novel Intercalation Compounds of Molybdenum Trioxide and Molybdenum Disulfide*, Ph. D. Dissertation, Department of Chemistry, Michigan State University, **1999**.
- 29 In the calculation to obtain the value 27.9 Å<sup>2</sup>, 7.76 Å rather than 7.8 Å was used to avoid too much approximation and too few significant figures.
- 30 2H-MoS<sub>2</sub> has a hexagonal structure (P6<sub>3</sub>/mmc): a=3.161 Å, c=12.295 Å; a MoS<sub>2</sub> unit occupies 8.653 Å<sup>2</sup>: P. Villars and L. D. Calvert,



*Pearson's Handbook of Crystallographic Data for Intermetallic Phases, 2nd Ed., Vol. 4, 1991, ASM International, Materials Park, OH 44073, pp 4445. (cited from: B. Schönfeld, J. J. Huang and S. C. Moss, Acta Crystallogr., Sec. B, 1983, 39 B, 404.)*



## Chapter 3

### LAMELLAR TaS<sub>2</sub>/POLYMER NANOCOMPOSITES THROUGH ENCAPSULATIVE PRECIPITATION OF EXFOLIATED LAYERS

#### Introduction

Two-dimensional inorganic/polymeric nanocomposites represent an important and growing class of hybrid materials with interesting physical properties. The research and development activity is concentrated mainly in two major fields, nanocomposites as structural materials [1] and as electro-active materials [2]. To synthesize two-dimensional nanocomposites, the insertion of polymers inside the layered hosts is the critical step. Polymers can be sandwiched between the galleries of the layered materials through one of four currently known approaches: (a) by monomer intercalation and subsequent polymerization in the galleries, (b) by *in situ* intercalative polymerization, (c) by direct polymer insertion and (d) by encapsulative precipitation of polymers from solutions of exfoliated lamellar solids. The latter two methods produce nanocomposites with preformed and well characterized polymers, and are capable of producing large varieties. The direct polymer insertion approach works well with organically modified aluminosilicates, or clays [1]. On the other hand, the encapsulative precipitation method, which has been developed in our laboratory, has been successful in making nanocomposites with electro-active layered hosts [3]. In this method, the layered host exfoliates to give monolayers in solution, which interact with dissolved polymer chains and encapsulate them during a restacking process. This approach has led to the synthesis of MoS<sub>2</sub> [3a], MoO<sub>3</sub> [3b] and NbSe<sub>2</sub> [3c] nanocomposites with various

polymers in our group, MoO<sub>3</sub>/poly(ethylene oxide) (MoO<sub>3</sub>/PEO) nanocomposites in Nazar's group [4], and MoS<sub>2</sub>, MoSe<sub>2</sub>, TiS<sub>2</sub>, TaS<sub>2</sub>, MoO<sub>3</sub> and MPS<sub>3</sub> nanocomposites with PEO [5a] and/or polyethylenimine (PEI) [5b] in Lerner's group.

Here we report the synthesis of TaS<sub>2</sub>/polymer nanocomposites through the encapsulative precipitation method [6, 7]. The encapsulation of PEO, PEI and poly(vinylpyrrolidinone) (PVP) into TaS<sub>2</sub> were examined in detail and the nanocomposites were characterized by a large variety of techniques. Most of all, our discovery about the different characters of various forms of Li<sub>x</sub>TaS<sub>2</sub> in exfoliation and polymer intercalation is extremely valuable to the synthesis of intercalative TaS<sub>2</sub> complexes. The difference between PEI and other polymers, and the subtleties of the exfoliation and encapsulation of exfoliated TaS<sub>2</sub> will be elucidated in this chapter.

The exfoliation of TaS<sub>2</sub> has long been known [8, 9, 10] and cations of many sizes have been encapsulated between the layers of this material. Early work in this area showed that electrolytically prepared H<sub>x</sub>TaS<sub>2</sub> could be monodispersed in aqueous surfactant solutions and formed adsorption complexes with cationic dyes [8]. Later, chemically prepared Na<sub>x</sub>TaS<sub>2</sub> was dispersed in water or NMF/water mixtures and cluster cations were included inside to form ordered intercalation compounds [10b].

Cation intercalation is driven more or less by cation exchange, which does not require an exfoliated solid [11]. Neutral polymer intercalation, however, needs a different driving force, for example, polymer-Li<sup>+</sup> interactions and/or polymer-TaS<sub>2</sub> van der Waals interaction. The intercalation of polymers most probably takes advantage of the affinity of

the polymer chains for the interlayer surface of the host and for the cations (*i.e.*  $\text{Li}^+$ ) in the interlayer galleries.

Given that some metal dichalcogenides become superconductors at low temperatures, it is intriguing to consider polymer nanocomposites containing superconductive components. Such materials would combine the superconducting properties of inorganic solids with the processible properties of polymers giving rise to new forms of superconductors such as polymer matrix-based wires and free standing films, thus enabling new kinds of applications. We have made a first step in this direction by inserting polymers into  $\text{NbSe}_2$  and  $\text{TaS}_2$  to produce lamellar inorganic/polymer superconducting solids with plastic-like characteristics. This work is an outgrowth of our studies of intercalative polymer nanocomposites of  $\text{MoS}_2$  [3a] using the exfoliation procedure [12]. Remarkably, the flexible metallic  $\text{TaS}_2$ /polymer nanocomposites display bulk superconductivity.

## Experimental Section

### 1. Reagents

PEO (5,000,000), PEO (100,000), PEI (25,000) and PVP (10,000) were purchased from Aldrich Chemical Company, Inc. After the polymers were dissolved, the polymer solutions were filtered to purify from insoluble polymer residues.  $\text{LiBH}_4$  (95%),  $\text{LiOH}\cdot\text{H}_2\text{O}$  (98%) and Ta (99.9%, 325 mesh) were also purchased from Aldrich. Sublimed sulfur was from Spectrum Chemical Mfg. Co. Anhydrous ether (99.0%), acetonitrile (99.5%) isopropanol (99.9%) and carbon disulfide (100%) were from Columbus Chemical Industries Inc., EM Science Inc.,

Mallinckrodt Chemical Inc. and J. T. Baker Inc. respectively. No further purification was applied to the chemicals above. The water was distilled and degassed by bubbling nitrogen through it for 30 min before use.

## 2. Synthesis of 2H-TaS<sub>2</sub>

2H-TaS<sub>2</sub> was synthesized with a modified literature procedure [13]. An amount of 3.619 g of tantalum (20 mmol) and 1.300 g of sulfur (40.5 mmol) sealed in a quartz tube was heated at 450 °C for 12 h and then 950 °C for 36 h. The quartz tube was 13 mm in diameter and ~13 cm long with a volume of about 12-14 ml. The tube was quenched from 950 °C in cold water and excess sulfur was deposited on the tube walls. The 1T-TaS<sub>2</sub> formed was ground and washed with CS<sub>2</sub> to remove any excess sulfur. The purified 1T-TaS<sub>2</sub> was transformed to 2H-TaS<sub>2</sub> by an annealing procedure of slow cooling from 910 to 450 °C in two weeks, according to the protocol shown in Table 3.1.

Table 3.1. The annealing procedure to produce 2H-TaS<sub>2</sub>

|                   |     |     |     |     |     |
|-------------------|-----|-----|-----|-----|-----|
| temperature (°C)  | 910 | 750 | 650 | 550 | 450 |
| time to reach (h) | 12  | 16  | 20  | 20  | 20  |
| time to hold (h)  | 12  | 24  | 48  | 72  | 72  |

## 3. Synthesis and Exfoliation of Li<sub>x</sub>TaS<sub>2</sub>

An amount of 4.00 g 2H-TaS<sub>2</sub> was reacted with n equivalents of LiBH<sub>4</sub> (n = 0.1, 0.2, 0.3, 0.4, 0.5, and 1.0) in 100 ml of anhydrous ether for 3 days under a nitrogen atmosphere to obtain Li<sub>x</sub>TaS<sub>2</sub>. Li<sub>x</sub>TaS<sub>2</sub> was

black when  $n = 0.1, 0.2$  and  $0.3$ , while it was reddish brown when  $n \geq 0.4$  [14].

$\text{Li}_x\text{TaS}_2$  was exfoliated in degassed water, in a concentration of  $1.0$  g/L, by  $30$  min of sonication in an ultrasonic cleaner under a nitrogen atmosphere. When  $n = 0.1$ , not much of  $\text{Li}_x\text{TaS}_2$  was exfoliated in water. The suspension was slightly yellowish black. When  $n = 0.2$  or  $0.3$ , most of the  $\text{Li}_x\text{TaS}_2$  went into water. Especially in the case of  $n = 0.2$ , the amount of unexfoliated  $\text{Li}_x\text{TaS}_2$  was very small ( $\sim 2.6\%$ ) and the colloidal suspension had an intense greenish yellow color. When  $n \geq 0.4$ , the  $\text{Li}_x\text{TaS}_2$  became increasingly difficult to exfoliate. The color of the resulting suspension ranged from brownish yellow to reddish brown. The higher the value of  $n$ , the lighter the color of the suspension. Therefore,  $\text{Li}_x\text{TaS}_2$  from reactions with  $n=0.2$  was chosen as the host material for polymer intercalation.  $\text{Li}_{0.2}\text{TaS}_2$  is used to present this form of  $\text{Li}_x\text{TaS}_2$  for convenience [15].

#### 4. Encapsulative Precipitation of Polymers

In a typical reaction,  $0.40$  g of  $\text{Li}_{0.2}\text{TaS}_2$  was exfoliated in  $400$  ml of degassed  $\text{H}_2\text{O}$  by  $30$  min of sonication. The resulting suspension was mixed with  $100$  ml of polymer solution ( $5$  or  $10$  times in excess by equivalents of repeat units) and stirred for  $2$  days under a nitrogen atmosphere. The supernatant of the reaction mixture was centrifuged. A half part of the polymer intercalated  $\text{TaS}_2$  was separated from the solution by centrifugation and is referred to as batch-I nanocomposite. The centrifuged supernatant was pumped to remove most of the water. A corresponding solvent (acetonitrile for PEO and isopropanol for PVP and PEI) was added to the concentrated supernatant to precipitate the intercalated  $\text{TaS}_2$

remaining in the supernatant. This precipitate is referred to as batch-II nanocomposite. The products were pumped to dryness and vacuum-sealed in glass ampules.

## 5. Instrumentation and Measurements

### a. Instrumentation

The instrumentation in the measurements such as thermal gravimetric analysis (TGA), differential scanning calorimetry (DSC) and infrared (IR) spectroscopy were the same as described in Chapter 1. Room temperature conductivity measurements, variable temperature direct-current electrical conductivity measurements and thermopower measurements, and magnetic susceptibility measurements were conducted as described in Chapter 2.

Generally, X-ray powder diffraction (XRD) patterns were collected as described in Chapter 1. For one-dimensional electron density calculations, we obtained XRD data (in the region  $2^\circ \leq 2\theta \leq 135^\circ$ ) from highly oriented samples and a stepwise scanning mode with  $0.1^\circ$  per step. Variable temperature solid state  $^7\text{Li}$  NMR spectra were taken on a 400 MHz Varian Nuclear Magnetic Resonance Instrument. Samples were loaded in a glove box under a nitrogen atmosphere.

Scanning electron microscopy (SEM) and energy dispersive X-ray microanalysis (EDS) were done with JEOL-JSM 35 CF microscope at an accelerating voltage of 15 kV and 20 kV respectively, at the Center for Electron Optics at MSU. Samples were mounted on the sample stub with a conductive tape. Electron diffraction was done on a transmission electron microscope (TEM) JEOL-100CX at 120 kV, at the Center for Electron Optics. Samples were ground and suspended in water or acetone before

deposition on copper grids. Gold film deposited on a copper grid was used as standard in the calibration of camera length.

b. Composition of nanocomposites

The amount of polymer in the nanocomposites was estimated by TGA in oxygen flow. For comparison, the weight loss of  $\text{Li}_{0.2}\text{TaS}_2$  in oxygen flow was checked by TGA up to 800 °C and was found to be about 8.2% [16]. The amount of polymer and water in the nanocomposites was calculated assuming that the  $\text{Li}_{0.2}\text{TaS}_2$  in the nanocomposites lost the same amount of weight. The final product from the TGA in an oxygen flow was mainly  $\text{Ta}_2\text{O}_5$ , which was confirmed by XRD and IR spectra, however, it probably also contains some  $\text{Li}_2\text{SO}_4$  [17].

In TGA measurements under either oxygen or nitrogen flow, the nanocomposites barely lost weight at a temperature lower than 190 °C (< 0.5% for batch-I nanocomposites and < 2.5% for batch-II nanocomposites), suggesting they contain almost no water. The major weight loss step for all the nanocomposites occurred between 200 °C to 350 °C and corresponds to polymer decomposition.

c. One-dimensional electron density measurements

One-dimensional electron density (1-D ED) maps were calculated according to XRD data collected from highly oriented film samples in a stepwise scanning mode. These film samples were made by casting aqueous nanocomposite solutions under a nitrogen flow, so that the basal planes of the  $\text{TaS}_2$  layers restacked parallel to the substrate. Several layers of a film were loaded in the sample plate so as to obtain maximum diffraction intensity. The XRD experiments were carried out under a nitrogen

atmosphere. In the measurements, slits for different beam width, as well as different data collection times, were used for different  $2\theta$  ranges, in order to achieve a compromise between peak broadening, peak intensity and experiment time. Specifically,  $0.5^\circ$  slits and a data collection time of 3 s per step were chosen for measurements in the range from  $2^\circ$  to about  $40^\circ$ ;  $1.0^\circ$  slits and 3 s per step between  $26^\circ$  and  $70^\circ$ ;  $2.0^\circ$  slits and 60 s per step between  $59^\circ$  and  $120^\circ$ ;  $4.0^\circ$  slits and 60 s per step from  $101^\circ$  to  $135^\circ$ . The step width was kept the same ( $0.1^\circ$ ) in the entire  $2\theta$  range.

A full range XRD pattern ( $2^\circ \leq 2\theta \leq 135^\circ$ ) was obtained by merging the data from the different  $2\theta$  ranges and normalizing (scaling) them based on the overlapped regions. The overlapped data regions had at least two peaks in common. The full data set was put into an XRD analysis program, PEAKOC [18], to calculate the integrated peak area of each  $00l$  reflection. In pattern analysis,  $00l$  peaks were fit with the split-pseudo-Voigt function with a linear background subtraction for each peak. In the case that an  $00l$  peak overlapped a little with another peak, or was cut off at the end of the pattern, it was fit with the pseudo-Voigt function (which is symmetric).

The integrated peak area of the  $00l$  peaks was used as the intensity of the peaks, and put in a FORTRAN program to calculate the 1-D ED map. The absolute value of the structure factor  $F$  of the  $00l$  reflections was calculated from the intensities and the Lorentz-polarization factor ( $L_p$ ) according to (1).

$$|F(l)| = (I/L_p)^{1/2} \quad (1)$$

The Lorentz-polarization factor ( $L_p$ ) is defined as:

$$L_p = (1 + \cos^2 2\theta) / (\sin^2 \theta \cos \theta) \quad (2)$$

The signs (phases) of the structure factors were assigned based on the signs of the corresponding structure factors of the TaS<sub>2</sub> framework alone. This reasonably assumes that the scattering contribution from the intercalated polymer is relatively small compared to that of TaS<sub>2</sub> component. The 1-D ED map was calculated from the structure factors of the *00l* reflections according to (3).

$$\rho(z) = (1/L) [ F_0 + 2 \sum_l F(l) \cos(2\pi lz) ] \quad (3)$$

In (3), *z* is the fractional coordinate on the *c* axis, *L* is the basal spacing of the layered structure, and *F*<sub>0</sub> is the zeroth-order structure factor.

To obtain their signs, the structure factors of the TaS<sub>2</sub> framework were calculated from:

$$F_{\text{cal}}(l) = \sum_{j=1}^N 2f_j(l) \cos(2\pi lz_j) \quad (4)$$

The scattering factor *f<sub>j</sub>(l)* for atom *j* was calculated according to (5) with *a<sub>i</sub>*, *b<sub>i</sub>* and *c* for the element obtained from literature [19], and *θ* corresponding to the reflection position.

$$f_j(\theta) = \left[ \sum_{i=1}^4 a_i \exp\left(-\frac{b_i \sin^2 \theta}{\lambda^2}\right) + c \right] \exp\left(-\frac{B \sin^2 \theta}{\lambda^2}\right) \quad (5)$$

After the model for the structure was established, the sign of the *F(l)* was checked by recalculating *F<sub>cal</sub>(l)* from the scattering of the atoms including those of the polymer.

## Results and Discussion

### 1. Exfoliation Properties of $\text{Li}_x\text{TaS}_2$

$\text{Na}_x\text{TaS}_2$ , as reported previously, did not form ideal suspensions in water, so formamide (FM), N-methylformamide (NMF) or NMF/ $\text{H}_2\text{O}$  1:1 mixture were used to produce concentrated suspensions [9, 10b]. FM and NMF are not preferred for the intercalation of polymers, because not only they are expensive and toxic, they also compete with the polymers and co-intercalate in the host. In order to be able to use  $\text{TaS}_2$  as a polymer host we needed a material which exfoliates well in water. Therefore, we explored the swelling and exfoliation properties of  $\text{Li}_x\text{TaS}_2$  as a function of  $x$ .  $\text{Li}_x\text{TaS}_2$  with different degrees of lithiation was prepared under different conditions, through (a) reaction with butyllithium in hexane, (b) reaction with sodium dithionate in water followed by ion exchange with  $\text{Li}^+$  ions, and (c) reaction with  $\text{LiBH}_4$  in ether in various stoichiometric ratios and conditions. The  $\text{LiBH}_4$  method [20] was most successful. We found that the best  $\text{Li}_x\text{TaS}_2$  suspension was obtained with  $x \sim 0.2$ . Namely,  $\text{Li}_{0.2}\text{TaS}_2$  formed concentrated and stable colloidal single layer solutions in water, superior to those formed with  $\text{Na}_x\text{TaS}_2$  in NMF/ $\text{H}_2\text{O}$  solution.

In all cases, there was always a fraction of  $\text{Li}_x\text{TaS}_2$  which did not exfoliate, regardless of how dilute the solution was. Usually, the more readily the  $\text{Li}_x\text{TaS}_2$  exfoliates, the more concentrated suspension it forms and the less residue it leaves behind. To demonstrate how the amount of the  $\text{LiBH}_4$ , in the lithiation reaction, affected the exfoliation of  $\text{Li}_x\text{TaS}_2$ , a semi-quantitative experiment was performed with 0.050 g  $\text{Li}_x\text{TaS}_2$  with  $n = 0.1, 0.2, 0.3$  and  $0.4$  [14]. After  $\text{Li}_x\text{TaS}_2$  was sonicated in 200 ml degassed water for 30 min, the precipitates were collected, dried and weighed. Based



on the  $\text{Li}_x\text{TaS}_2$  used, the unexfoliated fraction was 53%, 2.6%, 21% and 21% respectively for  $\text{Li}_x\text{TaS}_2$  with  $n = 0.1, 0.2, 0.3$  and  $0.4$ . These results showed that 0.1 equivalent of  $\text{LiBH}_4$  was not enough, while 0.3 or 0.4 equivalent of  $\text{LiBH}_4$  were over the optimum ratio. It needs to be pointed out that the charge density of  $\text{Li}_{0.2}\text{TaS}_2$ ,  $\sim 48 \text{ \AA}^2/e^-$  [21], is close to the up limit of the  $40 - 120 \text{ \AA}^2/e^-$  range [22], in which stable colloidal dispersions are most likely to form.

$\text{Li}_x\text{TaS}_2$  used by Oriakhi et al [5b] to prepare the PEI/ $\text{TaS}_2$  nanocomposite was lithiated by reacting with  $\text{LiOH}$  [23]. Our investigation into that lithiation reaction reveals that control of the amount of  $\text{LiOH}$  is equally important and the optimum stoichiometric ratio is approximately the same.

## 2. Polymer Encapsulation

The success of polymer encapsulation depends on the nature of both  $\text{Li}_x\text{TaS}_2$  and polymer. Table 3.2 shows which attempts succeeded or failed in the preparation of nanocomposites. PEO was intercalated only in “ $\text{Li}_{0.2}\text{TaS}_2$ ”. PVP was intercalated in  $\text{Li}_x\text{TaS}_2$  prepared with  $0.2 < x < 0.4$ . PEI has the most affinity for  $\text{Li}_x\text{TaS}_2$  and intercalated in all  $\text{Li}_x\text{TaS}_2$  samples [24]. This must be due to the fact that PEI is a strong organic base which could be protonated in solution. The protonated PEI has positive charges which facilitate (through electrostatic attraction) the interaction with the  $[\text{TaS}_2]^{x-}$  layers. In this sense, the insertion of PEI in  $[\text{TaS}_2]^{x-}$  is an ion-exchange process where  $\text{Li}^+$  ions are replaced with positively charged PEI molecules. Other polymers such as polyacrylamide (PAM) and methyl cellulose (MCell) were also tried, with partial intercalation achieved with PAM and no intercalation with MCell.

Table 3.2. Polymer Intercalation in  $\text{Li}_x\text{TaS}_2$

|       | intercalation of polymers |     |     |
|-------|---------------------------|-----|-----|
|       | PEI                       | PVP | PEO |
| n=0.1 | Yes                       | No  |     |
| n=0.2 | Yes                       | Yes | Yes |
| n=0.3 | Yes                       | Yes |     |
| n=0.4 | Yes                       | Yes | No  |
| n=0.5 | Yes                       | No  |     |
| n=1.0 | Yes                       |     | No  |

\* "Yes" indicates that the intercalation was successful, while "No" shows that the intercalation failed.

### 3. Characterization of $\text{Li}_x\text{TaS}_2$ /Polymer Nanocomposites

The formation of lamellar  $\text{Li}_x\text{TaS}_2$ /polymer nanocomposites was evident in the XRD patterns of the products. The presence and position of  $00l$  reflections indicated the separation of the  $\text{TaS}_2$  slabs, which is evidence for the insertion of polymer chains. The pristine  $\text{TaS}_2$  and the hydrated  $\text{Li}_x(\text{H}_2\text{O})_y\text{TaS}_2$  show interlayer spacings of 6.0 Å and 7.4 Å respectively, which can be readily distinguished from a polymer intercalated phase. The d-spacings of batch-I and batch-II for both PEO and PVP intercalated compounds were comparable within  $\pm 1$  Å. The XRD patterns of the two types of products were similar, except that in the former type (batch-I) we could observe some weak diffraction peaks from residual un-intercalated solid. In the case of PEI, the d-spacing of batch-I product was about 10.0 Å, while that of batch-II product was about 37 Å indicating the encapsulation of multiple layers of polymer. Some typical XRD patterns of



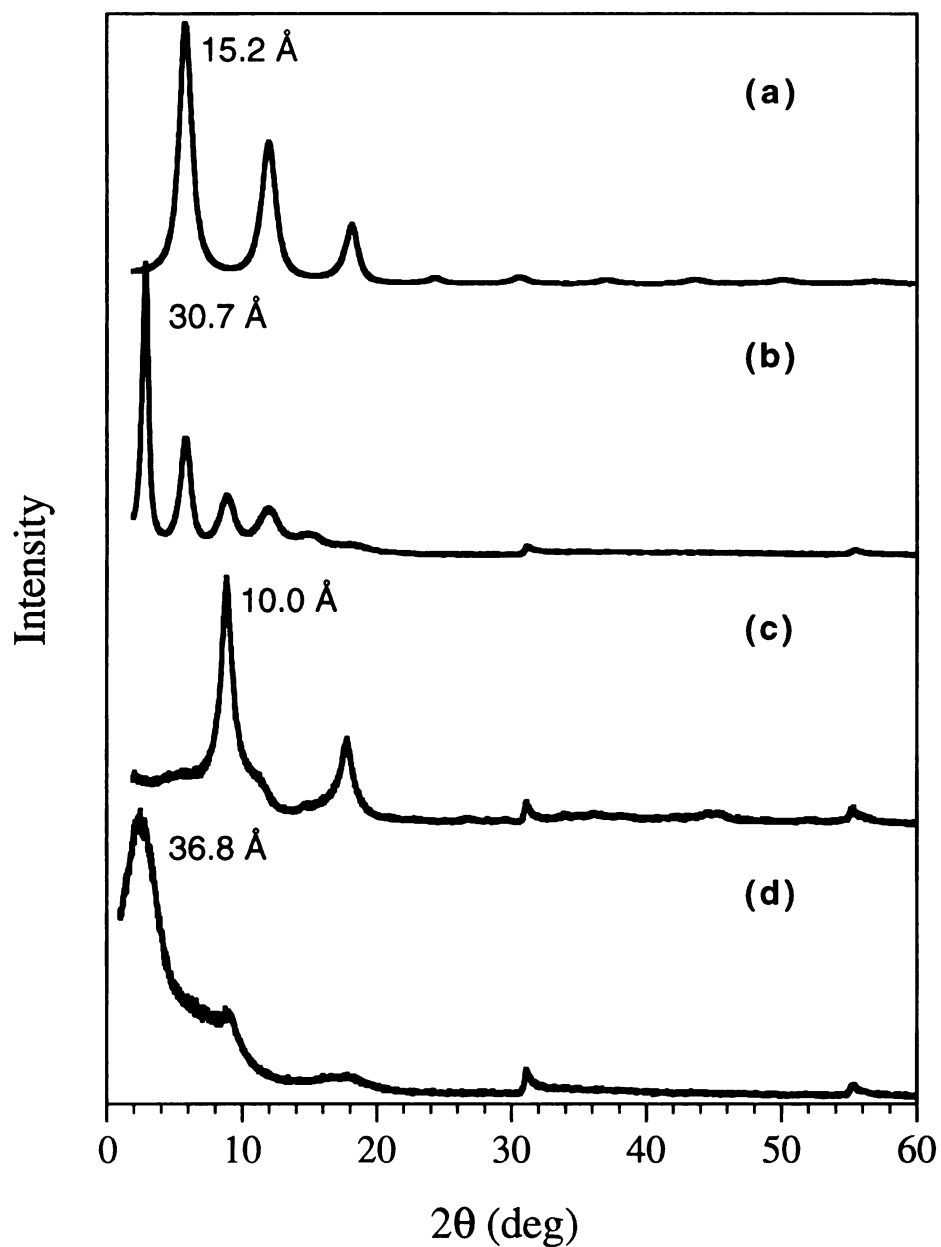


Figure 3.1. XRD patterns of  $\text{Li}_x\text{TaS}_2$ /polymer nanocomposites. (a)  $\text{Li}_{0.2}(\text{PEO})_y\text{TaS}_2$  (batch-II), (b)  $\text{Li}_{0.2}(\text{PVP})_y\text{TaS}_2$  (batch-II), (c)  $\text{Li}_x(\text{PEI})_y\text{TaS}_2$  (batch-I) and (d)  $\text{Li}_x(\text{PEI})_y\text{TaS}_2$  (batch-II).



Table 3.3. Properties of  $\text{Li}_{0.2}\text{TaS}_2$  and polymer nanocomposites

| sample   | d-spacing<br>(Å) | coherence<br>length<br>(Å) | composition   | room<br>temperature<br>conductivity<br>(S/cm) |
|--|------------------|----------------------------|---|---|
| $\text{Li}_{0.2}\text{TaS}_2$                                    | 6.0              |                            |   | $>10^3$                                       |
| Hydrated $\text{Li}_{0.2}\text{TaS}_2$                           | 7.4              |                            |   |   |
| $\text{Li}_{0.2}(\text{PEO})_y\text{TaS}_2$<br>(100K) (batch I)  | 15.6             | 93                         | $\text{Li}_{0.2}(\text{PEO})_{1.36}(\text{H}_2\text{O})_{0.00}\text{TaS}_2$ | 19  |
| $\text{Li}_{0.2}(\text{PEO})_y\text{TaS}_2$<br>(100K) (batch II) | 15.2             | 83                         | $\text{Li}_{0.2}(\text{PEO})_{1.51}(\text{H}_2\text{O})_{0.23}\text{TaS}_2$ | 2.2   |
| $\text{Li}_{0.2}(\text{PEO})_y\text{TaS}_2$<br>(5M) (batch I)    | 15.1             | 106                        | $\text{Li}_{0.2}(\text{PEO})_{0.75}(\text{H}_2\text{O})_{0.06}\text{TaS}_2$ | 17  |
| $\text{Li}_{0.2}(\text{PEO})_y\text{TaS}_2$<br>(5M) (batch II)   | 15.5             | 83                         | $\text{Li}_{0.2}(\text{PEO})_{1.68}(\text{H}_2\text{O})_{0.00}\text{TaS}_2$ | 3.0   |
| $\text{Li}_{0.2}(\text{PVP})_y\text{TaS}_2$<br>(10K) (batch I)   | 31.1             | 256                        | $\text{Li}_{0.2}(\text{PVP})_{0.95}(\text{H}_2\text{O})_{0.08}\text{TaS}_2$ | 31  |
| $\text{Li}_{0.2}(\text{PVP})_y\text{TaS}_2$<br>(10K) (batch II)  | 30.7             | 186                        | $\text{Li}_{0.2}(\text{PVP})_{1.28}(\text{H}_2\text{O})_{0.35}\text{TaS}_2$ | 0.5   |
| $\text{Li}_x(\text{PEI})_y\text{TaS}_2$<br>(25K) (batch I)       | 10.0             | 93                         | $\text{Li}_x(\text{PEI})_{0.82}(\text{H}_2\text{O})_{0.07}\text{TaS}_2$     | 125   |
| $\text{Li}_x(\text{PEI})_y\text{TaS}_2$<br>(25K) (batch II)      | 36.8             | -                          | $\text{Li}_x(\text{PEI})_{3.2}(\text{H}_2\text{O})_{0.56}\text{TaS}_2$      | 0.18  |

\* The X-ray scattering coherence length is determined from the half-width of the peak using Scherrer formula  $L_{hkl} = K \lambda / \beta \cos\theta$ , see Reference 18 of Chapter 2.



the nanocomposites are shown in Figure 3.1. More information about d-spacings and coherence lengths in the direction of layer stacking is listed in Table 3.3. From these, one can estimate the ordered domains in particles of the nanocomposites to be between 5 and 10 TaS<sub>2</sub> layers thick. As the number of layers in the nanocomposite particles is considered, Li<sub>x</sub>(PEI)<sub>y</sub>(H<sub>2</sub>O)<sub>z</sub>TaS<sub>2</sub> (batch I) has the largest value (9.3), Li<sub>0.2</sub>(PVP)<sub>y</sub>(H<sub>2</sub>O)<sub>z</sub>TaS<sub>2</sub> has medium values (6.1-8.2), and Li<sub>0.2</sub>(PEO)<sub>y</sub>(H<sub>2</sub>O)<sub>z</sub>TaS<sub>2</sub> has the smallest values (5.4-7.0). Table 3.3 also lists the compositions of the nanocomposites. It is obvious that a batch-II nanocomposite contains a little more polymer than its batch-I analog. This is understandable because batch-II product was well dissolved in water and reacted more completely with the dissolved polymer.

DSC measurements on a Li<sub>0.2</sub>(PEO)<sub>1.04</sub>TaS<sub>2</sub> showed no phase transition between room temperature and 300 °C, see Figure 3.2.

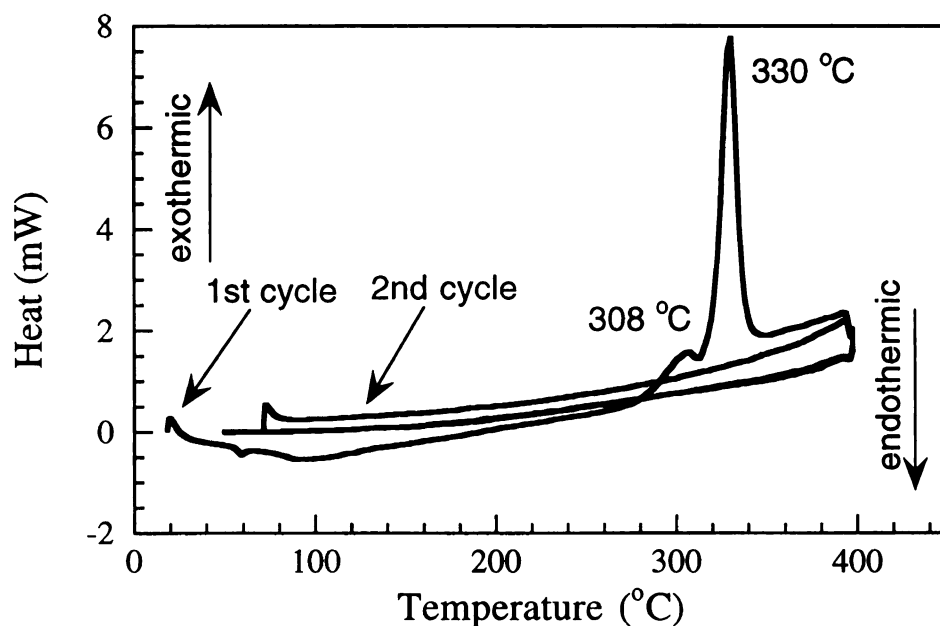


Figure 3.2. DSC of a Li<sub>0.2</sub>(PEO)<sub>y</sub>TaS<sub>2</sub> nanocomposite.

the amount

of

the

of

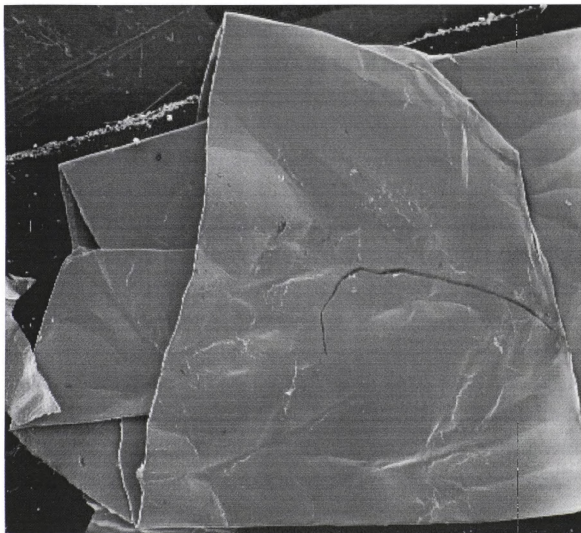


Figure 3.3. SEM photograph of a  $\text{Li}_{0.2}(\text{PEO})_y\text{TaS}_2$  film (batch-II; M.W. = 5M).



The melting peak of PEO at 66 °C is not observed in the nanocomposite. A small exothermic peak at 308 °C (2.21 J/g) and a large one at 330 °C (46.18 J/g) correspond to the decomposition of the PEO in the nanocomposite and are associated with massive weight loss, detected by TGA under nitrogen flow. Pure PEO shows an exothermic decomposition peak around 370 °C.

Mass spectra of the  $\text{Li}_{0.2}(\text{PEO})_{1.04}\text{TaS}_2$  in a temperature increase ramp showed that the major decomposition fragments around 350 °C had molecular masses of 45, 58, 73, 87, 88, 89, 103, 120, 133 and so on, which were all PEO related fragments. There was no obvious evidence that the decomposition fragments combined with sulfur from the  $\text{TaS}_2$  layers [25].

The  $\text{Li}_x\text{TaS}_2/\text{polymer}$  nanocomposites described here can be cast into free-standing films readily. The films of batch-II nanocomposites are stronger than that of batch-I products and can be folded without breaking. This is attributed to the higher polymer content of the batch-II materials. Figure 3.3 shows a photo of a folded  $\text{Li}_{0.2}(\text{PEO})_{1.68}\text{TaS}_2$  film ( batch-II, Mw = 5,000,000) taken on SEM. The film was folded before it was pressed onto the conductive tape. The folding edge did not crack under pressure.

#### 4. Structural Studies: The Conformation of PEO in $\text{Li}_x(\text{PEO})_y\text{TaS}_2$

There are many known PEO chain conformations. The most common is the helical conformation [26] which exists in PEO spherulites [27]. Planar zigzag conformation was obtained in stretched PEO samples [28]. Two kinds of conformations were found in  $\text{PEO-HgCl}_2$  complexes [29, 30]. More PEO conformations have been found in other PEO complexes in literature and they will be described in Chapter 5. Models for the most important PEO conformations will be shown in Figure 5.11.

The conformation and orientation of polymer chains in the interlayer galleries of the layered nanocomposites has always been an important issue. We calculated 1-D ED maps for  $(\text{PEO})_x\text{V}_2\text{O}_5 \cdot n\text{H}_2\text{O}$  [31], and determined that the helical conformation of PEO in that nanocomposite was not possible. A bilayer planar zigzag structure was proposed. In the present case, films of batch-II  $\text{Li}_{0.2}(\text{PEO})_y\text{TaS}_2$  nanocomposite had well defined sharp XRD patterns with seventeen  $00l$  reflections corresponding to a resolution of 0.85 Å, see Figure 3.4. This intense XRD pattern offered a good starting point for 1-D ED calculation for  $\text{Li}_{0.2}(\text{PEO})_y\text{TaS}_2$  nanocomposite, which provides information for the internal structure of the intercalated species projected on the  $c$  axis. As mentioned in the experimental section, the phases for calculating this 1-D ED map were obtained from the positions of the Ta and S atoms which are taken to be known. A 1-D ED map is shown in Figure 3.5d.

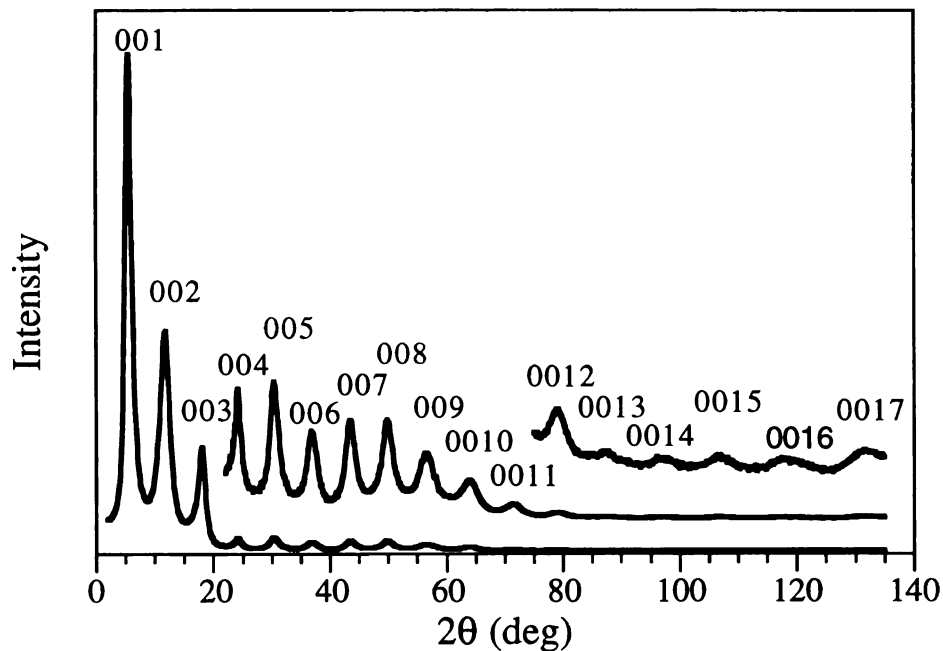


Figure 3.4. Powder XRD patterns of a folded  $\text{Li}_{0.2}(\text{PEO})_y\text{TaS}_2$  film (batch-II; M.W. = 100K).

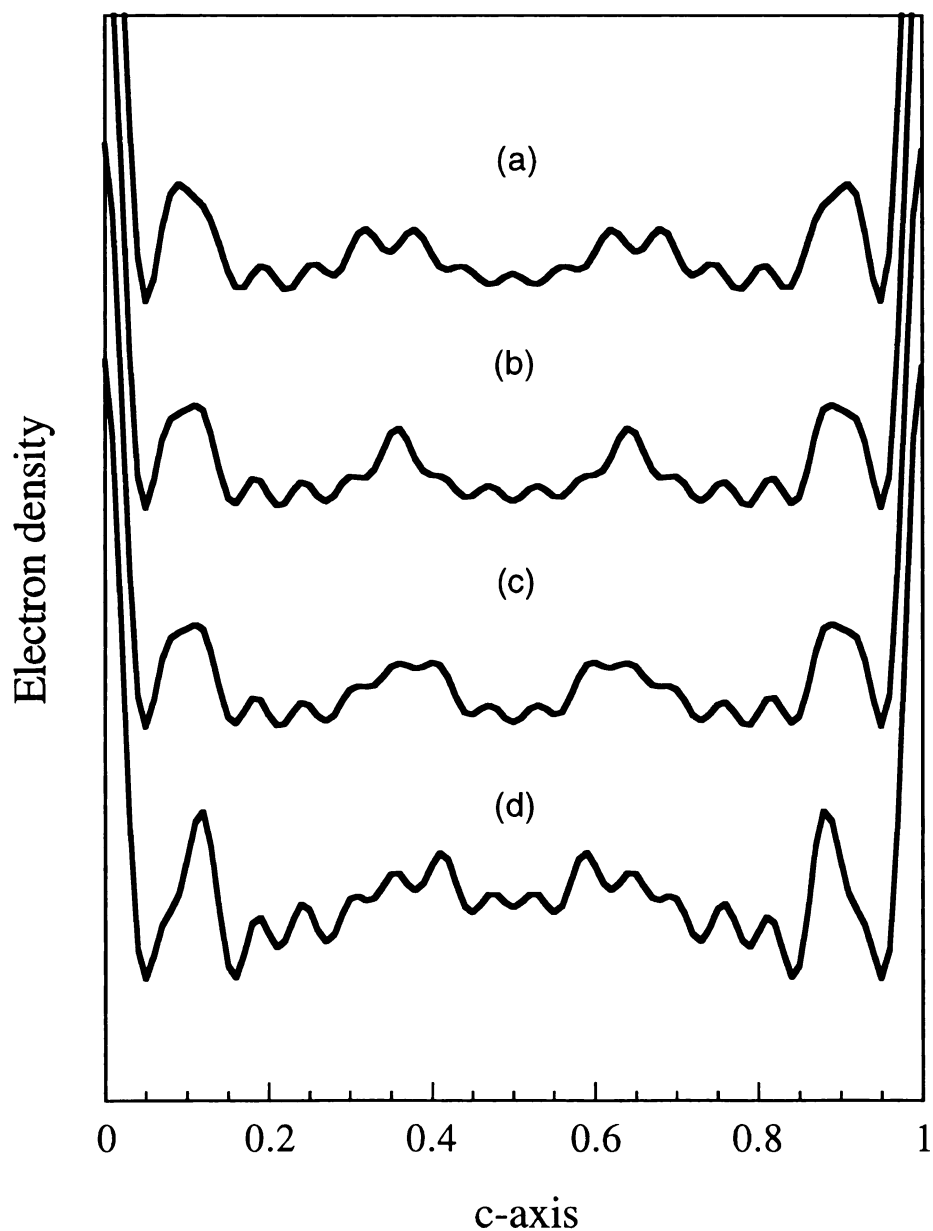


Figure 3.5. One-dimensional electron density maps for the  $\text{Li}_x(\text{PEO})_y\text{TaS}_2$  nanocomposite. (a) Model with two layers of planar zigzag PEO chains while the zigzag planes are perpendicular to the  $\text{TaS}_2$  layers, (b) Model with two layers of planar zigzag PEO chains while the zigzag planes are parallel to the  $\text{TaS}_2$  layers, (c) Model with two layers of PEO in the type II PEO- $\text{HgCl}_2$  complex conformation, and (d) Computed from experimental data.

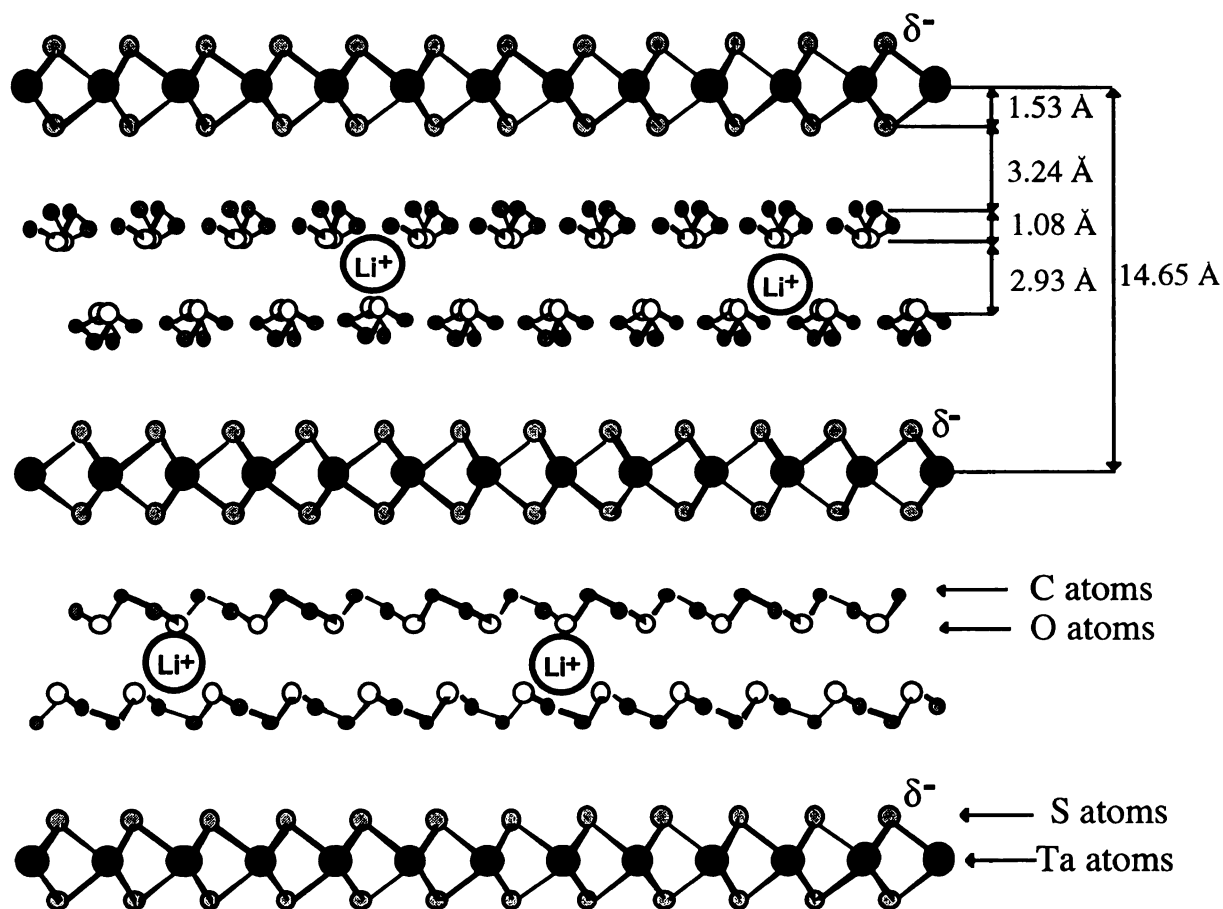


Figure 3.6. Structural model for the  $\text{Li}_{0.2}(\text{PEO})_y\text{TaS}_2$  nanocomposite. The oxygen atom region in the middle of the gallery accommodates the  $\text{Li}^+$  ions.



The profile of 1-D ED map of  $\text{Li}_{0.2}(\text{PEO})_y\text{TaS}_2$  shows clearly the presence of substantial electron density between the  $\text{TaS}_2$  peaks. This density is due to the organic polymer and it is distributed away from the center of the gallery, peaking in two separate locations symmetrically above and below the gallery central plane. The peak shape in each location is asymmetric. This immediately excludes the helical conformation of PEO, which must have one symmetric envelop of electron density in the central region of the gallery.

The observed profile in the  $\text{Li}_{0.2}(\text{PEO})_y\text{TaS}_2$  is also different from that of the  $(\text{PEO})_x\text{V}_2\text{O}_5 \cdot n\text{H}_2\text{O}$  system which displays two symmetric bumps with two maxima on each of them, so the planar zag-zig model does not fit here. Figures 3.5a and 3.5b present the profiles of the 1-D ED map calculated for two layers of planar zigzag PEO chains arranged parallel and perpendicular inside the gallery space of  $\text{TaS}_2$  [32]. As expected, they have two symmetric bumps and their maxima are too far apart to match the profile calculated from XRD data of  $\text{Li}_{0.2}(\text{PEO})_y\text{TaS}_2$ .

The structural model best matching the experimental data is set up with two layers of PEO with the conformation found in the type II PEO- $\text{HgCl}_2$  complex. This conformation has oxygen atoms on one side and carbon and hydrogen atoms on the other side of the molecule. By putting two layers of PEO inside the gallery so that the oxygen atoms face each other in the middle of the gallery, as shown in the model in Figure 3.6, two asymmetric bumps appear in the electron density map and the positions of the atoms can be decided by fitting maxima of the bumps (see Figure 3.5c). In this model, the atoms of PEO occupy reasonable positions in the gallery. In addition, the orientation of the PEO chains is chemically plausible because the hydrophobic part of the PEO ( $-\text{CH}_2-\text{CH}_2-$  groups) forms van



der Waals contacts with the sulfur atoms in the TaS<sub>2</sub> layers and the oxygen atoms form a more polar, hydrophilic environment in which, presumably, the small Li<sup>+</sup> cations reside. This model not only matches the experimental data very well, it also makes good chemical sense. The type II PEO-HgCl<sub>2</sub> complex conformation proposed here is probably brought about by coordinating interactions of PEO with the Li<sup>+</sup> ions, just as for the HgCl<sub>2</sub> complex. That the PEO conformation in Li<sub>x</sub>(PEO)<sub>y</sub>TaS<sub>2</sub> is different from that of (PEO)<sub>x</sub>V<sub>2</sub>O<sub>5</sub>·nH<sub>2</sub>O [29] is attributed to the lack of coordinating ions (e.g. Li<sup>+</sup>) in the latter.

## 5. Superconductive State

The magnetic properties of Li<sub>x</sub>TaS<sub>2</sub> and nanocomposites were measured with a SQUID. As observed earlier with the NbSe<sub>2</sub> system [3c], the lamellar nanocomposites reported here undergo superconducting transitions at temperatures higher than that of the pristine 2H-TaS<sub>2</sub>, 0.6 K (or 0.8 K according to different publications). It is known that the T<sub>c</sub> of TaS<sub>2</sub> is pushed down by the periodic lattice distortion-charge density wave (PLD-CDW) of TaS<sub>2</sub>. If the PLD-CDW is suppressed, the T<sub>c</sub> could be raised to 4.1-4.5 K. In fact 0.08 equivalents of electrons are enough to suppress the PLD-CDW in TaS<sub>2</sub> [33, 34]. Therefore in the Li<sub>x</sub>TaS<sub>2</sub> we expect a higher T<sub>c</sub>. The Cooper pairs in the superconductive state have a coherence length in the magnitude of a micron. This spatial correlation length is much longer than the gallery space in the Li<sub>x</sub>TaS<sub>2</sub>/polymer nanocomposites which is occupied by the insulating polymer chains. The Cooper pairs can penetrate the barrier of the polymer layers and move around in the nanocomposites, so the intercalation of polymers (at least up to a certain expansion of the TaS<sub>2</sub> layers) does not destroy the

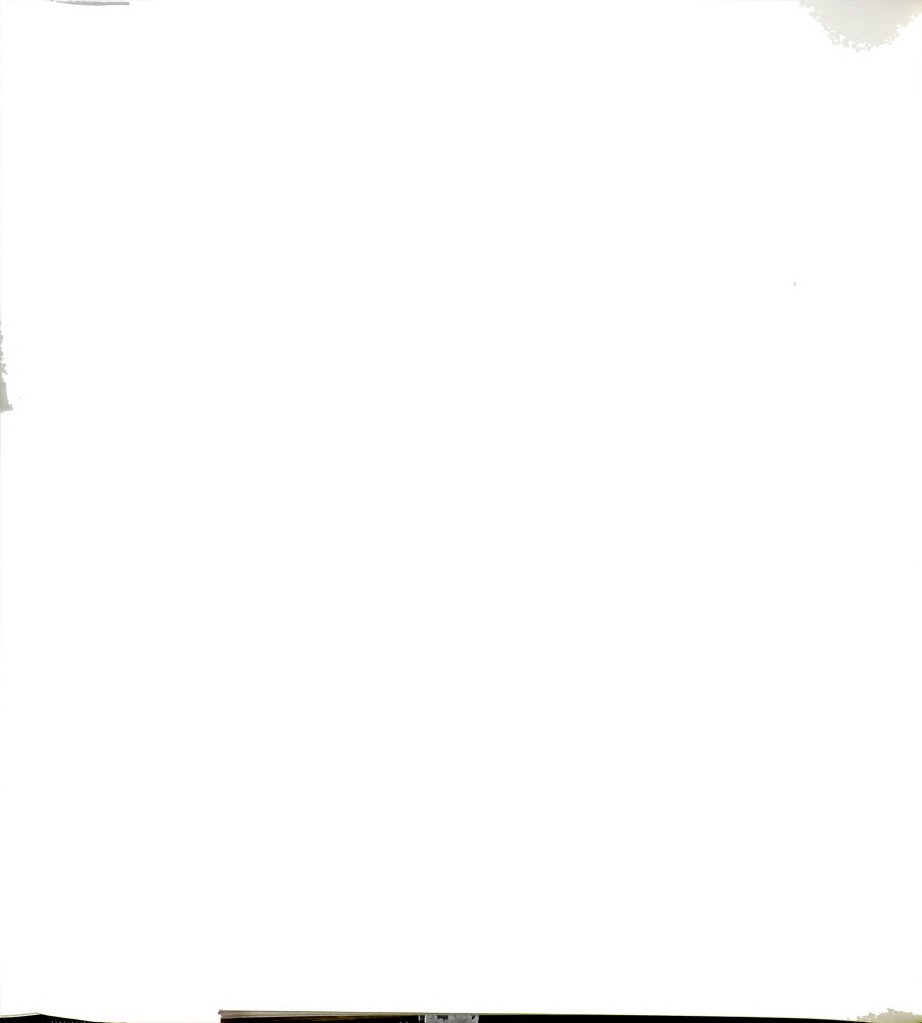
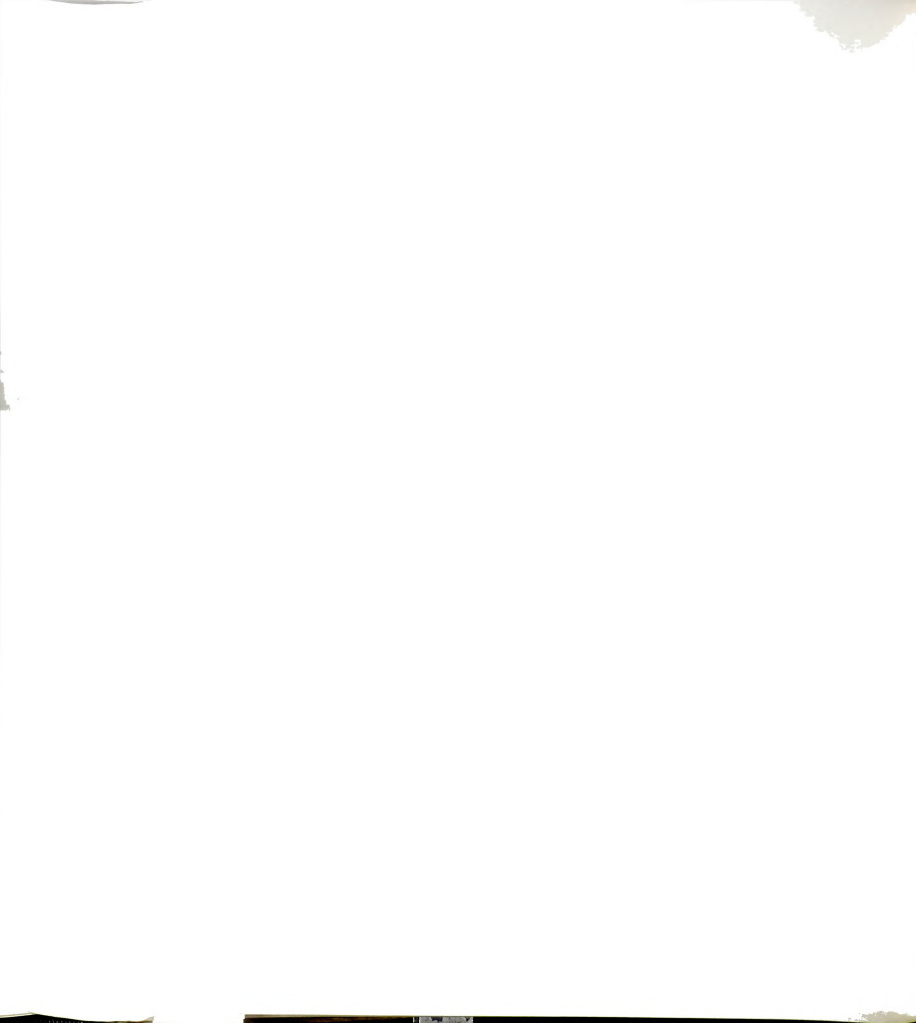


Table 3.4. Properties of the superconductive state for TaS<sub>2</sub> intercalates

| sample   | sample state       | T <sub>c</sub> (K) | $\chi_{\text{molar}}$ (2K,5G) | percentage of pure superconductor |
|--|--------------------|--------------------|-------------------------------|-----------------------------------|
| Li <sub>x</sub> TaS <sub>2</sub> (n=0.2)                         | powder             | 3.7, 4.3           | -2.64                         | 82                                |
| Li <sub>x</sub> TaS <sub>2</sub> (n=0.4)                         | powder             | 4.1, 4.6           | -0.128                        | 4.0                               |
| Li <sub>x</sub> TaS <sub>2</sub> (n=0.5)                         | powder             | 2.7, 4.3           | -1.1*10 <sup>-3</sup>         | 3.4*10 <sup>-2</sup>              |
| Li <sub>x</sub> (PEI) <sub>y</sub> TaS <sub>2</sub> (batch I)    | powder             | 2.9                | -0.60                         | 14                                |
| Li <sub>0.2</sub> (PVP) <sub>y</sub> TaS <sub>2</sub> (batch I)  | powder             | 2.5                | -0.82                         | 5.8                               |
| Li <sub>0.2</sub> (PEO) <sub>y</sub> TaS <sub>2</sub> (batch I)  | film parallel      | 2.7                | -0.17                         |                                   |
|  | film perpendicular | 2.6                | -2.7                          | 42                                |
| Li <sub>0.2</sub> (PEO) <sub>y</sub> TaS <sub>2</sub> (batch II) | film parallel      | 2.9                | -5.6*10 <sup>-3</sup>         |                                   |
|  | film perpendicular | 2.9                | -5.8*10 <sup>-2</sup>         | 0.9                               |

\* Densities of the materials are needed in the calculation. The density of 2H-TaS<sub>2</sub>, 6.075 g/cm<sup>3</sup> is used in the calculation of Li<sub>x</sub>TaS<sub>2</sub> (n=0.2, 0.4 and 0.5). The densities deduced from the compositions and structural parameters of the nanocomposites are used in the calculation of the percentage of superconductive state in the nanocomposites.



superconductive state.

Measurements of  $T_c$  and Meissner effect are summarized in Table 3.4. A pure superconductor has the magnetic susceptibility of  $\chi = -1/4\pi$ . The percentage of the superconductive state in the samples is calculated by comparing the susceptibility of the samples at 2 K with  $-1/4\pi$ . The high percentages found in many of the nanocomposites indicate that we are observing bulk superconductivity. The  $T_c$  values were determined by the point of intersection of the extrapolations from the linear magnetization of the superconductive state and the normal-state magnetization.

The  $\text{Li}_x\text{TaS}_2$  ( $n=0.2, 0.4$  and  $0.5$ ) samples exhibit two  $T_c$ 's, so they are mixed phase superconductors. This can be compared to the multiphase samples prepared from reaction of 2H-TaS<sub>2</sub> with less than 0.5 equivalent of NaOH reported by Biberacher et al [23]. After  $\text{Li}_{0.2}\text{TaS}_2$  is intercalated with polymers, the second phase disappears or is not detectable because  $T_c$  moves to lower temperature. From Table 3.4, it can be seen that the more the TaS<sub>2</sub> is reduced, the lower the percentage of superconductive state in the sample. From  $\text{Li}_x\text{TaS}_2$  ( $n=0.2$ ) to  $\text{Li}_x\text{TaS}_2$  ( $n=0.5$ ), the value decreases three orders of magnitude. This shows the enormous effect of reduction to the electronic structure of TaS<sub>2</sub>. It explains why the control of the amount of  $\text{LiBH}_4$  in the lithiation reaction is so important to the exfoliation and intercalation properties of the  $\text{Li}_x\text{TaS}_2$ . The intercalation of polymer causes the percentage of superconductive state to drop, but not by orders of magnitude. This is shown by the powder samples of  $\text{Li}_x(\text{PEI})_y\text{TaS}_2$  and  $\text{Li}_{0.2}(\text{PVP})_y\text{TaS}_2$ , and the film sample of batch-I  $\text{Li}_{0.2}(\text{PEO})_y\text{TaS}_2$ , see Table 3.4. The low percentage values of batch-II  $\text{Li}_x(\text{PEO})_y\text{TaS}_2$  films could result from the smaller dimensions of TaS<sub>2</sub> slabs in the nanocomposite.

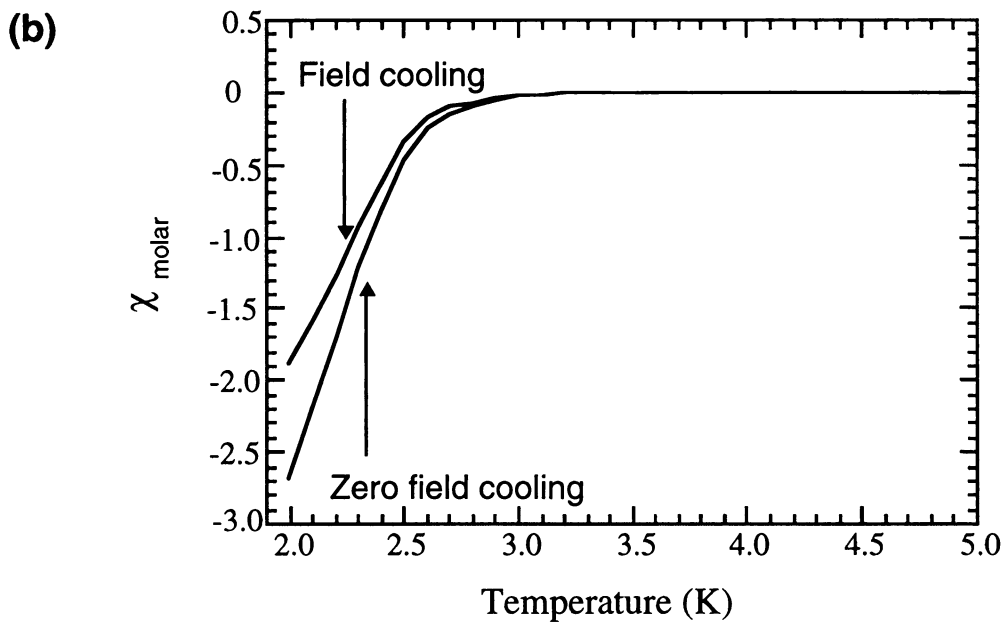
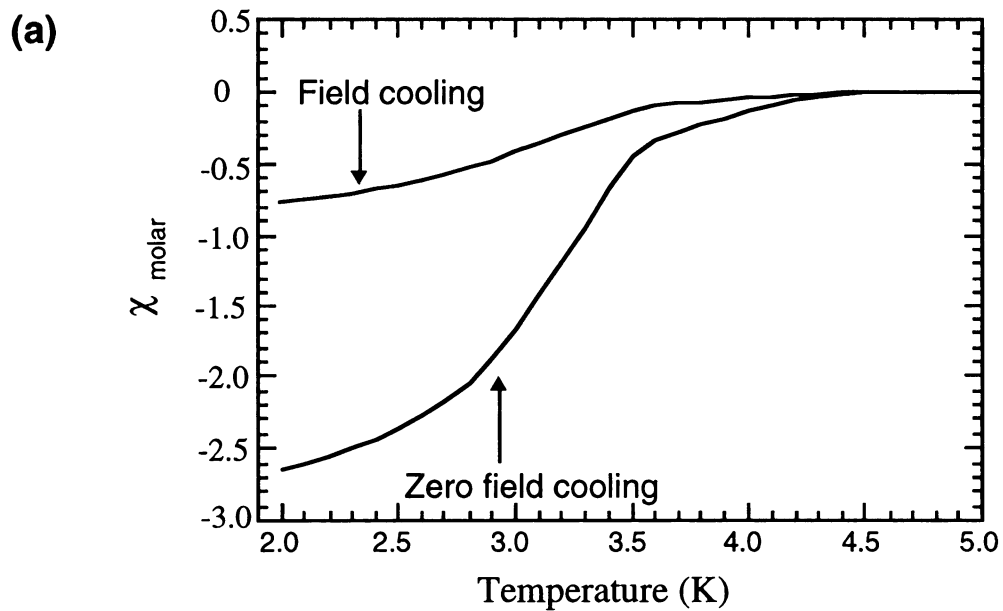


Figure 3.7. Variable temperature magnetic susceptibility (at 5 Gauss) for (a)  $\text{Li}_{0.2}\text{TaS}_2$  (powder), and (b)  $\text{Li}_{0.2}(\text{PEO})_y\text{TaS}_2$  (batch-I; M.W. = 100K; films perpendicular to the applied magnetic field).

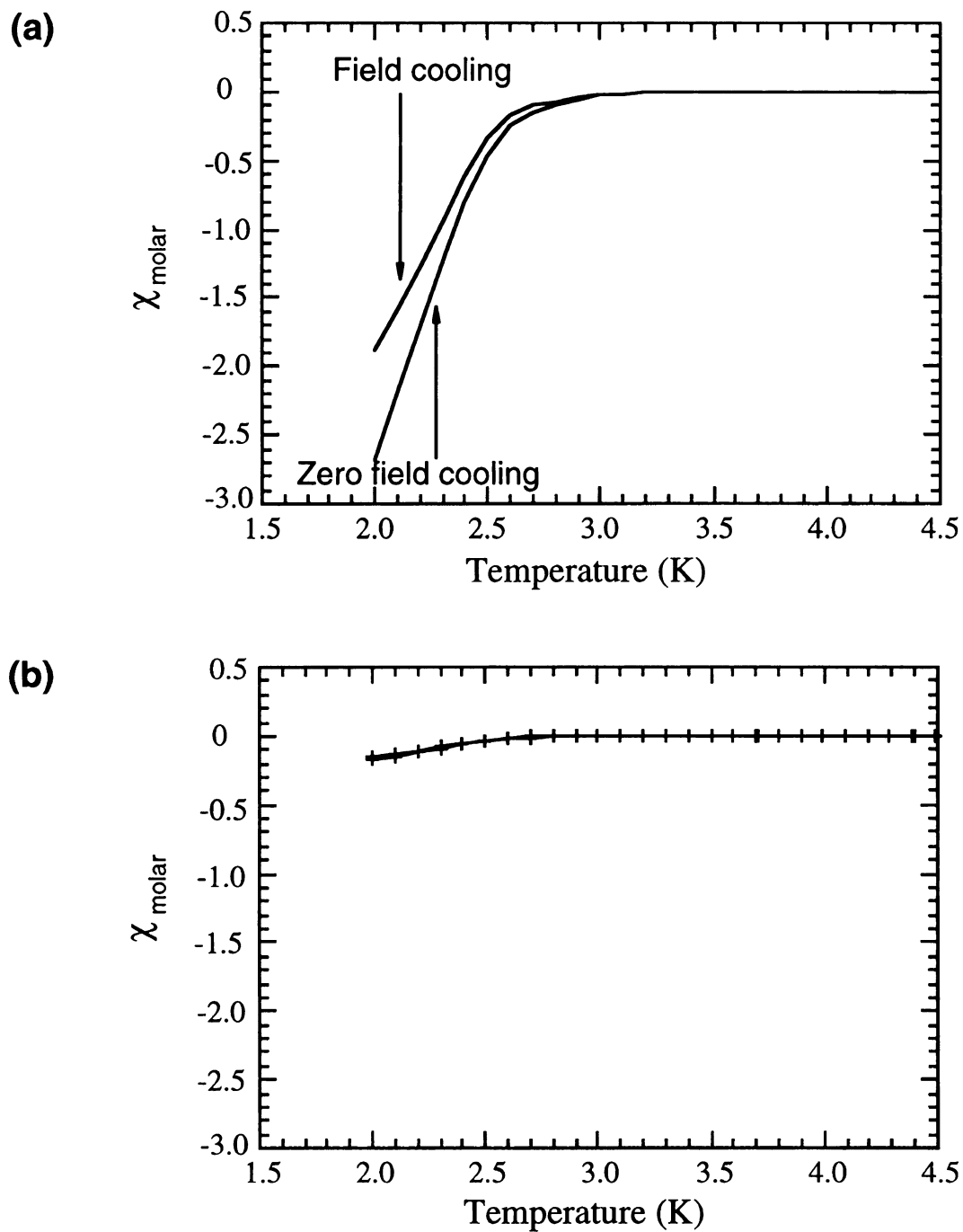
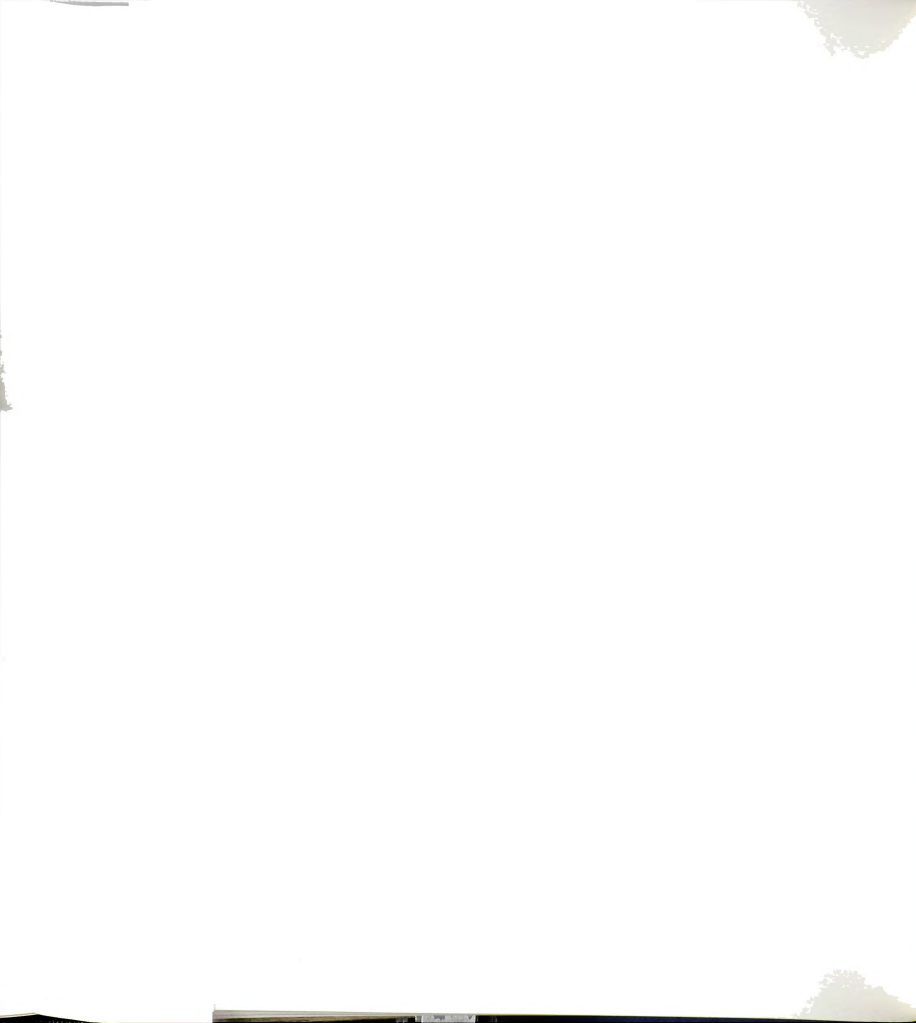


Figure 3.8. Variable temperature magnetic susceptibility (at 5 Gauss) for  $\text{Li}_{0.2}(\text{PEO})_y\text{TaS}_2$  films (batch-I; M.W. = 100K). (a) films perpendicular to the applied magnetic field, (b) films parallel to the applied magnetic field.



Field dependent magnetic measurements on  $\text{Li}_x\text{TaS}_2$  and the nanocomposites show that the Meissner effect decreases with increasing magnetic field. Variable temperature magnetic susceptibility measurements show that the Meissner effect decreases gradually with increasing temperature. Furthermore, the field cooling curve diverges from the zero-field cooling curve in these materials, which is consistent with a type-II superconductor [35].

In the variable temperature magnetic susceptibility measurements, displayed in Figure 3.7, the field cooling curve was very different from the zero-field cooling curve in  $\text{Li}_{0.2}\text{TaS}_2$  [Figure 3.7(a)], while the two curves were much closer together in batch-I  $\text{Li}_{0.2}(\text{PEO})_y\text{TaS}_2$  [Figure 3.7(b)] . The two curves of batch-II  $\text{Li}_{0.2}(\text{PEO})_y\text{TaS}_2$  were also close together. The drift of the field cooling curve toward the zero-field cooling curve, which was also found in the PEI and PVP intercalated nanocomposites, indicates that these materials are less able to pin the electromagnetic vortices present in the material. This is typical of granular superconductivity which appears in materials composed of tiny grains of superconductor particles surrounded by insulating layers [35]. In contrast,  $\text{NbSe}_2$  nanocomposites do not show this effect [3c].

A dramatic difference is observed with sample orientation in the magnetization curves below  $T_c$ , see Figure 3.8. The Meissner effect is much stronger when the film is placed perpendicular to the magnetic field. In both batch-I and batch-II  $\text{Li}_x\text{TaS}_2/\text{PEO}$  samples, the  $\chi_{\text{molar}}$  was  $> 10$  times larger when the film was perpendicular to the field (*i.e.*  $\text{TaS}_2$  layers perpendicular to field) than when it was parallel. This observation suggests that the Cooper pairs are moving predominantly in a circular way within the  $\text{TaS}_2$  layers without passing through the polymer layers. This is a

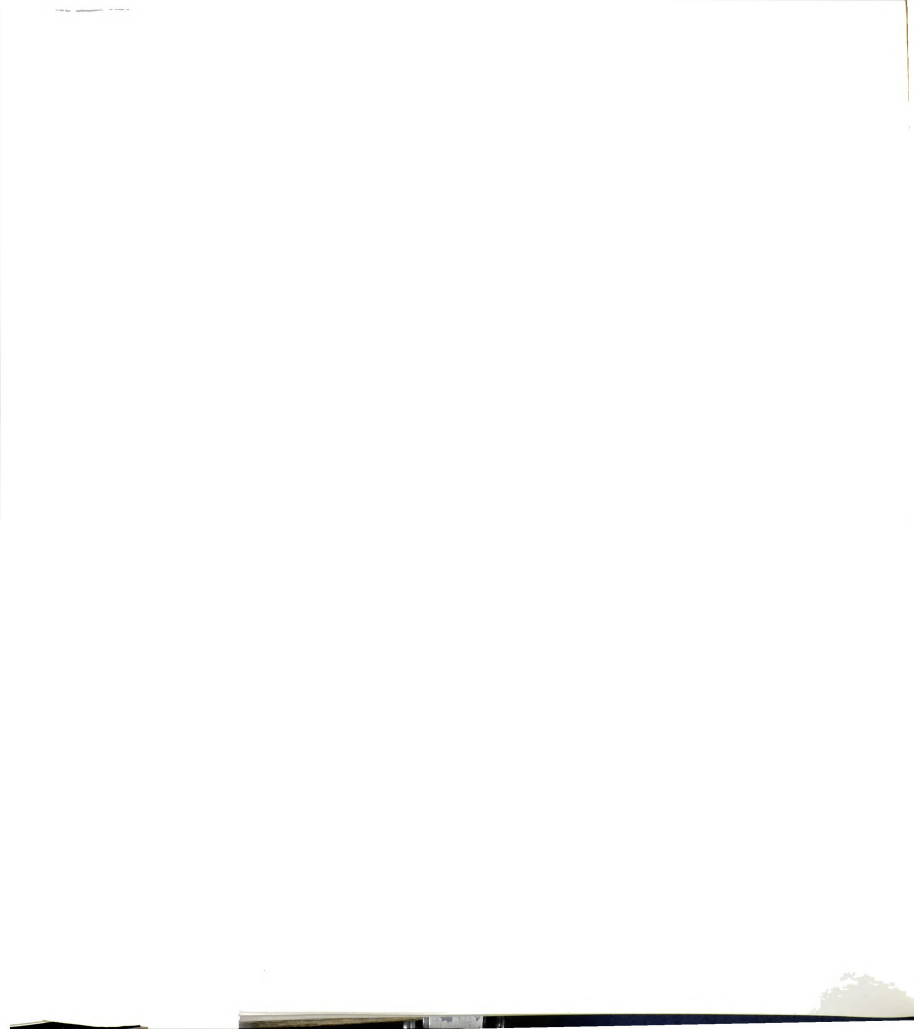


beautiful demonstration of the two-dimensional nature of these nanocomposites.

The magnetic properties of  $\text{Li}_x\text{TaS}_2$  and  $\text{Li}_x\text{TaS}_2/\text{polymer}$  nanocomposites were also measured at temperatures above  $T_c$ . In this temperature range the magnetic susceptibility of  $\text{Li}_x\text{TaS}_2$  ( $x=0.2$  and  $0.4$ ) was Pauli-like and temperature independent with molar  $\chi_{\text{TIP}}$  around  $1.0 \times 10^{-4} \text{ cm}^3/\text{mol}$ .

## 6. Electrical Transport Properties

Room temperature electrical conductivity measurements show that  $\text{Li}_{0.2}\text{TaS}_2$  and its nanocomposites are good conductors, see Table 3.3.  $\text{Li}_{0.2}\text{TaS}_2$  itself is highly conductive, with a conductivity higher than 1000 S/cm. The intercalation of polymers brings the conductivity down by several orders of magnitude. The batch-I products of nanocomposites are 1 to 2 orders of magnitude less conductive, while the batch-II products are 3 to 4 orders of magnitude less conductive. This is probably because the batch-II products contain more polymer, and have  $\text{TaS}_2$  slabs of smaller dimensions. Variable temperature measurements for batch-I and batch-II of  $\text{Li}_{0.2}(\text{PEO})_y\text{TaS}_2$  showed that the conductivity of both increases with falling temperature, consistent with metallic charge transport in these materials, see Figure 3.9. The conductivity reached a broad maximum at 75 K in batch-I  $\text{Li}_{0.2}(\text{PEO})_y\text{TaS}_2$  and at about 130 K in batch-II  $\text{Li}_{0.2}(\text{PEO})_y\text{TaS}_2$  before it started to drop. The superconductive behavior was not detected because our experimental set up could not reach the low temperature at which the metallic to superconductive transition occurs. The metallic character is further confirmed by thermopower data shown in Figure 3.10. The Seebeck coefficient is very small and negative suggesting n-type



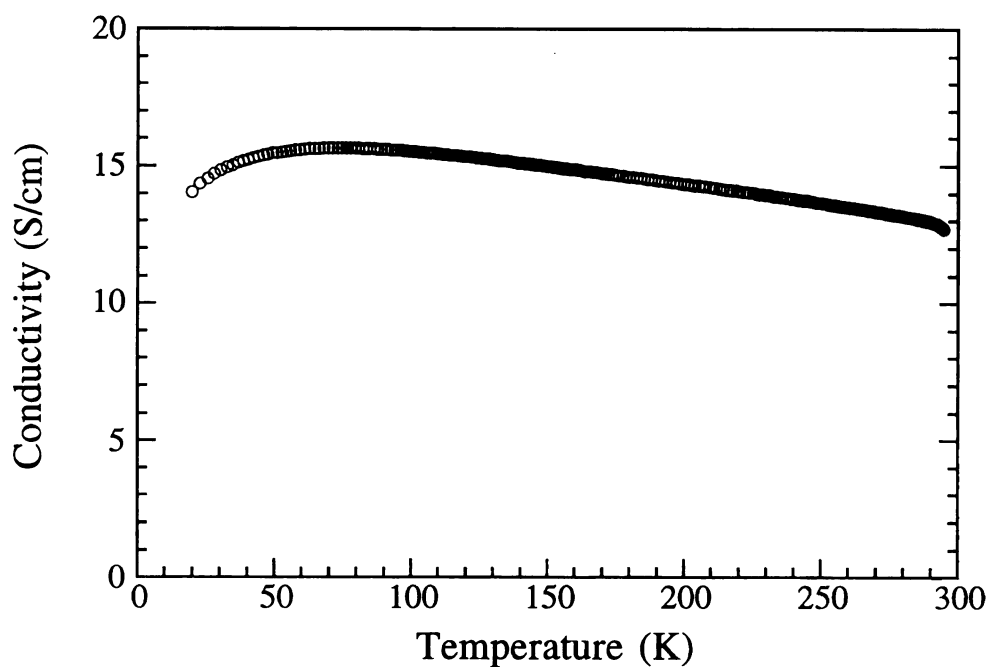


Figure 3.9. Variable temperature electrical conductivity measurements for pressed pellets of  $\text{Li}_{0.2}(\text{PEO})_y\text{TaS}_2$  (batch-I product).

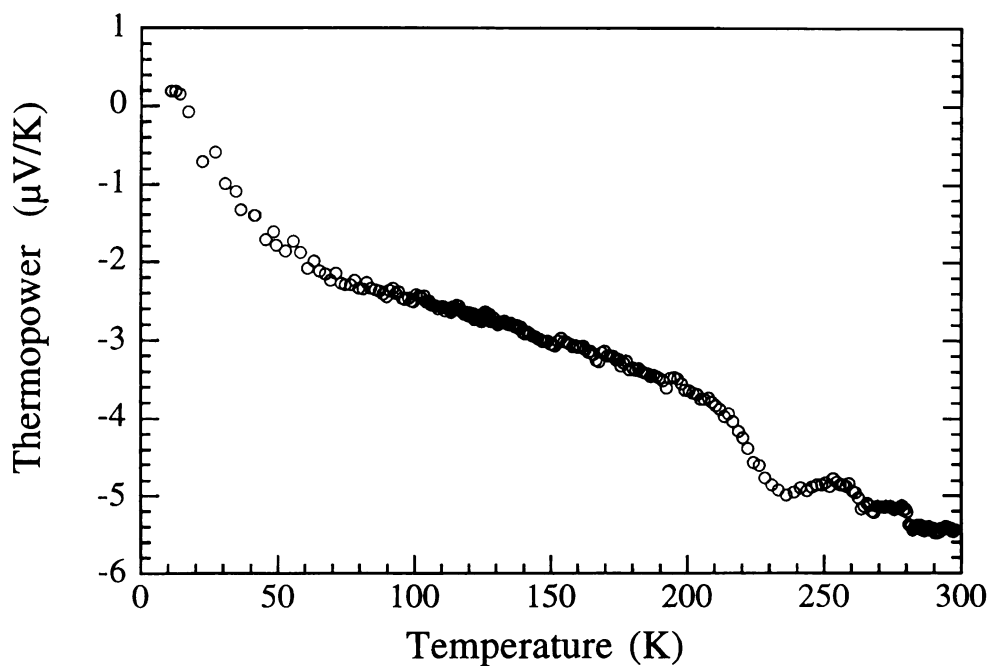


Figure 3.10. Variable temperature thermopower data of pressed pellets of  $\text{Li}_{0.2}(\text{PEO})_y\text{TaS}_2$  (batch-I product).



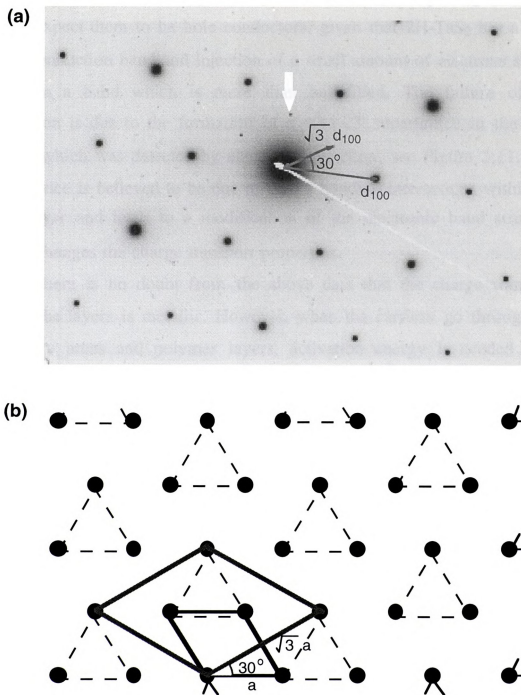


Figure 3.11. Electron diffraction pattern and superstructure of  $\text{Li}_{0.2}\text{TaS}_2$ . The sample was exfoliated in water before deposition on carbon-coated copper grids. The  $\sqrt{3} \times \sqrt{3}$  superlattice reflections are shown with an arrow.



metallic behavior. The n-type transport is somewhat surprising since one might expect them to be hole conductors, given that 2H-TaS<sub>2</sub> has a half-filled conduction band and injection of a small amount of electrons should result in a band which is more than half-filled. The failure of this prediction is due to the formation of a  $\sqrt{3} \times \sqrt{3}$  superlattice in the TaS<sub>2</sub> layers, which was detected by electron diffraction, see Figure 3.11. This superlattice is believed to be due to Ta-Ta bonding interactions within the TaS<sub>2</sub> layer and leads to a modification of the electronic band structure which changes the charge transport properties.

There is no doubt from the above data that the charge transport within the layers is metallic. However, when the carriers go through the boundary areas and polymer layers, activation energy is needed. This contributes a thermally activated contribution to the conductivity, especially when the TaS<sub>2</sub> slabs become more separated as the polymer content increases.

## 7. Solid State NMR Spectroscopy

In order to probe the behavior of lithium ions in the two different gallery environments, (*i.e.* gallery with and without polymer) we measured the variable temperature static solid state <sup>7</sup>Li NMR spectra for Li<sub>0.2</sub>TaS<sub>2</sub> and Li<sub>0.2</sub>(PEO)<sub>y</sub>TaS<sub>2</sub> (batch-II). Examination of the temperature dependence of the <sup>7</sup>Li NMR line-width provides an independent perspective on the cation mobility in inhomogeneous solid, especially in (Li salt)/polymer complexes [36, 37] and Li/polymer/inorganic nanocomposites [38]. Both Li<sub>0.2</sub>TaS<sub>2</sub> and Li<sub>0.2</sub>(PEO)<sub>y</sub>TaS<sub>2</sub> showed just one resonance peak due to a first order quadrupolar transition with no significant satellite peaks.



The spectra of  $\text{Li}_{0.2}\text{TaS}_2$  at  $-80\text{ }^\circ\text{C}$  and  $100\text{ }^\circ\text{C}$  are presented in Figures 3.12(a) and 3.12(b). At  $-80\text{ }^\circ\text{C}$ ,  $\text{Li}_{0.2}\text{TaS}_2$  exhibits a broad peak with the maximum situated at a chemical shift of 5.5 ppm higher than the solid LiCl reference. The peak was somewhat asymmetric with a barely noticeable shoulder on the low field side. With rising temperature the position of the peak maximum did not change, but the shoulder protruded more and moved towards lower field. At  $100\text{ }^\circ\text{C}$ , the shoulder became a second peak at a chemical shift of 15 ppm higher than that of LiCl. The shape and position of the peak changed reversibly over many cooling and heating cycles. The change of the linewidth (the width at half-height) of the whole peak, versus temperature, is presented in Figure 3.13A(a). The broadening of the  $^7\text{Li}$  resonance peak is mostly due to many overlapping signals corresponding to slightly different lithium ion sites. The slow decrease of the linewidth with increasing temperature suggests that there is a large activation barrier for  $\text{Li}^+$  to hop from site to site. The presence of the shoulder in the spectrum indicates a different chemical environment for  $\text{Li}^+$  ions, which might be related to the multiphase observed in the superconductive state discussed above.

The low temperature ( $-80\text{ }^\circ\text{C}$ ) static solid state  $^7\text{Li}$  NMR spectra of  $\text{Li}_{0.2}(\text{PEO})_y\text{TaS}_2$  (batch-II) showed a broad symmetric resonance peak with a chemical shift almost identical to that of solid LiCl, see Figure 3.12(c). With increasing temperature, the position of the peak did not change, but its shape became asymmetric, see Figure 3.12(d). The peak base on the low field side extended a little farther than on the opposite side. The linewidth did not change appreciably in the temperature range from  $-80\text{ }^\circ\text{C}$  to  $-40\text{ }^\circ\text{C}$  but it narrowed dramatically from  $-40\text{ }^\circ\text{C}$  to  $60\text{ }^\circ\text{C}$  and then continued to narrow albeit at a lower rate. At  $100\text{ }^\circ\text{C}$ , the linewidth of the peak was only

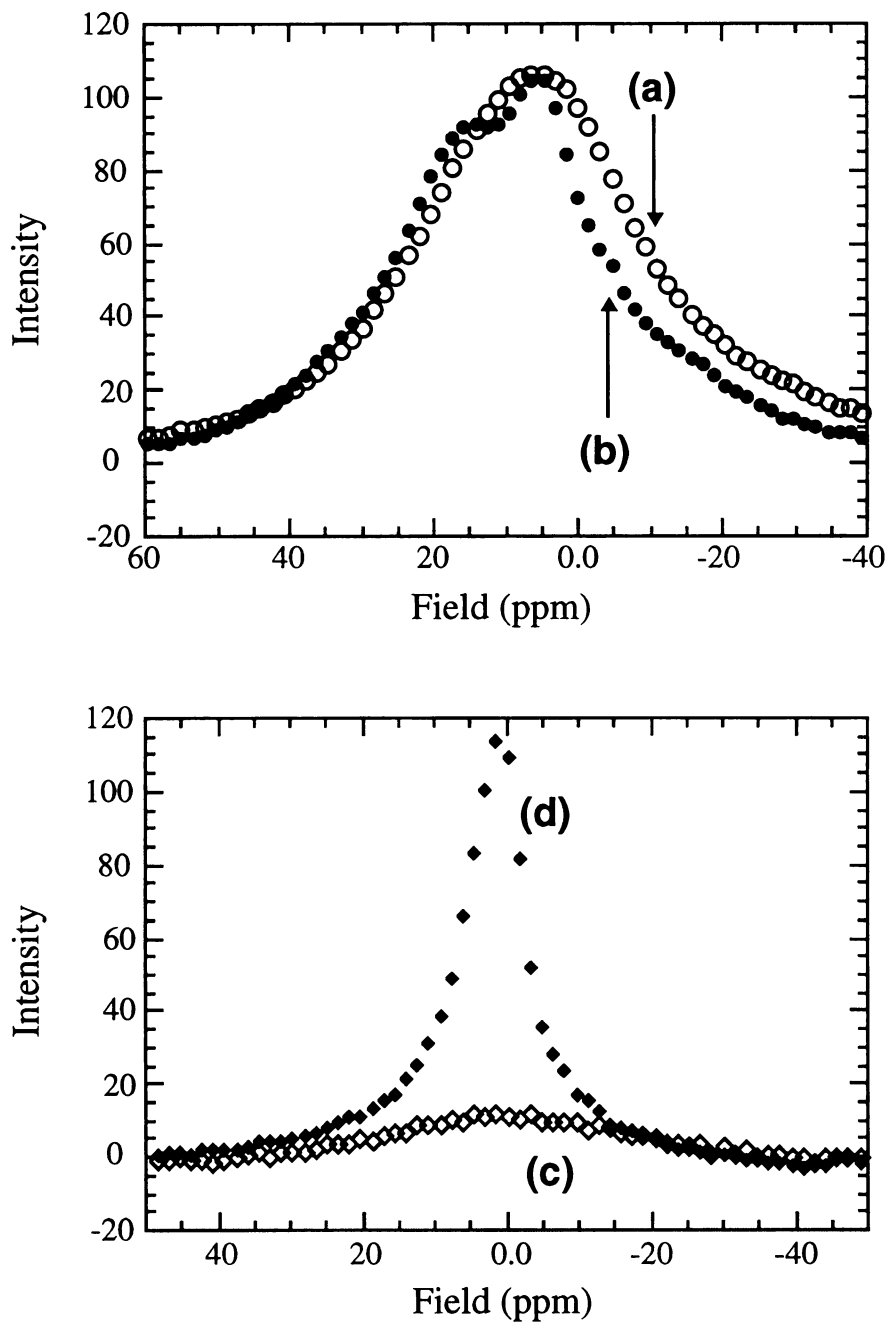


Figure 3.12. Static solid state  $^7\text{Li}$  NMR spectra of (a)  $\text{Li}_{0.2}\text{TaS}_2$  at  $-80\text{ }^\circ\text{C}$ , (b) at  $100\text{ }^\circ\text{C}$ , (c)  $\text{Li}_{0.2}(\text{PEO})_y\text{TaS}_2$  (batch-II; M.W. = 100K) at  $-80\text{ }^\circ\text{C}$  and (d) at  $100\text{ }^\circ\text{C}$ .

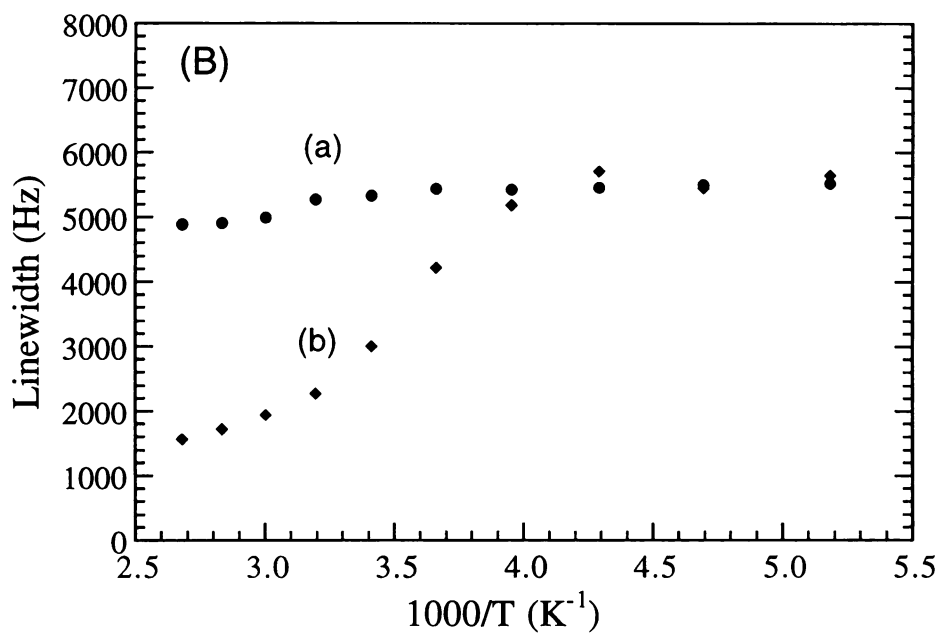
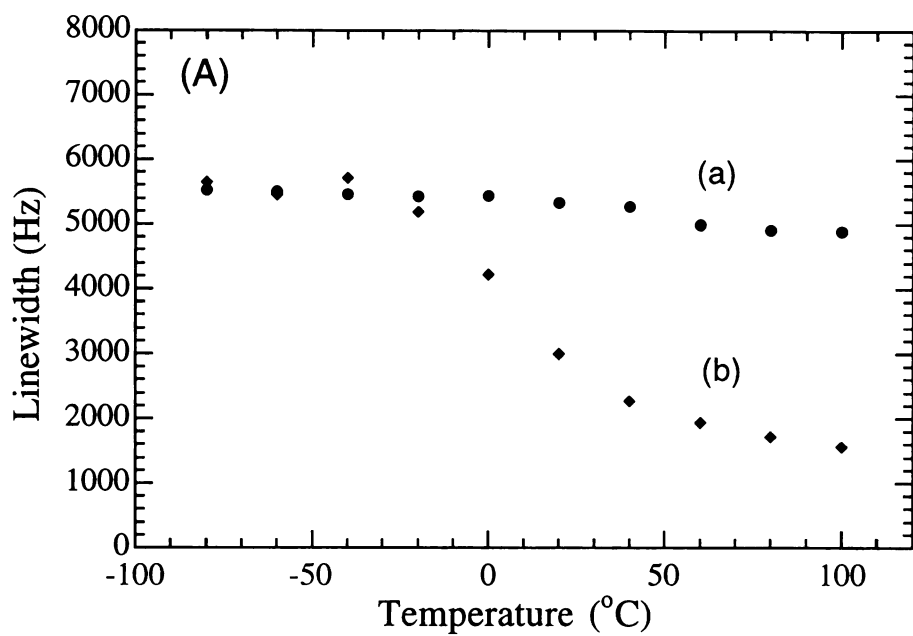
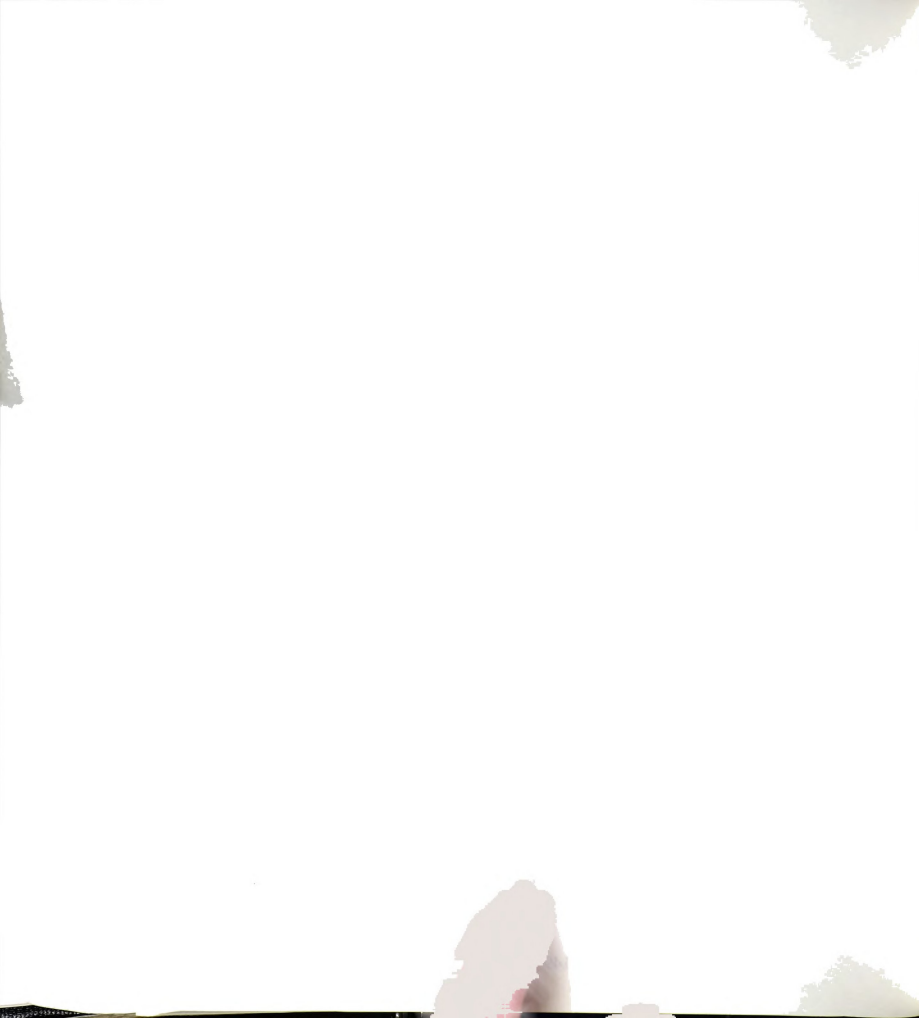


Figure 3.13. Temperature dependence of the linewidth of  ${}^7\text{Li}$  NMR resonance peaks for (a)  $\text{Li}_{0.2}\text{TaS}_2$  and (b)  $\text{Li}_{0.2}(\text{PEO})_y\text{TaS}_2$  (batch-II; M.W. = 100K).



28% of that at -80 °C, see Figure 3.13A(b). This behavior is called dynamical motional narrowing and has been intensively studied in many solid polymer electrolytes [36, 37] and some PEO [or poly(ethylene glycol) (PEG)] nanocomposites [38]. The change of line-width is caused by the averaging of magnetic couplings over the local magnetic field associated with other spins such as other Li nuclei, proton nuclei and unpaired electrons, due to dynamical motion. In most solid polymer electrolytes and PEO [or (PEG)] nanocomposites, dynamical motional narrowing is caused by the dissociation of a dipole-dipole coupling between pairs of nuclear spins, specifically  $^7\text{Li}$  and proton of the PEO [36, 37, 38] and reflects the onset of the dynamical motion of either the polymer chains or the  $\text{Li}^+$  ions. In some materials with unpaired electrons, which produce much larger spin fields than nuclei, the line narrowing is caused by the averaging over the dipole coupling in the electron spin field [38].

$\text{Li}_{0.2}(\text{PEO})_y\text{TaS}_2$  is close to Li/PEO/fluorohectorite [38b], a PEO intercalated nanocomposite without paramagnetic centers in the inorganic layers. One might expect that the broadening of the  $^7\text{Li}$  resonance peak mainly results from the dipole-dipole coupling between  $^7\text{Li}$  and  $^1\text{H}$  of the PEO, as in the case of Li/PEO/fluorohectorite [38b]. This assignment would be supported by the similar linewidths before narrowing in these two nanocomposites, ~5 kHz, and the appearance of the plateau on the low-temperature as well as high-temperature side. If this is the case, the dynamical motional narrowing should correspond to the onset of the segmental motion of the polymer chains. However, the temperature range of the narrowing, -40 °C ~ 60°C, is more close to the onset temperature of the  $\text{Li}^+$  ion motion obtained in Li/PEO/montmorillonite, -20 °C ~ 40°C [38a, b], rather than that of the polymer segmental motion observed in



28% of that at -80 °C, see Figure 3.13A(b). This behavior is called dynamical motional narrowing and has been intensively studied in many solid polymer electrolytes [36, 37] and some PEO [or poly(ethylene glycol) (PEG)] nanocomposites [38]. The change of line-width is caused by the averaging of magnetic couplings over the local magnetic field associated with other spins such as other Li nuclei, proton nuclei and unpaired electrons, due to dynamical motion. In most solid polymer electrolytes and PEO [or (PEG)] nanocomposites, dynamical motional narrowing is caused by the dissociation of a dipole-dipole coupling between pairs of nuclear spins, specifically  $^7\text{Li}$  and proton of the PEO [36, 37, 38] and reflects the onset of the dynamical motion of either the polymer chains or the  $\text{Li}^+$  ions. In some materials with unpaired electrons, which produce much larger spin fields than nuclei, the line narrowing is caused by the averaging over the dipole coupling in the electron spin field [38].

$\text{Li}_{0.2}(\text{PEO})_y\text{TaS}_2$  is close to Li/PEO/fluorohectorite [38b], a PEO intercalated nanocomposite without paramagnetic centers in the inorganic layers. One might expect that the broadening of the  $^7\text{Li}$  resonance peak mainly results from the dipole-dipole coupling between  $^7\text{Li}$  and  $^1\text{H}$  of the PEO, as in the case of Li/PEO/fluorohectorite [38b]. This assignment would be supported by the similar linewidths before narrowing in these two nanocomposites, ~5 kHz, and the appearance of the plateau on the low-temperature as well as high-temperature side. If this is the case, the dynamical motional narrowing should correspond to the onset of the segmental motion of the polymer chains. However, the temperature range of the narrowing, -40 °C ~ 60°C, is more close to the onset temperature of the  $\text{Li}^+$  ion motion obtained in Li/PEO/montmorillonite, -20 °C ~ 40°C [38a, b], rather than that of the polymer segmental motion observed in

Li/PEO/fluorohectorite,  $-100\text{ }^{\circ}\text{C} \sim 40^{\circ}\text{C}$  [38b]. In  $\text{LiClO}_4(\text{PEG})_9$ ,  $\text{LiClO}_4(\text{PEG})_{25}$  and  $\text{LiBF}_4(\text{PEG})_9$ , where the motion of  $\text{Li}^+$  ions is essentially governed by the segmental motion of the polymer chains so that the line narrowing corresponds to both the onset of the correlated motions of  $\text{Li}^+$  ions and polymer segments, the narrowing occurs in the range  $-50\text{ }^{\circ}\text{C} \sim 50^{\circ}\text{C}$  [36a]. Considering the line narrowing of  $\text{Li}_{0.2}\text{TaS}_2$ , which happens in the same temperature range as that of  $\text{Li}_{0.2}(\text{PEO})_y\text{TaS}_2$ , we believe that this dynamical motional narrowing observed in  $\text{Li}_{0.2}(\text{PEO})_y\text{TaS}_2$  is caused by the onset of the  $\text{Li}^+$  ion hopping in the gallery. This is because the  $[\text{TaS}_2]^{x-}$  anions are massive and only the motion of  $\text{Li}^+$  ions can cause the line narrowing in  $\text{Li}_{0.2}\text{TaS}_2$ . On the other hand, the linewidth after the narrowing is much wider in  $\text{Li}_{0.2}(\text{PEO})_y\text{TaS}_2$  ( $\sim 1500\text{ Hz}$ ) than in  $\text{LiClO}_4(\text{PEG})_9$ ,  $\text{LiClO}_4(\text{PEG})_{25}$  and  $\text{LiBF}_4(\text{PEG})_9$  ( $60 - 90\text{ Hz}$ ), which also suggests that the broadening of the  $^7\text{Li}$  resonance peak in  $\text{Li}_{0.2}(\text{PEO})_y\text{TaS}_2$  is not caused only by the dipole-dipole coupling between  $^7\text{Li}$  and the polymer protons. For comparison with literature data, the  $^7\text{Li}$  NMR linewidths of  $\text{Li}_{0.2}\text{TaS}_2$  and  $\text{Li}_{0.2}(\text{PEO})_y\text{TaS}_2$  are plotted against  $1/T$  in Figure 3.13B.

The considerable narrowing of the  $^7\text{Li}$  resonance peak of  $\text{Li}_{0.2}(\text{PEO})_y\text{TaS}_2$  at high temperatures suggests that the lithium ions begin to undergo facile site hopping. The mobility of lithium ions is affected by temperature more readily in the polymer intercalated galleries than in the un-intercalated galleries. This is attributed to the more disordered state of the Li lattice sites in the nanocomposites which lowers the activation barrier for hopping, relative to the more ordered, crystallographically well defined sites in  $\text{Li}_{0.2}\text{TaS}_2$ . The narrowing of linewidth in solid state  $^7\text{Li}$

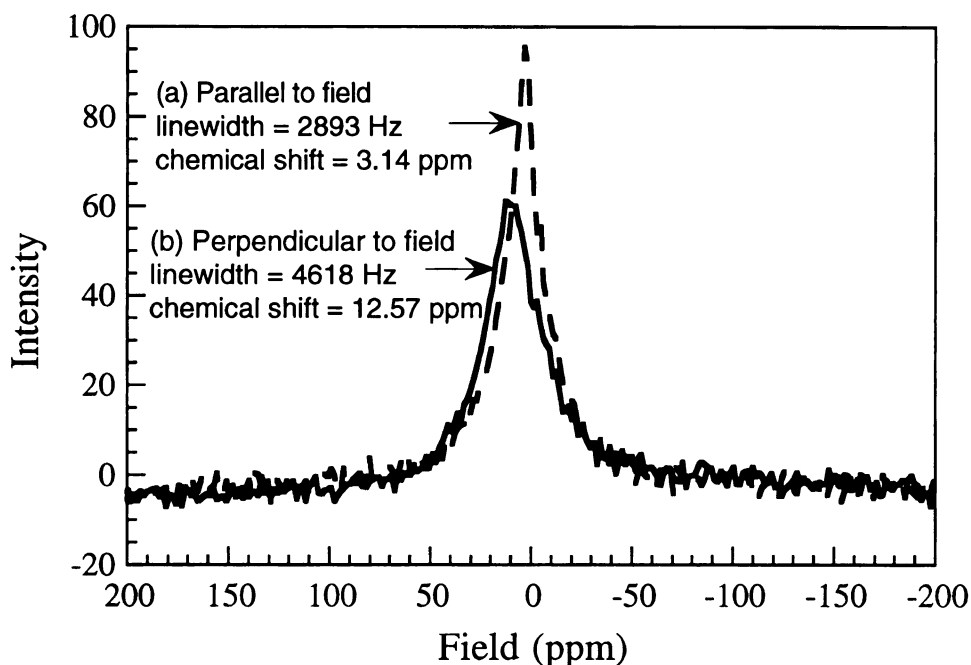


Figure 3.14. Room temperature  ${}^7\text{Li}$  NMR spectra for a  $\text{Li}_{0.2}(\text{PEO})_y\text{TaS}_2$  film (batch-I; M.W. of PEO, 100K). (a) film parallel to the magnetic field and (b) film perpendicular to the field.

NMR has also been observed in  $\text{Li}_x\text{V}_2\text{O}_5$  [31] and  $\text{Li}_x\text{MoO}_3$  [3b], as well as their PEO nanocomposites.

A high degree of anisotropy was observed in the solid state  ${}^7\text{Li}$  NMR spectra of  $\text{Li}_{0.2}(\text{PEO})_y\text{TaS}_2$  films (both batch-I and batch-II). As shown in Figure 3.14, both the resonance peak position and peak-width vary with the change in the orientation of the film of batch-I relative to the direction of applied magnetic field. When the film is perpendicular to the magnetic field, the peak width is broadened considerably more than when it is parallel. The mechanism of the change of the linewidth corresponding to the orientation is not yet clear. However, the high electron mobility in the two-dimensional  $\text{TaS}_2$  slab probably couples to the external applied magnetic field and causes local magnetic field distortions which affect the



Li nuclei and consequently the  $^7\text{Li}$  NMR signals. This orientation effect is less pronounced in films of batch-II  $\text{Li}_{0.2}(\text{PEO})_y\text{TaS}_2$  probably due to the fact that the dimensions of  $\text{TaS}_2$  slabs are smaller and the slabs are less well stacked and more separated by PEO. The results of these experiments are summarized in Table 3.5.

Table 3.5. Effect of film orientation on the  $^7\text{Li}$ -NMR spectrum of  $\text{Li}_{0.2}(\text{PEO})_y\text{TaS}_2$

|                                      | $\text{Li}_{0.2}(\text{PEO})_y\text{TaS}_2$ (batch-I) |               | $\text{Li}_{0.2}(\text{PEO})_y\text{TaS}_2$ (batch-II) |               |
|--------------------------------------|---|---------------|--|---------------|
|                                      | parallel  | perpendicular | parallel   | perpendicular |
| chemical shift of peak position(ppm) | 3.14  | 12.57         | 10.99  | 9.42          |
| linewidth (Hz)                       | 2893  | 4618          | 2924   | 2902          |

\* "parallel" and "perpendicular" refer to the film with respect to the instrument's applied magnetic field.

## Concluding Remarks

The exfoliation properties of  $\text{Li}_x\text{TaS}_2$  were systematically explored and it was found that  $\text{Li}_x\text{TaS}_2$ , prepared from controlled lithiation with 0.2 equivalent  $\text{LiBH}_4$ , exfoliates well in water and has high affinity for various polymers. Lamellar nanocomposites of PEO, PEI and PVP were thus obtained through the encapsulative precipitation method. The nanocomposites dissolve in water and are easily cast into free-standing films. These plastic like films convert into superconductors at temperatures below their  $T_c$ 's, which raises the possibility of developing flexible superconductors with these or other materials in the future. Solid state  $^7\text{Li}$

NMR measurements indicate that  $\text{Li}_x(\text{PEO})_y\text{TaS}_2$  provides a more facile hopping environment for Li ions. According to the 1-D EM calculation for  $\text{Li}_x(\text{PEO})_y\text{TaS}_2$ , the nanocomposites are probably constructed with two sheets of PEO chains inserted in each gallery. The PEO chains adapt a conformation similar to that found in type II PEO-HgCl<sub>2</sub> complex and are arranged with -CH<sub>2</sub>- groups facing the TaS<sub>2</sub> layers and -O- atoms towards the center of the gallery where the Li<sup>+</sup> ions seem to be located.



## References

- 1 (a) E. P. Giannelis, *Adv. Mater.* **1996**, 8, 29. (b) R. Krishnamoorti, R. A. Vaia. and E. P. Giannelis, *Chem. Mater.* **1996**, 8, 1728.
- 2 (a) E. Ruiz-Hitzky, *Adv. Mater.* **1993**, 5, 334. (b) E. Ruiz-Hitzky, P. Aranda, B. Casal and J. C. Galván, *Adv. Mater.* **1995**, 7, 180.
- 3 (a) R. Bissessur, M. G. Kanatzidis, J. L. Schindler and C. R. Kannewurf, *J. Chem. Soc., Chem. Commun.*, **1993**, 1582. (b) L. Wang, J. Schindler, C. R. Kannewurf and M. G. Kanatzidis, *J. Mater.Chem.* **1997**, 7, 1277. (Also Chapter 4 of this dissertation.) (c) H.-L. Tsai, J. L. Schindler, C. R. Kannewurf and M. G. Kanatzidis, *Chem. Mater.* **1997**, 9, 875.
- 4 L. F. Nazar, H. Wu and W. P. Power, *J. Mater. Chem.* **1995**, 5, 1985.
- 5 (a) J. P. Lemmon, J. Wu, C. Oriakhi and M. M. Lerner, *Electrochim. Acta* **1995**, 40 , 2245. (b) C. O. Oriakhi, R. L. Nafshun and M. M. Lerner, *Mater. Res. Bull.* **1996**, 31, 1513.
- 6 A TaS<sub>2</sub>/PEI nanocomposite by almost the same preparation approach has been reported by Oriakhi et al <sup>[5b]</sup>.
- 7 TaS<sub>2</sub>/Polymer(oligomer) nanocomposites were also synthesized by other methods. (a) TaS<sub>2</sub>/Poly(4-vinylpyridine) nanocomposite was synthesized by *in situ* monomer intercalation and interlayer gallery polymerization: C.-H. Hsu, M. M. Labes, J. T. Breslin, D. J. Edmiston, J. J. Winter, H. A. Leupold and F. Rothwarf, *Nature, Phys. Sci.*, **1973**, 246(155), 122. (b) Polypeptides were intercalated into 2H-TaS<sub>2</sub> by direct insertion: V. M. Chapela and G. S. Parry, *Nature* **1979**, 281, 134.
- 8 D. W. Murphy and G. W. Hull Jr., *J. Chem. Phys.* **1975**, 62, 973.
- 9 A. Lerf and R. Schöllhorn, *Inorg. Chem.* **1977**, 16, 2950.
- 10 (a) A. J. Jacobson, *Mater. Sci. Forum* **1994**, 152-153 (Soft Chemistry Routes to New Materials), 1. (b) L. F. Nazar and A. J. Jacobson, *J. Mater. Chem.* **1994**, 4, 1419. (c) A. J. Jacobson, in G.



Alberti and T. Bein ed., *Comprehensive Supramolecular Chemistry*, Vol. 7, Elsevier Science Ltd., 1996, pp 315.

- 11 A. Lerf, E. Lalik, W. Kolodziejski and J. Klinowski, *J. Phys. Chem.* **1992**, 96, 7389.
- 12 (a) P. Joensen, R. F. Frindt and S. R. Morrison, *Mater. Res. Bull.* **1986**, 21, 457. (b) M. A. Gee, R. F. Frindt, P. Joensen and S. R. Morrison, *Mater. Res. Bull.* **1986**, 21, 543. (c) D. W. Murphy and G. W. Hull, *Chem. Phys.* **1975**, 62, 973.
- 13 J. F. Lomax, *Intercalation Chemistry of Layered Transition Metal Dichalcogenides with Organic Bases*, Ph. D. Dissertation, Department of Chemistry, Northwestern University, **1986**.
- 14 The equivalent of  $\text{LiBH}_4$  used in the lithiation reaction,  $n$ , directly affects the amount of Li,  $x$ , in  $\text{Li}_x\text{TaS}_2$ . Since no experiments were arranged to determine the  $x$  values for different forms of  $\text{Li}_x\text{TaS}_2$ ,  $n$  is used here and in the discussion.
- 15 When  $n$  is small ( $< 0.5$ ),  $x$ , the amount of Li in  $\text{Li}_x\text{TaS}_2$ , is expected close to the value of  $n$ . However, this expectation is not checked with experiments. Therefore, " $\text{Li}_{0.2}\text{TaS}_2$ " is used to present the form of  $\text{Li}_x\text{TaS}_2$  prepared under the stoichiometry  $n=0.2$  only for convenience.
- 16 Under oxygen flow,  $\text{Li}_{0.2}\text{TaS}_2$  gained weight at first and then lost weight at about  $600\text{ }^\circ\text{C}$ . The net loss up to  $750\text{ }^\circ\text{C}$  was 9.18%, 8.55%, 7.63% and 7.37% respectively in 4 measurements due to the transformation to  $\text{Ta}_2\text{O}_5$  and  $\text{Li}_2\text{SO}_4$ .
- 17 For  $\text{Li}_{0.2}\text{TaS}_2$  to become  $\text{Li}_2\text{SO}_4$  and  $\text{Ta}_2\text{O}_5$ , the weight loss should be 5.89%. Because Li compounds can be volatile at high temperatures, the weight loss of the sample in an oxygen flow could be somewhat higher than the theoretical value. In addition, a trace of small molecules such as water and diethyl ether in the  $\text{Li}_{0.2}\text{TaS}_2$  can also cause a slightly higher weight loss than the theoretical value.
- 18 PEAKOC is an XRD powder pattern analysis program provided by Inel Inc. (Mail Address in U.S.A.: P. O. Box 147, Stratham, NH 03885.)



- 19 *International Tables for X-ray Crystallography*, Kynoch Press, **1974**.
- 20 M. G. Kanatzidis and T. J. Marks, *Inorg. Chem.* **1987**, 26, 783.
- 21 While we expect the n values to be close to the x values in  $\text{Li}_x\text{TaS}_2$  when n is  $< 0.5$ , no attempt was made to determine the exact x in the samples.
- 22 A. Jacobson, *Mater. Sci. Forum* **1994**, 1, 152.
- 23 W. Biberacher, A. Lerf, F. Buheitel, T. Butz and A. Hübler, *Mat. Res. Bull.* **1982**, 17, 633.
- 24 PEI was also intercalated in the  $\text{Li}_x\text{TaS}_2$  prepared from either 2H-TaS<sub>2</sub> or 1T-TaS<sub>2</sub> through a solid state reaction with 3 equivalent of  $\text{LiBH}_4$  in the temperature range from 300 °C to 525 °C.
- 25 The  $\text{Li}_{0.2}\text{TaS}_2$  and  $\text{Li}_{0.2}(\text{PEO})_{1.04}\text{TaS}_2$  were heated to 350 °C under nitrogen atmosphere and kept for 10 minutes at this temperature to check if there was any loss of sulfur in the TaS<sub>2</sub> layers. The sulfur content in these two samples as well as the untreated samples was checked with EDS, using synthesized 2H-TaS<sub>2</sub> as a standard. The stoichiometric number for sulfur, m (as TaS<sub>m</sub>), was 1.96, 2.01, 1.98 and 1.96 for  $\text{Li}_{0.2}\text{TaS}_2$ ,  $\text{Li}_{0.2}(\text{PEO})_{1.04}\text{TaS}_2$ , treated  $\text{Li}_{0.2}\text{TaS}_2$  and treated  $\text{Li}_{0.2}(\text{PEO})_{1.04}\text{TaS}_2$  respectively. This indicates that almost no sulfur is lost in the lithiation, intercalation and heating treatment of  $\text{Li}_{0.2}\text{TaS}_2$  and  $\text{Li}_{0.2}(\text{PEO})_{1.04}\text{TaS}_2$  up to 350 °C under nitrogen. This is consistent with TGA which showed that  $\text{Li}_{0.2}\text{TaS}_2$  had no weight loss in nitrogen up to 530 °C.
- 26 (a) Y. Takahashi and H. Tadokoro, *Macromolecules* **1973**, 6, 672.  
(b) J. Brandrup and E. H. Immergut, *Polymer Handbook*, 3rd Ed., John Wiley & Sons, New York, **1989**, pp VI/72.
- 27 F. P. Price and R. W. Kilb, *J. Polym. Sci.* **1962**, 57, 395.
- 28 Y. Takahashi, I. Sumita and H. Tadokoro, *J. Polym. Sci., Polym. Phys. Ed.*, **1973**, 11, 2113.



- 29 R. Iwamoto, Y. Saito, H. Ishihara and H. Tadokoro, *J. Polym. Sci., A-2*, **1968**, 6, 1509.
- 30 M. Yokoyama, H. Ishihara, R. Iwamoto and H. Tadokoro, *Macromolecules* **1969**, 2, 184.
- 31 Y.-J. Liu, J. L. Schindler, D. C. DeGroot, C. R. Kannewurf, W. Hirpo and M. G. Kanatzidis, *Chem. Mater.* **1996**, 8, 525.
- 32 The positions of the atoms of PEO were decided according to the structural data available from the PEO crystal structure with planar zigzag conformation [28]. When the ac plane of the unit cell is parallel to the layers, the PEO zigzag plane is almost parallel to the TaS<sub>2</sub> layers; when the bc plane of the unit cell is parallel to the TaS<sub>2</sub> layers, the PEO zigzag plane is almost perpendicular to the layers.
- 33 P. Garoche, P. Manuel, J. J. Veyssie and P. J. Molinié, *Low. Temp. Phys.* **1978**, 30, 323.
- 34 R. H. Friend and A. D. Yoffe, *Adv. Phys.* **1978**, 36, 1.
- 35 V. Z. Kresin and S. A. Wolf, *Fundamentals of Superconductivity*, Plenum Press, New York/London, **1990**, pp 95.
- 36 (a) S. Panero, B. Scrosati and S. G. Greenbaum, *Electrochim. Acta* **1992**, 40, 1533. (b) W. Gorecki, E. Belorizky, C. Berthier, P. Donoso and M. Armand, *Electrochim. Acta* **1992**, 37, 1685.
- 37 (a) S. H. Chung, K. R. Jeffrey and J. R. Stevens, *J. Chem. Phys.* **1991**, 94, 1803. (b) J. P. Donoso, T. J. Bonagamba, P. L. Frare, N. C. Mello, C. J. Magon, H. Panepucci, *Electrochim. Acta* **1995**, 40, 2361.
- 38 (a) S. Wong, S. Vasudevan, R. A. Vaia, E. P. Giannelis and D. B. Zax, *J. Am. Chem. Soc.* **1995**, 117, 7568. (b) S. Wong and D. B. Zax, *Electrochim. Acta* **1997**, 42, 3513. (c) D.-K. Yang and D. B. Zax, *J. Chem. Phys.* **1999**, 110, 5325.



## Chapter 4

### LAMELLAR $\text{Li}_x\text{MoO}_3$ /POLYMER NANOCOMPOSITES VIA ENCAPSULATIVE INSERTION

#### Introduction

The investigation of inorganic/polymer nanophase composites is motivated by many reasons, including the need for novel electronic anisotropic materials, better performing battery cathode materials, functionalized structural materials with superior mechanical properties, hierarchical materials, and systems in which to study polymer orientation, epi- and endo-taxty and polymer/inorganic surface interactions [1-14]. Polymer-based nanocomposites have been reported with layered silicates (e.g. montmorillonite, hectorite, *etc.*) [1],  $\text{FeOCl}$  [2],  $\text{V}_2\text{O}_5$  [3, 4],  $\text{MoO}_3$  [5, 6, 7], layer metal phosphates [8],  $\text{MS}_2$  ( $\text{M}=\text{Mo}$  [9, 10, 11, 7a],  $\text{Ti}$  [11a]),  $\text{NbSe}_2$  [12], layered metal phosphorus chalcogenides ( $\text{MPS}_3$ ) [13, 7] and layered double hydroxides [14]. The most common methods of preparing inorganic/polymer nanocomposites are (a) by monomer intercalation followed by polymerization, (b) by *in situ* intercalative polymerization, (c) by direct insertion and (d) by encapsulative precipitation from solutions of exfoliated lamellar solids. The last two methods give inorganic/polymer nanocomposites in which the molecular masses and nature of the polymers can be decided before intercalation. Encapsulative precipitation has been applied with  $\text{V}_2\text{O}_5$  [3a-c, 4],  $\text{MoO}_3$  [5a-c, 7a],  $\text{MoS}_2$  [10b, c, 11, 7a],  $\text{TiS}_2$  [11a] and  $\text{NbSe}_2$  [12], in combination with various polymers.

$\text{MoO}_3$  is one of the layered metal oxides which shows reversible Li ion insertion properties which are relevant to rechargeable Li batteries [15].



In intercalative electrodes of rechargeable batteries, ion conductivity is very important. Other solid-state ionic applications such as electrochromic devices also need good ion conductivity. Inorganic/Polymer nanocomposites should exhibit fast ion conduction [1g] and introduction of a polymer with affinity for Li ions between the sheets of MoO<sub>3</sub> could improve its performance as an intercalative electrode.

Polymer insertion into MoO<sub>3</sub> has been reported previously, namely, with a polymeric ionomer [5a, b], with PEO [5c, 7a] and with polyaniline [5d, 6, 7b]. This research develops further the polymer intercalation chemistry associated with MoO<sub>3</sub> and introduces a new family of Li<sub>x</sub>MoO<sub>3</sub>/polymer nanocomposites. Nanocomposites with poly(ethyleneoxide) (PEO), poly(ethyleneglycol) (PEG), poly(propyleneglycol) (PPG), poly(vinylpyrrolidinone) (PVP), methylcellulose (MCel), polyacrylamide (PAM) and nylon-6 (PA-6) are reported here. These nanocomposites were characterized by thermal gravimetric analysis (TGA), differential scanning calorimetry (DSC), powder X-ray diffraction, FTIR and solid-state UV-VIS spectroscopy, variable-temperature solid-state <sup>7</sup>Li and <sup>13</sup>C NMR spectroscopy, magnetic susceptibility measurements and electrical conductivity measurements.

## **Experimental Section**

### **1. Reagents**

PEO (5,000,000), PEO (100,000), PEG (10,000), PEG (2,000), PEG (400), PPG (1,000), PVP (10,000), MCel (63,000), PAM (5,000,000), PA-6 (10,000) and LiBH<sub>4</sub> (95%) were purchased from Aldrich Chemical Company, Inc. After the polymers were dissolved, the



polymer solutions were filtered to remove insoluble polymer residues. MoO<sub>3</sub> (99.95%) was purchased from Johnson Matthey Catalog Company. Anhydrous diethyl ether (99.0%), 2,2,2-trifluoroethanol (99%), acetonitrile (99.5%), isopropynol (99.9%) and 200 proof ethanol were from Columbus Chemical industries Inc., Lancaster Synthesis Inc., EM Science Inc., Mallinckrodt Chemical Inc. and Quantum Chemical Company respectively. No further purification was applied to the chemicals above. Water used in the reactions was distilled water provided by the Department of Chemistry, and was degassed by bubbling nitrogen for 30 min before use.

## 2. Synthesis of Li<sub>x</sub>MoO<sub>3</sub> (0.30 < x < 0.40)

Commercial MoO<sub>3</sub>, used as the starting material, was fired in an open quartz vial in the air at 600 °C for 36 h during which the crystal size of MoO<sub>3</sub> remarkably increased. This MoO<sub>3</sub> was used to react with LiBH<sub>4</sub> to prepare the lithium molybdenum bronze [16]. In a typical reaction, 0.1 mol of MoO<sub>3</sub> was reacted with 0.04 mol of LiBH<sub>4</sub> in 80 ml diethyl ether for 24 h, under a nitrogen atmosphere. The product was collected by filtration, washed with ether and dried *in vacuo*. The yield was >98%. The lithium molybdenum bronze was thereafter stored in a nitrogen dry-box. The X-ray powder diffraction pattern can be indexed on the basis of an orthorhombic cell similar to that of MoO<sub>3</sub> but expanded along the stacking (*a*-axis) direction, with *a*= 16.528 Å, *b*=3.775 Å and *c*=3.969 Å. The *d*<sub>*hkl*</sub>-spacings (Å) are: 8.26<sub>200</sub> (vs), 4.132<sub>400</sub> (s), 3.578<sub>201</sub> (m), 3.434<sub>210</sub> (m), 2.755<sub>600</sub> (w), 2.453<sub>311</sub> (m) and 2.372<sub>411</sub> (m).

The amount of lithium in the bronze was analyzed by TGA under oxygen flow, heating up to 650 °C, and by elemental analysis which was



accomplished by Oneida Research Services, Inc., Whitesboro, New York. Elemental analysis of Li in the molybdenum bronze was done by ion chromatography, while Mo was measured by X-ray fluorescence.

### 3. Preparation of $\text{Li}_x\text{MoO}_3$ /Polymer Nanocomposites

The  $\text{Li}_x\text{MoO}_3$  was exfoliated in degassed water by 5 minutes of sonication, to form a suspension with a concentration of 5 g/L. This suspension was added dropwise into a stirred polymer solution of the same volume, which contained five times of excess polymer (per repeat unit) to  $\text{MoO}_3$  and the mixture was stirred for 2 days under a nitrogen atmosphere. The nanocomposites formed were isolated in different ways according to their behavior in solution. Nanocomposites of methylcellulose, polyacrylamide and nylon-6 precipitated and were collected by filtration. Those containing MCell and PAM were washed with water, while the nanocomposites of PA-6 were washed with trifluoroethanol. Nanocomposites with poly(ethylene oxide) (PEO), poly(ethylene glycol) (PEG), poly(propylene glycol) (PPG) and poly(vinylpyrrolidinone) (PVP) remained in colloidal form and were isolated by pumping off the water to dryness. The dried material was stirred in an appropriate solvent for several hours to dissolve the extraneous polymer. The solid product was filtered and was washed again with the solvent. The solvents used to process the products are list in Table 4.1. The products were pumped to dryness and stored in a nitrogen atmosphere.

### 4. Instrumentation

The instrumentation in the measurements such as X-ray powder diffraction (XRD) patterns, thermal gravimetric analysis (TGA),

redalig@redalig.com  
123456789

differential scanning calorimetry (DSC) and infrared (IR) spectroscopy were the same as described in Chapter 1. Room temperature conductivity measurements, variable temperature direct-current electrical conductivity measurements and thermopower measurements, and magnetic susceptibility measurements were conducted as described in Chapter 2.

Variable-temperature solid-state  $^7\text{Li}$  and  $^{13}\text{C}$  NMR measurements were taken on a 400 MHz Varian Nuclear Magnetic Resonance Instrument. Samples were loaded in a glove-box under a nitrogen atmosphere. Electronic transmission spectra were recorded with a Shimadzu UV-3101PC UV-VIS-NIR scanning spectrophotometer. Samples were dried as thin films on quartz slides.

## Results and Discussion

### 1. Synthesis and Characterization of $\text{Li}_x\text{MoO}_3$

The lithium molybdenum bronze exfoliates readily in water to form stable colloidal solutions, and this makes it an appealing candidate for polymer intercalation. The  $\text{LiBH}_4$  route to  $\text{Li}_x\text{MoO}_3$  is the best one to date in providing the material conveniently and in high yield. The previously reported method for  $\text{Li}_x(\text{H}_2\text{O})_y\text{MoO}_3$  [17] involves one step to prepare  $\text{Na}_x(\text{H}_2\text{O})_y\text{MoO}_3$  and two steps to accomplish ion-exchange and gives only 26% yield [18]. An additional advantage of the  $\text{LiBH}_4$  method is that it is conducted in diethyl ether and so provides the anhydrous form of the molybdenum bronze. The  $\text{Li}_x\text{MoO}_3$  product prepared in this fashion, though still crystalline, shows broader diffraction maxima than the precursor  $\text{MoO}_3$ . The Li insertion into  $\text{MoO}_3$  is topotactic as evidenced by

our ability to fully index the X-ray powder diffraction pattern of the product.

The amount of Li in  $\text{Li}_x\text{MoO}_3$  was determined both by TGA and by direct elemental analysis. When the material is heated in an oxygen atmosphere to 650 °C, it gains 1.71 mass%, owing to a change from  $\text{Li}_x\text{MoO}_3$  to  $\text{Li}_2\text{O}$  and  $\text{MoO}_3$ . This gain of mass is reproducible and corresponds to an  $x$  value of 0.31(3). On the other hand, the elemental analysis showed that the molybdenum bronze consisted of 1.64% Li and 56.39% Mo. This gives a ratio of Li to Mo of 0.4:1 corresponding to the molar ratio of  $\text{LiBH}_4$  used in the lithiation reaction. It is of course possible that  $x$  varies slightly from sample to sample in the range  $0.3 < x < 0.4$ .

The lithium molybdenum bronze is metastable and undergoes an intense, irreversible and exothermic phase change at 356 °C, as detected by DSC (Figure 4.1) and X-ray powder diffraction. The product appears to be

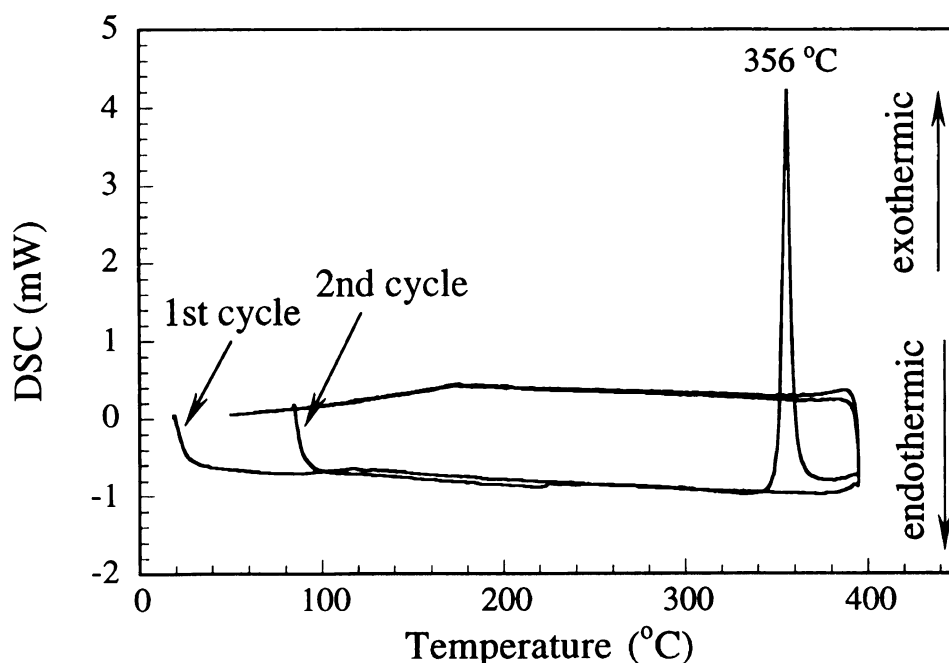
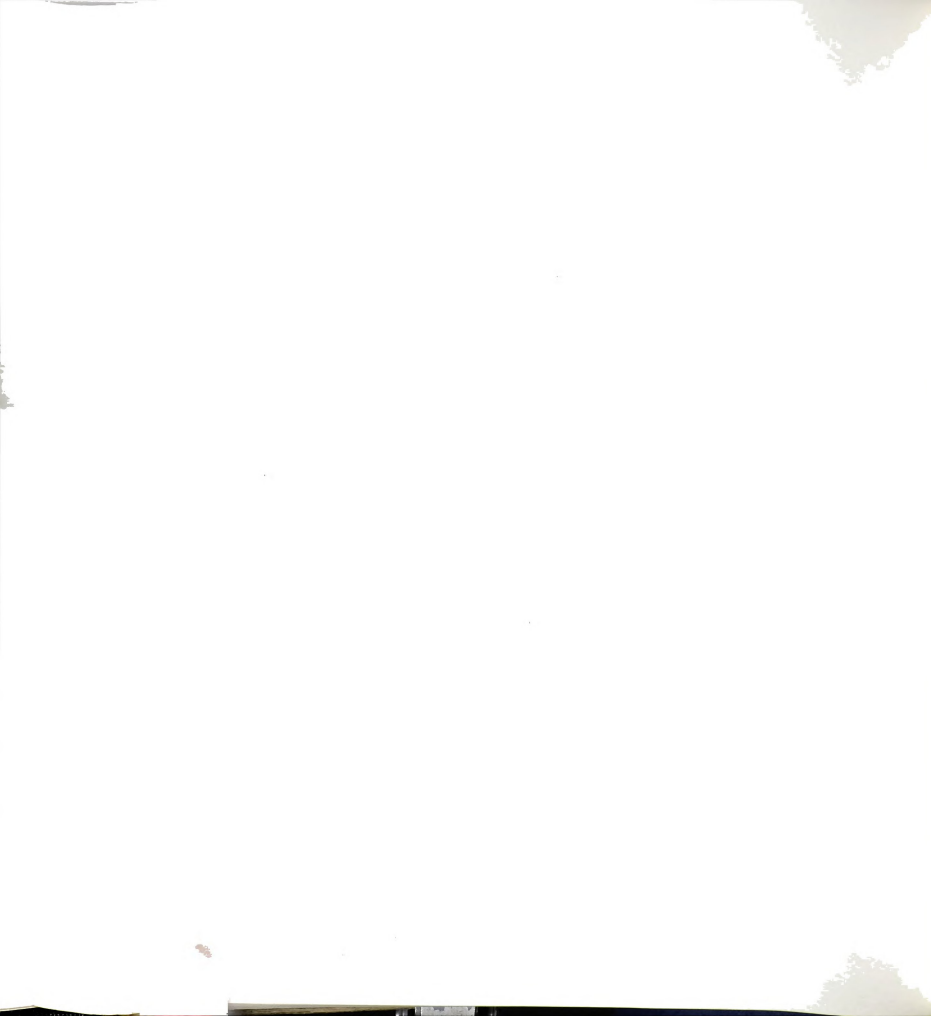


Figure 4.1. DSC diagram of  $\text{Li}_x\text{MoO}_3$ .



a mixture of at least two unknown phases. As this mixture is heated to higher temperatures it undergoes additional phase changes yielding other new phases.

## 2. Exfoliation and Polymer Encapsulation Chemistry

The lithium molybdenum bronze described above can be readily exfoliated in water after several minutes of sonication. The exfoliated product forms supramolecular complexes with most water-soluble polymers. The complexes form solutions or precipitates in water, depending on the type and molecular mass of the polymers. We have encapsulated PEO, PEG, PPG, PAM, MCel and PVP inside the lithium molybdenum bronze to obtain lamellar nanocomposite materials.

Poly(ethylenimine) (PEI) could not be successfully intercalated. Instead, the blue  $\text{Li}_x(\text{H}_2\text{O})_y\text{MoO}_3$  monolayer suspension decolorized and totally dissolved in the aqueous PEI solution. The same phenomenon occurred when ammonia was introduced in the  $\text{Li}_x(\text{H}_2\text{O})_y\text{MoO}_3$  suspension, suggesting that the PEI solution is too basic and attacks the  $\text{MoO}_3$  lattice. Water-insoluble polymers were also tried, however of these, only PA6 was successfully intercalated. Details of the reactions are given in Table 4.1.

The existence of polymer chains between the layers of the lithium molybdenum bronze was verified by IR spectroscopy and X-ray powder diffraction. Figure 4.2 shows a comparison of the IR spectra of a nanocomposite  $\text{Li}_x(\text{H}_2\text{O})_y(\text{PVP})_z\text{MoO}_3$  and its components; from this, it is obvious that the vibrational peaks of  $\text{Li}_x(\text{H}_2\text{O})_y(\text{PVP})_z\text{MoO}_3$  is a combination of the vibrational peaks of PVP and that of  $\text{Li}_x(\text{H}_2\text{O})_y\text{MoO}_3$ . The positions of the vibrational peaks arising from the encapsulated PVP are close to those of pure PVP, while the positions of the peak due to the



Table 4.1. Chemical and structural characteristics of  $\text{Li}_x\text{MoO}_3$ /polymer nanocomposites

| nanocomposite                   | polymer Mw      | solubility <sup>a</sup> | washing solvent                   | d-spacing (Å)             | expansion of gallery (Å) | coherence length (Å) |
|---------------------------------|-----------------|-------------------------|-----------------------------------|---------------------------|--------------------------|----------------------|
| $\text{Li}_x\text{MoO}_3$ /PEO  | $5 \times 10^6$ | yes                     | MeCN                              | 16.6                      | 9.7                      | 64                   |
| $\text{Li}_x\text{MoO}_3$ /PEO  | 100,000         | yes                     | MeCN                              | 16.6                      | 9.7                      | 121                  |
| $\text{Li}_x\text{MoO}_3$ /PEO  | 10,000          | yes                     | MeCN                              | 16.8                      | 9.9                      | 108                  |
| $\text{Li}_x\text{MoO}_3$ /PEG  | 2,000           | yes                     | MeCN                              | 13.8<br>12.6-14.7         | 6.9<br>5.7-7.8           | 72<br>- b            |
| $\text{Li}_x\text{MoO}_3$ /PEG  | 400             | yes                     | MeCN                              | 13.5<br>12.6              | 6.6<br>5.7               | 111<br>97            |
| $\text{Li}_x\text{MoO}_3$ /PEG  | 1,000           | yes                     | EtOH                              | 17.2<br>11.8<br>18.0&11.5 | 10.3<br>4.9<br>-         | 113<br>108<br>- b    |
| $\text{Li}_x\text{MoO}_3$ /MCel | 63,000          | no                      | $\text{H}_2\text{O}$              | 27.6                      | 20.7                     | 92                   |
| $\text{Li}_x\text{MoO}_3$ /PVP  | 10,000          | yes                     | PrOH                              | 38.6                      | 31.7                     | 154                  |
| $\text{Li}_x\text{MoO}_3$ /PAM  | $5 \times 10^6$ | no                      | $\text{H}_2\text{O}$              | 38.0<br>33.8<br>41.2      | 31.1<br>26.9<br>34.3     | 69<br>80<br>- b      |
| $\text{Li}_x\text{MoO}_3$ /PA6  | 10,000          | no                      | $\text{CF}_3\text{CH}_2\text{OH}$ | 22.1<br>16.8              | 15.2<br>9.9              | 39<br>26             |

a. Nanocomposites dissolved in water, except for  $\text{Li}_x\text{MoO}_3$ /PA6, dissolved in 222-trifluoroethanol.

b. Peaks too broad to obtain estimate.



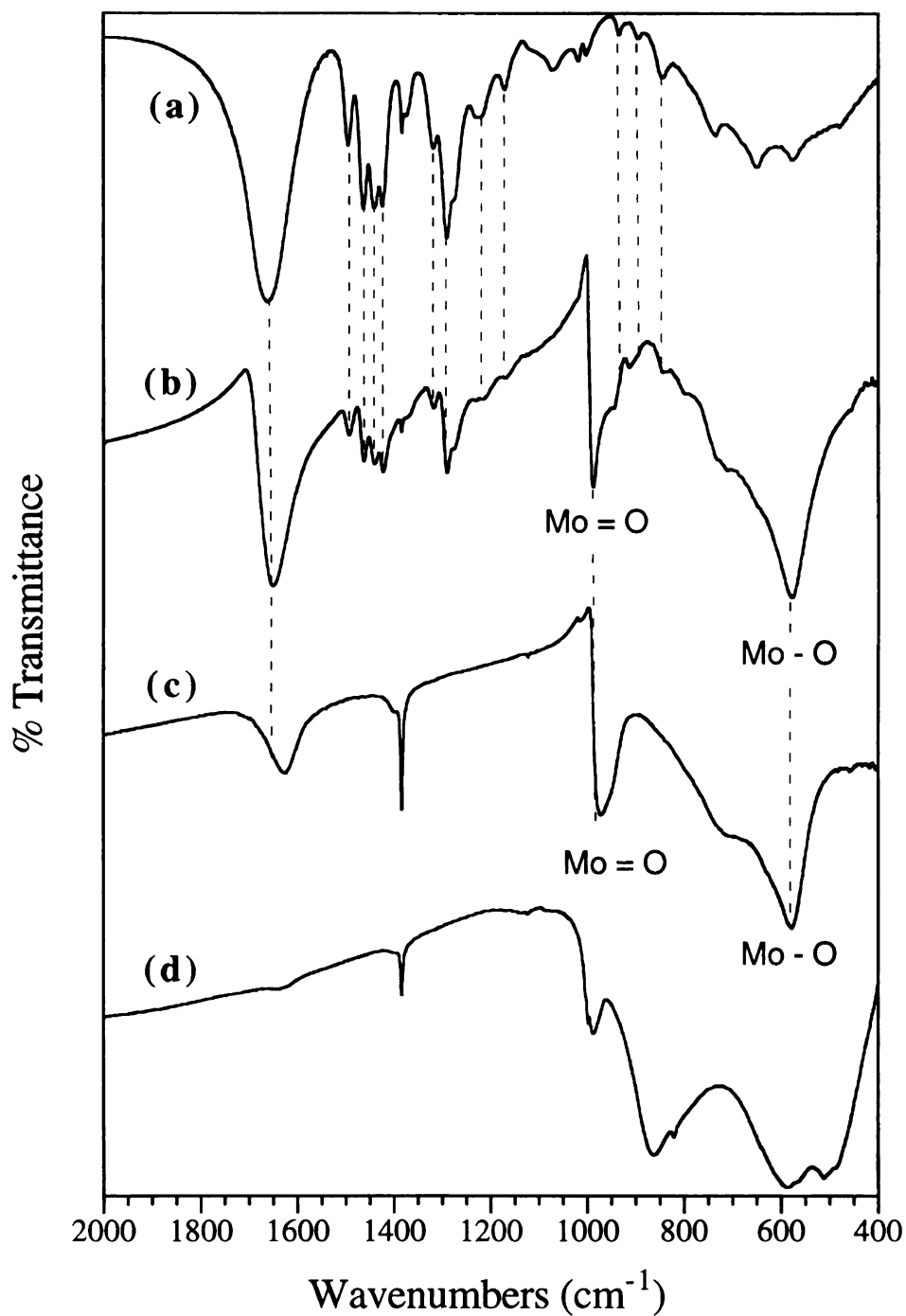


Figure 4.2. IR spectra of (a) poly(vinylpyrrolidinone), (b)  $\text{Li}_x(\text{H}_2\text{O})_y(\text{PVP-10,000})_z\text{MoO}_3$ , (c) hydrated lithium molybdenum bronze, and (d)  $\text{MoO}_3$ .



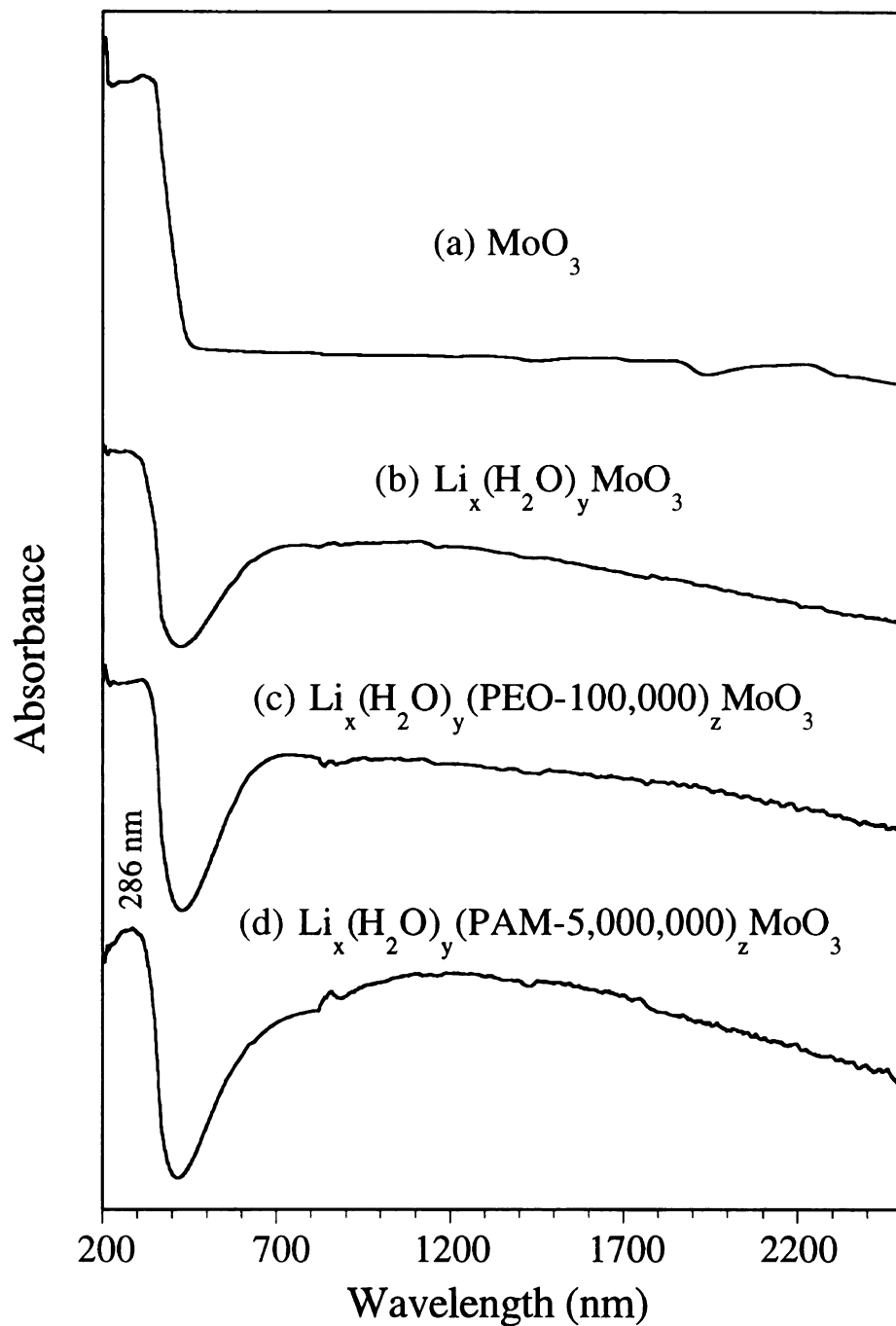


Figure 4.3. Solid-state optical absorption spectra of the  $\text{Li}_x\text{MoO}_3$ /polymer nanocomposites. The polymer and its molecular mass are indicated on each spectrum.



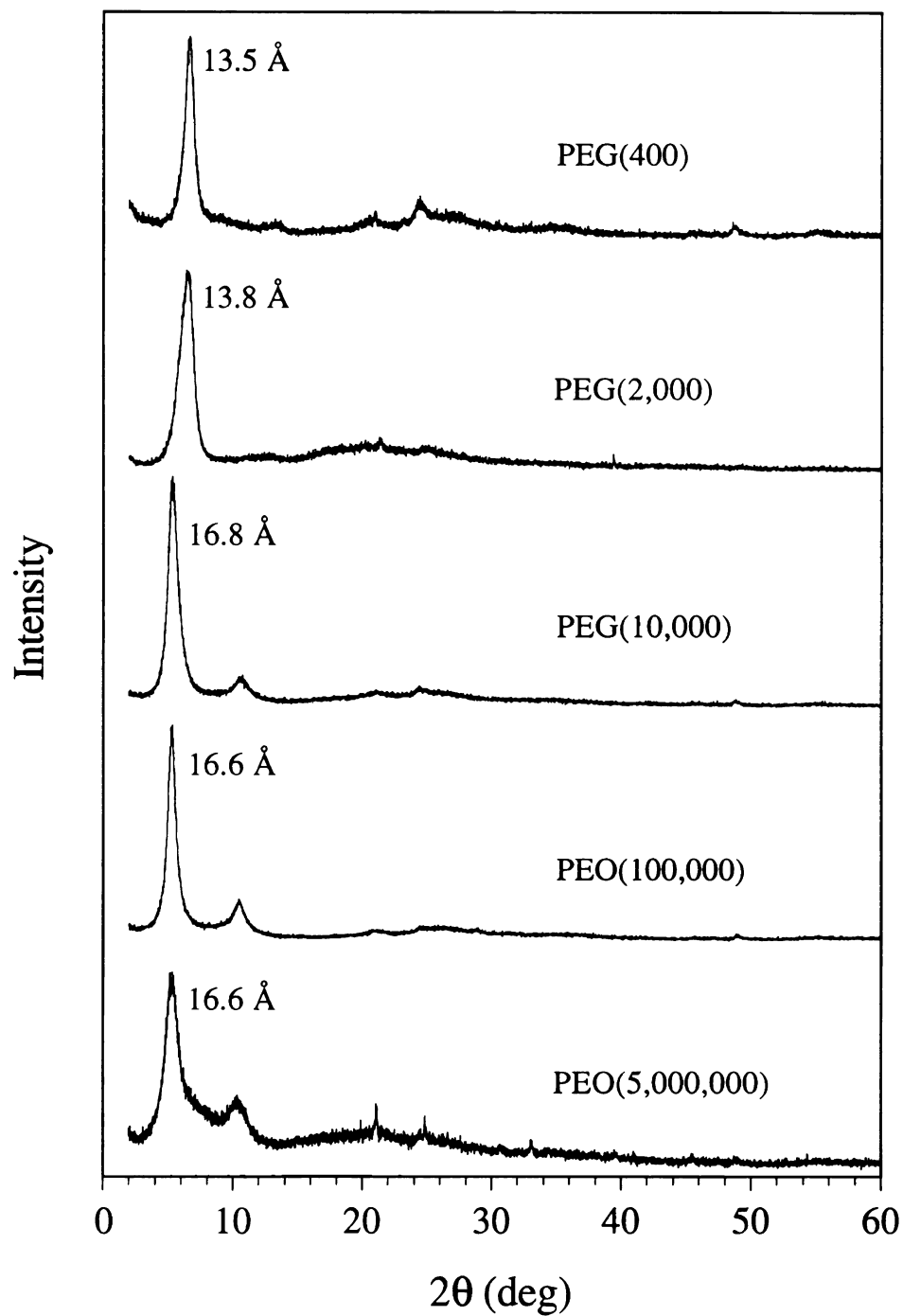


Figure 4.4. Typical XRD patterns of nanocomposites with poly(ethylene glycol) and poly(ethylene oxide) of different molecular mass. The polymer and its molecular mass are indicated on each spectrum.



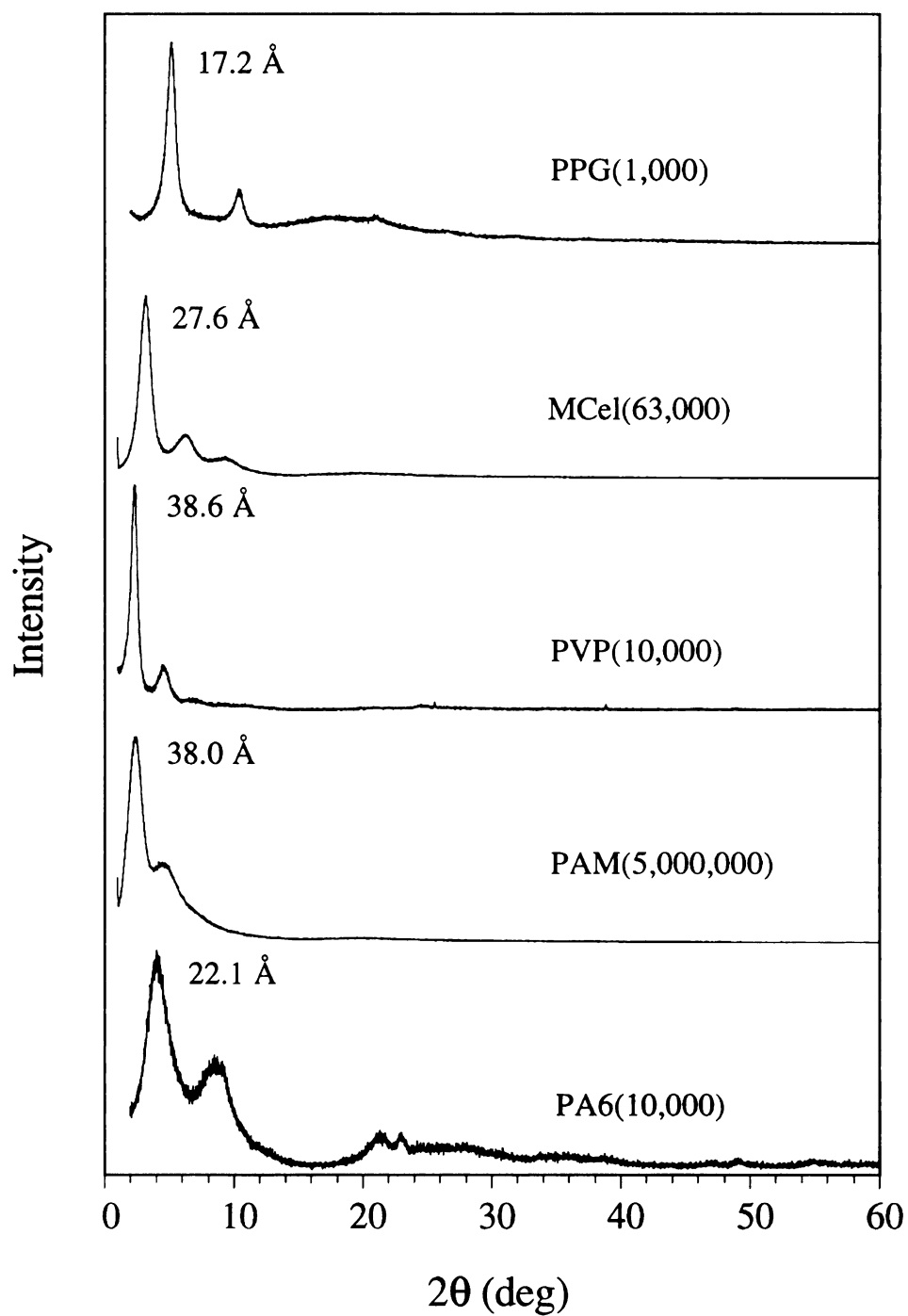
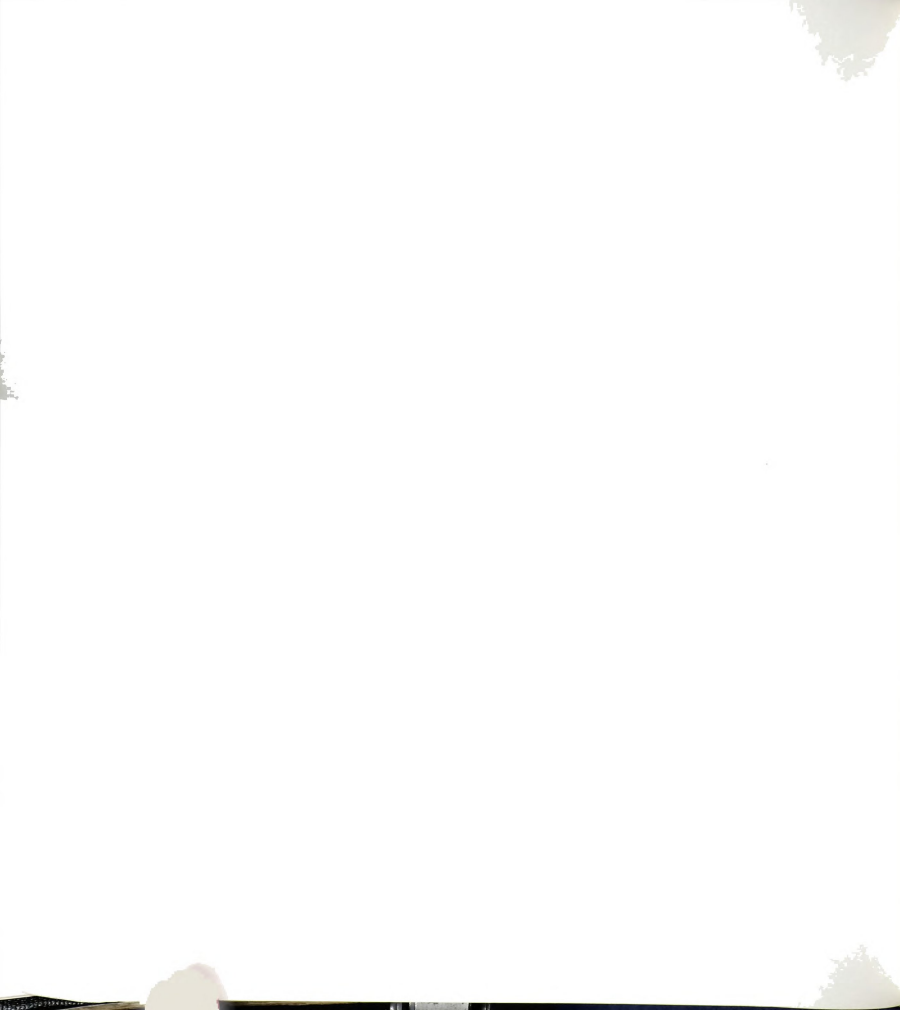


Figure 4.5. Typical XRD patterns of the various  $\text{Li}_x\text{MoO}_3$ /polymer nanocomposites.



Mo=O stretch [for  $\text{Li}_x(\text{H}_2\text{O})_y\text{MoO}_3$ ] is shifted to higher wavenumbers, suggesting that the  $\text{MoO}_3$  layers in the nanocomposite are slightly more oxidized.

The optical transmission absorption spectra of these macromolecular intercalates were examined. The dark-blue color of these systems arises from the intense intervalence transitions associated with the  $\text{Mo}^{5+}/\text{Mo}^{6+}$  couple. These electronic transitions are broad and range from the IR region to the visible (Figure 4.3) and are responsible for the electrical conductivity of these materials. The absorption at 286 nm arises from excitations across the band-gap from the  $\text{O}^{2-}$  p-band to the  $\text{Mo}^{6+}$  d-band and is present in all compounds including pristine  $\text{MoO}_3$  and  $\text{Li}_x(\text{H}_2\text{O})_y\text{MoO}_3$ . This is consistent with the expectation that host metal oxide structure is not disturbed upon intercalation.

The encapsulation of polymers inside the interlayer galleries of  $\text{MoO}_3$  is also demonstrated by X-ray powder diffraction, which shows an expansion of the gallery space. Figures 4.4 and 4.5 show typical XDR patterns of some of the nanocomposites. The sharp and intense (001) reflections indicate that the  $\text{MoO}_3$  layers are well stacked. X-Ray scattering coherence lengths, which are calculated from the Scherrer formula  $L_{hkl} = K\lambda/\beta\cos\theta$  (see Reference 18 of Chapter 2), and the gallery spacings are given in Table 4.1.

The basal spacing of some nanocomposites depends on the preparation procedure. For example,  $\text{Li}_x(\text{H}_2\text{O})_y(\text{PVP})_z\text{MoO}_3$ , which is water soluble, showed a d-spacing of 59.0 Å before washing with isopropyl alcohol and 38.3 Å after washing. Washing these materials may not only remove extra-lamellar polymer, but could lead to polymer loss from the galleries changing their composition. This behavior makes it difficult to



determine at what polymer loading we begin to saturate the intralamellar space. Similar phenomena were described in polymer-V<sub>2</sub>O<sub>5</sub> xerogel systems [3a]. Nevertheless, the observed d-spacings were consistent to within  $\pm 1$  Å, as long as the preparation procedures were not altered significantly from batch to batch. The d-spacings and the degrees of lamellar stacking of products which contained polymers at the very extremes of the molecular mass range (very high or very low) were hard to control, as for example in PEO(5,000,000), PEG(2,000) and PPG(1,000). The Li<sub>x</sub>(H<sub>2</sub>O)<sub>y</sub>(PEO-5,000,000)<sub>z</sub>MoO<sub>3</sub> had a consistent d-spacing *ca.* 16.6 Å, but the peaks were broad. Li<sub>x</sub>(H<sub>2</sub>O)<sub>y</sub>(PEG-2,000)<sub>z</sub>MoO<sub>3</sub> showed broad peaks in the range 12.6-14.7 Å. Li<sub>x</sub>(H<sub>2</sub>O)<sub>y</sub>(PPG-1,000)<sub>z</sub>MoO<sub>3</sub> sometimes showed a peak in the range 11.8 Å-17.2 Å, while other samples showed two peaks in this range suggesting a mixture of phases. Evidently, for low molecular masses the polymers are mobile enough in the galleries to form several different arrangements leading to multiple phases.

The effect of polymer molecular mass on product formation was examined, particularly with PEO and PEG, and was found to be significant. The high molecular mass PEO(5,000,000) immediately formed a precipitate with lithium molybdenum bronze in water upon mixing while this phenomenon did not occur with PEO of lower molecular mass. The molecular mass also affects the structure of the nanocomposites. Table 4.1 shows that the Li<sub>x</sub>(H<sub>2</sub>O)<sub>y</sub>(PEO-5,000,000)<sub>z</sub>MoO<sub>3</sub> sample has a lower coherence scattering length than its lower molecular mass analogues, which is attributed to the fact that it is kinetically unfavorable for extremely long polymer chains to align in an ordered structure. When the molecular mass is extremely low, *i.e.* in oligomer range, the gallery expansion of the intercalate is lower, almost one half of that of the long polymers. For PEO

and PEG, a molecular mass of 2,000 is about the upper limit of this situation. The data listed in Table 4.1 show that the  $\text{Li}_x(\text{H}_2\text{O})_y(\text{PEG}-2,000)_z\text{MoO}_3$  sample has a much shorter coherence length than its analogues with higher or lower molecular masses. An analogous  $\text{Li}_x(\text{H}_2\text{O})_y(\text{PEG}-2,000)_z\text{MoO}_3$  sample, prepared under similar conditions, had a broad X-ray basal peak which corresponded to a d-spacing varying from 12.6 to 14.7 Å, suggesting that the local conformation of the polymer is important.

Annealing the  $\text{Li}_x(\text{H}_2\text{O})_y(\text{PEG})_z\text{MoO}_3$  and the  $\text{Li}_x(\text{H}_2\text{O})_y(\text{PEO})_z\text{MoO}_3$  samples at 150 °C and then gradually cooling them to room temperature tends to improve their lamellar order, especially when the starting coherence length is short. For example, after annealing, the  $\text{Li}_x(\text{H}_2\text{O})_y(\text{PEG}-2,000)_z\text{MoO}_3$  sample whose XRD pattern had a broad peak centered at 13.4 Å gave a pattern with a sharp peak at 12.7 Å, (Figure 4.6).

The water-insoluble nanocomposite  $\text{Li}_x(\text{H}_2\text{O})_y(\text{PAM}-5,000,000)_z\text{MoO}_3$  gave samples with d-spacings of 38.0, 33.8 and 41.2 Å. The  $\text{Li}_x(\text{H}_2\text{O})_y(\text{PA6}-10,000)_z\text{MoO}_3$  showed d-spacings of 22.1 and 16.8 Å. Occasionally, in the intercalation of PA-6 a mixed-phase material with basal spacings of 12.8 and 9.8 Å was obtained. This shows the difficulty to control the reaction when quick precipitation is used to obtain a specific phase. To prepare nanocomposites of this type, a very dilute  $\text{Li}_x(\text{H}_2\text{O})_y\text{MoO}_3$  suspension of < 0.5 mass% is recommended.

The polymer composition of the nanocomposites were determined by TGA in an oxygen atmosphere and are listed in Table 4.2. The water in the nanocomposites was estimated by the mass loss step observed below 230 °C, and the amount of polymer was determined by the mass loss steps observed at higher temperatures. Despite drying under vacuum, the nanocomposites



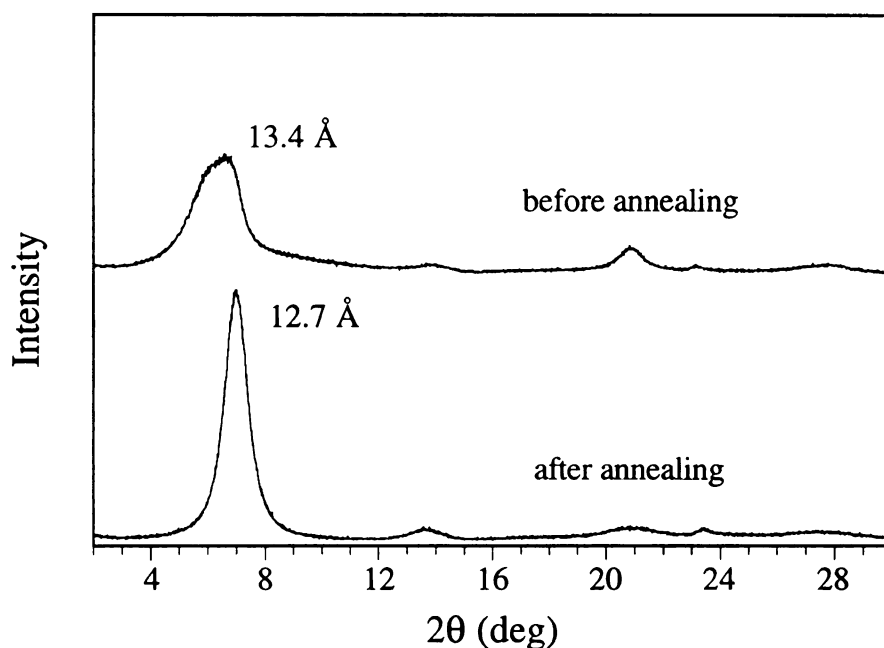


Figure 4.6. XRD patterns of  $\text{Li}_x(\text{H}_2\text{O})_y(\text{PEO-2000})_z\text{MoO}_3$  showing the effect of annealing on the stacking regularity of the layered structure of a nanocomposite.

contain some water in the galleries. The water-soluble nanocomposites,  $\text{Li}_x(\text{H}_2\text{O})_y(\text{PEO})_z\text{MoO}_3$ ,  $\text{Li}_x(\text{H}_2\text{O})_y(\text{PEG})_z\text{MoO}_3$ ,  $\text{Li}_x(\text{H}_2\text{O})_y(\text{PPG})_z\text{MoO}_3$ , and  $\text{Li}_x(\text{H}_2\text{O})_y(\text{PVP})_z\text{MoO}_3$ , usually contain 2-4 mass% water which is very difficult to remove. This water is thought to be coordinated to  $\text{Li}^+$  ions. The water-insoluble nanocomposites  $\text{Li}_x(\text{H}_2\text{O})_y(\text{MCell})_z\text{MoO}_3$  and  $\text{Li}_x(\text{H}_2\text{O})_y(\text{PAM})_z\text{MoO}_3$ , however, contain much less water.

Compared to the corresponding  $\text{MoS}_2$ /polymer intercalates [10b], most  $\text{Li}_x\text{MoO}_3$ /polymer intercalates have much higher polymer contents and larger gallery spacings. As in the case of  $\text{MoS}_2$ /polymer intercalates, PVP and MCell give the largest expansions. A marked difference is found in PAM which gives  $\text{Li}_x\text{MoO}_3$ /PAM an expansion as large as 27-35  $\text{\AA}$ , while  $\text{MoS}_2$ /PAM has only an expansion of 9.4  $\text{\AA}$  (see Chapter 1). This confirms

Table 4.2. Composition and physicochemical properties of the  $\text{Li}_x\text{MoO}_3$ /polymer nanocomposites

| nanocomposite                   | polymer $M_w$   | d-spacing (Å) | composition (according to TGA)   | limit of thermal stability in $\text{N}_2/^\circ\text{C}$ | limit of thermal stability in $\text{O}_2/^\circ\text{C}$ | electronic conductivity $/\text{Scm}^{-1}$ |
|---------------------------------|-----------------|---------------|--|---|---|--|
| pure $\text{Li}_x\text{MoO}_3$  |                 | 8.27          |  |   |   | $1.3 \times 10^{-2}$                       |
| pure $\text{MoO}_3$             |                 | 6.93          |  |   |   | $3.3 \times 10^{-5}$                       |
| $\text{Li}_x\text{MoO}_3$ /PEO  | $5 \times 10^6$ | 16.6          | $\text{Li}_x(\text{H}_2\text{O})_{0.20}\text{PEO}_{0.83}\text{MoO}_3$  | 260   | 220   | $2.4 \times 10^{-5}$                       |
| $\text{Li}_x\text{MoO}_3$ /PEO  | 100,000         | 16.6          | $\text{Li}_x(\text{H}_2\text{O})_{0.32}\text{PEO}_{1.04}\text{MoO}_3$  | 260   | 220   | $2.9 \times 10^{-5}$                       |
| $\text{Li}_x\text{MoO}_3$ /PEG  | 10,000          | 16.8          | $\text{Li}_x(\text{H}_2\text{O})_{0.29}\text{PEG}_{0.75}\text{MoO}_3$  | 260   | 220   | $5.2 \times 10^{-5}$                       |
| $\text{Li}_x\text{MoO}_3$ /PEG  | 2,000           | 13.8          | $\text{Li}_x(\text{H}_2\text{O})_{0.28}\text{PEG}_{0.57}\text{MoO}_3$  | 260   | 220   | $2.2 \times 10^{-4}$                       |
| $\text{Li}_x\text{MoO}_3$ /PEG  | 400             | 13.5          | $\text{Li}_x(\text{H}_2\text{O})_{0.38}\text{PEG}_{0.33}\text{MoO}_3$  | 260   | 220   | $3.1 \times 10^{-4}$                       |
| $\text{Li}_x\text{MoO}_3$ /PPG  | 1,000           | 17.2<br>11.8  | $\text{Li}_x(\text{H}_2\text{O})_{0.18}\text{PPG}_{0.99}\text{MoO}_3$<br>$\text{Li}_x(\text{H}_2\text{O})_{0.52}\text{PPG}_{0.14}\text{MoO}_3$ | 220   | 200   | -<br>$5.3 \times 10^{-4}$                  |
| $\text{Li}_x\text{MoO}_3$ /MCel | 63,000          | 27.6          | $\text{Li}_x\text{MCel}_{0.70}\text{MoO}_3$  | 180   | 170   | $2.0 \times 10^{-6}$                       |
| $\text{Li}_x\text{MoO}_3$ /PVP  | 10,000          | 38.6          | $\text{Li}_x(\text{H}_2\text{O})_{0.43}\text{PVP}_{1.17}\text{MoO}_3$  | 220   | 220   | $1.8 \times 10^{-7}$                       |
| $\text{Li}_x\text{MoO}_3$ /PAM  | $5 \times 10^6$ | 38.0          | $\text{Li}_x\text{PAM}_{3.2}\text{MoO}_3$  | 150   | 150   | $6.3 \times 10^{-7}$                       |
| $\text{Li}_x\text{MoO}_3$ /PA6  | 10,000          | 22.1<br>16.8  | $\text{Li}_x(\text{H}_2\text{O})_{0.44}\text{PA6}_{0.32}\text{MoO}_3$<br>$\text{Li}_x(\text{H}_2\text{O})_{0.48}\text{PA6}_{0.23}\text{MoO}_3$ | 280   | 270   | -<br>$2.1 \times 10^{-4}$                  |



that multiple layers of this polymer can enter the accessible space of  $\text{Li}_x\text{MoO}_3$ .

The water-soluble  $\text{Li}_x\text{MoO}_3$ /polymer nanocomposites can be cast into films and other shapes, which may provide opportunities for applications. The nanocomposites with high molecular mass polymers are strong, though their mechanical properties depend on the polymer. For example, the nanocomposite of PEO(5,000,000) is tough, while that of PAM(5,000,000) is hard.  $\text{Li}_x(\text{H}_2\text{O})_y(\text{PEO}-5,000,000)_z\text{MoO}_3$  can be swollen by acetonitrile and becomes resilient and plastic with the consistency of unsulfurized rubber. When the  $\text{Li}_x(\text{H}_2\text{O})_y(\text{PAM}-5,000,000)_z\text{MoO}_3$  is swollen by water, it is not as plastic, but is stronger and tougher. Precise mechanical measurements have not been taken.

### 3. Solid State NMR Spectroscopy

In order to probe the effect of the polymer on the behavior of the lithium ions in the gallery, variable-temperature solid-state  $^7\text{Li}$  NMR static spectra were measured for  $\text{Li}_x\text{MoO}_3$  and  $\text{Li}_x(\text{H}_2\text{O})_y(\text{PEO}-100,000)_z\text{MoO}_3$ . In both cases a broad peak was observed with a chemical shift very similar to that of the solid  $\text{LiCl}$  standard. At  $-80^\circ\text{C}$  the lineshape in the two spectra differs, with that of the  $\text{Li}_x(\text{H}_2\text{O})_y(\text{PEO}-100,000)_z\text{MoO}_3$  spectrum being slightly more asymmetric, Figure 4.7. This suggests that the presence of PEO causes a distribution of Li ions over several, slightly different sites in the gallery. Some of the sites may involve coordination of water molecules while other sites are associated with the ether-like oxygen atoms in PEO or even those in the  $\text{MoO}_3$  layers. The linewidth (width at half maximum) of the resonance peak is greater in the PEO intercalated sample than in the host  $\text{Li}_x\text{MoO}_3$  material and this too is consistent with a distribution of the



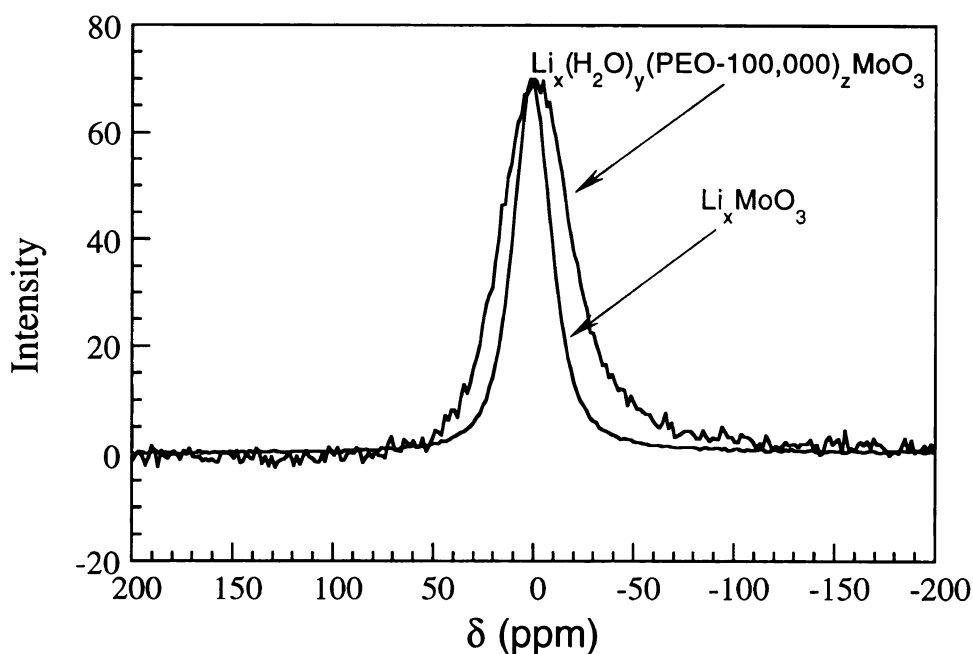


Figure 4.7. Static  ${}^7\text{Li}$  NMR spectra of  $\text{Li}_x\text{MoO}_3$  and  $\text{Li}_x(\text{H}_2\text{O})_y(\text{PEO-100,000})_z\text{MoO}_3$  at  $-80\text{ }^\circ\text{C}$ . The broader asymmetric line in the spectrum of the nanocomposite is evident in the upfield region.

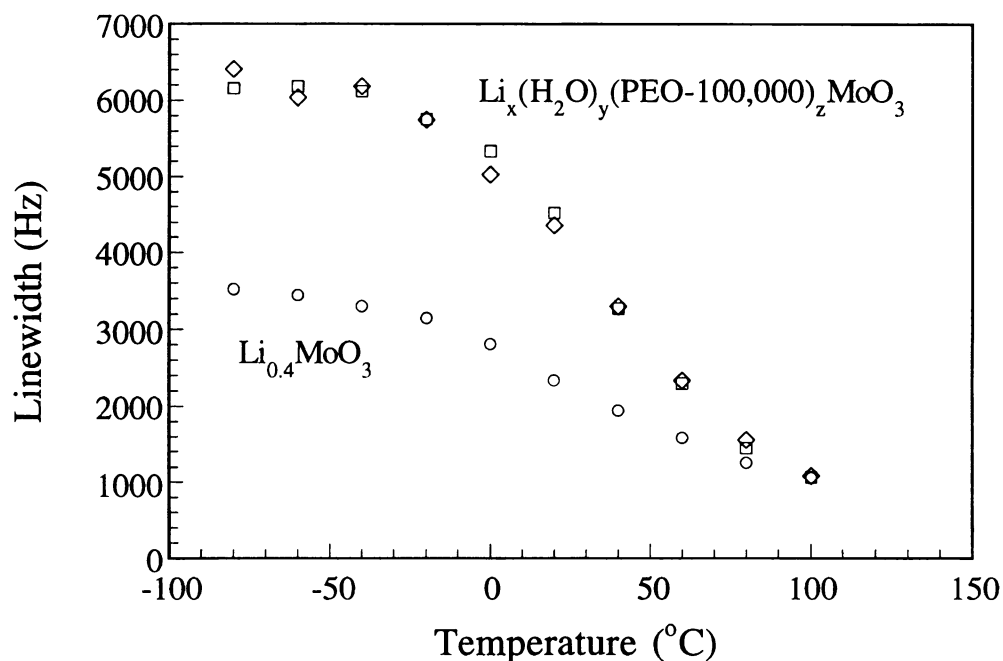
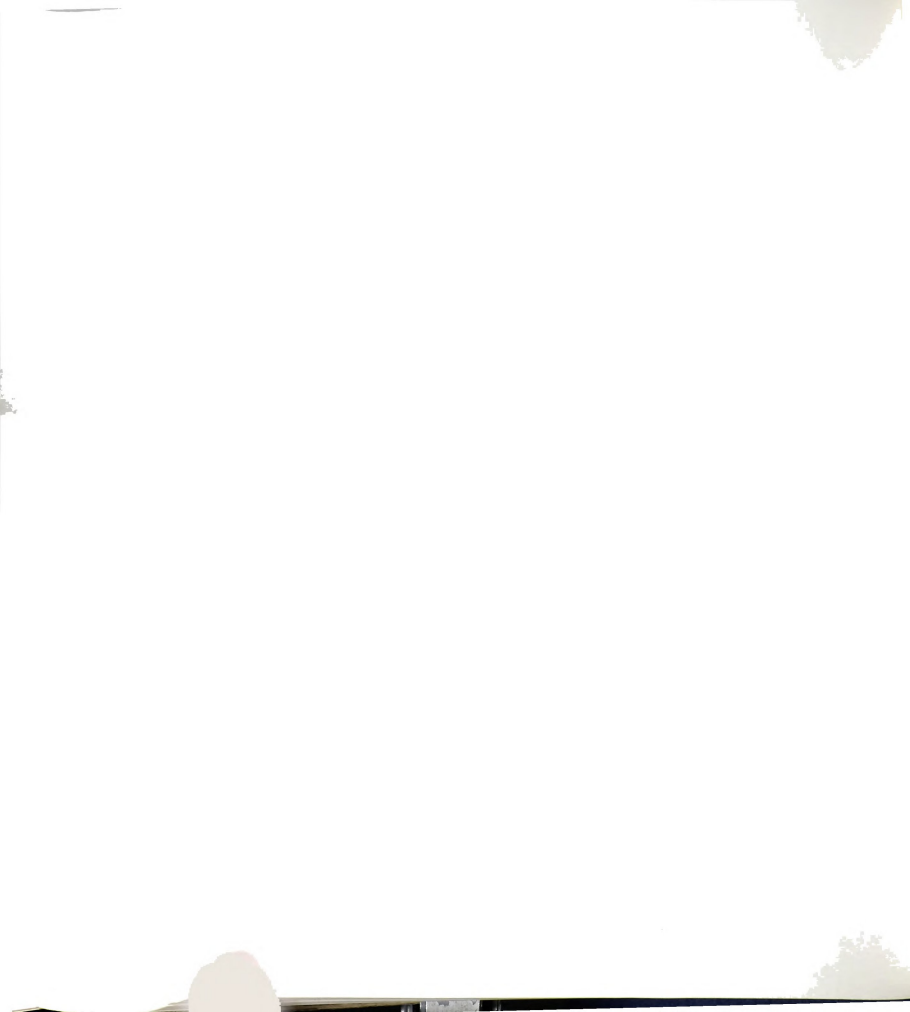


Figure 4.8. Temperature dependence of the linewidth of the resonance peak in solid-state  ${}^7\text{Li}$  MNR spectra of  $\text{Li}_x\text{MoO}_3$  and  $\text{Li}_x(\text{H}_2\text{O})_y(\text{PEO-100,000})_z\text{MoO}_3$ .



$\text{Li}^+$  ions over several sites in the former. The data in the low-temperature region suggest a more well defined coordination environment for the  $\text{Li}^+$  ion in  $\text{Li}_x\text{MoO}_3$  as would be expected in this crystalline solid.

The linewidth of 2300 Hz in  $\text{Li}_x\text{MoO}_3$  at 23 °C is much narrower than that of ~12000 Hz observed for  $\text{Li}_2\text{Mo}_2\text{O}_4$  indicating substantial degree of ion motion in the lattice of  $\text{Li}_x\text{MoO}_3$  relative to that of  $\text{Li}_2\text{Mo}_2\text{O}_4$  [19]. This is rationalized by the fact that in the latter the  $\text{Li}^+$  ions fully occupy well defined crystallographic positions in the lattice [20] while the non-stoichiometric nature of  $\text{Li}_x\text{MoO}_3$  gives rise to Li mobility *via* vacant crystallographic sites.

The resonance peak in both samples narrows dramatically as the temperature is increased from -80 °C to 100 °C, Figure 4.8. This is attributed to rapid motion of  $\text{Li}^+$  ions between the  $\text{MoO}_3$  layers. At 100 °C the peak linewidth in the spectra of  $\text{Li}_x(\text{H}_2\text{O})_y(\text{PEO-100,000})_z\text{MoO}_3$  is comparable to that of  $\text{Li}_{0.5}(\text{H}_2\text{O})_{1.3}\text{Mo}_2\text{O}_4$  [19]. The onset temperature of the transition from a wide to a narrow peak in  $\text{Li}_x(\text{H}_2\text{O})_y(\text{PEO-100,000})_z\text{MoO}_3$  and  $\text{Li}_x\text{MoO}_3$  is similar. The spectra of both materials end up with an equally narrow peak at 100 °C indicating comparable rates of hopping of Li ions between different positions in the interior of the two materials.

#### 4. Magnetism

Because the materials are formally mixed-valence compounds and exhibit intense intervalence  $\text{Mo}^{5+}$ - $\text{Mo}^{6+}$  optical transitions, we expect unpaired electrons to be delocalized over the d-orbitals of the Mo atoms. Magnetic susceptibility measurements were carried out as a function of temperature for  $\text{Li}_x\text{MoO}_3$  and  $\text{Li}_x(\text{H}_2\text{O})_y(\text{PEO-100,000})_z\text{MoO}_3$  and the data are displayed in Figure 4.9. Surprisingly, the susceptibility of both



compounds is rather small with substantial contributions from temperature independent paramagnetism ( $\chi_{\text{TIP}}$ ). Correcting for the latter  $1/(\chi_{\text{molar}} - \chi_{\text{TIP}})$  vs. T plots for  $\text{Li}_x\text{MoO}_3$  and  $\text{Li}_x(\text{H}_2\text{O})_y(\text{PEO-100,000})_z\text{MoO}_3$  are linear in the temperature ranges 5-120 K and 2-300 K, respectively. The Curie constants estimated from the slope of the plots yield  $\mu_{\text{eff}}$  of 0.15 and 0.09 respectively, however, the weak susceptibilities and the large diamagnetic and  $\chi_{\text{TIP}}$  corrections make  $\mu_{\text{eff}}$  values unreliable. It is interesting that the magnetic properties of  $\text{Li}_x\text{MoO}_3$  are more similar to those of  $\text{Li}_{0.9}\text{Mo}_6\text{O}_{17}$  [21] than of other molybdenum bronzes such as the blue bronze  $\text{A}_{0.3}\text{MoO}_3$  (A=K,Tl) and purple bronzes  $\text{A}_{0.9}\text{Mo}_6\text{O}_{17}$  (A=K, Na, Tl) [22]. In the latter bronzes the temperature dependence of the magnetic susceptibility shows transitions at low temperature associated with charge density waves. Such phenomena were not observed in the  $\text{Li}_x\text{MoO}_3$  samples reported here.

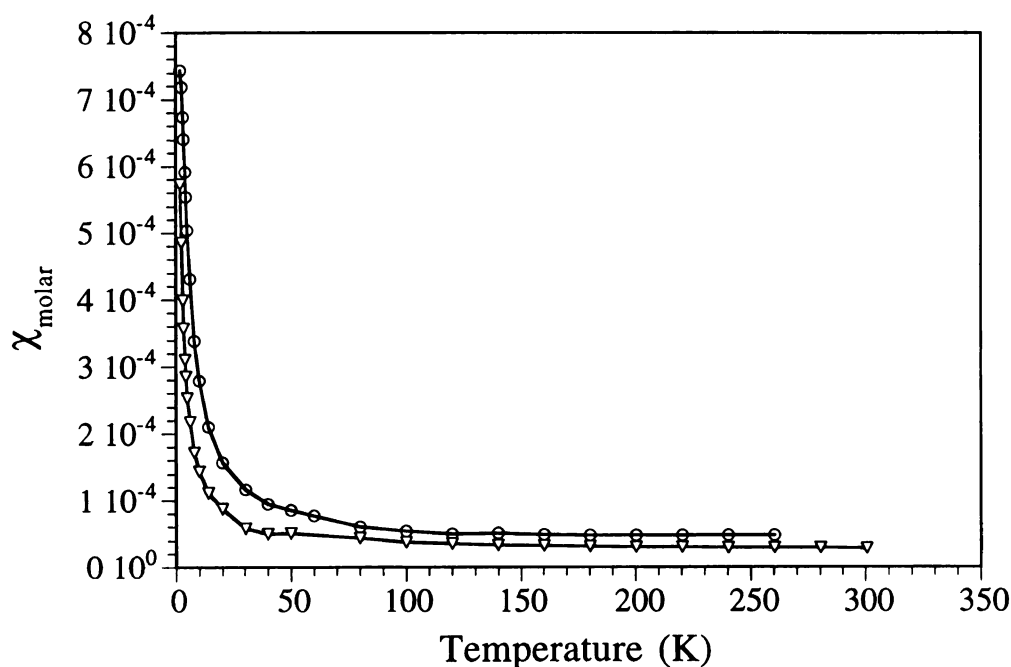
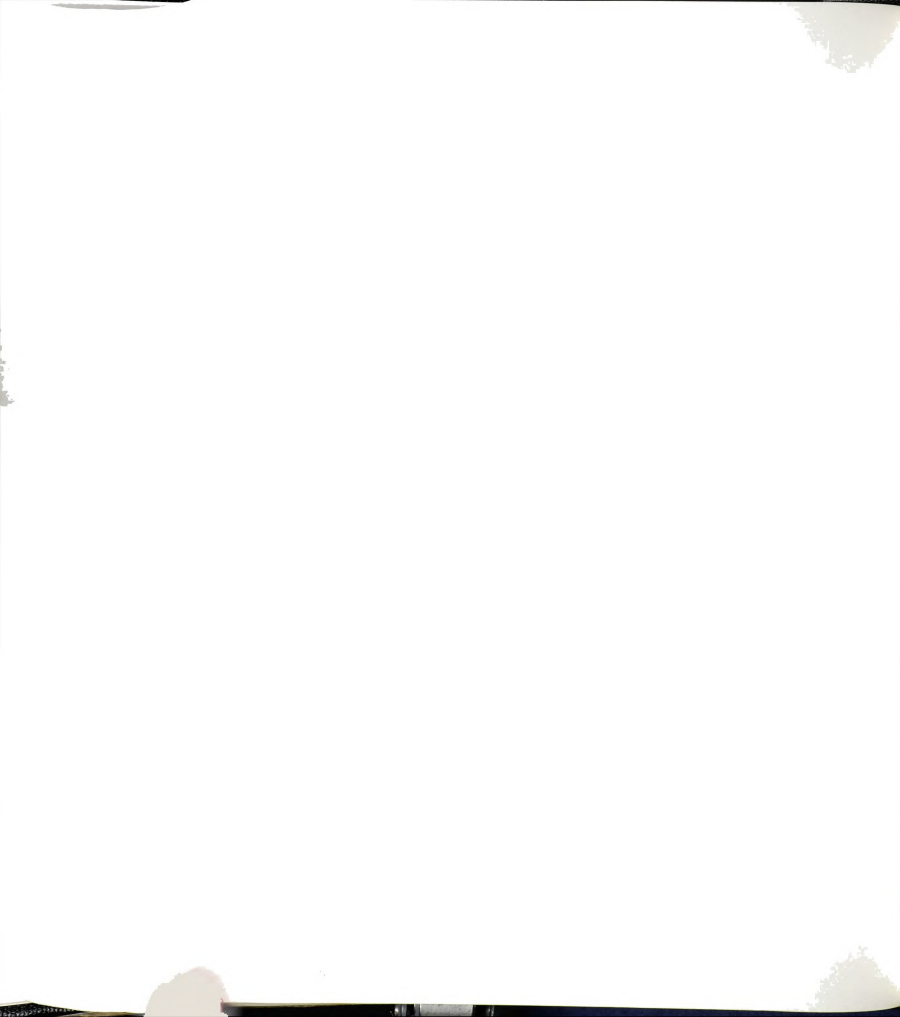


Figure 4.9. Temperature dependence of magnetic susceptibility of  $\text{Li}_x\text{MoO}_3$  (circles) and  $\text{Li}_x(\text{H}_2\text{O})_y(\text{PEO-100,000})_z\text{MoO}_3$  (triangles). The measurements were conducted at 1000 G with powder samples.



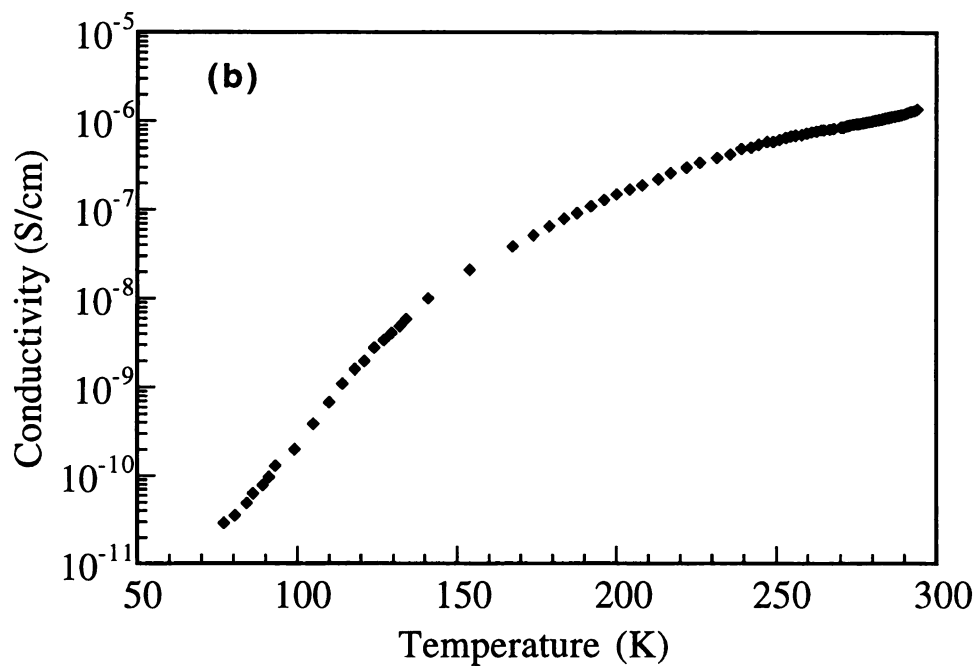
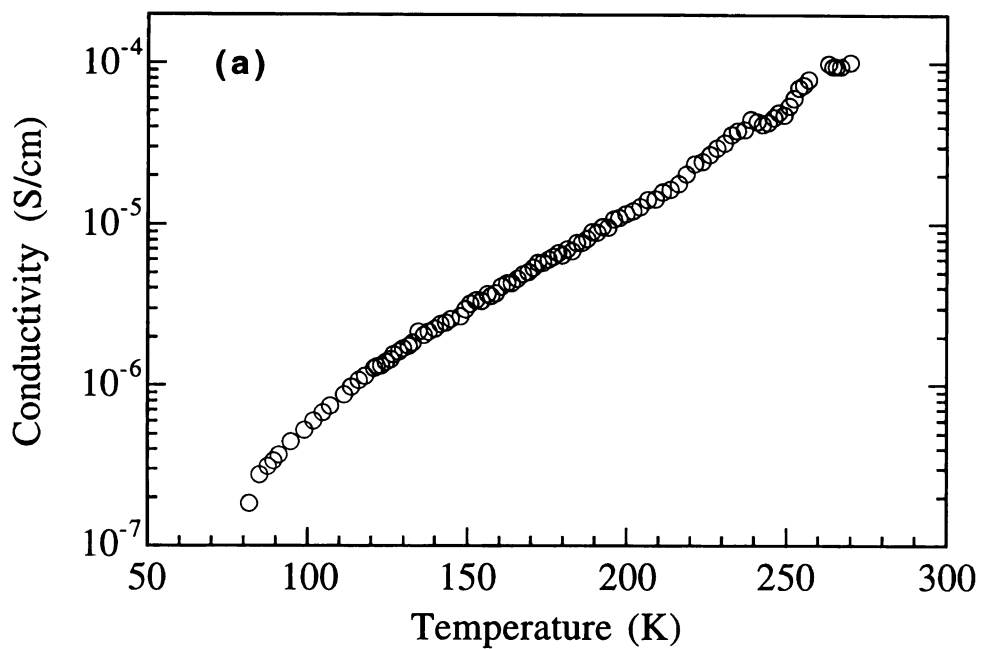


Figure 4.10. Variable-temperature electrical conductivity measurements for (a)  $\text{Li}_x\text{MoO}_3$  and (b)  $\text{Li}_x(\text{H}_2\text{O})_y(\text{PEO-100,000})_z\text{MoO}_3$ .



## 5. Electrical Conductivity

Electrical conductivity values for all the nanocomposites are listed in Table 4.2. The room-temperature electrical conductivity of the  $\text{Li}_x\text{MoO}_3$  was 0.013 S/cm, which is slightly lower than values reported in related materials [23]. As shown in Table 4.2, the conductivity of the nanocomposites is significantly lower than that of  $\text{Li}_x\text{MoO}_3$  and decreases with increasing layer expansion. For materials with extremely large gallery spacing, the electrical conductivity is lower than that of  $\text{MoO}_3$  itself. When the measurements are performed under vacuum the conductivity decreases concomitantly with the loss of water from the galleries. This suggests that water is contributing to charge transport in these materials probably via proton mobility. Figure 4.10 shows the temperature dependence of the electrical conductivity of  $\text{Li}_x\text{MoO}_3$  and  $\text{Li}_x(\text{H}_2\text{O})_y(\text{PEO-100,000})_z\text{MoO}_3$ , which are thermally activated. Mixed ionic/electronic conducting nanocomposites are of current interest [4a].

## Concluding Remarks

A new family of polymer-molybdenum bronze nanocomposites have been synthesized. The host material,  $\text{Li}_x\text{MoO}_3$ , was synthesized *via* a  $\text{LiBH}_4$  route which is different from the conventional approach. This material exfoliates in water and has affinity for a large variety of polymers. Polymers such as PEG, PEO, PPG, PVP, MCEl, PAM and PA6 give well stacked lamellar nanocomposites. Depending on the nature of the polymer and its molecular mass, some of the nanocomposites are soluble and can be processed into films. Electronic transmission spectra show the broad transition associated with the  $\text{Mo}^{5+}$ - $\text{Mo}^{6+}$  couple in these nanocomposites

ranging from the IR to the visible region. Solid-state  $^7\text{Li}$  NMR spectroscopy indicates a more versatile chemical environment in the nanocomposites than in the host which may lead to high ionic conductivities in these lamellar systems. The electrical conductivity of these materials is thermally activated and ranges from  $10^{-2}$  to  $10^{-7}$  S/cm.



## References

- 1 (a) Y. Fukushima and S. Inagaki, *J. Inclusion Phenom.* **1987**, 5, 473. (b) E. Ruiz-Hitzky and P. Aranda, *Adv. Mater.* **1990**, 2, 545. (c) A. Okada and A. Usuki, *Mat. Sci. Eng. C-Biomin.* **1995**, 3, 109. (d) E. P. Giannelis, *Adv. Mater.* **1996**, 8, 29. (e) Z. Wang, T. Lan and T. J. Pinnavaia, *Chem. Mater.* **1996**, 8, 2200. (f) J. J. Tunney and C. Detellier, *Chem. Mater.* **1996**, 8, 927. (g) J. C. Hutchison, R. Bissessur and D. F. Shriver, *Chem. Mater.* **1996**, 8, 1597.
- 2 (a) M. G. Kanatzidis, L. M. Tonge, T. J. Marks, H. O. Marcy and C. R. Kannewurf, *J. Am. Chem. Soc.* **1987**, 109, 3797. (b) M. G. Kanatzidis, H. O. Marcy, W. J. McCarthy, C. R. Kannewurf and T. J. Marks, *Solid State Ionics* **1989**, 32-33, 594. (c) M. G. Kanatzidis, C.-G. Wu, H. O. Marcy, D. C. DeGroot, C. R. Kannewurf, A. Kostikas and V. Papaefthymiou, *Adv. Mater.* **1990**, 2, 364. (d) C.-G. Wu, H. O. Marcy, D. C. DeGroot, J. L. Schindler, C. R. Kannewurf, W.-Y. Leung, M. Benz, E. LeGoff and M. G. Kanatzidis, *Synth. Met.* **1991**, 41-43, 797.
- 3 (a) Y.-J. Liu, D. C. DeGroot, J. L. Schindler, C. R. Kannewurf and M. G. Kanatzidis, *Chem. Mater.* **1991**, 3, 992. (b) Y.-J. Liu, D. C. DeGroot, J. L. Schindler, C. R. Kannewurf and M. G. Kanatzidis, *Adv. Mater.* **1993**, 5, 369. (c) Y.-J. Liu, J. L. Schindler, D. C. DeGroot, C. R. Kannewurf, W. Hirpo and M. G. Kanatzidis, *Chem. Mater.* **1996**, 8, 525. (d) C.-G. Wu, M. G. Kanatzidis, H.O. Marcy, D. C. DeGroof and C. R. Kannewurf, in R. M. Metzger, et al, ed., *Lower-Dimensional Systems and Molecular Electronics*, Plenum Press, New York, **1991**, pp 427. (e) Y.-J. Liu, D. C. DeGroot, J. L. Schindler, C. R. Kannewurf and M. G. Kanatzidis, *J. Chem. Soc., Chem. Commun.*, **1993**, 593. (f) C.-G. Wu, D. C. DeGroot, H. O. Marcy, J. L. Schindler, C. R. Kannewurf, Y.-J. Liu, W. Hirpo and M. G. Kanatzidis, *Chem. Mater.* **1996**, 8, 1992.
- 4 (a) G. M. Kloster, J. A. Thomas, P. W. Brazis, C. R. Kannewurf and D. F. Shriver, *Chem. Mater.* **1996**, 8, 2418. (b) F. Leroux, B. E. Koene and L. F. Nazar, *J. Electrochem. Soc.* **1996**, 143(9), L181.
- 5 (a) L. F. Nazar, X. T. Yin, D. Zinkweg, Z. Zhang and S. Liblong, *Mat. Res. Soc. Symp. Proc.* **1991**, 210, 417. (b) L. F. Nazar, Z. Zhang and D. Zinkweg, *J. Am. Chem. Soc.* **1992**, 114, 6239. (c) L. F. Nazar, H. Wu and W. P. Power, *J. Mater. Chem.* **1995**, 5, 1985.

- (d) T. A. Kerr, H. Wu and L. F. Nazar, *Chem. Mater.* **1996**, 8, 2005.
- 6 R. Bissessur, D. C. DeGroot, J. L. Schindler, C. R. Kannewurf and M. G. Kanatzidis, *J. Chem. Soc., Chem. Commun.*, **1993**, 687.
- 7 (a) C. O. Oriakhi and M. M. Lerner, *Chem. Mater.* **1996**, 8, 2016. (b) P. G. Hill, P. J. S. Foot and R. Davis, *Synth. Met.* **1996**, 76, 289.
- 8 (a) G. Cao and T. E. Mallouk, *J. Solid State Chem.* **1991**, 94, 59. (b) J. E. Pillion and M. E. Thompson, *Chem. Mater.* **1991**, 3, 777. (c) A. Clearfield and C. Y. Ortiz-Avila, in T. Bein ed., *Supramolecular Architecture* ( ACS Symposium 499), American Chemical Society, **1992**, pp 178. (d) Y.-J. Liu and M. G. Kanatzidis, *Inorg. Chem.* **1993**, 32, 2989. (e) Y. Ding, D. J. Jones, P Maireles-Torres and J. Rozière, *Chem. Mater.* **1995**, 7, 562.
- 9 W. M. R. Divigalpitiya, R. F. Frindt and S. R. Morrison, *J. Mater. Res.* **1991**, 6, 1103.
- 10 (a) M. G. Kanatzidis, R. Bissessur, D. C. DeGroot, J. L. Schindler and C. R. Kannewurf, *Chem. Mater.* **1993**, 5, 595. (b) R. Bissessur, M. G. Kanatzidis, J. L. Schindler and C. R. Kannewurf, *J. Chem. Soc., Chem. Commun.*, **1993**, 1582. (c) R. Bissessur, J. L. Schindler, C. R. Kannewurf and M.G. Kanatzidis, *Mol. Cryst. Liq. Cryst.* **1993**, 245, 249. (d) L. Wang, J. L. Schindler, J. A. Thomas, C. R. Kannewurf and M. G. Kanatzidis, *Chem. Mater.* **1995**, 7, 1753.
- 11 (a) E. Ruiz-Hitzky, R. Jimenez, B. Casal, V. Manriquez, A. S. Ana and G. Gonzalez, *Adv. Mater.* **1993**, 5, 738. (b) J. P. Lemmon and M. M. Lerner, *Chem. Mater.* **1994**, 6, 207.
- 12 Hui-Lien Tsai, Jon L. Schindler, Carl R. Kannewurf and Mercuri G. Kanatzidis, *Chem. Mater.* **1997**, 9, 875.
- 13 I. Lagadic, A. Léaustic and R. Clément, *J. Chem. Soc., Chem. Commun.*, **1992**, 1396.
- 14 P. B. Messersmith and S. I. Stupp, *Chem. Mater.* **1995**, 7, 454.
- 15 (a) N. Margalit, *J. Electrochem. Soc.* **1974**, 121, 1460. (b) J. Desilvestro and O. Haas, *J. Electrochem. Soc.* **1990**, 137, 5C.
- 16 M. G. Kanatzidis and T. J. Marks, *Inorg. Chem.* **1987**, 26, 783.

- 17 D. M. Thomas and E. M. McCarron III, *Mat. Res. Bull.* **1986**, 21, 945.
- 18 Yield obtained by reproducing the experiment in Reference 17.
- 19 S. Colson, J. M. Tarascon, S. Szu and L. C. Klein, *Mat. Res. Soc. Symp. Proc.* **1991**, 210, 405.
- 20 J. M. Tarascon and S. Colson, *Mat. Res. Soc. Symp. Proc.* **1989**, 135, 421.
- 21 Y. Matsuda, M. Sato, M. Onoda and K. Nakao, *J. Phys. C: Solid State Phys.* **1986**, 19, 6039.
- 22 (a) M. Greenblatt, in *Low-Dimensional Electronic Properties of Molybdenum Bronzes and Oxides*, ed. C. Schlenker, Kluwer Academic Publishers, **1989**. (b) L. F. Schneemeyer, F. J. DiSalvo, R. M. Fleming and J. V. Waszczak, *J. Solid State Chem.* **1984**, 54, 358. (c) G. H. Bouchard, Jr., J. Perlstein and M. J. Sienko, *Inorg. Chem.* **1967**, 6, 1682. (d) D. C. Johnston, *Phys. Rev. Lett.* **1984**, 52, 2049.
- 23 (a) C. Julien and G. A. Nazri, *Solid State Ionics* **1994**, 68, 111. (b) J. O. Besenhard, J. Heydecke, E. Wudy and H. P. Fritz, *Solid State Ionics* **1983**, 8, 61.



## Chapter 5

### $\alpha$ -RuCl<sub>3</sub>/POLYMER NANOCOMPOSITES: THE FIRST GROUP OF INTERCALATIVE NANOCOMPOSITES WITH TRANSITION-METAL-HALIDES

#### Introduction

Intercalation compounds with polymers as the guest species are a rapid growing class of nanocomposite materials [1]. The combination of the two extremely different components, at the molecular level, provides an excellent opportunity to modulate the properties of one or more of the component materials [2]. In some circumstances, it is also a unique way to generate materials which have special properties that are unknown in the individual components [3]. Intercalative polymer hybrids have advantages over their small molecular analogs in compositional stability and mechanical strength, which make them more suitable for applications. As a result of recent efforts, a large variety of intercalative nanocomposites have been prepared using hosts from most major classes of layered inorganic compounds, *i.e.*, clays, layered transition metal chalcogenides, metal oxides, metal phosphates and metal thiophosphates [4].

Layered transition metal compounds such as oxides, chalcogenides, halides and thiophosphates have interesting electronic, magnetic, optical and catalytic properties [5]. These properties arise from the close-packed intralayer atomic arrangement and the special atomic interactions which results in partially filled *d*-electron bands. For example,  $\alpha$ -RuCl<sub>3</sub> shows intralayer ferromagnetism, interlayer antiferromagnetism [6a] and photoconductivity [6b]. On the other hand TaS<sub>2</sub> and NbSe<sub>2</sub> exhibit charge



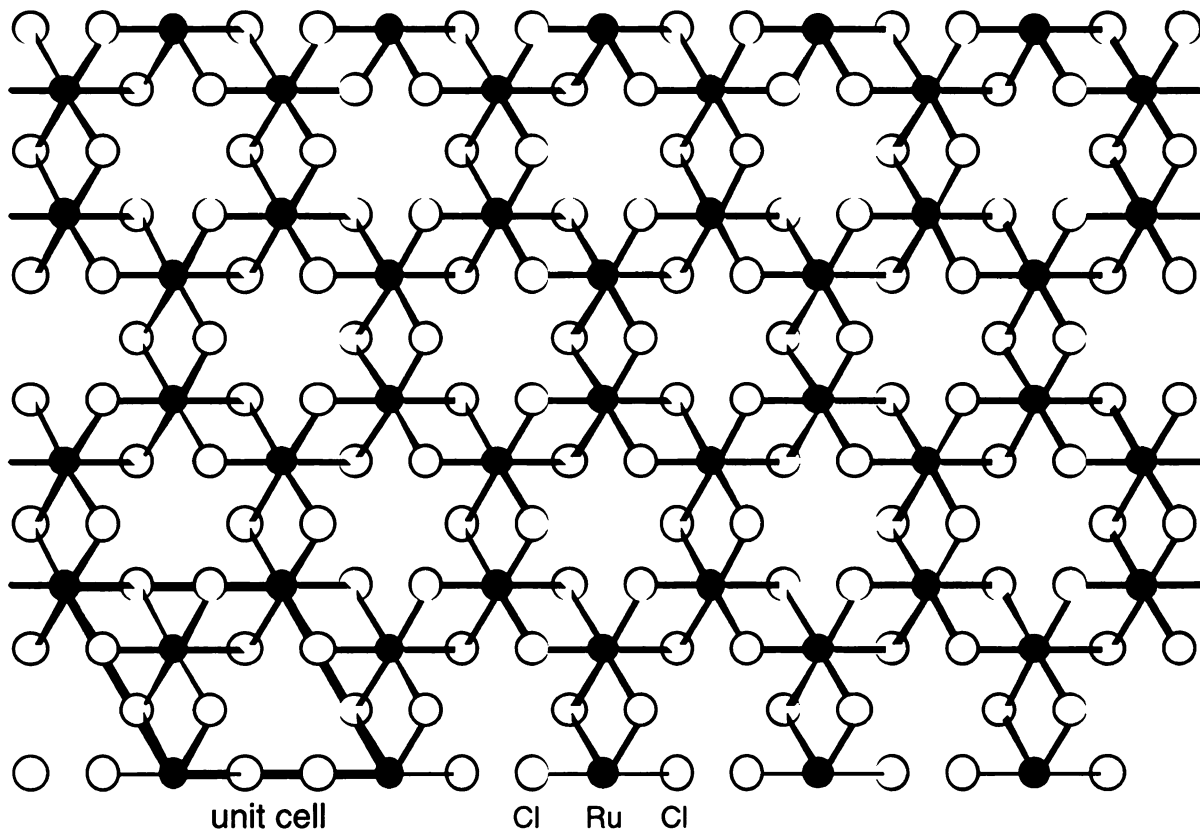
density waves and superconductivity [7]. One can expect that the physical properties of these materials can be tuned or changed by means of intercalation.

Layered transition metal halides, in contrast to layered transition metal chalcogenides [8], oxides [9] and thiophosphates [10], have not received much attention in the study of intercalation, because most of them are not very stable under even mild conditions for soft chemical reactions. Hydrolysis, dissolution and other decomposition reactions are often common properties of this group of materials.  $\alpha$ -RuCl<sub>3</sub> is an exception, and is very stable under these conditions.

$\alpha$ -RuCl<sub>3</sub> has a lamellar structure of defect CdI<sub>2</sub> structure type [6a], see Figure 5.1. The intercalation chemistry of  $\alpha$ -RuCl<sub>3</sub> has been reported with the insertion of simple cations and neutral polar molecules [11]. Cations can be intercalated through a reduction reaction of  $\alpha$ -RuCl<sub>3</sub> or through an ion-exchange reaction, while neutral polar molecules can be incorporated through solvent exchange. These properties are similar to those of layered chalcogenides and oxides such as TiS<sub>2</sub>, 2H-TaS<sub>2</sub> and MoO<sub>3</sub>, suggesting the possibility of intercalating polymers in this material. In fact,  $\alpha$ -RuCl<sub>3</sub> behaves as an excellent polymer-intercalation host. It has affinity for various polymers and is suitable for several of the existing polymer intercalation methods. For example,  $\alpha$ -RuCl<sub>3</sub>/polyaniline ( $\alpha$ -RuCl<sub>3</sub>/PANI) nanocomposites were synthesized with *in situ* redox intercalative polymerization [12], while soluble polymers such as poly(ethylene oxide) (PEO), poly(vinyl pyrrolidone) (PVP) and polyethylenimine (PEI) are intercalated through encapsulative co-precipitation [13] of polymers and  $\alpha$ -RuCl<sub>3</sub> from solutions of exfoliated  $\alpha$ -RuCl<sub>3</sub>. A modification of the second method, *in situ* polymerization coupled with encapsulative precipitation [14]



View down the 001 plane



View down the 100 plane

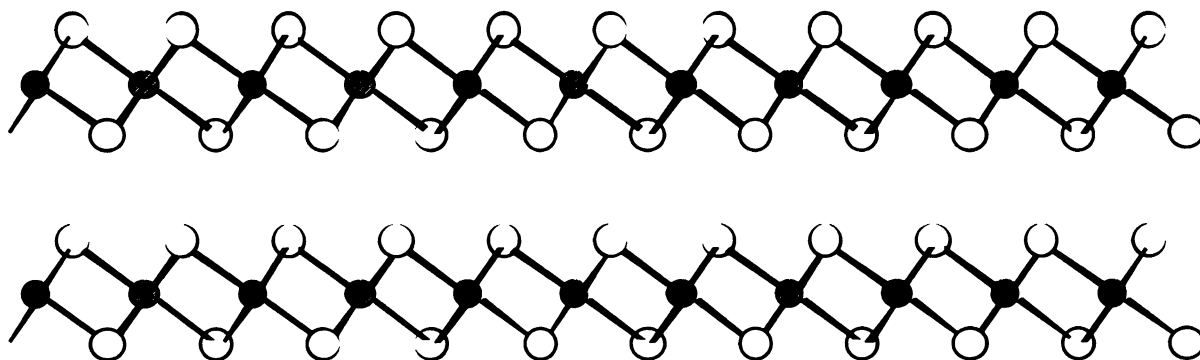


Figure 5.1. The structure of  $\alpha$ - $\text{RuCl}_3$ .



from suspensions of exfoliated  $\alpha$ -RuCl<sub>3</sub>, can be used to intercalate intractable polymers such as polypyrrole (PPY). This chapter describes the insertion of polymers into  $\alpha$ -RuCl<sub>3</sub> producing a new group of lamellar nanocomposites with various physicochemical properties.

## Experimental Section

### 1. Reagents

Ru (99.95%, 325 mesh) was purchased from Cerac Inc. Cl<sub>2</sub> (99.5%) and CO (99.5) gases were from AGA Specialty Gases. LiBH<sub>4</sub> (95%), PEO (100,000), PVP (10,000) and PEI (25,000) were purchased from Aldrich Chemical Company, Inc. After the polymers were dissolved, the polymer solutions were filtered to remove insoluble residues. Aniline and pyrrole were purchased from Aldrich and Mallinckrodt Inc. respectively, and were distilled before use. Br<sub>2</sub> (reagent grade) and anhydrous FeCl<sub>3</sub> (purified) were from Fisher Scientific. Anhydrous ether (99.0%), acetonitrile (99.5%) and isopropanol (99.9%) were from Columbus Chemical Industries Inc., EM Science Inc. and Mallinckrodt Chemical Inc. respectively.

### 2. Reactions and Sample Preparations

#### a. Preparation of $\alpha$ -RuCl<sub>3</sub>

$\alpha$ -RuCl<sub>3</sub> was synthesized as described in the literature [15]. The set-up for the reaction, as shown in Figure 5.2, was first purged with nitrogen overnight. An amount of 10 g Ru spread in an alumina boat was then reacted with mixed Cl<sub>2</sub> and CO gases at 800 °C for 8 h. The ratio of Cl<sub>2</sub> to CO gas was adjusted to about 1:2 or 1:3 and the flow was set at



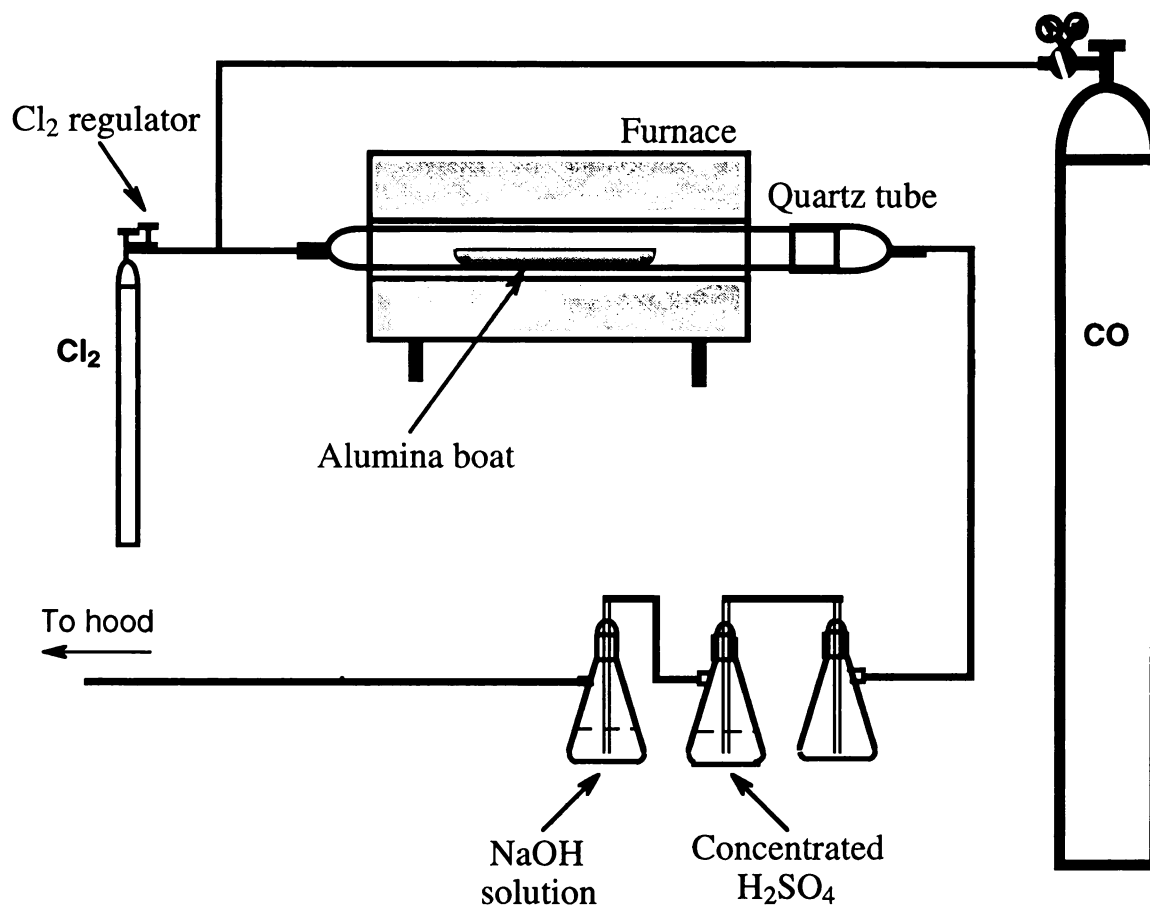


Figure 5.2 Experimental set-up for the synthesis of  $\alpha$ - $\text{RuCl}_3$ .



approximately 60-120 ml/min. The gas was set to flow before heating and was turned off after the reaction tube cooled to about 50 °C. It is important to keep the gas under constant flow, otherwise a negative pressure could build up and the H<sub>2</sub>SO<sub>4</sub> (aq.) could be pushed into the reaction tube.

b. Synthesis of (PANI)<sub>x</sub>RuCl<sub>3</sub>

An amount of 0.1 g  $\alpha$ -RuCl<sub>3</sub> in 10 ml of 4% aniline/acetonitrile solution was stirred in open air for 1 week. The product was washed with copious acetonitrile and dried in vacuum. Elemental analysis, done by Quantitative Technologies Inc., gave: 15.33% C, 1.43% H, 3.11% N, which suggests the formula (PANI)<sub>0.57</sub>(H<sub>2</sub>O)<sub>0.50</sub>RuCl<sub>3</sub> (calculated: 15.3% C, 1.43% H, 2.97% N). The above formula contains 22.7 wt% intercalated species, which agrees with the thermogravimetric analysis (TGA) measurement indicating 22.8 wt% organics and water inside this nanocomposite [16].

c. Synthesis of Li<sub>x</sub>RuCl<sub>3</sub> and preparation of RuCl<sub>3</sub> monolayer suspensions

In a typical reaction, 18 mmol  $\alpha$ -RuCl<sub>3</sub> was mixed with 3.6 mmol LiBH<sub>4</sub> in 40 ml anhydrous ether under N<sub>2</sub> atmosphere for 3 days. The product was collected by filtration, washed with anhydrous ether and pumped to dryness. It was stored in a glove box under N<sub>2</sub> atmosphere. The product is designated as Li<sub>x</sub>RuCl<sub>3</sub>, where  $x \approx 0.2$ . An aqueous 0.5 wt% Li<sub>x</sub>RuCl<sub>3</sub> monolayer suspension was prepared simply by stirring Li<sub>x</sub>RuCl<sub>3</sub> in water for half an hour.

10/10/10  
10/10/10  
10/10/10

d. Synthesis of  $\text{Li}_x(\text{PEO})_y\text{RuCl}_3$ ,  $\text{Li}_x(\text{PEI})_y\text{RuCl}_3$  and  $\text{Li}_x(\text{PVP})_y\text{RuCl}_3$

In the preparation of PEO and PVP nanocomposites, an amount of 40 ml 0.5 wt%  $\text{Li}_x\text{RuCl}_3$  monolayer suspension (containing 0.96 mmol  $\text{Li}_x\text{RuCl}_3$ ) was mixed with 40 ml of polymer solution containing 3 mmol repeat-units of polymer. The mixture was stirred for 2 days in ambient atmosphere. The nanocomposites of PEO and PVP are water-soluble, and have to be collected from very concentrated solutions. Therefore, the reaction mixture was condensed to less than 20 ml under vacuum before it was poured in an organic solvent to precipitate the product. Acetonitrile and isopropanol were used as solvents for PEO and PVP respectively. In the preparation of PEI nanocomposite, the amount of 40 ml 0.5 wt%  $\text{Li}_x\text{RuCl}_3$  monolayer suspension was mixed with 40 ml of PEI solution containing 7 mmol repeat-units of polymer. The PEI nanocomposite precipitated out from water immediately upon mixing. It was collected with centrifugation after having been stirred as a suspension for 2 days. The nanocomposites were dried under vacuum. The compositions of the three nanocomposites were  $\text{Li}_x(\text{PEO})_{1.5}\text{RuCl}_3$  ( $x \sim 0.2$ ),  $\text{Li}_x(\text{PVP})_{2.2}\text{RuCl}_3$  ( $x \sim 0.2$ ) and  $\text{Li}_x(\text{PEI})_{4.6}\text{RuCl}_3$  according to TGA measurements under oxygen flow [16].

e. Synthesis of  $(\text{PPY})_x\text{RuCl}_3$

An amount of 0.45 g pyrrole (6.7 mmol) was dissolved in 40 ml of water and mixed with 40 ml of aqueous  $\text{Li}_x\text{RuCl}_3$  suspension which contained 0.20 g  $\text{Li}_x\text{RuCl}_3$  (0.96 mmol). The mixture was cooled in an ice bath before the dropwise addition of 10 ml aqueous solution of 0.11 g  $\text{FeCl}_3$  (0.67 mmol) which was also cooled in an ice bath. The reaction was carried out by stirring in a stoppered, ice-cooled flask for 24 h. The



product was collected by centrifugation, washed with copious water, and dried first in air and then under vacuum.

Elemental analysis showed that a  $(\text{PPY})_x\text{RuCl}_3$  sample contained 13.88% C, 1.32% H and 3.95% N. This corresponds to a formula  $(\text{PPY})_{0.77}(\text{H}_2\text{O})_{0.60}\text{RuCl}_3$  (calculated: 13.78% C, 1.31% H and 4.01% N). TGA measurements showed that the material lost 50.2% (theoretical 50.4%) of weight in oxygen flow up to temperatures higher than 450 °C. X-ray powder patterns of the final residue indicated  $\text{RuO}_2$ .

f. Oxidation of  $\text{Li}_x\text{RuCl}_3$  and nanocomposites with  $\text{Br}_2$

The oxidized  $\text{RuCl}_3$  was obtained by reacting exfoliated  $\text{Li}_x\text{RuCl}_3$  ( $x \sim 0.2$ ) with 10 equiv. of  $\text{Br}_2$  in water for one day. The  $\text{RuCl}_3$ , which flocculated, was collected by centrifugation, washed with copious water and dried under vacuum. The oxidized “ $(\text{PEO})_y\text{RuCl}_3$ ” was prepared by reacting directly the nanocomposite solutions, produced by the intercalation reaction, with 10 equiv. of  $\text{Br}_2$  in water for one day.

g. Preparation of oriented  $\text{Li}_x(\text{PEO})_y\text{RuCl}_3$  sample for one-dimensional electron density map calculations

One-dimensional electron density (1-D ED) map calculations need highly oriented samples.  $\text{Li}_x(\text{PEO})_y\text{RuCl}_3$  samples for this purpose were cast films. Immediately before the X-ray experiments, the samples were pumped at 75 °C for at least 3 days to remove excess water from the nanocomposite. This procedure ensures that the whole sample has only one phase with a single basal spacing. The X-ray patterns were collected under a nitrogen atmosphere to prevent absorption of moisture from the air, which causes peak broadening and drifting.



### 3. Instrumentation

The instrumentation in the measurements such as thermal gravimetric analysis (TGA) and infrared (IR) spectroscopy were the same as described in Chapter 1. X-ray diffraction (XRD) powder patterns were obtained as described in Chapter 1, except the increment for the continuous scanning mode was  $0.05^\circ$  for general purpose spectra.

Room temperature conductivity measurements, variable temperature direct-current electrical conductivity measurements and thermopower measurements, and magnetic susceptibility measurements were conducted as described in Chapter 2. Scanning electron microscopy (SEM) and energy dispersive X-ray microanalysis (EDS) and electron diffraction were done as described in Chapter 3.

XRD patterns for one-dimensional electron-density calculations were done as described in Chapter 3. Slits for beam width control and time of data collection were as follows:  $0.5^\circ$  slits and a data collection time of 12 s per step were chosen for measurements in the range from  $2^\circ$  to about  $29^\circ$ ;  $1.0^\circ$  slits and 60 s per step between  $16^\circ$  and  $71^\circ$ ;  $2.0^\circ$  slits and 60 s per step between  $57^\circ$  and  $83.5^\circ$ ;  $4.0^\circ$  slits and 90 s per step from  $72^\circ$  to  $136^\circ$ . The step width was kept the same ( $0.1^\circ$ ) in the entire  $2\theta$  range.

## Results and Discussion

### 1. Preparation of $(\text{PANI})_x\text{RuCl}_3$ by *in situ* Redox Intercalative Polymerization

The *in situ* redox intercalative polymerization reaction is the most direct method to intercalate conductive polymers. Its topotactic character least disturbs the crystalline structure of the host. In the case of



FeOCl/polyaniline, even single crystals of the nanocomposite could be obtained [17]. This type of reaction requires a strongly oxidizing host to provide a driving force to pull electrons from the monomers and oxidize them into polymers. In addition, the host should be able to distribute efficiently those electrons through out their structure. Because of the scarcity of such highly oxidizing and conducting hosts, the reaction has been limited to FeOCl [12a], V<sub>2</sub>O<sub>5</sub> [12b] and VOPO<sub>4</sub> [12c]. We discovered that  $\alpha$ -RuCl<sub>3</sub> also happens to be a suitable such host, and can form intercalative nanocomposites with polyaniline.

The reaction of an aniline CH<sub>3</sub>CN solution with  $\alpha$ -RuCl<sub>3</sub> in air results in the formation of polyaniline (PANI) within the gallery space of RuCl<sub>3</sub>. The reflection-mode powder X-ray diffraction (XRD) patterns of the product show a 6.2 Å increase in the separation of the RuCl<sub>3</sub> layers, see Figure 5.3 [18]. This expansion is reasonable for insertion of a monolayer of PANI molecules, and comparable to the 5.94 Å observed in (PANI)<sub>x</sub>FeOCl [17], and 5.2 Å in (PANI)<sub>x</sub>V<sub>2</sub>O<sub>5</sub> [12b]. The transmission-mode powder XRD patterns show that the *hk0* reflections of (PANI)<sub>x</sub>RuCl<sub>3</sub> remain the same as those of  $\alpha$ -RuCl<sub>3</sub>, indicating that the structure of  $\alpha$ -RuCl<sub>3</sub> is preserved, see Figure 5.4. This result is supported by electron diffraction experiments which provide the same *hk0* diffraction patterns for (PANI)<sub>x</sub>RuCl<sub>3</sub> and  $\alpha$ -RuCl<sub>3</sub>.

The formation of polyaniline between the RuCl<sub>3</sub> layers is supported by IR spectroscopy. Almost all peaks in the IR spectra of (PANI)<sub>x</sub>RuCl<sub>3</sub> are associated with polyaniline (emeraldine salt) and only a few with anilinium, see Figure 5.5(a). The peaks corresponding to the polymer are much more intense than those of anilinium. Heating the product at 120 °C in air for 5 days removes the peaks corresponding to anilinium at 744 cm<sup>-1</sup>



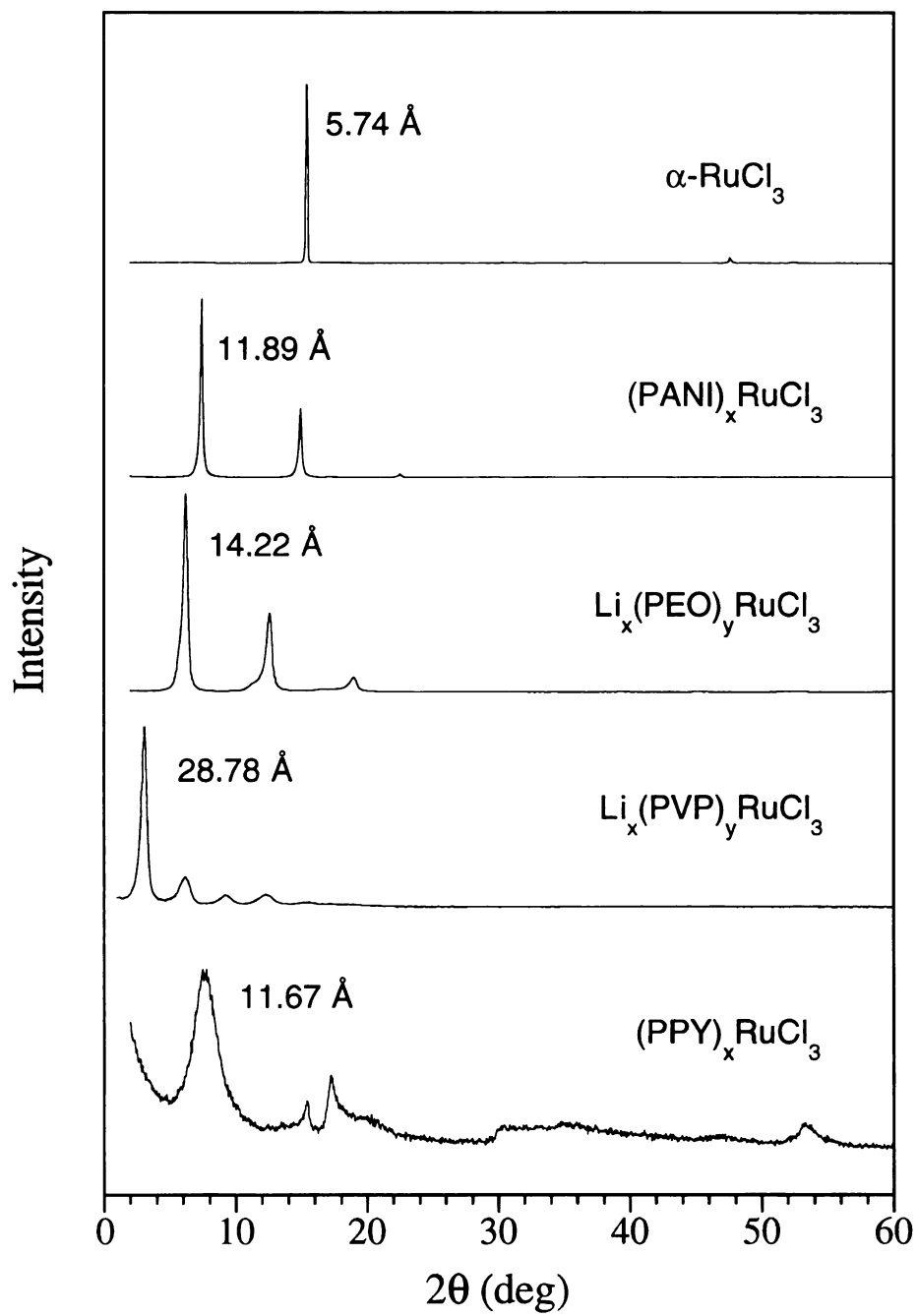


Figure 5.3. X-ray diffraction patterns of  $\alpha\text{-RuCl}_3$  and nanocomposites.



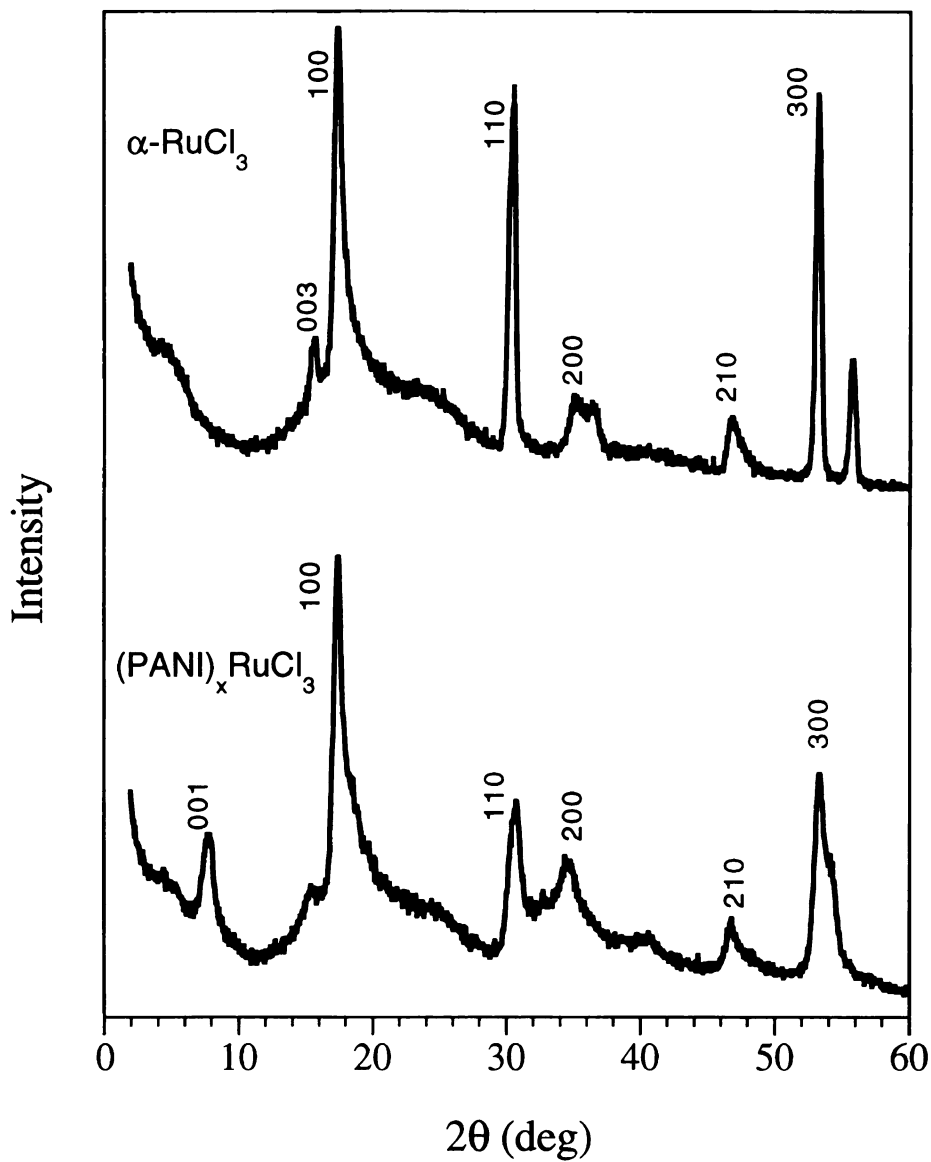


Figure 5.4. Transmission X-ray diffraction patterns of  $\alpha\text{-RuCl}_3$  and  $(\text{PANI})_x\text{RuCl}_3$  with indexing.



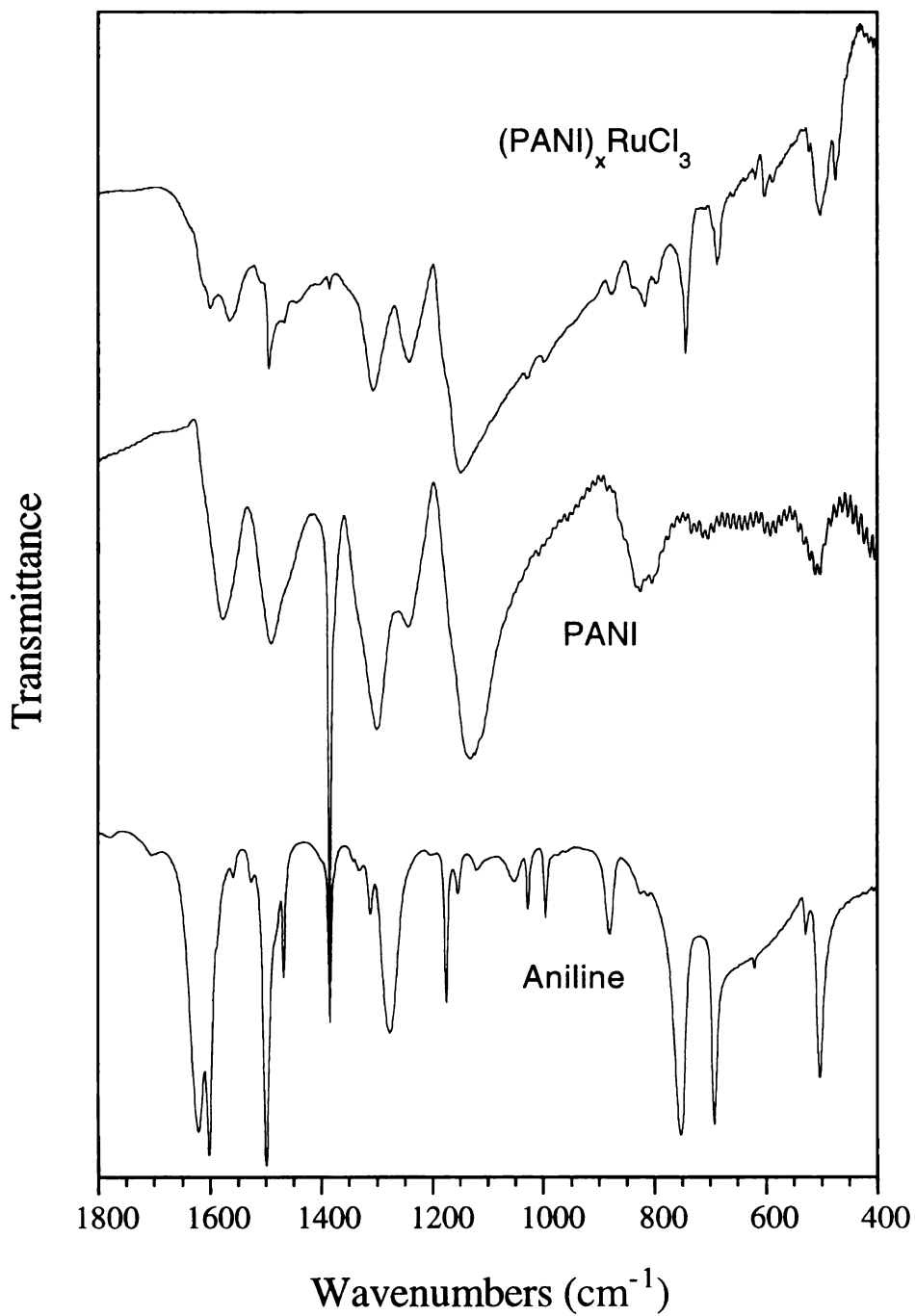
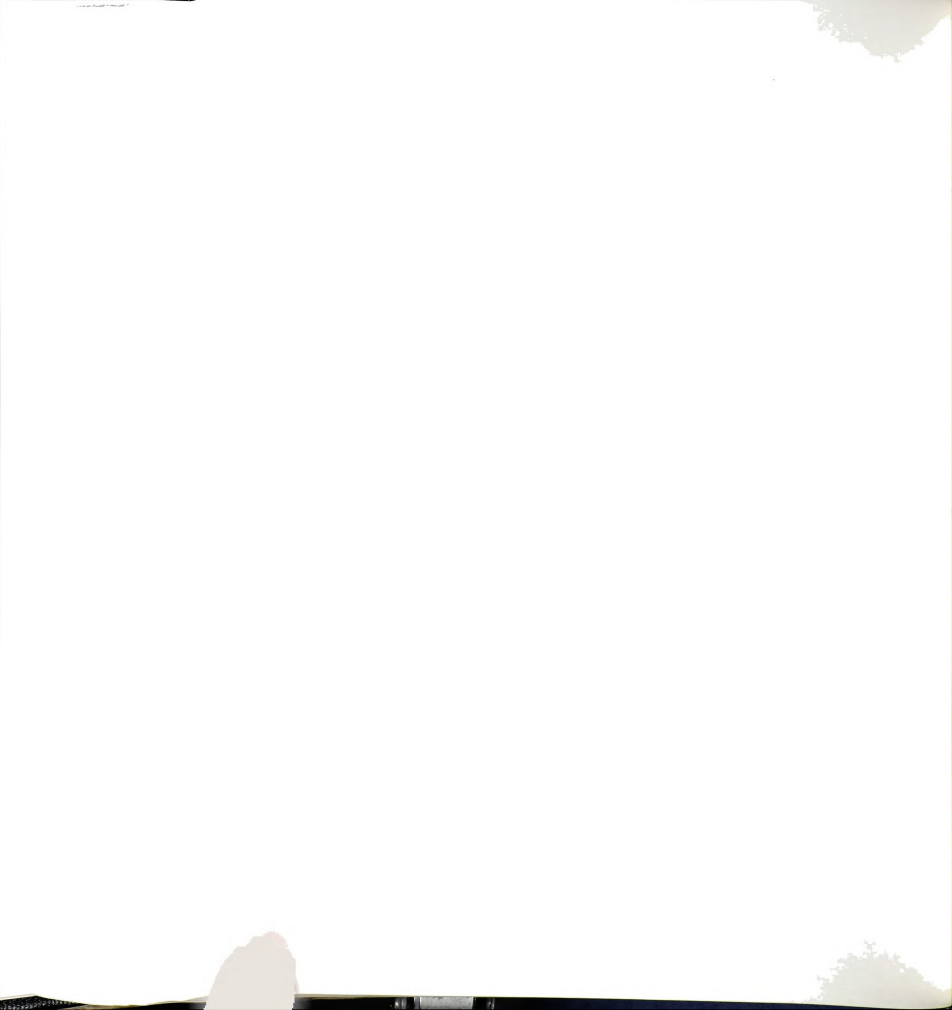


Figure 5.5(a). Infrared spectra of (PANI)<sub>x</sub>RuCl<sub>3</sub>, PANI and aniline. (The peak at 1385 cm<sup>-1</sup> is due to an impurity in KBr.)



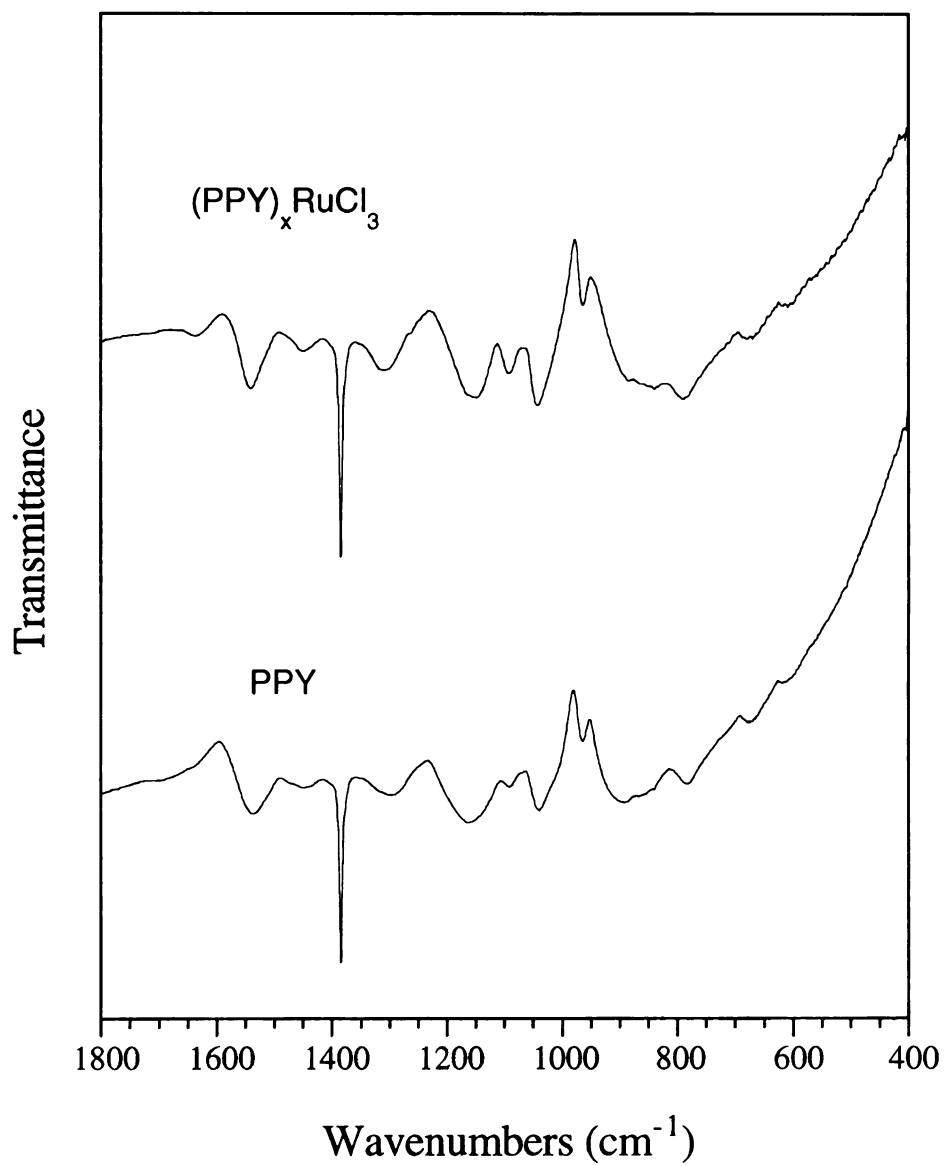


Figure 5.5(b). Infrared spectra of (PPY)<sub>x</sub>RuCl<sub>3</sub> and PPY. (The peak at 1385 cm<sup>-1</sup> is due to an impurity in KBr.)



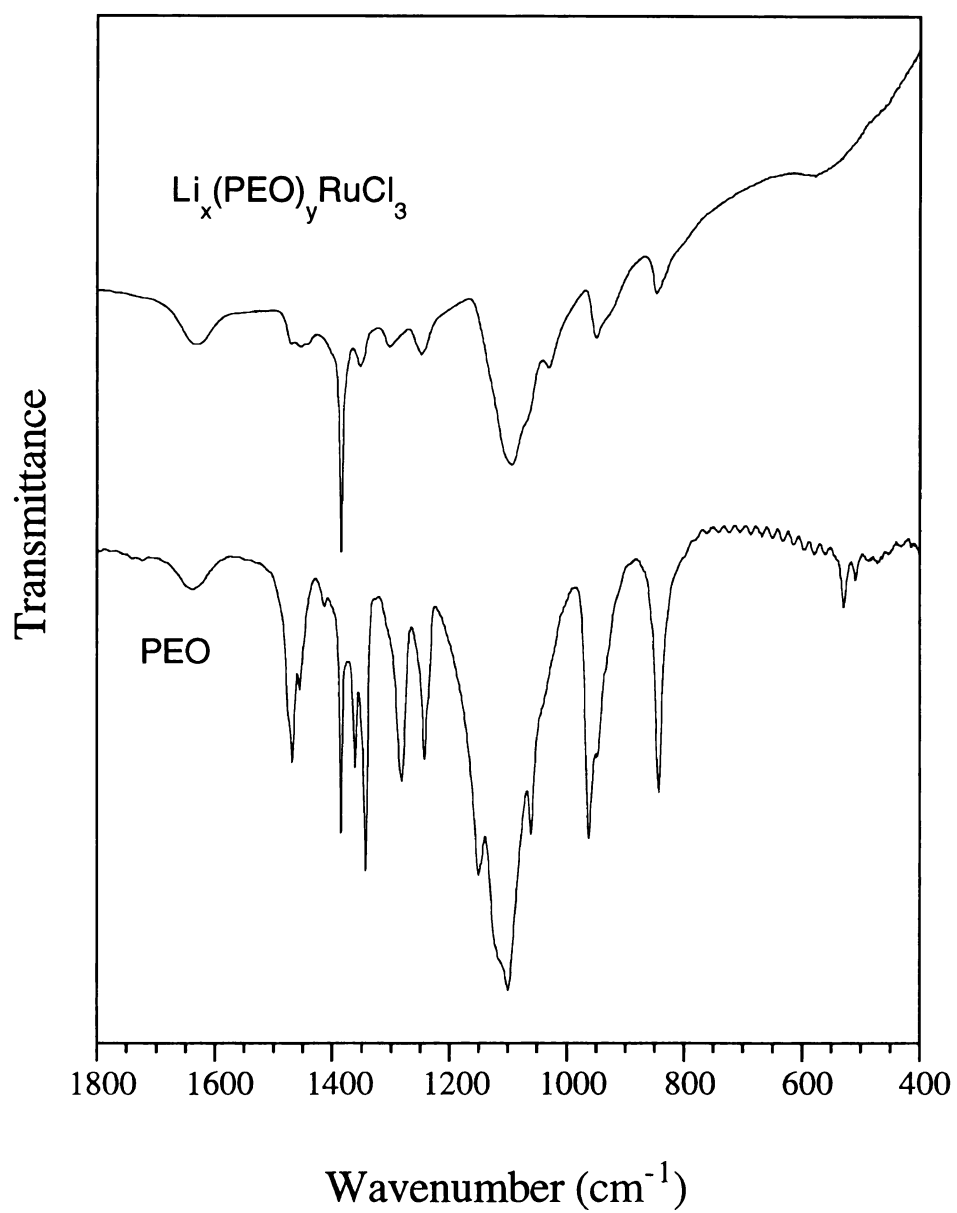


Figure 5.5(c). Infrared spectra of  $\text{Li}_x(\text{PEO})_y\text{RuCl}_3$  and PEO. (The peak at 1385 cm<sup>-1</sup> is due to an impurity in KBr.)



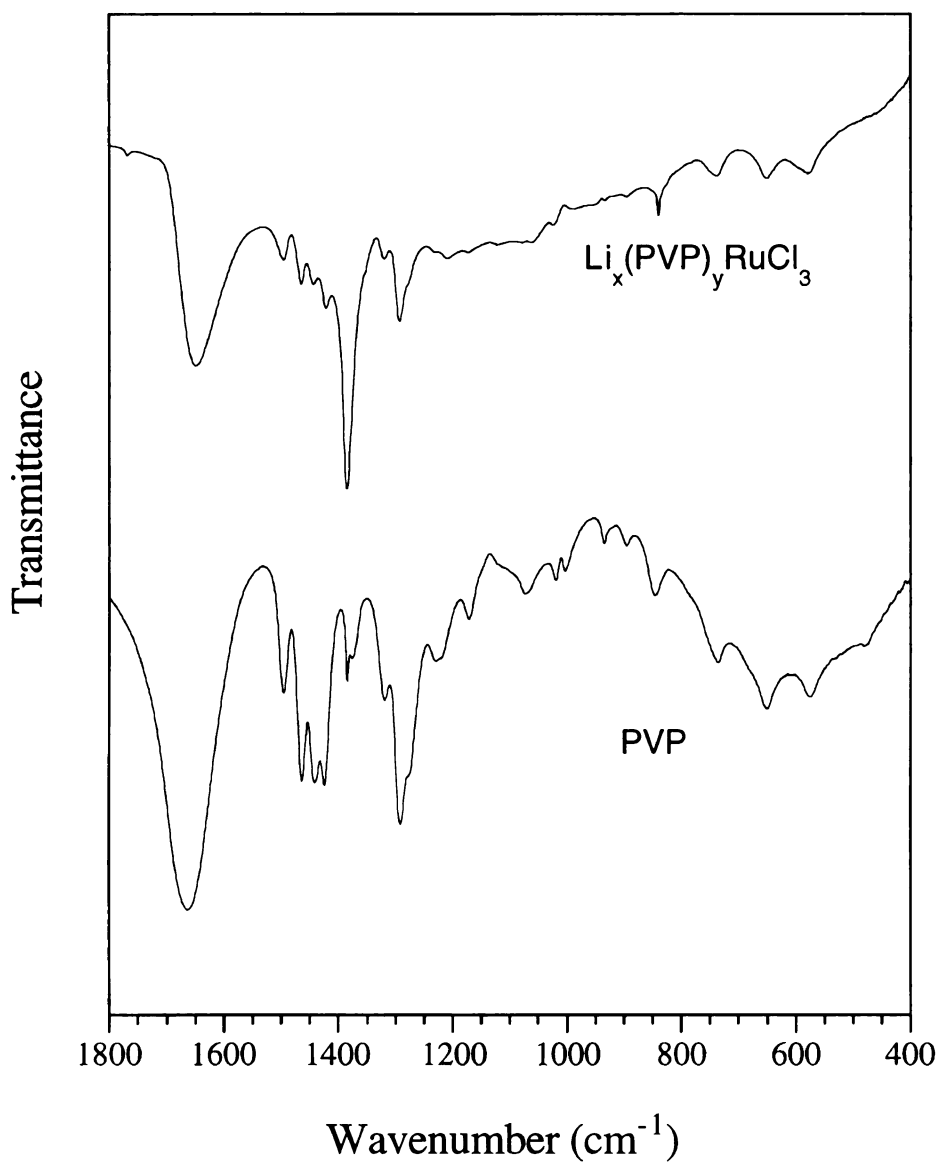


Figure 5.5(d). Infrared spectra of  $\text{Li}_x(\text{PVP})_y\text{RuCl}_3$  and PVP. (The peak at  $1385\text{ cm}^{-1}$  is due to an impurity in KBr.)



and 687  $\text{cm}^{-1}$ . The appearance of such monomer peaks indicates that the polyaniline formed in the galleries does not have very high molecular weight. This is reasonable since both the concentration and mobility of the aniline in the gallery are limited and the polymer is expected to be similar to the  $\sim 5,000$  daltons found in the  $(\text{PANI})_x\text{FeOCl}$  system.

In the process of intercalation, a fraction of  $\text{Ru}^{3+}$  is reduced to  $\text{Ru}^{2+}$ , giving a mixed valence compound. The  $\text{Ru}^{2+}$  centers are very stable because they are low spin diamagnetic  $d^6$  systems. This probably acts as a powerful driving force for the oxidation of aniline by virtue of the maximized Ligand Field Stabilization Energy (LFSE) in low spin  $d^6$  metal centers. Similar to the intercalative polymerization of aniline in  $\text{FeOCl}$  [12a] and  $\text{V}_2\text{O}_5$  [12b], the presence of oxygen is key to a successful outcome of the reaction. This was verified by control experiments where in the absence of air or oxygen no intercalation reaction occurred in 23 days.

## 2. Nanocomposites of $\alpha\text{-RuCl}_3$ with Water Soluble Polymers

The method of encapsulative precipitation from solutions of exfoliated lamellar solids provides a most convenient way to prepare nanocomposites with water-soluble polymers. With a stable and concentrated aqueous  $\text{Li}_x\text{RuCl}_3$  monolayer suspension, the intercalation is performed with water-soluble polymers: PEO, PVP and PEI. The reflection XRD patterns of the products show that the interlayer spacings of the  $\text{Li}_x(\text{PEO})_y\text{RuCl}_3$ ,  $\text{Li}_x(\text{PVP})_y\text{RuCl}_3$  and  $\text{Li}_x(\text{PEI})_y\text{RuCl}_3$  nanocomposites increase by 8.5, 23.0 and 3.6  $\text{\AA}$  respectively, see Figure 5.3. The existence of PEO, PVP and PEI in the nanocomposites is proven by IR spectroscopy. (See Figures 5.5(c) and (d) for IR spectra of  $\text{Li}_x(\text{PEO})_y\text{RuCl}_3$  and  $\text{Li}_x(\text{PVP})_y\text{RuCl}_3$ .)



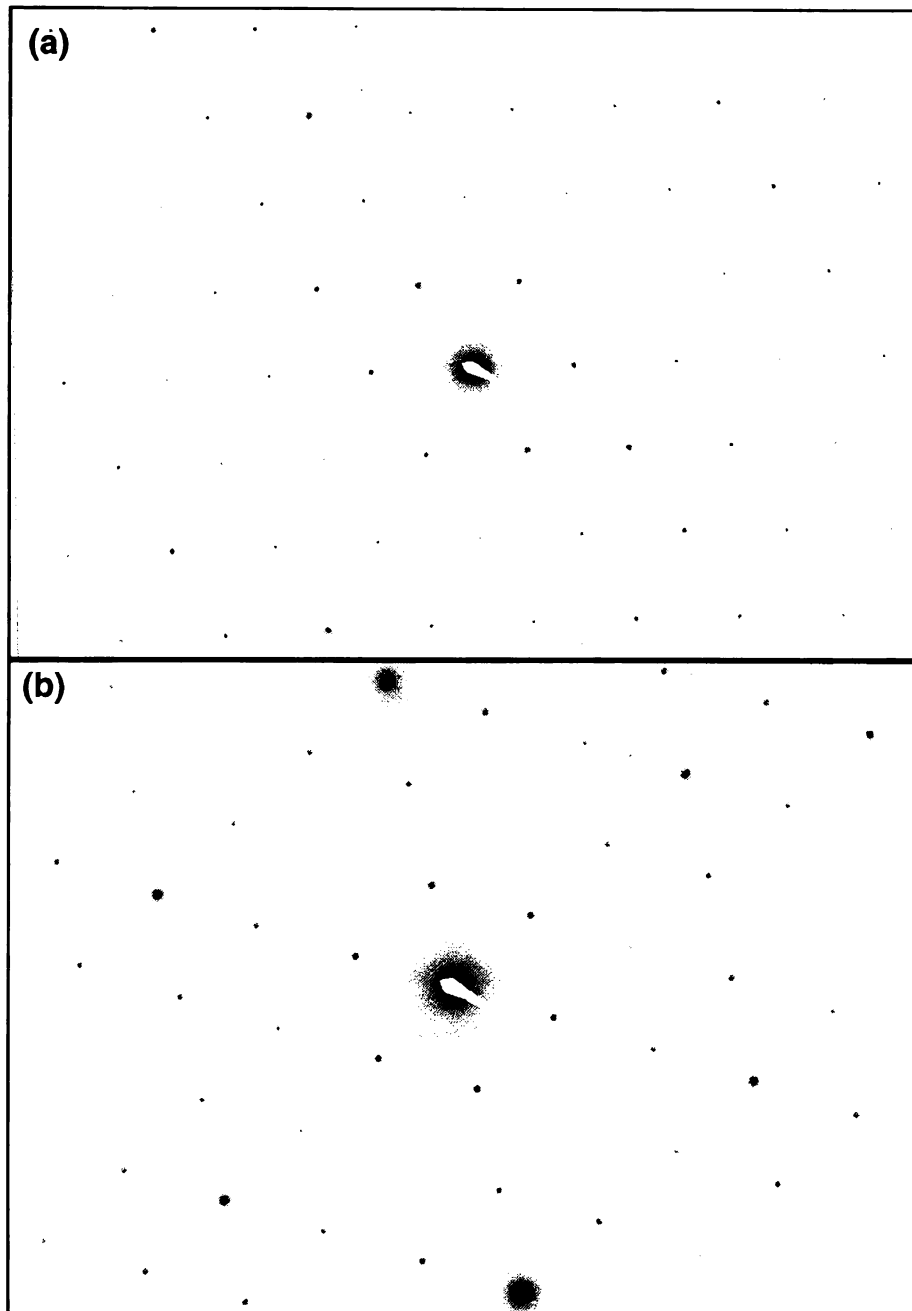
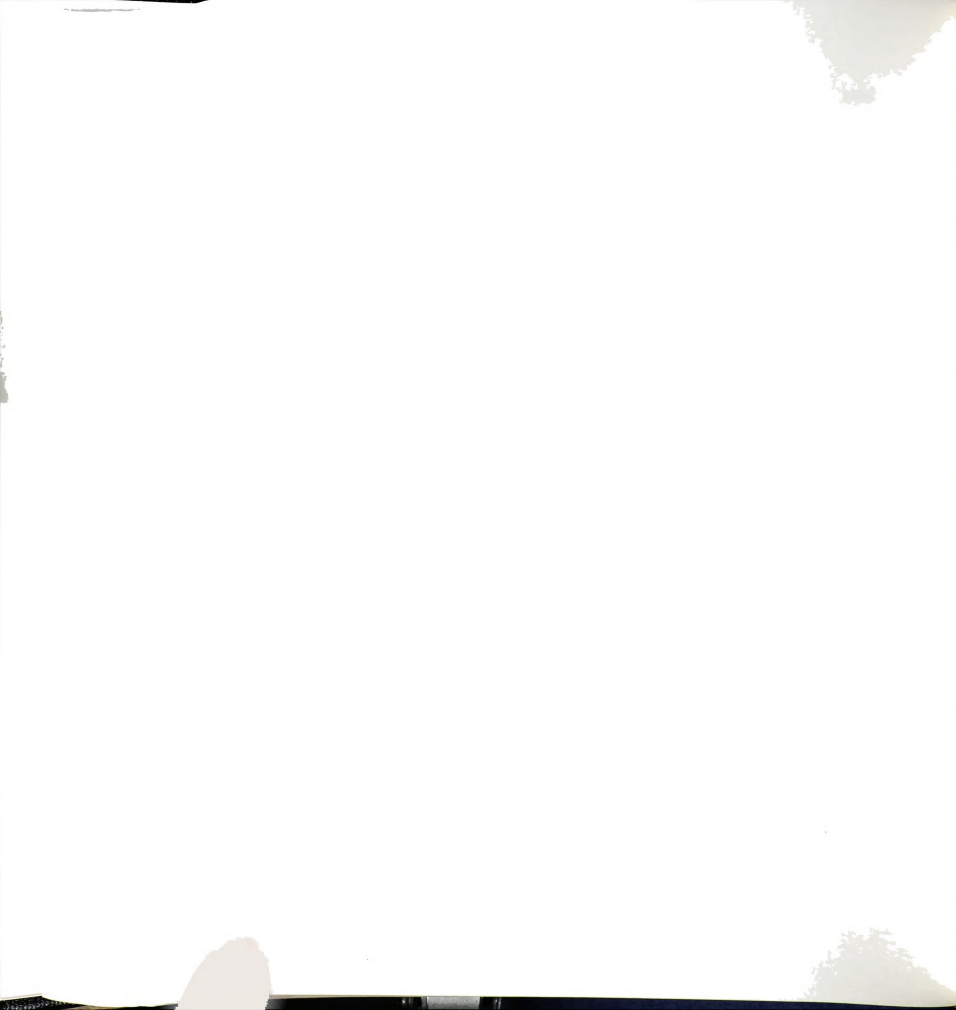


Figure 5.6. Electron diffraction patterns for (a)  $\alpha$ - $\text{RuCl}_3$  and (b)  $\text{Li}_x\text{RuCl}_3$ .



Electron diffraction experiments show that the exfoliated  $\text{RuCl}_3$  has the same  $hk0$  diffraction pattern as  $\alpha\text{-RuCl}_3$ , see Figure 5.6. The same electron diffraction pattern was seen in  $(\text{PANI})_x\text{RuCl}_3$ , suggesting no intralayer structure change during intercalation.

### 3. $\alpha\text{-RuCl}_3$ /Polypyrrole Nanocomposites

The exfoliation property of  $\alpha\text{-RuCl}_3$  offers the possibility to synthesize nanocomposites with insoluble polymers, by *in situ* polymerization-encapsulative precipitation [14]. In this method, a solution of a monomer (such as pyrrole) is mixed with an exfoliated inorganic host. When an initiator is added, the polymerization causes the co-precipitation of the polymer and the host monolayers, forming a nanocomposite with a certain lamellar thickness. As described in the Experimental section,  $(\text{PPY})_x\text{RuCl}_3$  was produced this way.

The production of  $(\text{PPY})_x\text{RuCl}_3$  nanocomposites is indicated by XRD patterns of the layered products with basal spacings around 11.7 Å, see Figure 5.3. The existence of the conductive form polypyrrole inside the galleries is confirmed by the characteristic IR spectrum, which exhibits peaks at 1541, 1314, 1150 1043 and 963  $\text{cm}^{-1}$  [19], see Figure 5.5(b).

The expansion between the  $\text{RuCl}_3$  layers, 6.0 Å, corresponds to a layer of polypyrrole chains arranged almost 40 degrees to the  $\text{RuCl}_3$  layers. This behavior is similar to that of  $(\text{PPY})_x\text{MoS}_2$  when pyrrole is used in excess in the reaction [14c]. The packing density of polypyrrole in  $(\text{PPY})_x\text{RuCl}_3$ , 0.77 pyrrole-unit per  $\text{RuCl}_3$ , is comparable to that in  $(\text{PPY})_x\text{MoS}_2$  prepared under similar conditions, 0.50 pyrrole-unit per  $\text{MoS}_2$  [20].



In the reaction to form  $(\text{PPY})_x\text{RuCl}_3$ , only 0.7 equivalent  $\text{FeCl}_3$  was used, which could oxidize at maximum 0.35 equivalent pyrrole to polypyrrole. Therefore, the amount of polypyrrole produced is more than the amount of pyrrole that  $\text{FeCl}_3$  could have oxidized. This is explained by the fact that the ambient oxygen takes part in the reaction as an electron acceptor. It has been proven that ambient oxygen can oxidize and polymerize pyrrole and its oligomers when  $\text{FeCl}_3$  is present as a catalyst<sup>[21]</sup>.

A control experiment, which was conducted under the same experimental conditions but without the addition of  $\text{FeCl}_3$ , produced a lamellar phase with a basal spacing of 10.1 Å (expansion of 4.4 Å). This phase cannot be de-intercalated by dynamic pumping. It must correspond to a  $\text{RuCl}_3$  intercalation compound with one layer of pyrrole or oligomers lying with the pyrrole rings parallel to the  $\text{RuCl}_3$  layers. This compound lost 48.0 wt% in a TGA experiment in oxygen flow up to 650 °C, which is comparable with that of  $(\text{PPY})_{0.77}(\text{H}_2\text{O})_{0.60}\text{RuCl}_3$ , 50.2 wt%. Another control experiment showed that no polymerization occurred when both  $\text{FeCl}_3$  and  $\text{RuCl}_3$  were absent.

As an alternative method, we also tried the *in situ* redox intercalative polymerization in order to prepare a  $\text{RuCl}_3/\text{PPY}$  nanocomposite. When  $\alpha\text{-RuCl}_3$  was stirred in an aqueous pyrrole solution <sup>[22]</sup> in open air, intercalation occurred in two weeks to form a product with 11.2 Å basal spacing. However, IR spectra showed that the polymer formed inside the gallery spacing was not ordinary polypyrrole and further investigation was not performed.



#### 4. Charge Transport Properties

The intercalation of polymers causes large changes in the properties of  $\alpha$ - $\text{RuCl}_3$ , as expected. Because of the formation of  $\text{Ru}^{2+}$  centers which provide free hopping electrons, the electrical conductivity of  $\text{Li}_x\text{RuCl}_3$  ( $x \sim 0.2$ ) at room temperature is  $\sim 0.3$  S/cm, about three orders of magnitude higher than that of  $\alpha$ - $\text{RuCl}_3$ ,  $5 \times 10^{-4}$  S/cm [23]. Intercalation of insulating polymers reduces the conductivity, with those of PEO and PVP nanocomposites being  $4.5 \times 10^{-3}$  and  $1.7 \times 10^{-3}$  S/cm respectively. Nanocomposites with conductive polymers have conductivities higher than that of  $\text{Li}_x\text{RuCl}_3$ .  $(\text{PANI})_x\text{RuCl}_3$  has a room temperature conductivity of  $\sim 1$  S/cm, while  $(\text{PPY})_x\text{RuCl}_3$  has one of 23 S/cm. It is obvious that the conductivities of these two materials are substantially enhanced by the presence of conductive polymers.

Variable temperature measurements on pressed pellets reveal that the electrical conductivities of all  $\alpha$ - $\text{RuCl}_3$ ,  $\text{Li}_x\text{RuCl}_3$  ( $x \sim 0.2$ ),  $\text{Li}_x(\text{PEO})_y\text{RuCl}_3$ ,  $(\text{PANI})_x\text{RuCl}_3$  and  $(\text{PPY})_x\text{RuCl}_3$  are thermally activated, see Figure 5.7. In the case of  $\alpha$ - $\text{RuCl}_3$ ,  $\text{Li}_x\text{RuCl}_3$  and  $\text{Li}_x(\text{PEO})_y\text{RuCl}_3$ , the  $\log(\sigma)$  versus  $1/T$  plots are almost linear. The activation energies, which are calculated according to the formula  $\sigma = \sigma_0 e^{-\Delta E/2kt}$ , are 0.36, 0.30 and 0.35 eV respectively. Since the pellets used in measurements have inter-particle boundaries, the activation energies do not necessarily correspond to the intrinsic band gaps. In  $(\text{PANI})_x\text{RuCl}_3$  and  $(\text{PPY})_x\text{RuCl}_3$ , the data do not form straight lines in the  $\log(\sigma)$  versus  $1/T$  plots, which suggests that several kinds of electrical barriers exist in these materials, including electron hopping barriers associated with transport through and across the chains of the conjugated polymer. At temperatures higher than 100 K, the data of  $(\text{PANI})_x\text{RuCl}_3$  and  $(\text{PPY})_x\text{RuCl}_3$  almost fall in straight lines. The



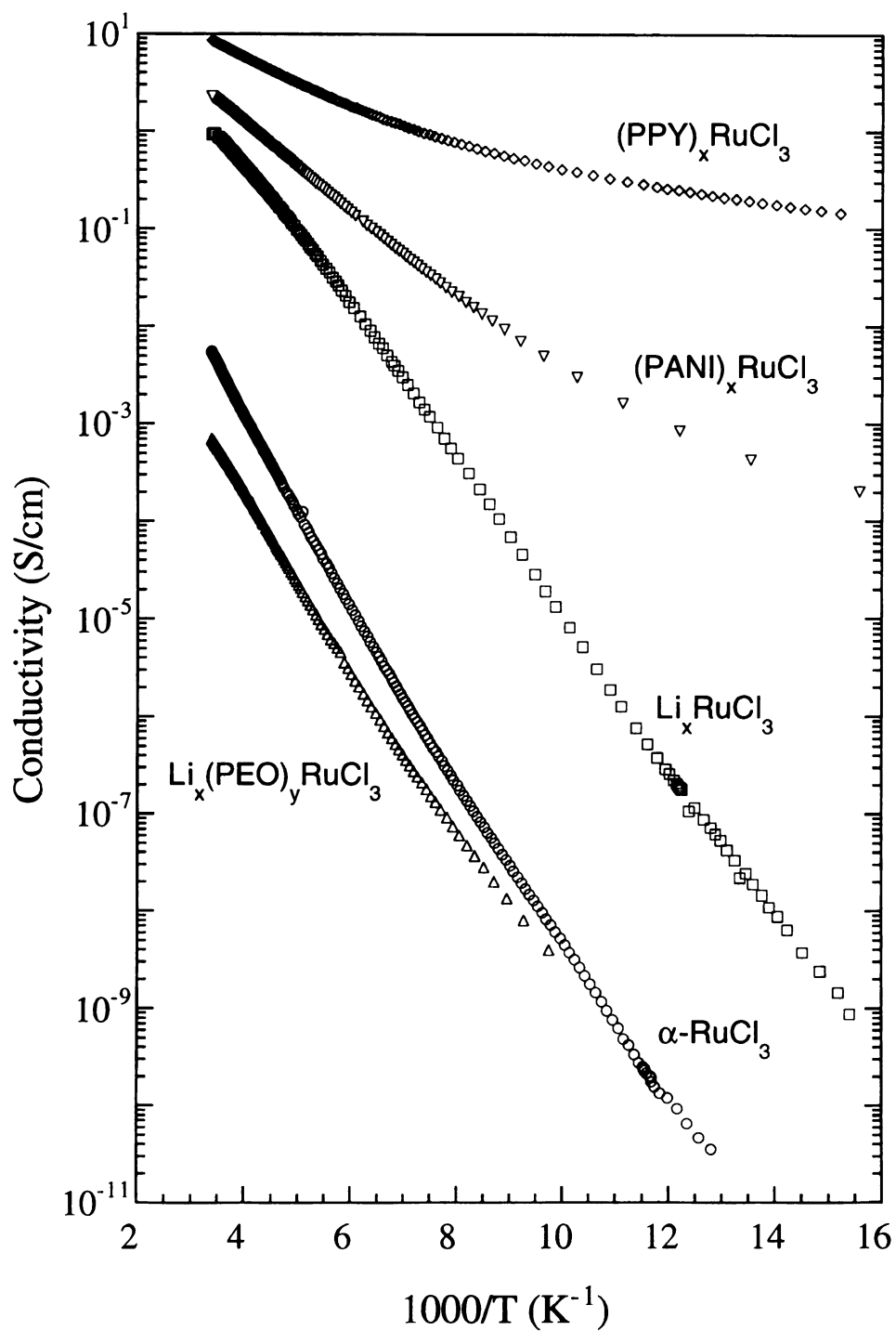


Figure 5.7. Variable temperature electrical conductivity measurements for pressed pellets of  $\alpha$ - $\text{RuCl}_3$  and nanocomposites.



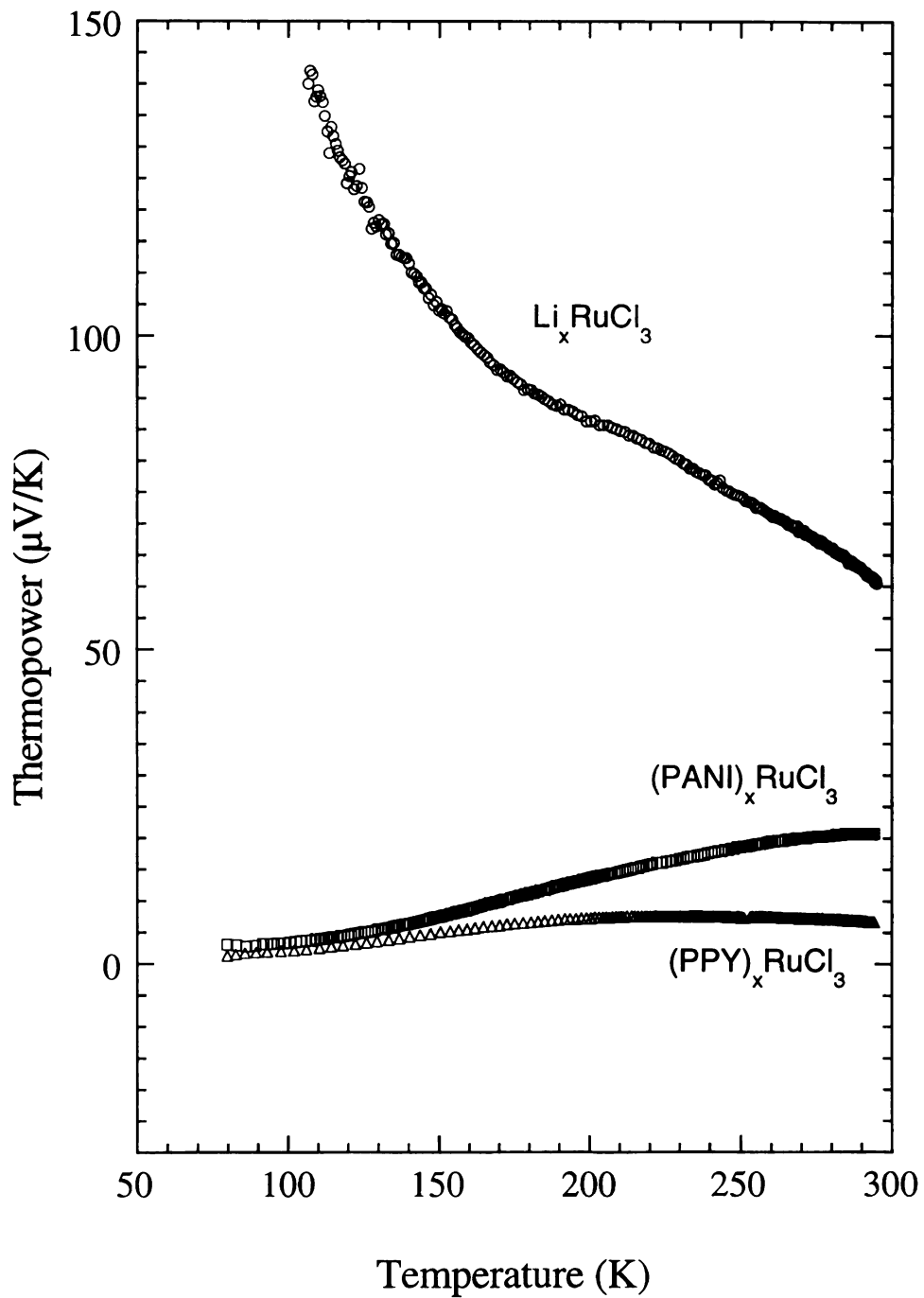


Figure 5.8. Thermopower measurements for pressed pellets of  $\text{Li}_x\text{RuCl}_3$  ( $x \sim 0.2$ ) and nanocomposites.



apparent activation energies are 0.18 eV for  $(\text{PANI})_x\text{RuCl}_3$  ( $> 125$  K) and 0.10 eV for  $(\text{PPY})_x\text{RuCl}_3$  ( $> 160$  K).

The thermopower, which is less affected by grain boundary effects, was measured for  $\text{Li}_x\text{RuCl}_3$  ( $x \sim 0.2$ ),  $(\text{PANI})_x\text{RuCl}_3$  and  $(\text{PPY})_x\text{RuCl}_3$ , see Figure 5.8. All three materials have positive Seebeck coefficients suggesting that the dominant carriers are holes. The p-type charge-transport behavior is consistent with the fact that the reduced  $\text{RuCl}_3$  layers, polyaniline (emeraldine salt) and polypyrrole are all p-type conductors. Both the high Seebeck coefficient value of  $\sim 60 \mu\text{V/K}$  for  $\text{Li}_x\text{RuCl}_3$  and its decreasing trend with rising temperature indicate that  $\text{Li}_x\text{RuCl}_3$  is a semiconductor. The hole type transport in the  $[\text{RuCl}_3]^{x-}$  layer arises from the partially empty band composed of  $t_{2g}$  type orbitals while electron configuration is somewhat between  $t_{2g}^5$  and  $t_{2g}^6$ .  $(\text{PANI})_x\text{RuCl}_3$  and  $(\text{PPY})_x\text{RuCl}_3$  have lower thermopower values which increase as the temperature increases. This trend is usually seen in metallic conductors. Considering that the reduced  $\text{RuCl}_3$  layers are semiconductors, the bulk metallic-like conductivity as suggested by the small thermopower indicates that charge transport in  $(\text{PPY})_x\text{RuCl}_3$  and  $(\text{PANI})_x\text{RuCl}_3$  is controlled by the conductive polymers.

## 5. Magnetic Susceptibility Studies

In  $\alpha\text{-RuCl}_3$  the intralayer  $\text{Ru}^{3+}$  ions are ferromagnetically coupled, however, in adjacent layers the  $\text{Ru}^{3+}$  ions are antiferromagnetically (AF) coupled [6a, 24]. The interlayer AF coupling becomes strong at low temperatures (2-20K), and causes a remarkable AF ordering at about 15.6 K [6a, 24], see Figure 5.9(a). At high temperatures (50-300K), the interlayer AF coupling is so weak that it has no significant effects on the magnetic



susceptibilities. The magnetic susceptibilities of  $\alpha$ -RuCl<sub>3</sub> in this range follow Curie-Weiss law with a positive Weiss constant  $\theta$ , which reflects the weak effect of the intralayer ferromagnetic coupling.

In Li<sub>x</sub>RuCl<sub>3</sub> ( $x \sim 0.2$ ), the conspicuous AF ordering disappears and the magnetic susceptibility follows Curie-Weiss law to temperatures as low as 2 K, see Figure 5.9(b). The Weiss constant  $\theta$  becomes negative, indicating a change from the weak overall ferromagnetic coupling to a weak overall AF coupling. These changes in magnetism are explained by the introduction of diamagnetic Ru<sup>2+</sup> centers in the Ru sublattice, which alters the magnetic couplings both in the layers and between the layers. The magnetic susceptibility data of Li<sub>x</sub>(PEO)<sub>y</sub>RuCl<sub>3</sub>, (PANI)<sub>x</sub>RuCl<sub>3</sub> and (PPY)<sub>x</sub>RuCl<sub>3</sub> are similar to those of Li<sub>x</sub>RuCl<sub>3</sub>, see Figures 5.9(c) and 5.9(d). Since the reduction of the RuCl<sub>3</sub> layers has already disrupted the original interlayer AF coupling, the subsequent insertion of the polymers does not have any additional effect on the magnetic susceptibility.

The  $\mu_{\text{eff}}$  for  $\alpha$ -RuCl<sub>3</sub> is 2.32  $\mu_{\text{B}}$  [25], while those for Li<sub>x</sub>RuCl<sub>3</sub> and nanocomposites Li<sub>x</sub>(PEO)<sub>y</sub>RuCl<sub>3</sub>, (PANI)<sub>x</sub>RuCl<sub>3</sub> and (PPY)<sub>x</sub>RuCl<sub>3</sub> range from 1.60-1.74  $\mu_{\text{B}}$ . The drop in paramagnetic moment is due to the decrease in the number of unpaired electrons in RuCl<sub>3</sub> layers because of the presence of diamagnetic low spin Ru<sup>2+</sup> centers. The derived paramagnetic moments  $\mu_{\text{eff}}$  and Weiss constants  $\theta$  for these compounds are listed in Table 5.1. The  $\chi_{\text{dia}}$  and  $\chi_{\text{TIP}}$  used in the manipulation of the magnetic data are also listed in Table 5.1.

As mentioned above, the intercalation of polymers does not bring much change in the magnetic susceptibility of the reduced RuCl<sub>3</sub> layers, because the interlayer magnetic coupling has already been broken down by the generation of Ru<sup>2+</sup> centers. If the RuCl<sub>3</sub> layers were not reduced, *i.e.*,

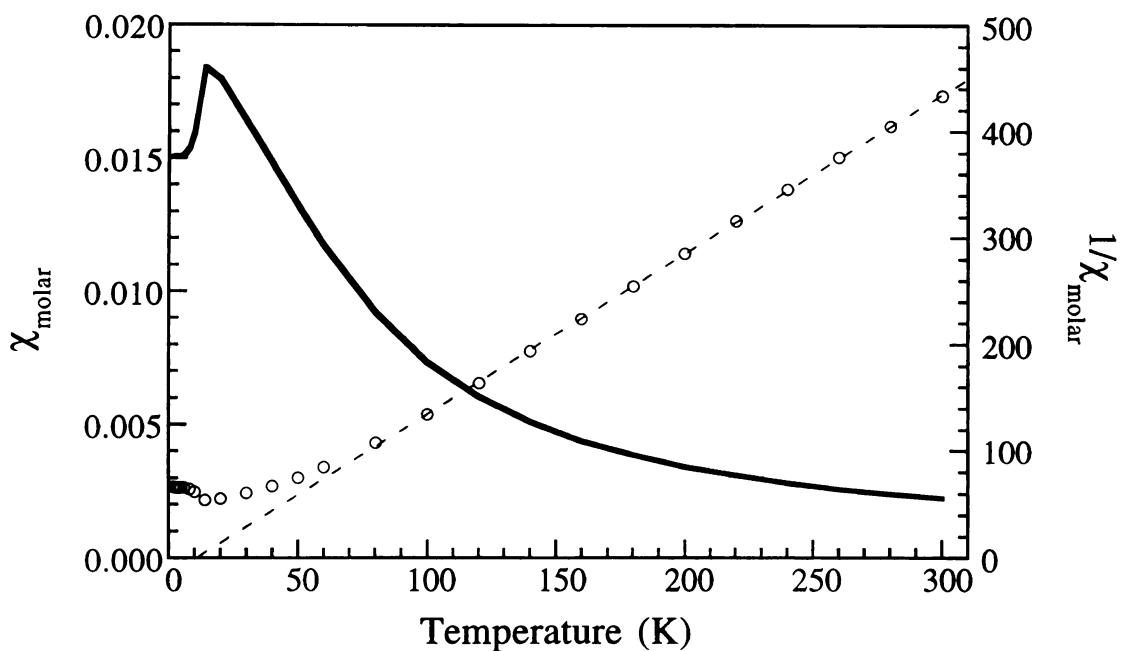


Figure 5.9(a). Magnetic susceptibility measurements for a sample of  $\alpha$ - $\text{RuCl}_3$ .

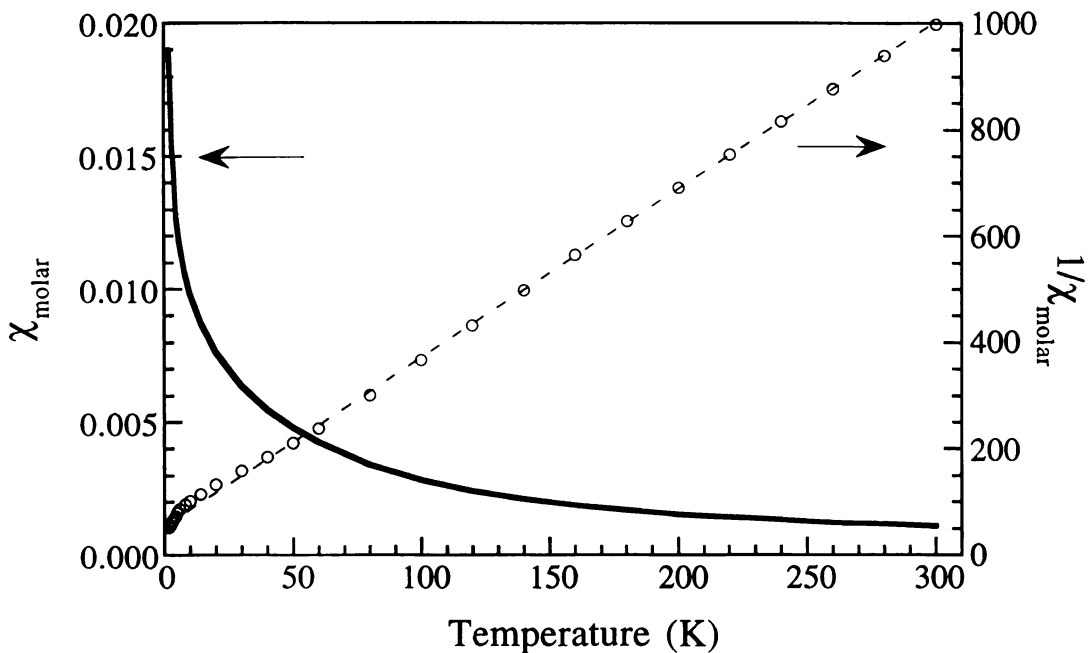


Figure 5.9(b). Magnetic susceptibility measurements for  $\text{Li}_x\text{RuCl}_3$  ( $x \sim 0.2$ ).



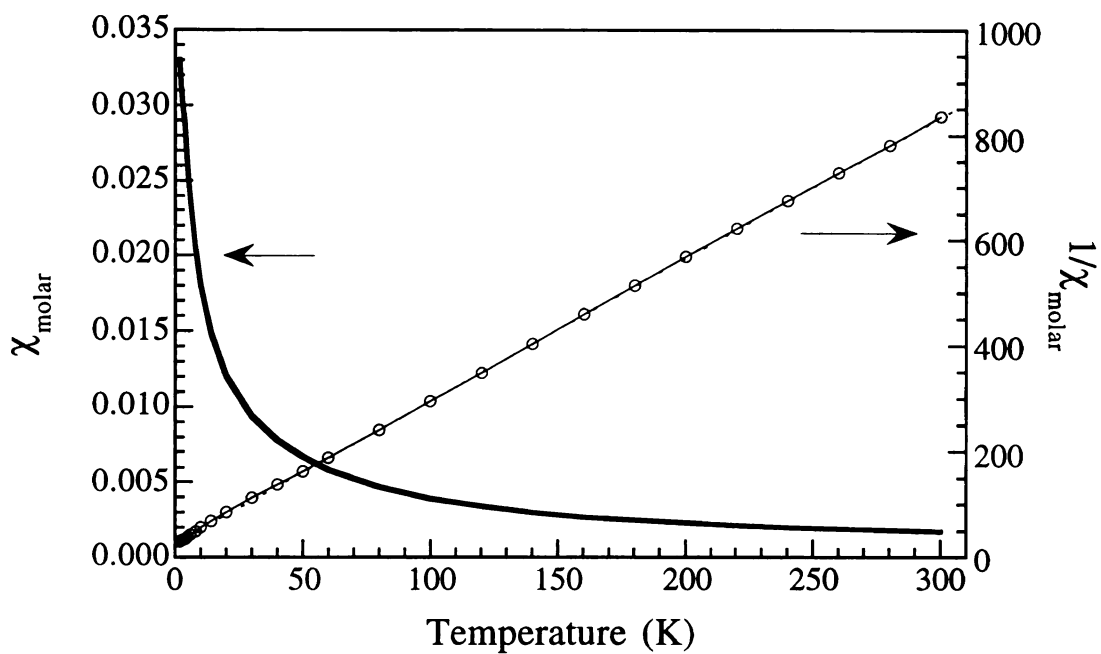


Figure 5.9(c). Magnetic susceptibility measurements for  $\text{Li}_x(\text{PEO})_y\text{RuCl}_3$ .

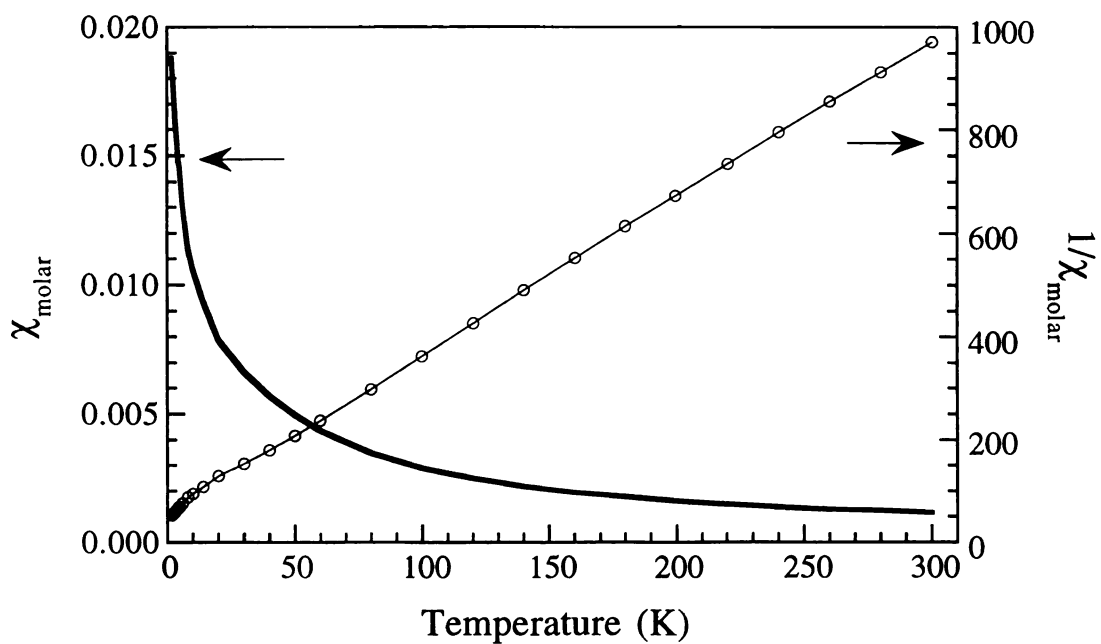


Figure 5.9(d). Magnetic susceptibility measurements for  $(\text{PANI})_x\text{RuCl}_3$ .



Table 5.1. Magnetic properties of  $\alpha$ -RuCl<sub>3</sub> and nanocomposites

| sample   | $\mu_{\text{eff}}$<br>( $\mu_{\text{B}}/\text{mol Ru}$ ) | $\theta$<br>(K) | $\chi_{\text{dia}} * 10^6$<br>(1/mol Ru) | $\chi_{\text{TIP}} * 10^6$<br>(1/mol Ru) |
|--|--|-----------------|--|--|
| $\alpha$ -RuCl <sub>3</sub>                          | 2.32   | 11              | -101                                     | 0  |
| Li <sub>x</sub> RuCl <sub>3</sub> (x~0.2)            | 1.60   | -18             | -101                                     | 176                                      |
| (PANI) <sub>x</sub> RuCl <sub>3</sub>                | 1.63   | -20             | -133                                     | 250                                      |
| Li <sub>x</sub> (PEO) <sub>y</sub> RuCl <sub>3</sub> | 1.73   | -10             | -167                                     | 667                                      |
| (PPY) <sub>x</sub> RuCl <sub>3</sub>                 | 1.74   | -15             | -142                                     | 247                                      |
| RuCl <sub>3</sub> (oxid.)                            | 2.33   | 6.2             | -101                                     | 450                                      |
| (PEO) <sub>x</sub> RuCl <sub>3</sub><br>(oxid.)      | 1.82   | 0.2             | -143                                     | 450                                      |

the magnetic coupling among the Ru<sup>3+</sup> ions existed, the weakening or elimination of the interlayer Ru<sup>3+</sup> ion magnetic coupling by the polymer intercalation should be observed. Such a phenomenon is expected in the “Br<sub>2</sub> oxidized Li<sub>x</sub>(PEO)<sub>y</sub>RuCl<sub>3</sub>” (*i.e.* “(PEO)<sub>x</sub>RuCl<sub>3</sub>”), in which the Ru<sup>2+</sup> centers in the reduced RuCl<sub>3</sub> layers are oxidized back to Ru<sup>3+</sup>. In this material the intralayer Ru<sup>3+</sup> ferromagnetic coupling should be restored, while the interlayer Ru<sup>3+</sup> AF coupling should still be retarded by the increased interlayer separation.

An investigation of the magnetic properties of “Br<sub>2</sub> oxidized Li<sub>x</sub>RuCl<sub>3</sub>” (*i.e.* RuCl<sub>3</sub>) was first carried out, because this material is structurally simpler than the oxidized nanocomposites yet intimately related to them. The oxidized product indeed reestablished the weak overall ferromagnetism at temperatures higher than 50 K. However, the significant AF ordering present in pristine  $\alpha$ -RuCl<sub>3</sub> did not recover. Instead, a gradual change from overall ferromagnetism to overall antiferromagnetism at low temperatures was observed, see Figure 5.10(a). It is obvious that



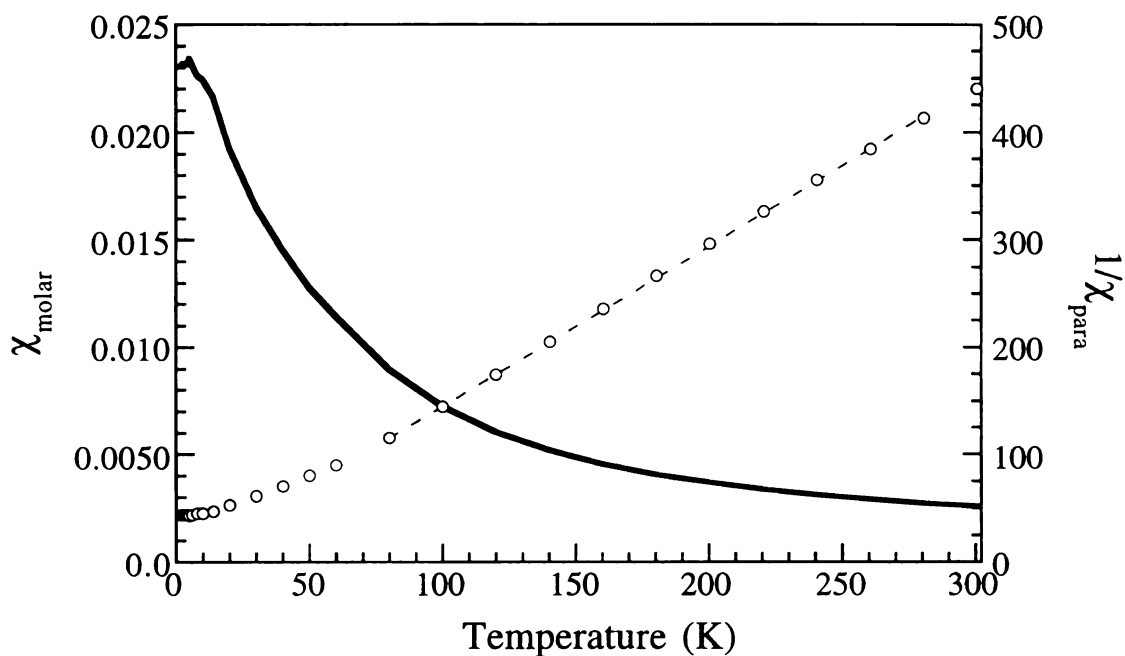


Figure 5.10(a). Magnetic susceptibility measurements for “Br<sub>2</sub> oxidized Li<sub>x</sub>RuCl<sub>3</sub>” (*i.e.* RuCl<sub>3</sub>).

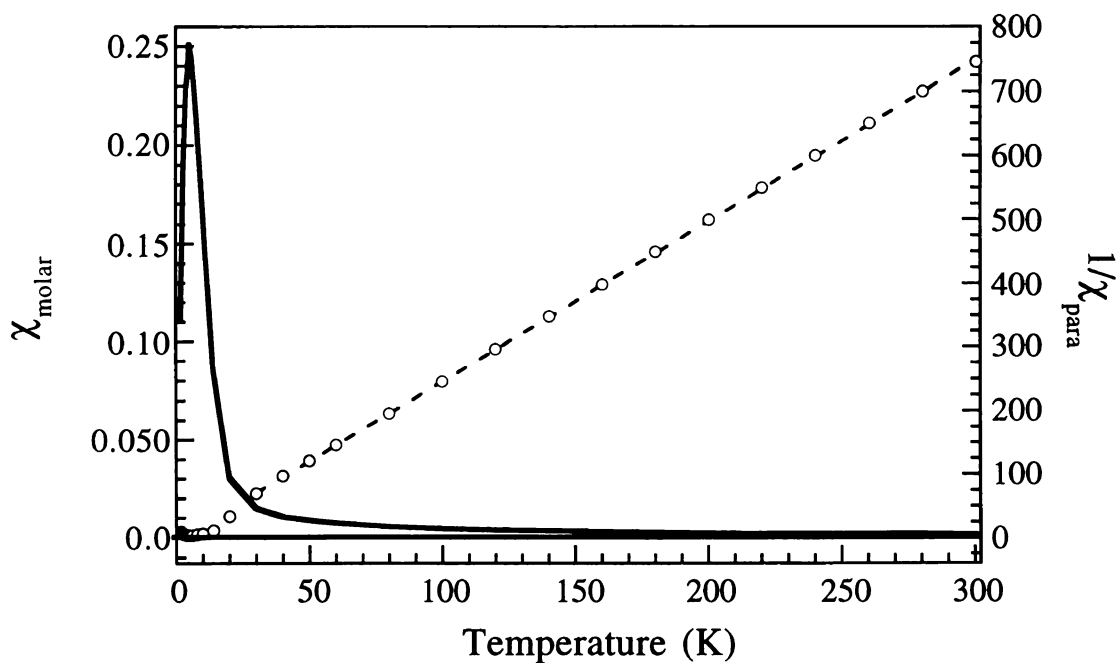
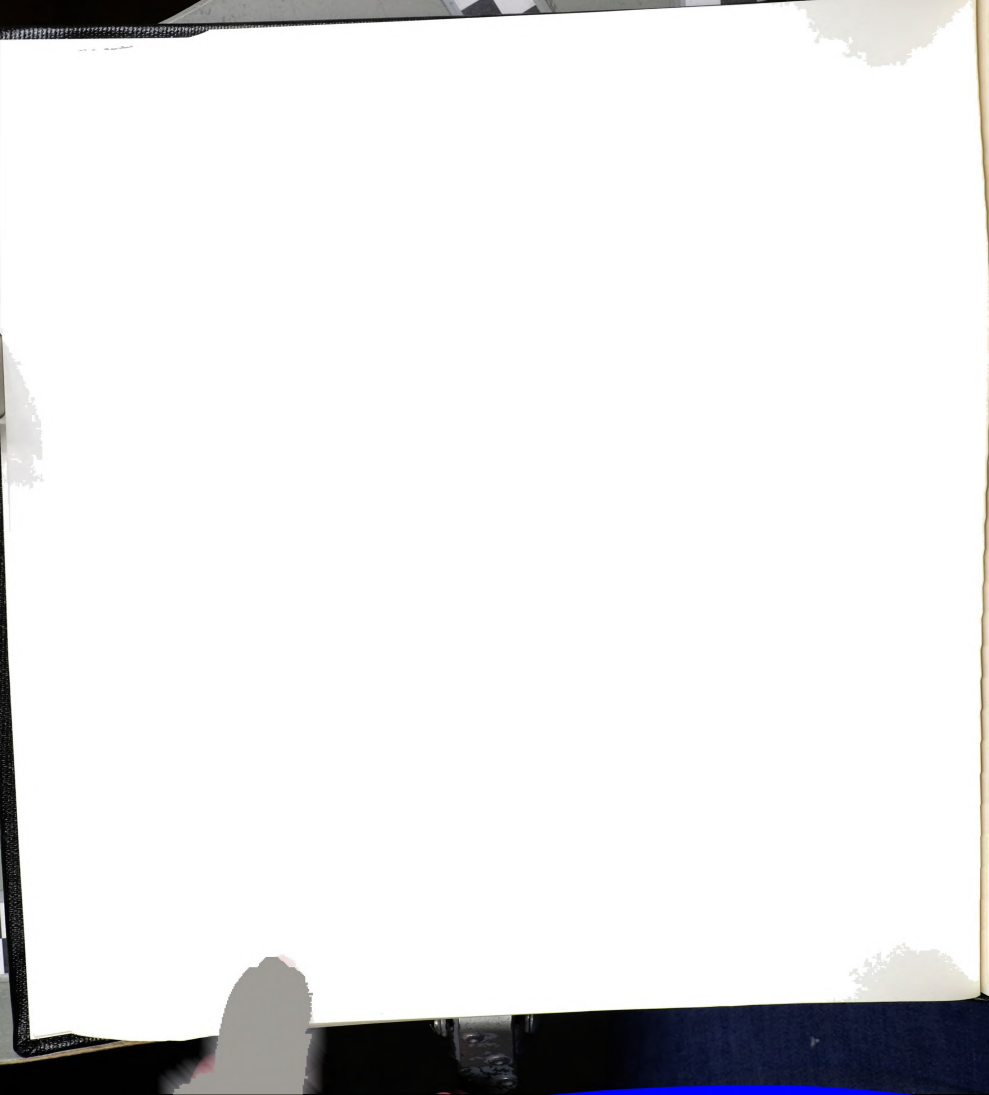


Figure 5.10(b). Magnetic susceptibility measurements for “Br<sub>2</sub> oxidized Li<sub>x</sub>(PEO)<sub>y</sub>RuCl<sub>3</sub>” (*i.e.* “(PEO)<sub>x</sub>RuCl<sub>3</sub>”).



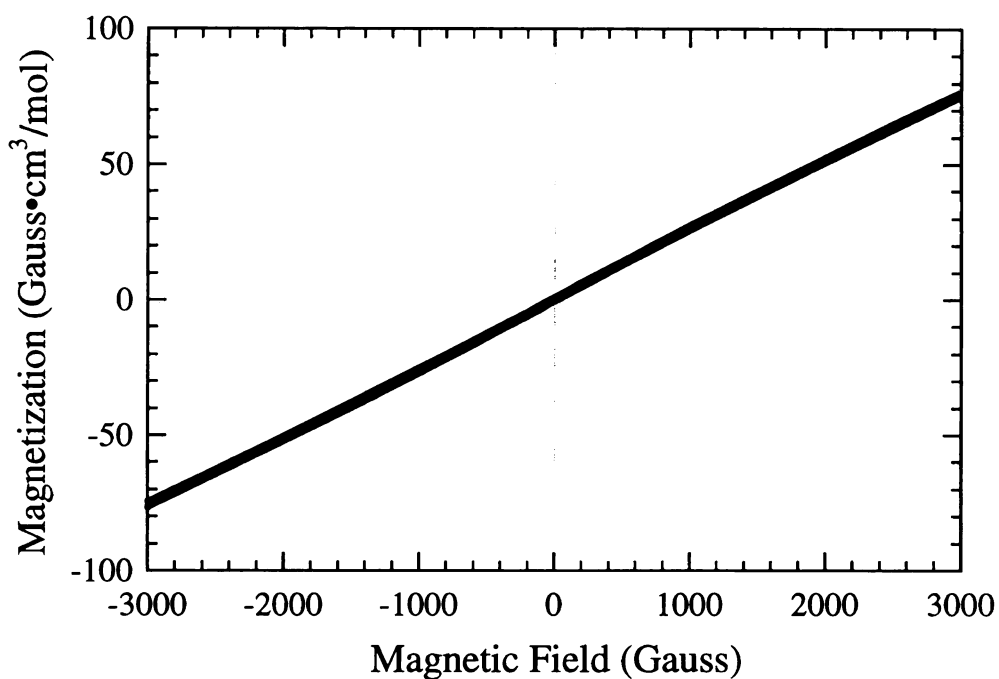


Figure 5.10(c). Magnetic hysteresis measurements for “Br<sub>2</sub> oxidized Li<sub>x</sub>RuCl<sub>3</sub>” (*i.e.* RuCl<sub>3</sub>).

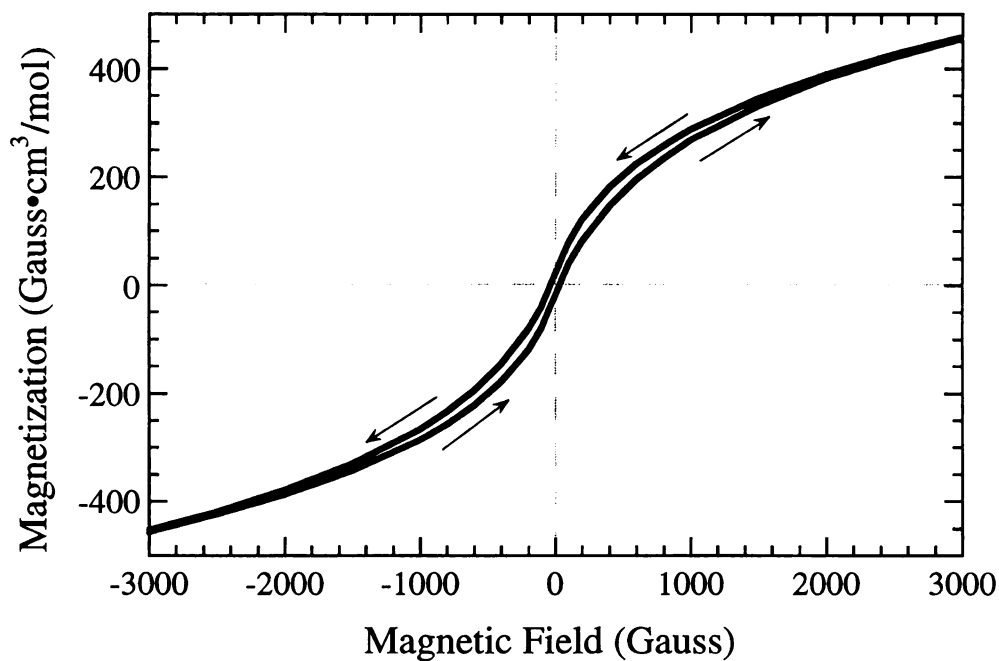
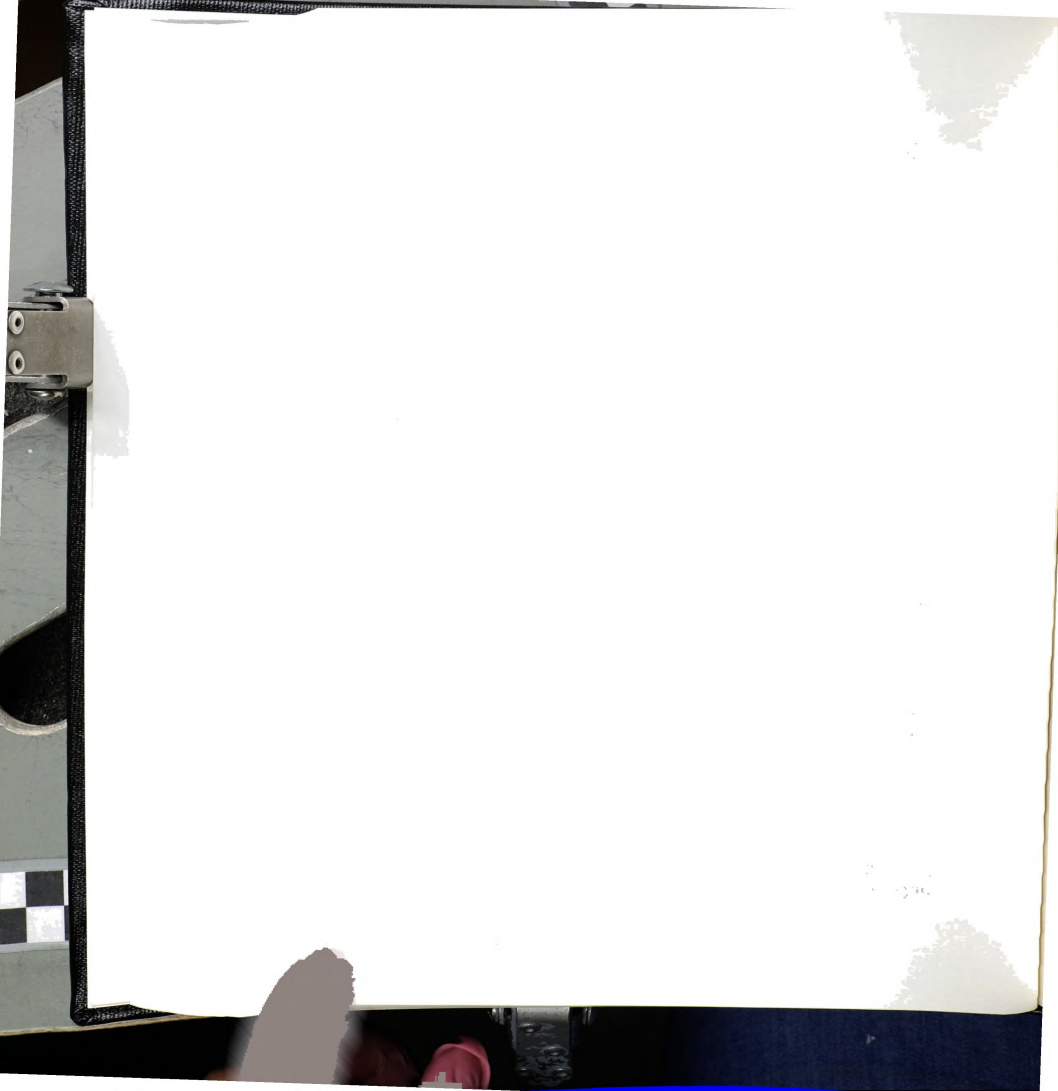


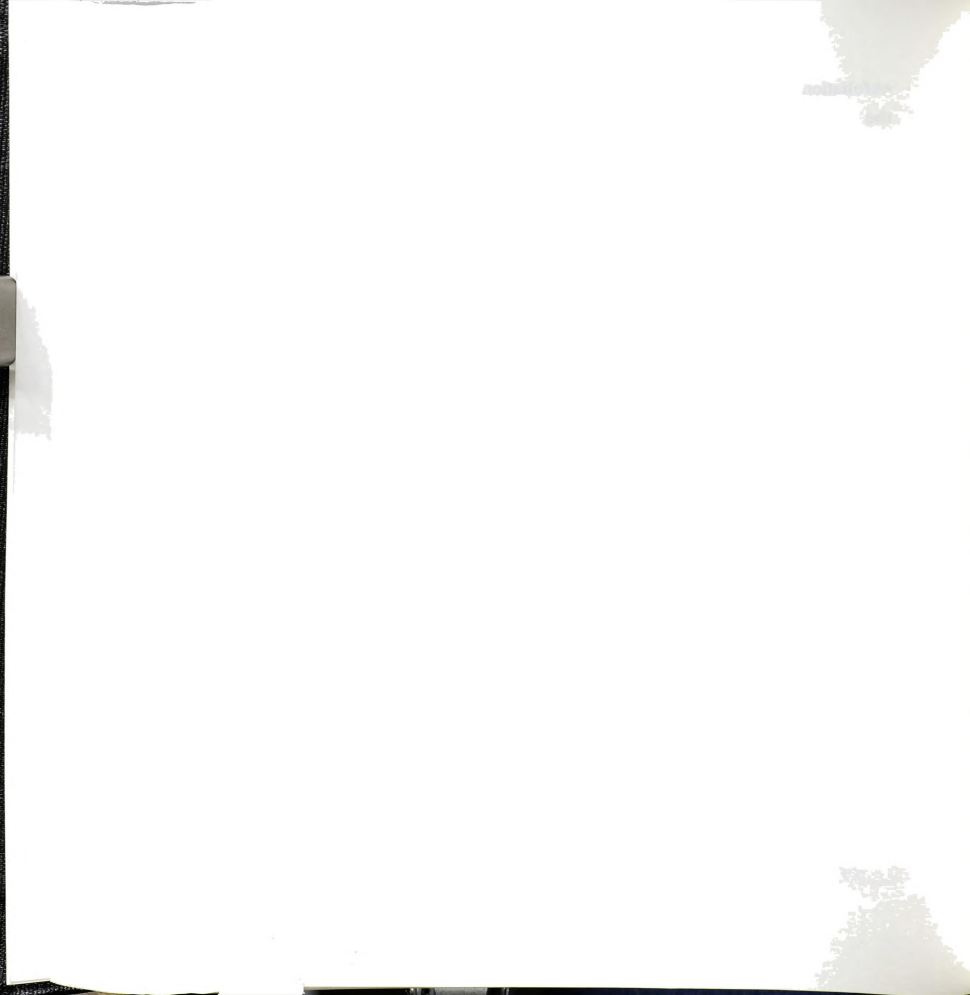
Figure 5.10(d). Magnetic hysteresis measurements for “Br<sub>2</sub> oxidized Li<sub>x</sub>(PEO)<sub>y</sub>RuCl<sub>3</sub>” (*i.e.* “(PEO)<sub>x</sub>RuCl<sub>3</sub>”).



exfoliation and restacking causes stacking disorder ( *e.g.* turbostratic) of the RuCl<sub>3</sub> layers, so that optimum interlayer AF coupling in oxidized RuCl<sub>3</sub> is not possible.

The overall ferromagnetic coupling for the oxidation derived “(PEO)<sub>x</sub>RuCl<sub>3</sub>” at temperatures higher than 5 K is slightly weaker than that of corresponding RuCl<sub>3</sub> (> 50 K), as is suggested by the less positive  $\theta$  value. The intercalation of polymer causes the AF coupling to almost disappear, as demonstrated by the persistence of the overall ferromagnetism to as low as 5 K, see Figure 5.10(b). The magnetic hysteresis measurement, which is characterized by a hysteresis loop, confirms that the “(PEO)<sub>x</sub>RuCl<sub>3</sub>” produced by Br<sub>2</sub> oxidation of Li<sub>x</sub>(PEO)<sub>y</sub>RuCl<sub>3</sub> is ferromagnetic at 5 K, see Figure 5.10(d). In contrast, RuCl<sub>3</sub> produced by Br<sub>2</sub> oxidation of Li<sub>x</sub>RuCl<sub>3</sub> does not show a hysteresis loop, see Figure 5.10(c).

The latter material has  $\mu_{\text{eff}}$  and  $\theta$  values close to that of  $\alpha$ -RuCl<sub>3</sub>, which means that almost all Ru<sup>2+</sup> centers are converted to the Ru<sup>3+</sup> state. The  $\mu_{\text{eff}}$  and  $\theta$  of “(PEO)<sub>x</sub>RuCl<sub>3</sub>” produced by Br<sub>2</sub> oxidation of Li<sub>x</sub>(PEO)<sub>y</sub>RuCl<sub>3</sub> are between those of un-oxidized nanocomposites and  $\alpha$ -RuCl<sub>3</sub>, which might suggest that some Ru<sup>2+</sup> centers remain. The incomplete conversion of Ru<sup>2+</sup> to Ru<sup>3+</sup> in the nanocomposite could be attributed to the presence of polymers in the interlayer galleries, which stabilize the reduced layers by offering coordination to Li<sup>+</sup> ions. Other reasons could include slower oxidation kinetics in the polymer intercalated systems. The paramagnetic moment  $\mu_{\text{eff}}$  and Weiss constant  $\theta$  of the oxidation derived RuCl<sub>3</sub> and “(PEO)<sub>x</sub>RuCl<sub>3</sub>” are shown in Table 5.1.



## 6. One-Dimensional Electron Density Calculations and Arrangement of Polymer Chains in $\text{Li}_x(\text{PEO})_y\text{RuCl}_3$

In inorganic/polymeric nanocomposites, the arrangement of the atoms in the inorganic layers is well defined. However, the arrangement of polymer chains in the interlayer galleries is not so clear, yet the structural issue is critical to a full understanding of the properties. Because the interlayer gallery provides a two-dimensional space for polymer chains, their arrangement in the interlayer gallery also stimulates a lot of interest in fundamental polymer physics. Many researchers have explored this type of situation with different approaches [26].

Because of the simple repeat structure and flexible chain of PEO, its intercalative nanocomposites have been the subject of most investigations [26b, c, d, e, f]. In addition, many structures for PEO and PEO-complexes are known.

The most common conformation of bulk PEO is the helical one [27], which exists in pure PEO spherulites [28]. The planar zigzag conformation has been observed in stretched PEO samples [29]. Two more types of conformations have been found in PEO- $\text{HgCl}_2$  complexes [30, 31]. There are many PEO-(alkali metal salt) complexes with versatile morphologies and the determination of their structures has been attempted. The conformation of PEO in these alkali metal salt complexes is thought to be either a double helix [32], a waving single helix, which accommodates itself around the alkali ion lattice [33], or one similar to that in the type II PEO- $\text{HgCl}_2$  complex [34]. In addition, many PEO complexes form with organic molecules: PEO-urea complex [35], PEO-thiourea complex [36], PEO-*para*-dibromobenzene complex [37] and PEO-*para*-nitrophenol complex [38]. Several common PEO conformations are shown in Figure 5.11.



Films of oriented  $\text{Li}_x(\text{PEO})_y\text{RuCl}_3$  have well defined sharp XRD patterns with up to fourteen  $00l$  reflections corresponding to a resolution of  $0.98 \text{ \AA}$ , see Figure 5.12. The 1-D ED maps for  $\text{Li}_x(\text{PEO})_y\text{RuCl}_3$ , which can provide information about the projected structure on the  $c$  axis, were calculated from the X-ray powder pattern of oriented films (see Figure 5.13 [39]), with formulas described in Chapter 3. In the calculation for 1-D ED map, the phases of structure factors are needed. The phase information for the calculation was obtained from the positions of the Ru and Cl atoms. Due to the minor contribution of the diffracted intensity from the polymer, the inorganic layer plays a critical role here in phasing the structure factors and consequently in the computation of the electron density map.

The 1-D ED map profile for  $\text{Li}_x(\text{PEO})_y\text{RuCl}_3$  shows clearly that the electron density due to the intercalates forms two asymmetric peaks placed symmetrically away from the center of the gallery, similar to that of  $\text{Li}_{0.2}(\text{PEO})_x\text{TaS}_2$  [13c]. As in the case of  $\text{Li}_{0.2}(\text{PEO})_x\text{TaS}_2$ , the 1-D ED map favors best the structural model with two layers of PEO in the gallery in the conformation of type II PEO- $\text{HgCl}_2$  complex [40]. (The model is shown in Figure 5.14.) The wide valley in the 1-D ED map in the center of the gallery immediately excludes the possibility of a layer of helically formed PEO, which must have appreciable electron density in the central region of the gallery. Considering that the basal spacing of the  $\text{Li}_x(\text{PEO})_y\text{RuCl}_3$  film used is  $13.76 \text{ \AA}$  [41], which gives an interlayer expansion of  $8.0 \text{ \AA}$ , the accommodation of two layers of helical PEO in such a gallery is physically impossible, because the Van der Waals diameter of one PEO helix is  $\sim 8.0 \text{ \AA}$  [27]. Furthermore, neither the arrangement of PEO in the zigzag conformation (which was proposed in the  $(\text{PEO})_x\text{V}_2\text{O}_5$  [26d]) nor that of the



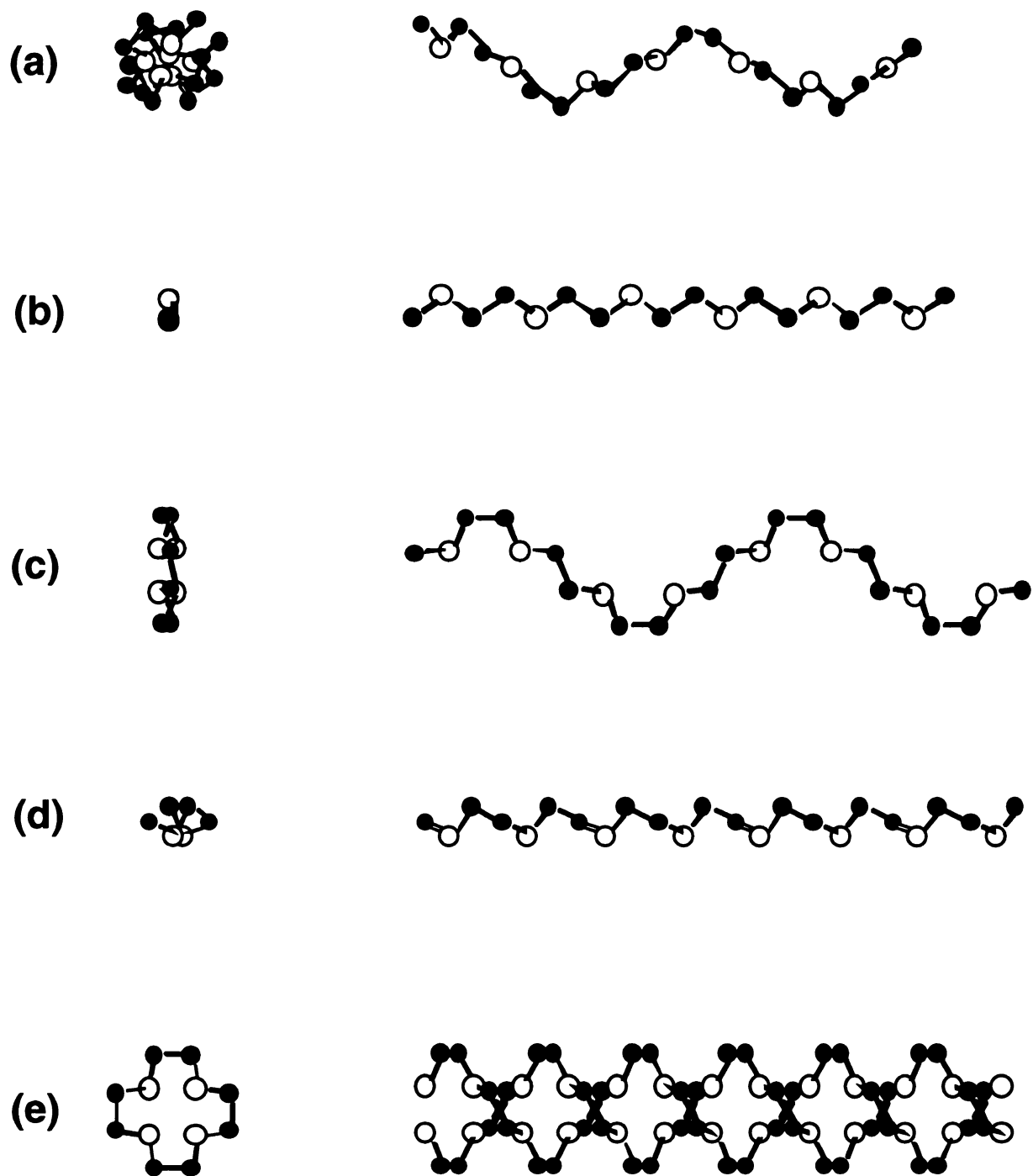


Figure 5.11. Possible PEO conformations: (a) single helix (7/2) [27], (b) zigzag [29], (c) type I PEO-HgCl<sub>2</sub> [30b], (d) type II PEO-HgCl<sub>2</sub> [31], (e) double helix [32].



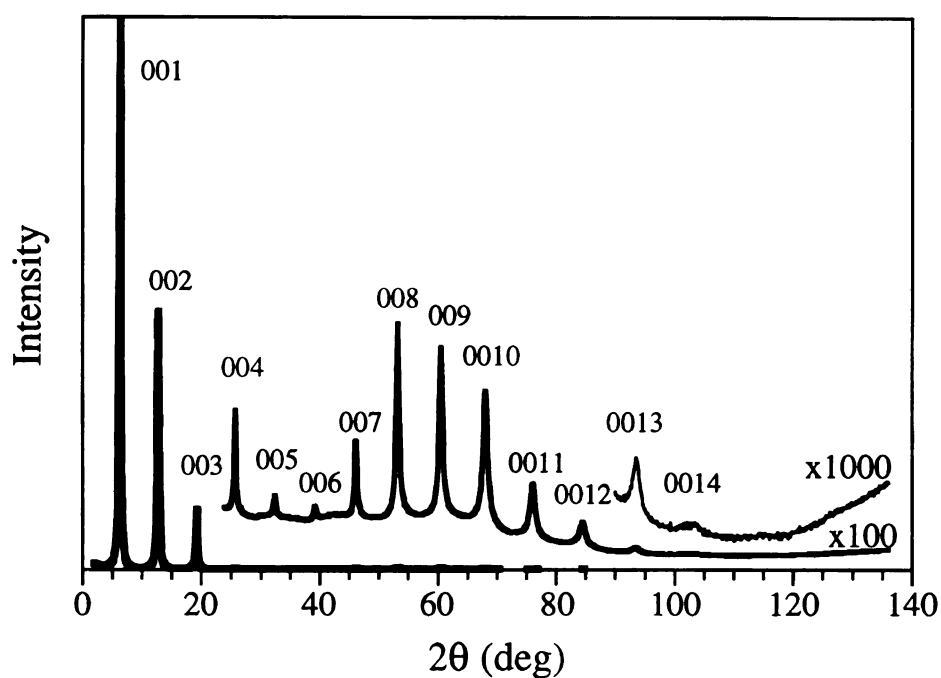


Figure 5.12. X-ray powder diffraction pattern of oriented  $\text{Li}_x(\text{PEO})_y\text{RuCl}_3$  film used for the calculation of one-dimensional electron density maps.

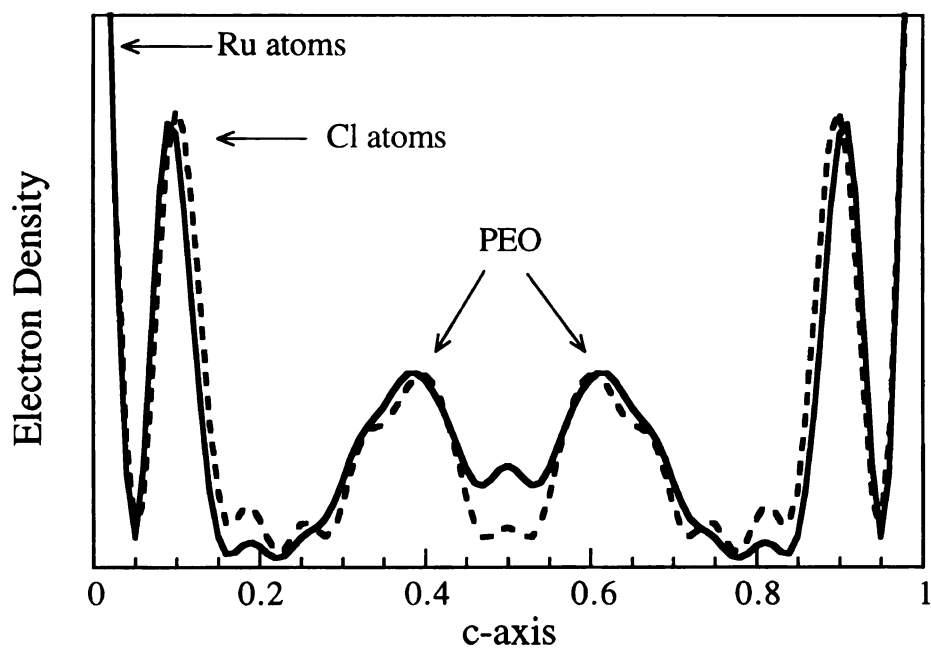
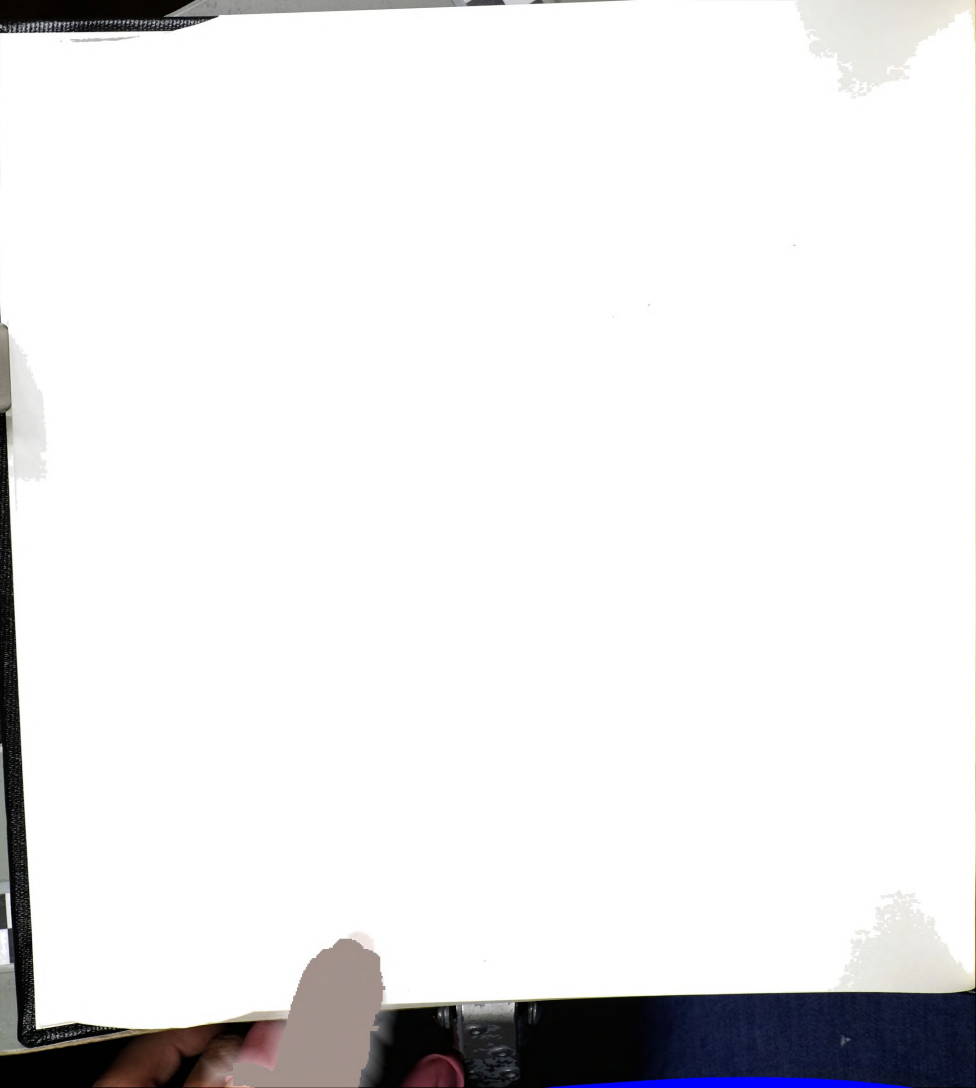


Figure 5.13(a). One-dimensional electron density map for  $\text{Li}_x(\text{PEO})_y\text{RuCl}_3$  using the model shown in Figure 5.14. (Solid line, calculated from experimental data; dash line, from model.)



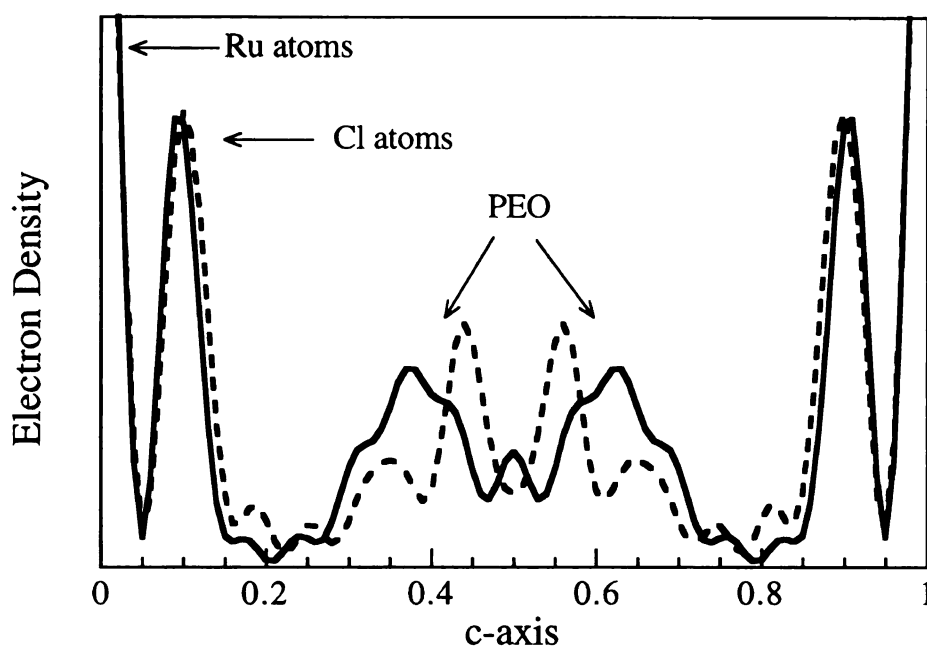


Figure 5.13(b). One-dimensional electron density map for  $\text{Li}_x(\text{PEO})_y\text{RuCl}_3$  using a model with intragallery double helical PEO that takes an orientation as shown in Figure 5.11(e). (Solid line, calculated from experimental data; dash line, from model.)

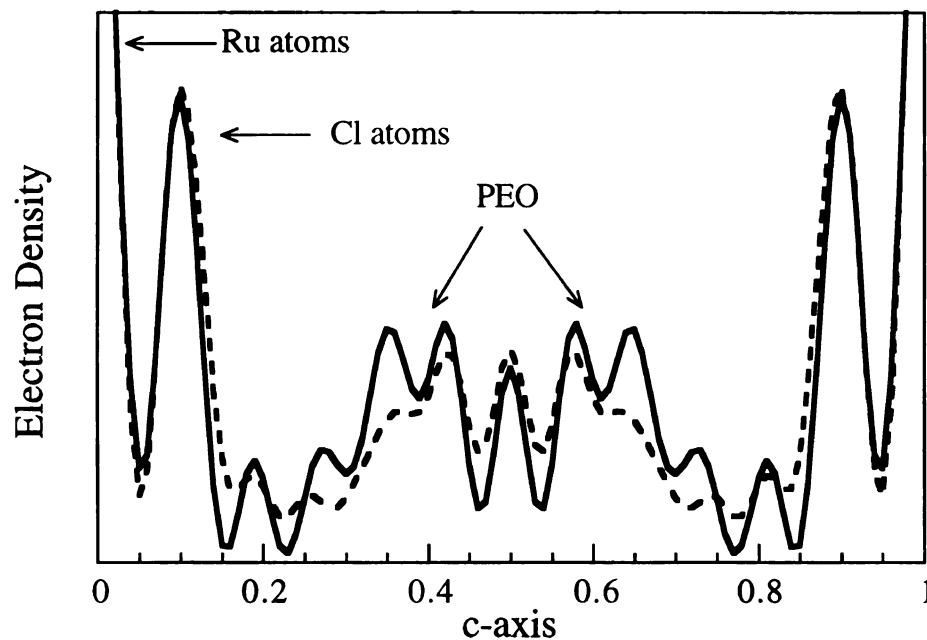
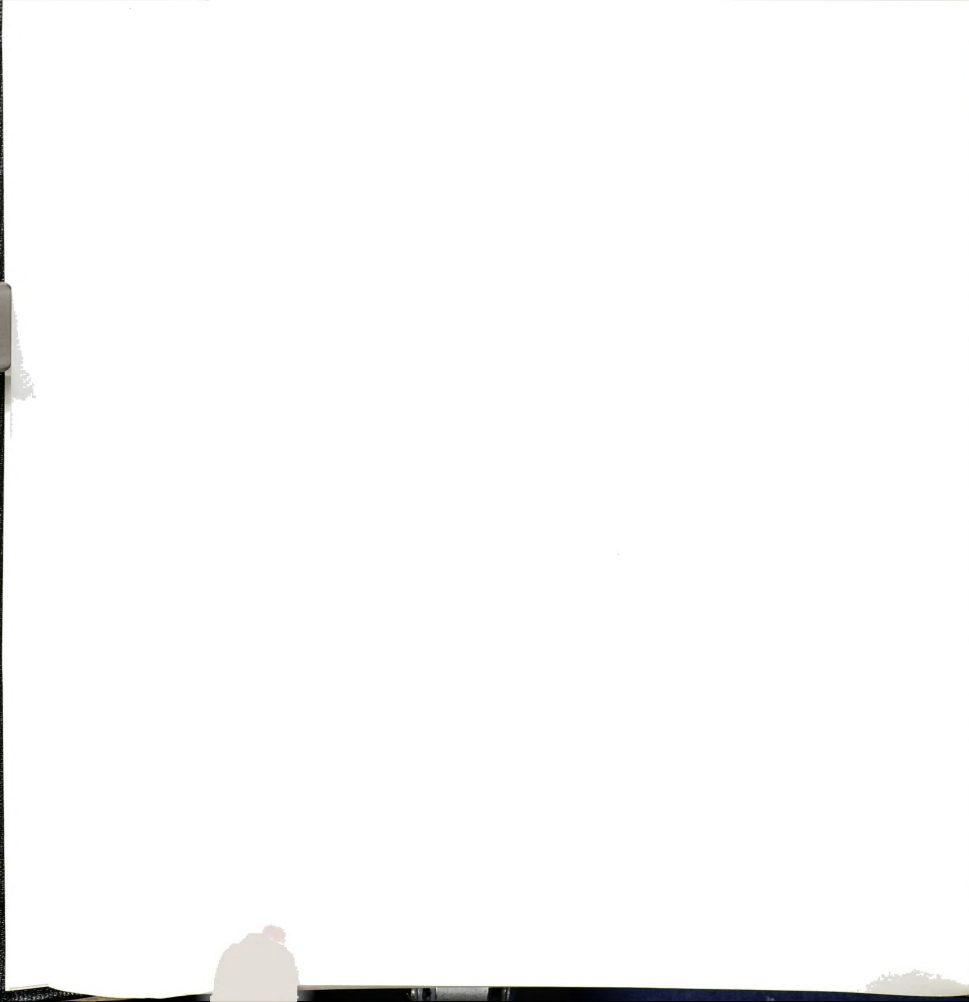


Figure 5.13(c). One-dimensional electron density map for  $\text{Li}_x(\text{PEO})_y\text{RuCl}_3$  using an intragallery double helical PEO model that assumes an orientation of  $45^\circ$  rotation relative to the one shown in Figure 5.11(e). (Solid line, calculated from experimental data; dash line, from model.)



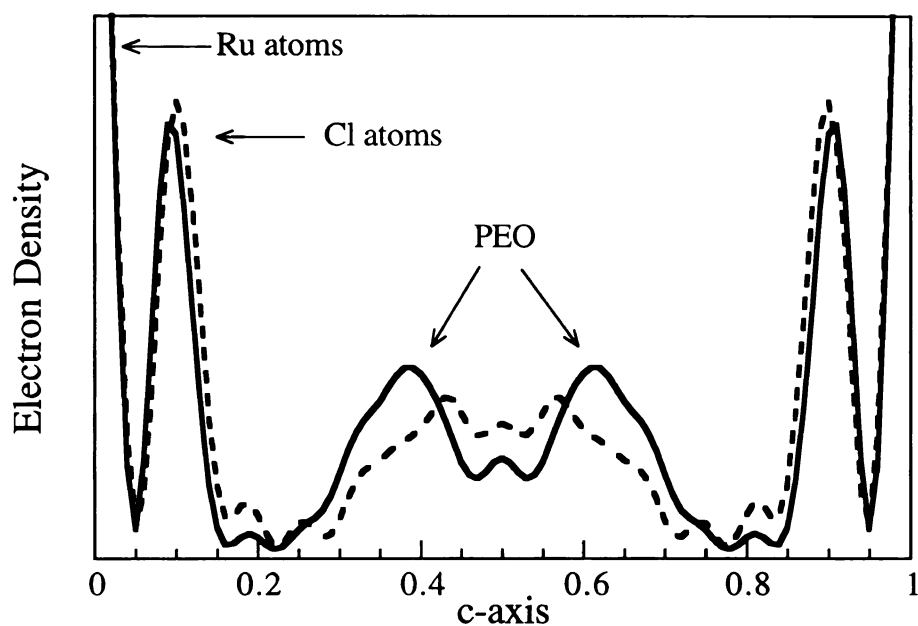


Figure 5.13(d). One-dimensional electron density map for  $\text{Li}_x(\text{PEO})_y\text{RuCl}_3$  using a model with randomly rotated intragallery double helical PEO. (Solid line, calculated from experimental data; dash line, from model.)

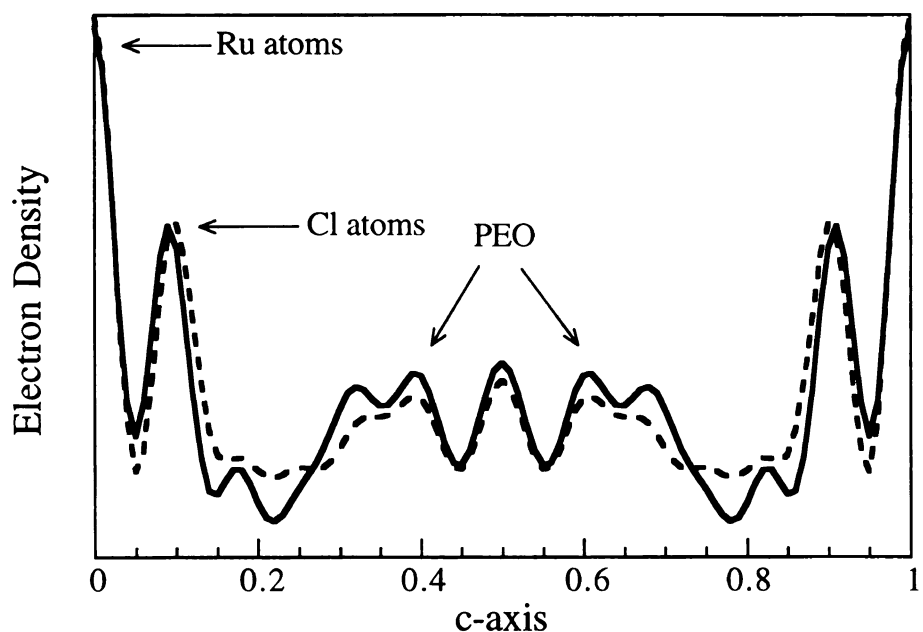


Figure 5.13(e). One-dimensional electron density map for  $\text{Ag}_x(\text{PEO})_y\text{RuCl}_3$  using a model similar to that shown in Figure 5.14. (Solid line, calculated from experimental data; dash line, from model.)



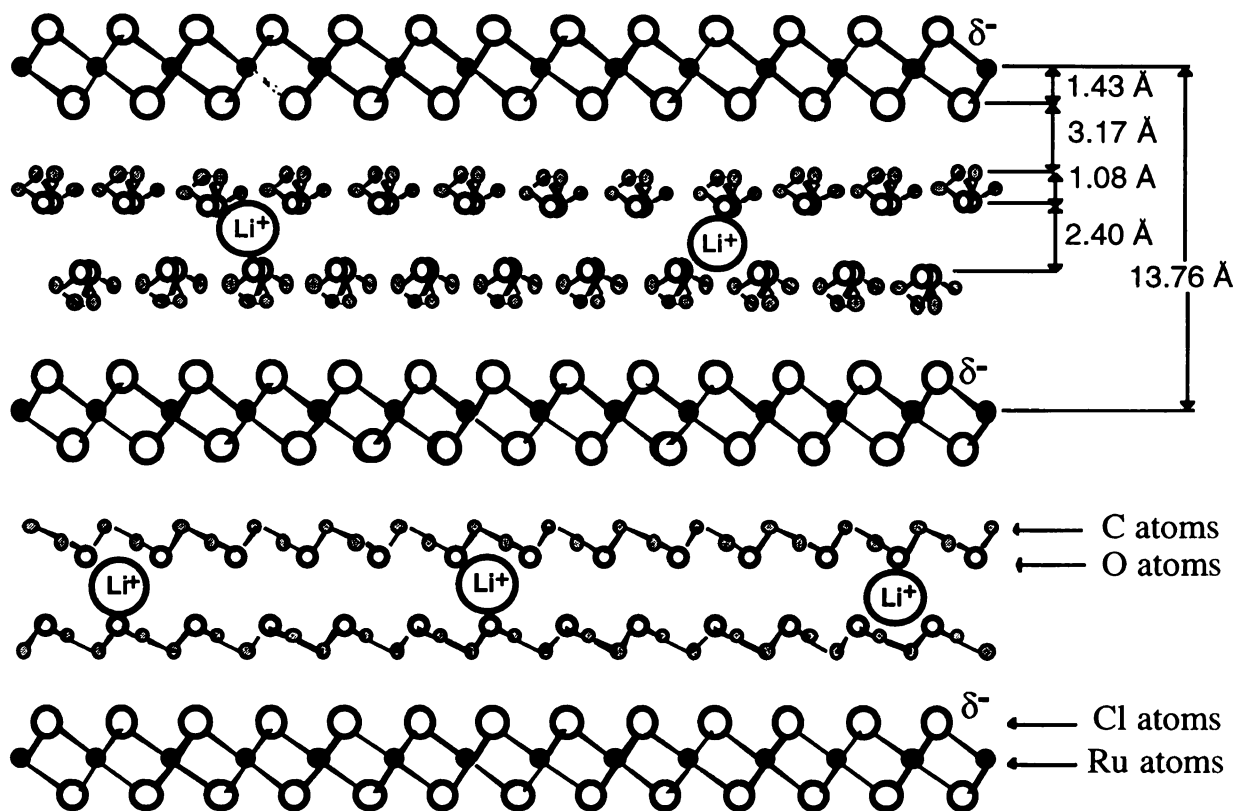


Figure 5.14. Structural model for  $\text{Li}_x(\text{PEO})_y\text{RuCl}_3$ . For clarity, in the two galleries the directions of the PEO are drawn orthogonal to each other.



type I PEO-HgCl<sub>2</sub> complex (which was proposed for the Na<sub>0.3</sub>(PEO)<sub>x</sub>MoO<sub>3</sub> [26c]) is consistent with the observed 1-D ED map profile.

In the model of Figure 5.14, the PEO chains are placed at a Van der Waals distance from the RuCl<sub>3</sub> layers, *i.e.*, it is in touch with RuCl<sub>3</sub>. The Van der Waals thickness of a layer of  $\alpha$ -RuCl<sub>3</sub> is 5.73(3) Å [6a]. According to the crystal structure of zigzag PEO [29], the distance of the outmost C atom in PEO to the Van der Waals boundary of the molecule should be about 1.73 Å. Therefore, the distance of the C atoms closer to RuCl<sub>3</sub> should be 4.60 Å from the Ru layer, and the distance of the O atoms to the middle of the gallery is 1.20 Å. As shown in Figure 5.13(a), the 1-D ED map profile of the model matches well the profile calculated from experimental data in all regions except the center of the gallery.

In the center of the gallery, the electron density of the model is obviously lower than that from the experiment due to the fact that disordered water molecules could accumulate around the lithium ions in the free space between the PEO layers. The fact that all the O atoms in the PEO face towards the center of the gallery makes this region hydrophilic, suggesting that the Li<sup>+</sup> ions may reside there. The width of this hydrophilic region is different in Li<sub>x</sub>(PEO)<sub>y</sub>RuCl<sub>3</sub> and Li<sub>0.2</sub>(PEO)<sub>x</sub>TaS<sub>2</sub> models, and depends on the amount of water molecules present in it.

Electron density due to the Li<sup>+</sup> ions themselves is probably not observable in these ED maps due to insufficient quantities of this very light metal in the material. The validity of the argument that the lithium ions could be in the center of the gallery was examined using a control experiment in which the Li<sup>+</sup> ions were replaced with Ag<sup>+</sup> ions. We reasoned that because both ions are single charged the heavier Ag<sup>+</sup> may behave similarly to Li<sup>+</sup> in the nanocomposite and at the same time

1000000000

1000000000

1000000000

1000000000

1000000000

1000000000

1000000000

1000000000

1000000000

1000000000

1000000000

1000000000

1000000000

1000000000

1000000000

1000000000

1000000000

1000000000

1000000000

1000000000

1000000000

1000000000

1000000000

1000000000

1000000000

substantially contribute to the diffraction pattern. The 1-D ED map of the  $\text{Ag}_x(\text{PEO})_y\text{RuCl}_3$  sample indicated substantially higher electron density in the central region, see Figure 13(e). (In the model for Figure 13(e), 0.2 equivalent of  $\text{Ag}^+$  ions are put in the center of the gallery. An electron density map calculated from the experimental data using a model without the  $\text{Ag}^+$  ions also shows the central peak.) This supports the argument that the ions occupy the center of the gallery.

There exists some similarity between the present model and the structure of PEO-NaSCN complex, in which PEO also has a conformation similar to that found in type II PEO-HgCl<sub>2</sub> complex [34]. In PEO-NaSCN, the chains are arranged with the CH<sub>2</sub>CH<sub>2</sub> units in proximity with the S atoms of NaSCN, which are less hydrophilic, whereas O atoms coordinate with the Na<sup>+</sup> ions, which are much more hydrophilic. This environment of PEO is reminiscent of the present  $\text{Li}_x(\text{PEO})_y\text{RuCl}_3$  model. In addition, this particular form of PEO-NaSCN complex exists under high tension and converts to another form with a helical PEO conformation if the tension is released. In the  $\text{Li}_x(\text{PEO})_y\text{RuCl}_3$  case, the polymer chains extend themselves over a 2-D environment, which of course represents a form of tension as well.

The proposed  $\text{Li}_x(\text{PEO})_y\text{RuCl}_3$  model matches well the observed 1-D ED map and is geometrically and chemically reasonable. This model is different from the one proposed for Li/PEO/montmorillonite nanocomposite in which the Li<sup>+</sup> ions are thought to be located near the surface oxides of the silicate layer [42]. Presumably the lower affinity of Li<sup>+</sup> for Cl<sup>-</sup> causes its migration in the middle of the gallery which presents an oxygen rich coordination environment. Such a PEO arrangement should provide a good diffusion environment for ions in directions parallel to the

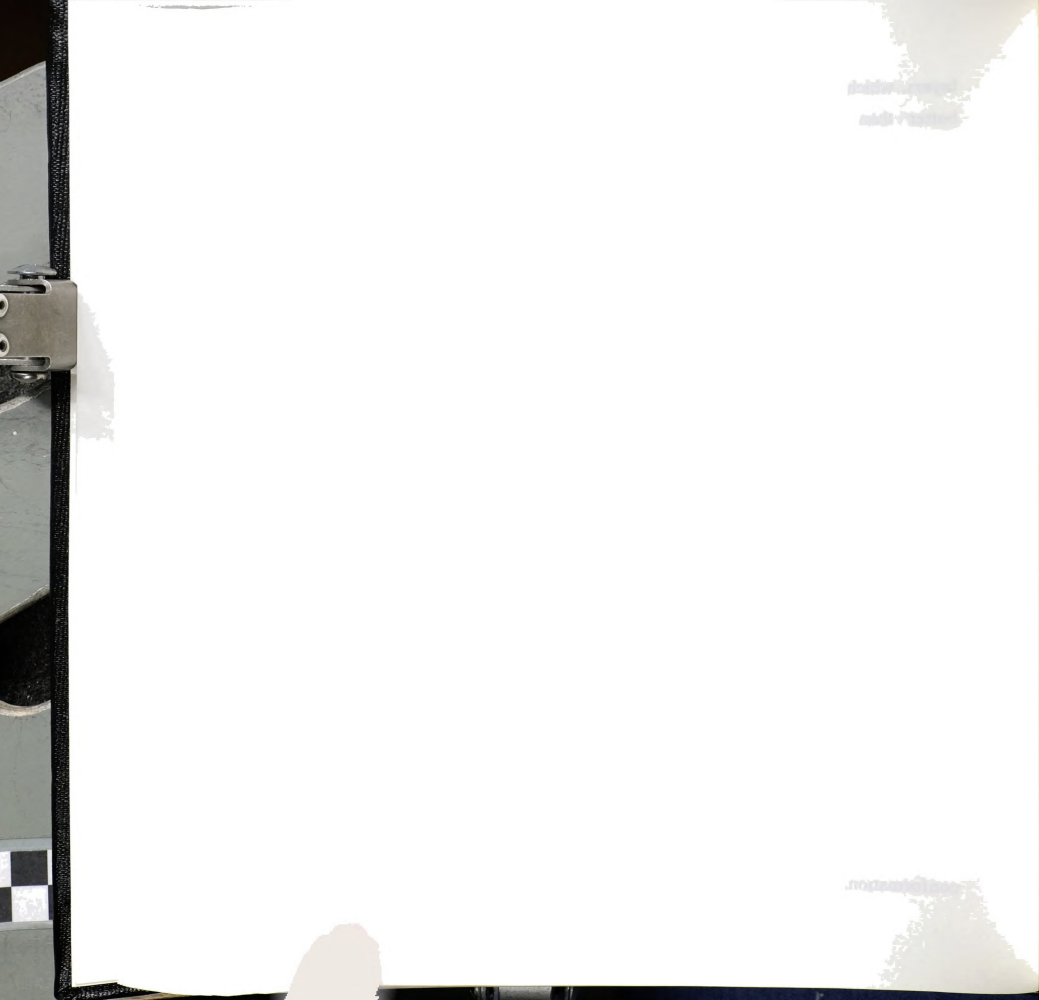


layers, which could make  $\text{Li}_x(\text{PEO})_y\text{RuCl}_3$  a good ion conductor, perhaps better than the amorphous PEO-(alkali-metal) complexes that have segments of helical PEO chains in the structure [43].

## 7. PEO Conformation from IR Spectra

IR spectroscopy may not be used as a decisive technique to probe the PEO conformation in a nanocomposite. The weakness of IR spectroscopy can be seen from the uncertainty of the predictions. The region from 800-1000  $\text{cm}^{-1}$  of the IR spectra is supposed to be sensitive to the conformation of PEO chains. A *trans* O-C-C-O would have absorption peaks around 773 and 992  $\text{cm}^{-1}$ , while a *gauche* O-C-C-O would have absorption around 880 and 944  $\text{cm}^{-1}$  [44]. However, all PEO conformations known have only absorptions around 850 and 950  $\text{cm}^{-1}$ , even those in type I PEO-HgCl<sub>2</sub> complex [30b] and PEO-*p*-nitrophenol complex [38b], in which the *trans* O-C-C-O exists.

Some controversy in the PEO IR peak assignment arises from the disagreement among the type I PEO-HgCl<sub>2</sub> IR data reported [30a, b]. The peaks observed at 1324, 1309, 1014 and 815  $\text{cm}^{-1}$  [30a] were assigned to the *trans* O-C-C-O conformation [44, 26c], because there were no corresponding peaks in the IR spectra of bulk PEO. The more recent and dependable IR spectra of type I PEO-HgCl<sub>2</sub> [30b] did not have peaks at 1309, 1014 and 815  $\text{cm}^{-1}$ , while the spectra of type II PEO-HgCl<sub>2</sub> had peaks at 1312 and 1015  $\text{cm}^{-1}$  [30b]. Recalling the fact that the type I PEO-HgCl<sub>2</sub> converts to type II PEO-HgCl<sub>2</sub> spontaneously [30b], one might suspect that the type I PEO-HgCl<sub>2</sub> sample used by Blumberg and Pollack [30a] contained type II PEO-HgCl<sub>2</sub>. If this is so, 1309 and 1014  $\text{cm}^{-1}$  do not belong to *trans* O-C-C-O conformation. Therefore, 1324  $\text{cm}^{-1}$  may be the only peak that can be



assigned to the *trans* O-C-C-O conformation, as used in some references [26b, e, f]. The spectrum of  $\text{Li}_x(\text{PEO})_y\text{RuCl}_3$  does not have a peak near  $1324\text{ cm}^{-1}$ , see Figure 5.5(c), which suggests that no *trans* O-C-C-O conformation exists. This agrees with the choice of the type II PEO-HgCl<sub>2</sub> conformation proposed in the previous section.

Absorption peaks of  $\text{Li}_x(\text{PEO})_y\text{RuCl}_3$  are compared in Table 5.2 with those of helical PEO, type I PEO-HgCl<sub>2</sub> and type II PEO-HgCl<sub>2</sub> read from the spectra in Reference 30b [45]. Because of the poor resolution of the IR spectrum of  $\text{Li}_x(\text{PEO})_y\text{RuCl}_3$ , some nearby peaks may merge and some weak peaks may not show. In regions II and VII, the peaks of  $\text{Li}_x(\text{PEO})_y\text{RuCl}_3$  match those of type II PEO-HgCl<sub>2</sub>. In region IV, the broad peak at  $1094\text{ cm}^{-1}$  matches the peak  $1100\text{ cm}^{-1}$  of the type II PEO-HgCl<sub>2</sub>. The peak is assigned to C-O stretching and its slight shift to the lower frequency is caused by the coordination of O atoms to  $\text{Li}^+$  ions. The peak at  $1154\text{ cm}^{-1}$  in type II PEO-HgCl<sub>2</sub> is weak, so it does not appear in the  $\text{Li}_x(\text{PEO})_y\text{RuCl}_3$  spectrum. Type II PEO-HgCl<sub>2</sub> has a pair of peaks in both regions III and V, while  $\text{Li}_x(\text{PEO})_y\text{RuCl}_3$  has only one peak in each of them. In type II PEO-HgCl<sub>2</sub> spectra, the two peaks in each pair have a difference of  $31\text{ cm}^{-1}$  or less. Each pair might merge to give a single peak in the nanocomposite spectrum.

The absorption of  $\text{Li}_x(\text{PEO})_y\text{RuCl}_3$  in regions I and VI is more different from that of type II PEO-HgCl<sub>2</sub> than in other regions. The peaks of  $\text{Li}_x(\text{PEO})_y\text{RuCl}_3$  at  $1465$ ,  $1455$  and  $950\text{ cm}^{-1}$ , which are close to those of the helical PEO, may come from PEO chains dangling outside the layers. (Other absorption peaks of free PEO chains may be buried in the absorption of  $\text{Li}_x(\text{PEO})_y\text{RuCl}_3$ .) This explanation satisfies region I. In region VI, the absence of the  $892$  and  $944\text{ cm}^{-1}$  peak in the  $\text{Li}_x(\text{PEO})_y\text{RuCl}_3$

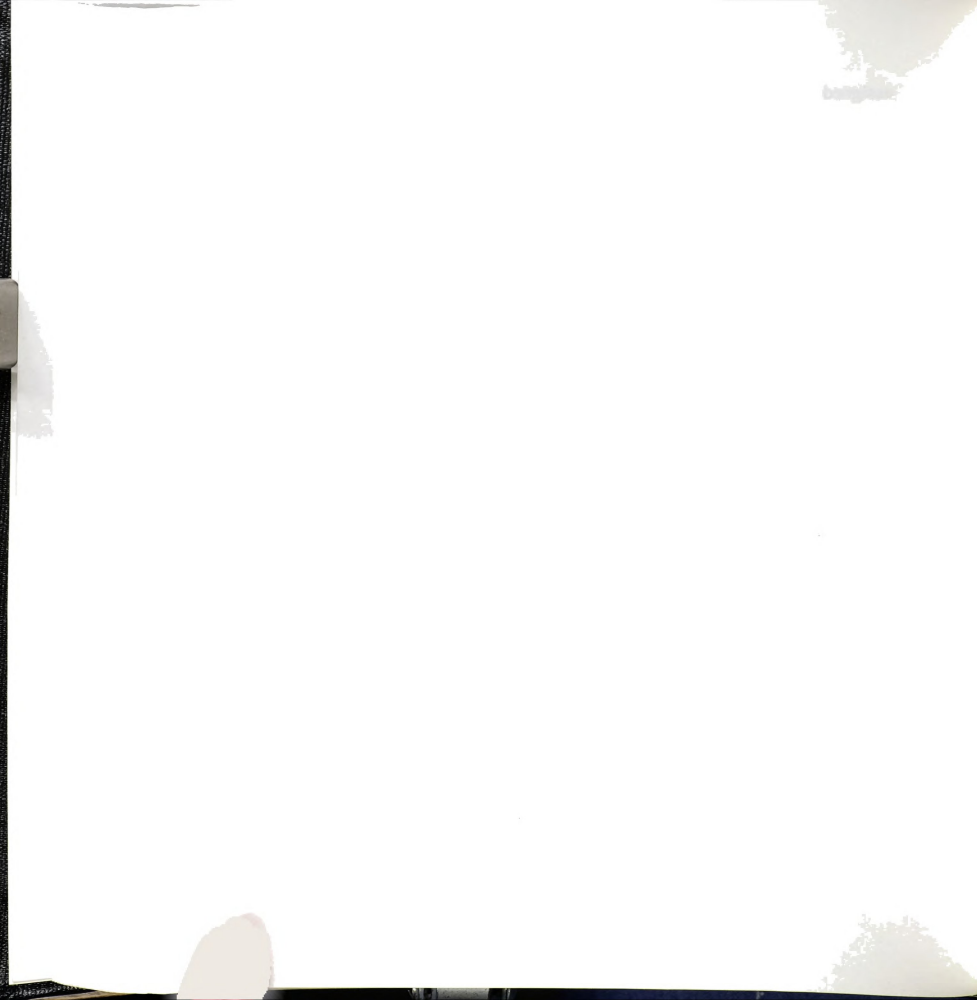


Table 5.2. A comparison of IR absorptions (cm<sup>-1</sup>) of PEO

| Li <sub>x</sub> (PEO) <sub>1.5</sub> RuCl <sub>3</sub><br>(x~0.5) | pure PEO                         | PEO.HgCl <sub>2</sub> (I)        | PEO.HgCl <sub>2</sub> (II)    | region |
|---|----------------------------------|----------------------------------|-------------------------------|--------|
| 1465 (w)<br>1455 (w)<br>1445 (w)                                  | 1462 (s)<br>1456 (w)             | 1468 (s)<br>1451 (s)             | 1445 (s)                      | I      |
| 1352 (w)<br>1303 (w)  | 1355 (w)<br>1338 (s)             | 1350 (s)<br>1328 (m)             | 1356 (m)<br>1312 (s)          | II     |
| 1248 (w)  | 1278 (s)<br><br>1237(m)          | 1278 (s)<br><br>1246 (s)         | 1262 (m)<br><br>1239 (s)      | III    |
| 1094 (vs)   | 1143 (vs) [46]<br>1110 (vs) [46] | 1110 (vs)                        | 1154 (m)<br>1100 (vs)         | IV     |
| 1060 (sh)<br><br>1031 (m)   | 1057 (s)                         | 1064 (s)<br>1044 (s)<br>1032 (s) | 1046 (vs)<br>1015 (vs)        | V      |
| 950 (m)<br>920 (sh)   | 950 (s)                          | 945 (s)                          | 944 (w)<br>923 (s)<br>892 (m) | VI     |
| 846 (m)   | 837 (s) [46]                     | 876 (s)<br>859 (m)<br>831 (m)    | 835 (s)                       | VII    |

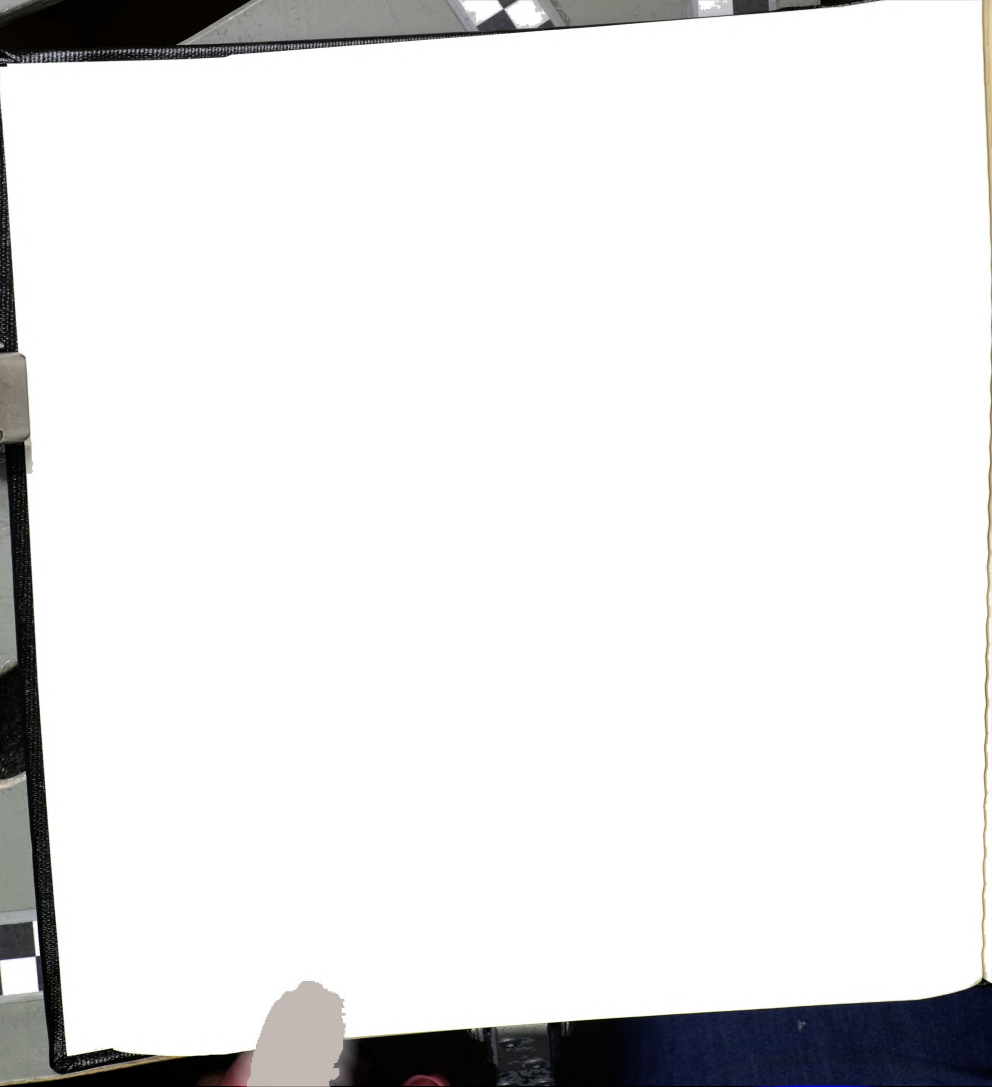


spectrum might be explained by its low intensity. The absorption in this region is contributed mostly by the 950  $\text{cm}^{-1}$  peak of the free PEO chains and the 923  $\text{cm}^{-1}$  peak of the type II PEO-HgCl<sub>2</sub> conformation. In any case, the IR absorption profile of Li<sub>x</sub>(PEO)<sub>y</sub>RuCl<sub>3</sub> matches the spectrum derived from a superposition of the absorption peaks of type II PEO-HgCl<sub>2</sub> conformation and free PEO chains.

### Concluding Remarks

The stability of  $\alpha$ -RuCl<sub>3</sub> in acidic or basic aqueous solutions as well as reducing and oxidizing conditions makes it a suitable compound for intercalation reactions. This is rare among transition-metal halides. The intercalation of  $\alpha$ -RuCl<sub>3</sub> with the conducting polymers PANI and PPY and the water soluble polymers PEO, PVP and PEI gives a new class of lamellar (metal halide)/polymer intercalative nanocomposites. The synthesis of these nanocomposites is enabled mainly by the successful exfoliation of  $\alpha$ -RuCl<sub>3</sub> after controlled lithiation, which allows the use of the exfoliation-encapsulative precipitation method. On the other hand,  $\alpha$ -RuCl<sub>3</sub> is also one of the few layered hosts that are suitable for *in situ* redox intercalative polymerization, which provides an additional approach for new nanocomposites.

$\alpha$ -RuCl<sub>3</sub> nanocomposites contain reduced layers in which free electron hopping, associated with Ru<sup>2+</sup>/Ru<sup>3+</sup> couples, raise the electrical conductivity by 2-3 orders of magnitude. The intercalation of conducting polymers can further increase the conductivity. The dominant carriers in the reduced RuCl<sub>3</sub><sup>x-</sup> layers are holes residing in a narrow t<sub>2g</sub> type band. The reduction of  $\alpha$ -RuCl<sub>3</sub> and its polymer intercalation profoundly affect



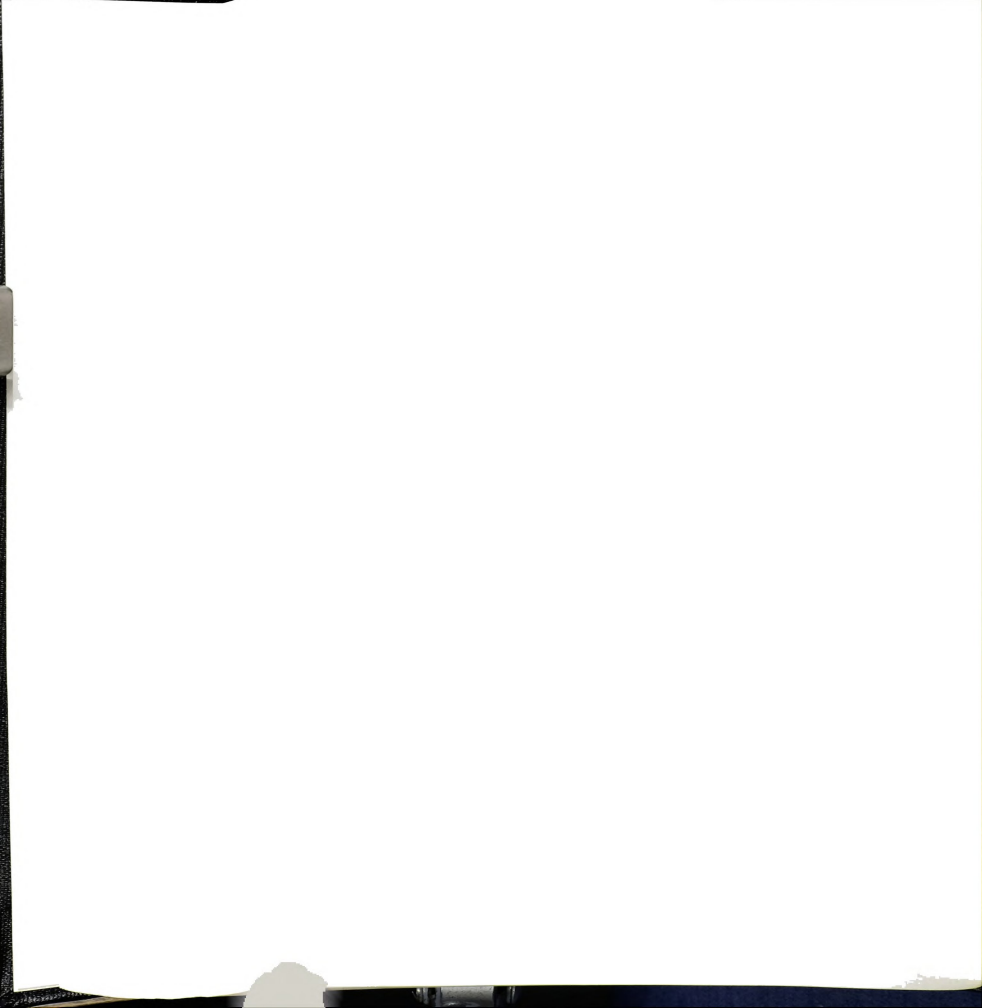
the intralayer and interlayer  $\text{Ru}^{3+}$  magnetic couplings, so that new magnetic properties appear in the nanocomposites. These magnetic properties can be adjusted by oxidation or other chemical manipulations.

Based on X-ray scattering and IR spectroscopy, a structural model is proposed for  $\text{Li}_x(\text{PEO})_y\text{RuCl}_3$ , in which each gallery contains two layers of PEO chains in a conformation found in type II PEO- $\text{HgCl}_2$ . The  $\text{Li}^+$  ions seem to reside exactly in the middle of the interlayer space sandwiched between two monolayer of PEO. The model suggests that  $\text{Li}_x(\text{PEO})_y\text{RuCl}_3$  could have good two-dimensional ion conductivity.

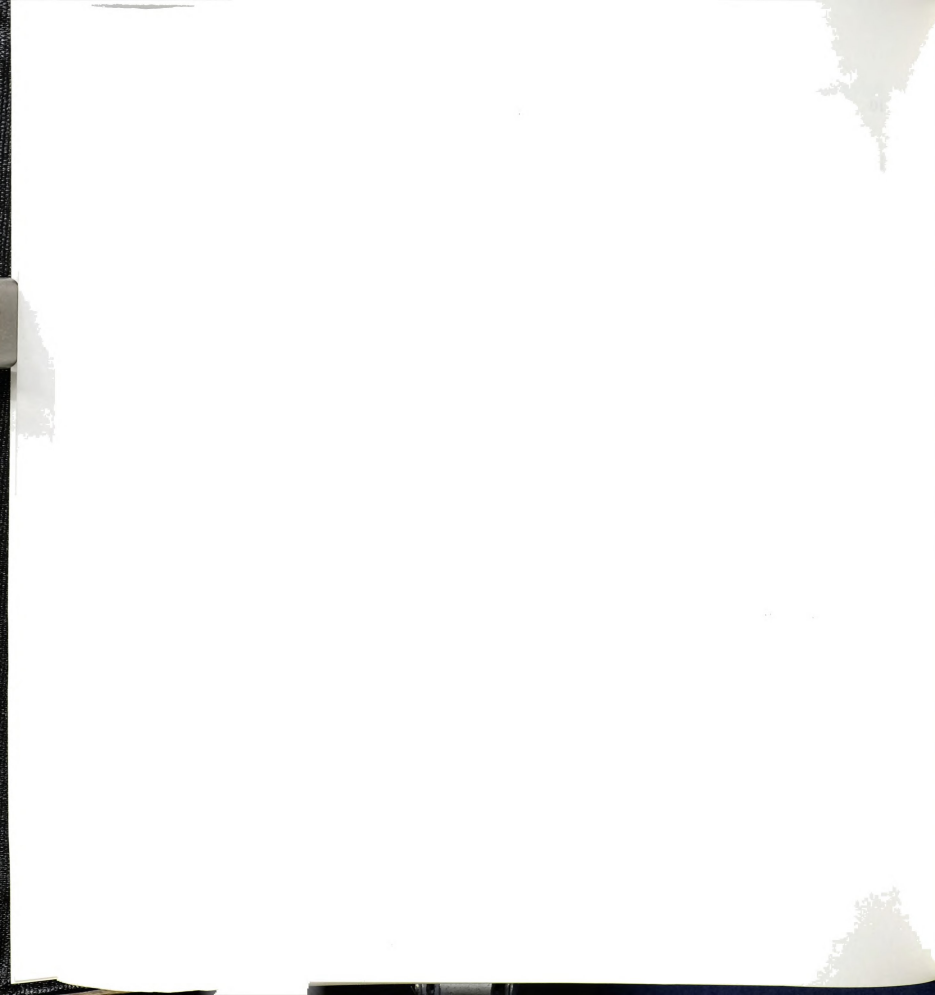


## References

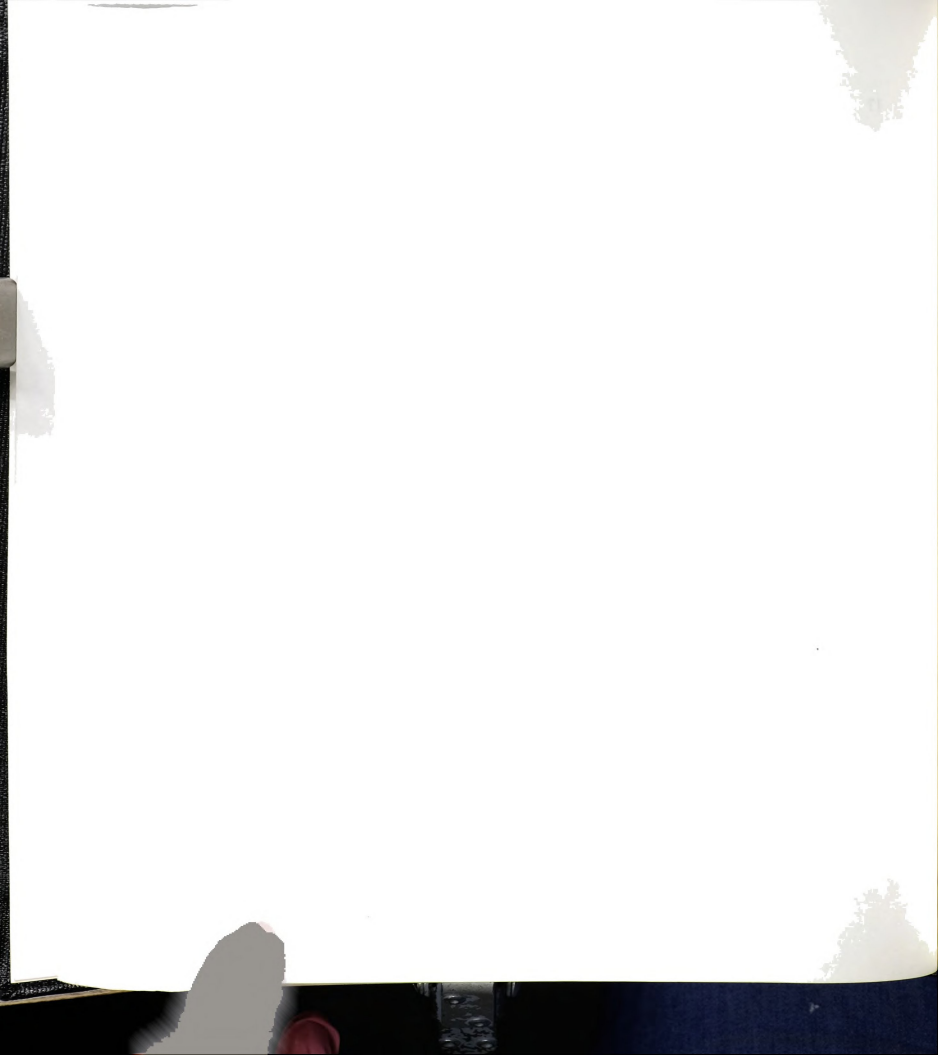
- 1 (a) D. O'Hare, in D. W. Bruce and D. O'Hare ed., *Inorganic Materials*, John Wiley & Sons Ltd, **1992**, pp 164. (b) G. Alberti and T. Bein ed., *Comprehensive Supramolecular Chemistry*, Vol. 7, Elsevier Science Ltd, **1996**.
- 2 (a) F. Leroux, B. E. Koene and L. F. Nazar, *J. Electrochem. Soc.* **1996**, 143(9), L181. (b) F. Leroux, G. Goward, W. P. Power and L. F. Nazar, *J. Electrochem. Soc.* **1997**, 144, 3886.
- 3 Y. Wang and N. Herron, *Science* **1996**, 273 (5275), 632.
- 4 (a) E. P. Giannelis, *Adv. Mater.* **1996**, 8, 29. (b) E. Ruiz-Hitzky, P. Aranda, B. Casal and J. C. Galván, *Adv. Mater.* **1995**, 7, 180.
- 5 (a) C. Schlenker (Ed.), *Low-Dimensional Electronic Properties of Molybdenum Bronzes and Oxides*, Kluwer Academic Pub., Netherlands, **1989**. (b) A. Manthiram and J. Gopalakrishnan, *Rev. Inorg. Chem.* **1984**, 6, 1. (c) J. A. Wilson and A. D. Yoffe, *Adv. Phys.* **1969**, 18, 193. (d) B. E. Taylor, J. Steger and A. Wold, *J. Solid State Chem.* **1973**, 7, 461. (e) R. Brec, D. M. Schleich, G. Ouvrard, A. Louisy and J. Rouxel, *Inorg. Chem.* **1979**, 18, 1814. (f) S. Harris, R. R. Chianelli, *J. Catal.* **1984**, 86, 400. (g) J. Brenner, C. L. Marshall, L. Ellis, N. Tomczyk, J. Heising, M. G. Kanatzidis, *Chem. Mater.* **1998**, 5, 1244.
- 6 (a) J. M. Fletcher, W. E. Gardner, A. C. Fox and G. Topping, *J. Chem.Soc. (A)*, **1967**, 1038. (b) I. Pollini, *Phys. Rev. B* **1994**, 50, 2095.
- 7 R. H. Friend and A. D. Yoffe, *Adv. Phys.* **1987**, 36, 1.
- 8 (a) C.-H. Hsu, M. M. Labes, J. T. Breslin, D. J. Edmiston, J. J. Winter, H. A. Leupold and F. Rothwarf, *Nature, Phys. Sci.*, **1973**, 246 (155), 122. (b) M. G. Kanatzidis, R. Bissessur, D. C. DeGroot, J. L. Schindler and C. R. Kannewurf, *Chem. Mater.* **1993**, 5, 595.
- 9 (a) Y.-J. Liu, D. C. DeGroot, J. L. Schindler, C. R. Kannewurf and M. G. Kanatzidis, *Adv. Mater.* **1993**, 5, 369. (b) L. F. Nazar, Z. Zhang and D. Zinkweg, *J. Am. Chem. Soc.* **1992**, 114, 6239.



- 10 I. Lagadic, A. Léaustic and R. Clément, *J. Chem. Soc., Chem. Commun.*, **1992**, 1396.
- 11 (a) R. Schöllhorn, R. Steffen and K. Wagner, *Angew. Chem. Int. Ed. Engl.* **1983**, 22, 555. (b) R. Steffen and R. Schöllhorn, *Solid State Ionics* **1986**, 22, 31. (c) W. Nonte, M. Lobert, W. Müller-Warmuth and R. Schöllhorn, *Synthetic Metals* **1989**, 34, 665.
- 12 *In situ* redox intercalative polymerization has been successfully applied to FeOCl, V<sub>2</sub>O<sub>5</sub> and VOPO<sub>4</sub>: (a) M. G. Kanatzidis, L. M. Tonge, T. J. Marks, H. O. Marcy and C. R. Kannewurf, *J. Am. Chem. Soc.* **1987**, 109, 3797. (b) C.-G. Wu, M. G. Kanatzidis, H. O. Marcy and C. R. Kannewurf, *J. Am. Chem. Soc.* **1989**, 111, 4139. (c) G. Matsubayashi and H. Nakajima, *Chem. Lett.* **1993**, 31.
- 13 The method of encapsulative precipitation from solutions of exfoliated lamellar solid has been applied to MoS<sub>2</sub>, MoO<sub>3</sub>, TaS<sub>2</sub> and NbSe<sub>2</sub>: (a) R. Bissessur, M. G. Kanatzidis, J. L. Schindler and C. R. Kannewurf, *J. Chem. Soc., Chem. Commun.*, **1993**, 1582. (b) L. Wang, J. Schindler, C. R. Kannewurf and M. G. Kanatzidis, *J. Mater. Chem.* **1997**, 7, 1277. (c) Chapter 3. (d) H.-L. Tsai, J. L. Schindler, C. R. Kannewurf and M. G. Kanatzidis, *Chem. Mater.* **1997**, 9, 875.
- 14 The method of *in situ* polymerization coupled with encapsulative precipitation has been applied to MoS<sub>2</sub>, MoO<sub>3</sub> and WS<sub>2</sub>: (a) L. Wang, J. L. Schindler, J. A. Thomas, C. R. Kannewurf, and M. G. Kanatzidis, *Chem. Mater.* **1995**, 7, 1753. (b) T. A. Kerr, H. Wu and L. F. Nazar *Chem. Mater.* **1996**, 8, 2005. (c) Chapter 2.
- 15 G. Grauer, *Handbook of Preparative Inorganic Chemistry*, Vol. 2, Academic Press Inc., New York, **1965**, pp 1597.
- 16 TGA indicated a total loss of 48.2% in oxygen flow at temperatures up to 650 °C. By comparing with the TGA results of α-RuCl<sub>3</sub> under the same condition which had losses of 32.85 and 33.07% in two trials, the amount of organics and water inside the nanocomposite was determined. The amount of intercalates inside Li<sub>x</sub>(PEO)<sub>y</sub>RuCl<sub>3</sub>, Li<sub>x</sub>(PVP)<sub>y</sub>RuCl<sub>3</sub> and Li<sub>x</sub>(PEI)<sub>y</sub>RuCl<sub>3</sub> was also determined this way.



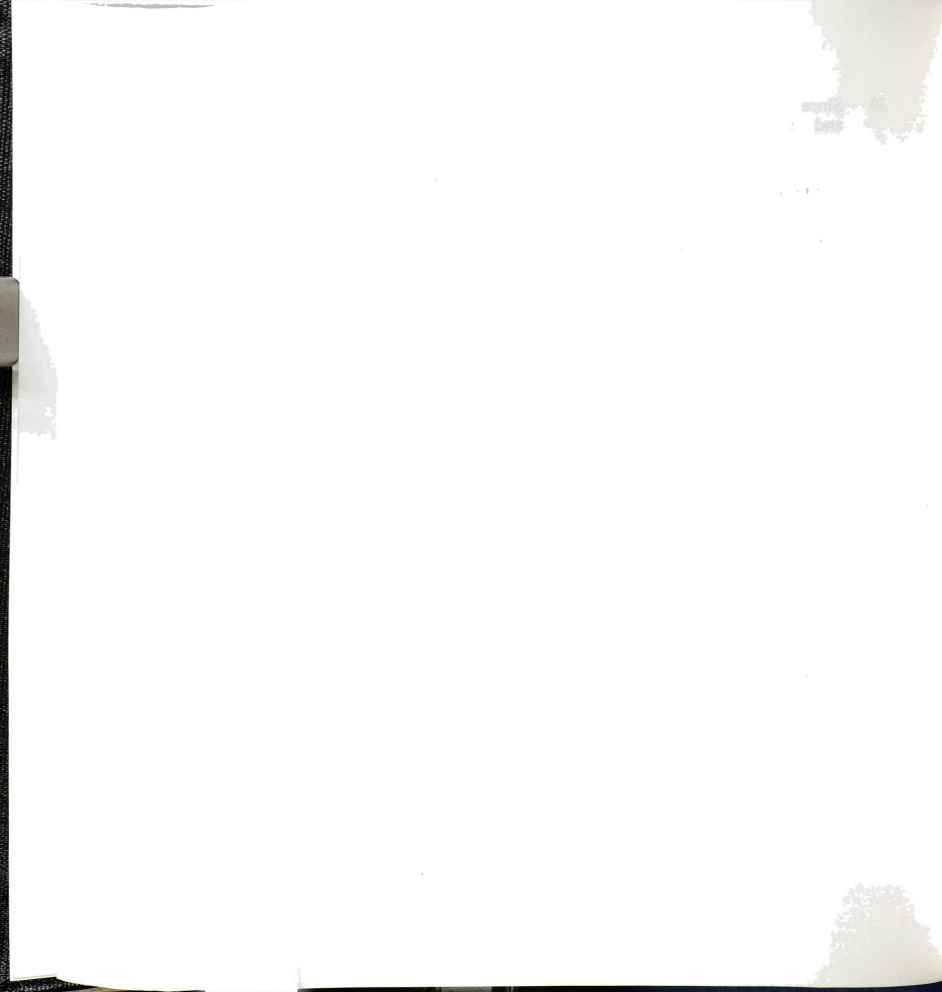
- 17 C.-G. Wu, D. C. DeGroot, H. O. Marcy, J. L. Schindler, C. R. Kannewurf, T. Bakas, V. Papaefthymiou, W. Hirpo, J. P. Yesinowski, Y.-J. Liu, and M. G. Kanatzidis, *J. Am. Chem. Soc.* **1995**, 117, 9229.
- 18 Due to the preferential orientation of the layers on the sample holder, the reflection-mode powder XRD patterns show predominantly the *00l* reflections. The transmission-mode powder XRD patterns show mainly *hk0* reflections.
- 19 Polypyrrole exhibits peaks at 1540, 1300, 1150, 1040 and 900  $\text{cm}^{-1}$ : E. T. Kang, K. G. Neoh, T. C. Tan and Y. K. Ong, *J. Macromol. Sci. -Chem.* **1987**, A24(6), 631.
- 20 The  $(\text{PPY})_x\text{MoS}_2$ , prepared under similar conditions, has an *x* about 0.5. Considering that the unit area of  $\text{RuCl}_3$  is 1.75 times that of  $\text{MoS}_2$ , the amounts of polypyrrole in the galleries are quite comparable. (A  $\text{MoS}_2$  unit cell has one  $\text{MoS}_2$ ; its *a* dimension is 3.159 Å. A  $\text{RuCl}_3$  unit cell has 2  $\text{RuCl}_3$ ; its *a* dimension is 5.87 Å.)
- 21 N. Toshima and O. Ihata, *Synth. Met.* **1996**, 79, 165.
- 22 The choice of solvent is important, because a pyrrole/ $\text{CH}_3\text{CN}$  solution significantly reduces the rate of the reaction and does not produce single-phase  $(\text{PPY})_x\text{RuCl}_3$  even after one month.
- 23 L. Binotto, I. Pollini and G. Spinolo, *Phys. Stat. Sol. (B)*, **1971**, 44, 245.
- 24 Y. Kobayashi, T. Okada, K. Asai, M. Katada, H. Sano and F. Ambe, *Inorg. Chem.* **1992**, 31, 4570.
- 25 The literature value was 2.25  $\mu_B$ , see Reference 24.
- 26 (a) L. F. Nazar, Z. Zhang and D. Zinkweg, *J. Am. Chem. Soc.* **1992**, 114, 6239. (b) P. Aranda and E. Ruiz-Hitzky, *Chem. Mater.* **1992**, 4, 1395. (c) L. F. Nazar, H. Wu and W. P. Power, *J. Mater. Chem.* **1995**, 5, 1985. (d) Y.-J. Liu, J. L. Schindler, D. C. DeGroot, C. R. Kannewurf, W. Hirpo and M. G. Kanatzidis, *Chem. Mater.* **1996**, 8, 525. (e) J. J. Tunney and C. Detellier, *Chem. Mater.* **1996**, 8, 927. (f) Y. Matsuo, K. Tahara and Y. Sugie, *Carbon* **1997**, 35,



113. (g) T. A. Kerr, H. Wu and L. F. Nazar, *Chem. Mater.* **1996**, 8, 2005. (h) G. R. Goward, T. A. Kerr, W. P. Power and L. F. Nazar, *Adv. Mater.* **1998**, 10, 449.
- 27 (a) Y. Takahashi and H. Tadokoro, *Macromolecules* **1973**, 6, 672. (b) J. Brandrup and E. H. Immergut, *Polymer Handbook*, 3rd Ed., John Wiley & Sons, **1989**, New York, pp VI/72.
- 28 F. P. Price and R. W. Kilb, *J. Polym. Sci.* **1962**, 57, 395.
- 29 Y. Takahashi, I. Sumita and H. Tadokoro, *J. Polym. Sci., Polym. Phys. Ed.*, **1973**, 11, 2113.
- 30 (a) A. A. Blumberg and S. S. Pollack, *J. Polym. Sci., Part A*, **1964**, 2, 2499. (b) R. Iwamoto, Y. Saito, H. Ishihara and H. Tadokoro, *J. Polym. Sci., A-2*, **1968**, 6, 1509.
- 31 M. Yokoyama, H. Ishihara, R. Iwamoto and H. Tadokoro, *Macromolecules* **1969**, 2, 184.
- 32 J. M. Parker, P. V. Wright and C. C. Lee, *Polymer* **1981**, 22, 1305.
- 33 (a) Y. Chatani and S. Okamura, *Polymer* **1987**, 28, 1815. (b) P. Lightfoot, M. A. Mehta and P. G. Bruce, *Science* **1993**, 262, 883. (c) P. Lightfoot, J. L. Nowinski and P. G. Bruce, *J. Am. Chem. Soc.* **1994**, 116, 7469. (d) P. Lightfoot, M. A. Mehta and P. G. Bruce, *J. Mater. Chem.* **1992**, 2, 379.
- 34 Y. Chatani, Y. Fujii, T. Takayanagi and A. Honma, *Polymer* **1990**, 31, 2238.
- 35 H. Tadokoro, T. Yoshihara, Y. Chatani and S. Murahashi, *J. Polym. Sci. B*, **1964**, 2, 363.
- 36 H. Tadokoro, *Macromol. Revs.* **1966**, 1, 119.
- 37 J. J. Point and C. Coutelier, *J. Polym. Sci., Polym. Phys. Ed.*, **1985**, 23, 231.
- 38 (a) J. J. Point and P. Damman, *Macromolecules* **1992**, 25, 1184. (b) P. Damman and J. J. Point, *Macromolecules* **1994**, 27, 3919.



- 39 Since the calculated 1-D ED maps for the models with zigzag PEO and type I PEO-HgCl<sub>2</sub> conformations are similar to those for their Li<sub>0.2</sub>(PEO)<sub>x</sub>TaS<sub>2</sub> analogs, Figure 5.13 shows only those for the models with type II PEO-HgCl<sub>2</sub> and double helical PEO conformations.
- 40 This conformation was also suggested for poly(ethylene glycol) (PEG) in kaolinite/PEG nanocomposites [26e], because its hydrophilic side has higher affinity for the highly polar gibbsite Al(OH)<sub>3</sub> side and its hydrophobic side suits the not so polar tetrahedral SiO<sub>2</sub> side.
- 41 This value is estimated from a  $(\cos 2\theta/\sin\theta + \cos 2\theta/\theta)$  correction: H. P. Klug and L. E. Alexander, *X-ray Diffraction Procedures (for polycrystalline and amorphous materials)*, 2nd ed., John Wiley & Sons, New York, 1974, pp 594.
- 42 D.-K. Yang and D. B. Zax, *J. Chem. Phys.* **1999**, 110, 5325.
- 43 Preliminary measurements done by Dr. Jin-Ho Choi's group at Seoul National University, Korea, demonstrate that the ion conductivity of Li<sub>x</sub>(PEO)<sub>y</sub>RuCl<sub>3</sub> at 20 °C is 6.3x10<sup>-5</sup> S/cm, equal to or better than the best (lithium salt)/polymer electrolytes: F. M. Gray, *Solid Polymer Electrolytes*, VCH Publisher, New York, 1991, Chapter 5, pp 83.
- 44 B. L. Papke, M. A. Ratner and D. F. Shriver, *J. Phys Chem. Solids* **1981**, 42, 493.
- 45 Reference 30b provides the spectra of two orientations with the electric vector perpendicular and parallel to the fiber axes. An un-oriented spectrum should be close to the superposition of the two spectra.
- 46 The peaks around 1148, 1112 and 851 cm<sup>-1</sup> are characteristic of the helical PEO conformation: H. Matsuura and T. Miyazawa, *Spectrochim. Acta* **1967**, 23A, 2433.





MICHIGAN STATE UNIV. LIBRARIES



31293018232094